TRINITY COLLEGE DUBLIN
COLÁISTE NA TRÍONÓIDE

THE UNIVERSITY OF DUBLIN

Investigation into the Interactions of Quantum Dot based Systems

Shane Gallagher

A thesis submitted to the University of Dublin, Trinity College for the degree of Doctor of Philosophy.

School of Chemistry and CRANN

Trinity College Dublin

Dublin 2

Ireland

2012

Declaration

This thesis is submitted by the undersigned to the University of Dublin, Trinity College for the examination of Doctorate of Philosophy.

I declare that this thesis has not been submitted as an exercise for a degree at this or any other university and it is entirely my own work. I agree to deposit this thesis in the University's open access institutional repository or allow the library to do so on my behalf, subject to Irish Copyright Legislation and Trinity College Library conditions of use and acknowledgement.

Summary

The main aim of this thesis is to develop a range of new nanomaterials and composite materials based on fluorescent semiconducting nanoparticles (quantum dots). The work involves the synthesis and characterisation of various cadmium containing quantum dots (QDs), along with the investigation of interactions of QDs with various species.

Chapter 1 provides an overview of nanotechnology and introduces the relevant nanomaterials, with particular focus given to fluorescent semiconducting nanoparticles and their properties, and some details of relevant characterisation techniques important to this work. This chapter also outlines the motivation for our research, and sets out our aims.

Chapter 2 describes the details of experimental procedures and techniques used for synthesis of the materials. The characterisation techniques used are also detailed here.

Chapter 3 details the aqueous synthesis of thioglycolic acid stabilised cadmium telluride quantum dots (CdTe TGA QDs) prepared *via* reflux, and a comprehensive characterisation thereof using a range of steady state and time resolved techniques. Subsequently, this chapter focuses on the interactions between CdTe QD and europium complexes, along with an in-depth analysis of optical and electronic properties of this system. This is followed by an investigation of this system as a potential biological sensor.

The investigation of interactions between three -porphyrin based species and CdTe QDs is described in Chapter 4. These materials are subsequently investigated in detail to elucidate the mechanisms and electronic dynamics, using a range of optical analysis techniques.

Chapter 5 details the preparation of novel chiral CdSe and CdTe QDs synthesised using penicilamine or cysteine enantiomeric molecules as stabilisers. The emission properties of these QDs are examined in detail, with both steady state and time

resolved methods employed to gain a deeper understanding of the nature of these QDs. An investigation attempting to control the chiral and luminescent properties of CdTe QDs is also undertaken.

Chapter 6 follows on the investigation of chiral CdSe QDs, using ultrafast transient absorption and time resolved infrared spectroscopy in order to probe the excited state dynamics of these QDs and elucidate the energetics of their defect luminescence. The isotope effect due to changing the solvent from water to deuterium oxide on QD synthesis is also briefly discussed.

The synthesis and optimisation of the deposition of titanium dioxide nanoparticle layers for the fabrication of a working electrode is detailed in Chapter 7, with extensive use of electron microscopy and profilometry. This is followed by the creation of quantum dot sensitised solar cells using chiral QDs, and the measurement of efficiencies achieved for the final devices. The preparation and investigation of QD-carbon composites, combining chiral QDs and either multiwalled carbon nanotubes or graphene, is also described.

Finally, Chapter 8 provides the conclusions of this work, summarising the main achievements, and outlines the aims and avenues of research that are planned for the future.

We expect that the new nanomaterials developed in this project will find a broader range of potential applications. We also believe that this research will contribute to further progress of relevant areas of nanotechnology, chemistry, biosciences and solar technology.

Acknowledgements

First and foremost I would like to thank my supervisor, Prof. Yurii Gun'ko, not only for the endless guidance and support you have provided throughout the past four years, but for giving me the opportunity to and learn and work in this field. I am overwhelmingly grateful for your continued forbearance, and your solid encouragement.

I would also like to thank Prof. John Kelly, and Dr. Susan Quinn for their constant guidance and willingness to discuss the work, your support has been truly invaluable. Thanks also to Dr. Paraic Keane; I greatly appreciate your time and knowledge of all things porphyrin. To Dr. Steve Combys, many thanks for your expertise and patience, even in the face of some genuinely ridiculous questions. To Dr. Michal Wojdyla thank you for sharing your knowledge, as well as a couple of glasses of whiskey in the world for RAL. Also, much gratitude to Dr. Miguel Magno, another fellow traveller in RAL, as well as a SAXS god!

Sincere thanks to the many people who have helped me to measure, examine, analyse and interpret over the last 4 years, both to the group in RAL, Ian Clark, Greg Greetham and Mike Towrie, as well as Manuel Ruther, Neal Leddy and Dr. Marcus Boese here in Trinity. Without all of you, literally none of this stuff makes any sense. Also, many thanks to Fred, Patsy and Martin for your perpetual help and good humour.

I must also extend my genuine gratitude to my fellow lab rats, past and present, for friendship, advice, support, laughter and other shenanigans. Thank you to Amro, Mícheál, Joe Govan, Finn, Lorcan, Cormac, Val, Gemma, Renata, Joe McCarthy, Arunas, Iftikhar, Sarah, Michele and Aine. Thanks too to my students, Miriam, Anna and Camille, your work has contributed in no small part to this thesis.

A big thank you too to my family, to Mum, Dad, Edith and Colin for your constant love and support. It would really make me happy to think I've made you proud.

Lastly, to Sonya (Walshy), the most amazing person I know and now my wife ☺ Everything is infinitely better with you. I cannot say enough how grateful I am for all that you do, and how happy you've made me. Thank you for everything. x

Abbreviations

Abs	Absorption
a.u.	Arbitrary units
B	Relative contribution
BEE	Band edge exciton
X	Chi
°C	degrees Celsius
Cd	Cadmium
CdSe	Cadmium selenide
CdTe	Cadmium telluride
CD	Circular Dichroism
CE	Charged exciton
cm^{-1}	wavenumbers
CNT	Carbon Nanotube
Cys	Cysteine
D-	Dextrorotary
DFT	Density Functional Theory
DMAP	4-Dimethylaminopyridine
DPA	Dipicolinic Acid
DSSC	Dye-Sensitised Solar Cell
e^-	Electron
E	Energy
EDC	N-(3-Dimethylaminopropyl)-N'-ethylcarbodiimide
E_g	Band Gap Energy
Em	Emission

Eq.	Equivalents
eT	Electron Transfer
ET	Energy Transfer
Eu	Europium
Eu.1	Europium cyclen complex
FTO	Fluorine doped Tin Oxide
FF	Fill Factor
FRET	Forster Resonance Energy Transfer
FWHM	Full Width Half Maximum
g	grams
h^+	Hole
$H_2TMPyP4$	Free base porphyrin
HRTEM	High Resolution Transmission Electron Microscopy
I-V	Current/Voltage
ICCD	Intensified Charge Coupled Device
Int.	Intensity
IR	Infrared
I_{SC}	Short Circuit Current
ITO	Indium doped Tin Oxide
λ_{em}	Emission wavelength
λ_{ex}	Excitation wavelength
L-	Levorotary
LED	Light Emitting Diode
LSC	Luminescent Solar Concentrator
M	Molar concentration
MEG	Multiple Exciton Generation

mL	millilitre
µL	microlitre
mM	millimolar
µM	micromolar
MMP	Maximum Power Point
MWNT	Multi Walled Carbon Nanotube
NIR	Near Infrared
nm	nanometre
PCE	Power Conversion Efficiency
Pen	Penicillamine
Pin	Power In
PL	Photoluminescence
P_{max}	Maximum Power
ps	picosecond
PTFE	Polytetrafluoroethylene
P_t	Theoretical Power
PtP	Platinum porphyrin
PV	Photovoltaic
QD	Quantum Dot
QDSSC	Quantum Dot Sensitised Solar Cell
Rac-	Racemate
R_S	Series Resistance
R_{Sh}	Shunt Resistance
SAXS	Small-Angle X-ray Scattering
SEM	Scanning Electron Microscope
SWNT	Single Walled Nanotube

τ	Lifetime
TA	Transient Absorption
TCSPC	Time Correlated Single Photon Counting
TEM	Transmission Electron Microscope
TGA	Thioglycolic Acid
TGA	Thermogravimetric Analysis
TiO_2	Titanium Dioxide
TRES	Time Resolved Emission Spectrum
TRIR	Time Resolved Infrared
UV-vis	Ultraviolet-visible
V_{OC}	Open Circuit Voltage
ZnP	Zinc porphyrin

Table of Contents

Chapter 1: Introduction 1

1.1 Why Nano? - The Huge Possibilities Offered by Small Things 1

1.2 Semiconductors 2

1.3 Quantum dots 5

1.4 Surface Stabilisers 8

1.5 Lanthanides 9

1.6 Porphyrins and Their Interactions with QD Systems 10

1.7 Chirality and Chiral QDs 13

1.8 Transient Absorption Spectroscopy 15

1.9 Solar Cells and Related Problems 17

1.10 The Third Generation - Dye Sensitised Solar Cells 24

1.11 Carbon Nanomaterials 26

1.12 Chirality in Carbon Nanotubes 29

1.13 Carbon Nanomaterials Functionalization 30

1.14 Carbon Nanomaterials and Their Potential for Solar Cells 31

1.15 Aims of this Project 32

References 37

Chapter 2: Experimental 51

2.1 Starting Materials 51

2.2 Synthesis for Chapter 3 51

2.2.1 Preparation of aqueous CdTe nanoparticles by heating under reflux 51

2.3 Synthesis for Chapter 5 52

2.3.1 Preparation of aqueous Selenium stock solution (Na_2SeSO_3) 52

2.3.2 Microwave preparation of aqueous chiral CdSe nanoparticles 52

2.3.3 Microwave preparation of aqueous chiral CdTe nanoparticles 52

2.4 Synthesis for Chapter 7 53

2.4.1 Functionalisation of MWNTs 53

2.4.2 Preparation of graphene oxide 54

2.4.3 Functionalisation of Graphene Oxide 54

2.4.4 Microwave preparation of aqueous chiral CdSe-carbon nanocomposites 55

2.4.5 Microwave preparation of aqueous chiral CdTe-carbon nanocomposites 55

2.4.6 TCO coated glass; specifications and preparation 56

2.4.7 Working electrode fabrication; TiO_2 deposition using the doctor blade method 56

2.4.8 Counter electrode fabrication; Pt deposition using the doctor blade method 57

2.4.9 Solar cell fabrication 57

2.5 Instrumental Techniques and Procedures 58

2.5.1 UV-Vis Absorption spectroscopy 58

2.5.2 PL spectroscopy 58

2.5.3 Fluorescence Lifetime measurements 58

2.5.4 Quantum Yields 59

2.5.5 Circular Dichroism measurements 59

2.5.6 Sonication 59

2.5.7 Microwave 59

2.5.8 Transmission electron microscopy 60

2.5.9 Zeta Potential 60

2.5.10 Small-Angle X-ray Scattering (SAXS) 60

2.5.11 Ultrafast Time-Resolved UV-Vis and Infrared Absorption Spectroscopy – ULTRA system (RAL) 61

2.5.12 Laser flash photolysis spectroscopy 62

2.5.13 Profilometer 62

2.5.14 Solar PCE Measurements 62

2.6 Calculations 65

References 68

Chapter 3: Investigation of the Interactions Between CdTe QDs and a Lanthanide Cyclen System **69**

3.1 Introduction 69

3.2 Synthesis and Characterisation of CdTe TGA QDs 70

3.3 CdTe QD – Eu Cyclen Interactions 77

3.4 Stern-Volmer Analysis and Quenching Dynamics 83

3.5 CdTe QD – $Ln(CF_3SO_3)_3$ Interactions 88

3.6 Transient Absorption Spectroscopy Studies 93

3.7 Low Concentration CdTe QD – Eu Cyclen Interactions 96

3.8 Investigation into Possible Sensing Using QD- Eu Cyclen Systems 97

3.9 Conclusions 105

References 106

Chapter 4: Study of interactions between CdTe QDs and Porphyrin Systems **110**

4.1 Introduction 110

4.2 Free-base Porphyrin (H_2TMPyP_4) and CdTe QDs system 111

4.2.1 Steady State Absorption Spectroscopy 112

4.2.1.1 Investigation of potential metal co-ordination 116

4.2.1.2 Investigation of a potential acid effect 117

4.2.1.3 Investigation of a potential base effect 118

4.2.1.4 Interim Findings 121

4.2.2 Steady State Photoluminescence 122

4.3 Zinc porphyrin ($ZnTMPyP_4$) and CdTe TGA QDs 124

4.3.1 Steady State Absorption Spectroscopy 125

4.3.2 Small-Angle X-ray Scattering 126

4.3.3 Steady State Photoluminescence 128

4.3.4 Transient Absorption Spectroscopy Studies 131

4.4 Platinum Porphyrin and CdTe TGA QDs 138

4.4.1 Steady State Absorption Spectroscopy 138

4.4.2 Steady State Photoluminescence 140

4.5 Conclusions 142

References 144

Chapter 5: Synthesis and Characterisation of New Chiral QDs 146

5.1 Introduction 146

5.2 Synthesis of Chiral Penicillamine Stabilised CdSe QDs 147

5.3 UV- Visible Absorbance Spectroscopy studies 150

5.4 Investigation of CD properties 151

5.5 Photoluminescence Spectroscopy studies 154

5.6 Time Resolved (TR) Spectroscopy studies of Defect Luminescence 158

5.7 Dependence of Emission Lifetimes on Emission Wavelength 159

5.8 Dependence of Emission Lifetimes on Excitation Wavelength 164

5.9 Synthesis of Chiral Cysteine Stabilised CdSe QDs 167

5.10 Synthesis of Chiral CdTe QDs 169

5.11 Conclusions 177

References 178

Chapter 6: Time Resolved Ultrafast Spectroscopy Studies of Chiral CdSe QDs **184**

6.1 Introduction 184

6.2 UV-visible Transient Absorption Spectroscopy Studies of Penicillamine Stabilised CdSe QDs 185

6.3 Picosecond Time-Resolved Infrared Spectroscopy (ps-TRIR) of Penicillamine Stabilised CdSe QDs 187

6.4 Power Dependent Studies 191

6.5 Nanosecond Laser Flash Photolysis Studies 192

6.6 Investigation of Chiral CdSe Prepared in D_2O 197

6.7 Conclusions 200

References 201

Chapter 7: QD-nanocomposites as components of DSSCs **203**

7.1 Introduction 203

7.2 Preparation of Solar Cells – Optimisation of the Working Electrode 204

7.3 Fabrication and Testing of QD /TiO_2 Based Solar Cells 221

7.4 Efficiencies 223

7.5 Preparation of Solar Cells Using QD-Carbon Composites 224

7.6 Carbon Nanomaterials Functionalisation 225

7.7 Synthesis of QD-carbon nanomaterials composites 228

7.8 Conclusions and Future Work 234

References 236

Chapter 8: Conclusions and Future Work **239**

8.1 Conclusions 239

8.2 Future Work 241

Publications

Presentations

List of Figures and Tables

Chapter 1: Introduction

Figure 1.1 Length scale (in nm) showing the nanometer in context. Adapted from literature[1]

Figure 1.2 Diagram of the energy bands of a) a conductor, b) an insulator, c) a semiconductor[2].

Figure 1.3 Diagram showing energy, in the form of a photon (hv), exciting an electron across the band gap of a semiconductor, from the valence band to the conduction band, and the creation of the positive hole.

Figure 1.4 Diagram of the exciton and its Bohr radius.

Figure 1.5 Diagram illustrating the quantum confinement of an exciton, spatially (left) and energetically (right).

Figure 1.6 Illustration showing the shifting absorbance wavelength a particle as a function of decreasing particle size (right to left). Adapted from literature[3].

Figure 1.7 Schematic representation of the band gap (E_g) structure of a semiconducting material and the change in that structure on going from the bulk to the nanoscale. The absorption and subsequent emission pathways upon excitation by a photon are also shown. Adapted from literature[4,5].

Figure 1.8 Photograph showing the effect of increasing quantum confinement/ decreasing particle size (right to left) and the resulting blue shifted, higher energy emission. Adapted from[6].

Figure 1.9 Structure of the parent porphine macrocycle .

Figure 1.10 Generalised Jablonski diagram for common transitions in porphyrins.

Figure 1.11 Illustration demonstrating the nature of chirality.

Figure 1.12 Diagram showing the different regions probed by steady state and transient absorption spectroscopy.

Figure 1.13 Diagram illustrating transient absorption spectroscopy.

Figure 1.14 Graphs showing (a) the maximum % efficiency and (b) outlining the % energy loss, as a function of the band gap energy. Reproduced from[7,8]

Figure 1.15 (Left) LSC with luminophores (dots) absorbing sunlight (blue) and emitting longer wavelength light (red) that is then harnessed by a PV cell. (Right) example of LSCs showing light guided to the edges. Reproduced from [9].

Figure 1.16 Representation of the DSSC structure. Reproduced from[10].

Figure 1.17 Schematic representation of light harvesting by CdSe QDs showing the movement of photogenerated electrons and holes. Reproduced from[9].

Figure 1.18 Illustration of graphene as a 2D building block for carbon materials of all other dimensions such as 0D fullerenes (left), 1D nanotubes (middle) and stacked to form 3D graphite. Reproduced from[11].

Figure 1.19 (a) The unrolled honeycomb lattice of a SWNT. The chiral vector, C_h, is defined by OA and is expressed in terms of integers (n,m). (b) Pictorial representation of the various ways a graphene sheet can be rolled to form a SWNT. (c) The resulting SWNT (adapted from[12]).

Figure 1.20 Pictorial representation of both enantiomers of the chiral diporphyrin.Adapted from literature[13]

Figure 1.21 (Right) Cysteamine molecule and (left) 11-mercaptoundecanoic acid.

Figure 1.22 Structure of the IL electrolyte, 1-methyl-3-propylimidazolium iodide.

Figure 1.23 Structure of the Eu(III) cyclen complex, Eu.1.

Figure 1.24 Structures of the free base H_2TMPyP4, zinc coordinated ZnTMPyP4, and platinum coordinated PtTMPyP4 porphyrins respectively.

Figure 1.25 The *L*- forms of penicillamine left), and cysteine (right).

Table 1.1 Mass and mobility properties of the electron and hole in CdSe.

Chapter 2: Experimental

Figure 2.1 I-V curve of a solar cell under illumination and darkness.

Figure 2.2 I-V curves showing P_{max} , I_{mpp} , V_{mpp} on left, I_{sc} , V_{oc} P_t,in middle and FF on right.

Figure 2.3 IV curves showing the effects of increasing R_s (left graph), increasing R_{sh} (middle graph) and how to estimate the magnitude of R_s and R_{sh} from the inverse of the slope at I_{sc} and V_{oc} (right).

Chapter 3: Investigation of the Interactions Between CdTe QDs and a Lanthanide Cyclen System

Figure 3.1 Illustration of the setup used to produce water soluble CdTe QDs. Al_2Te_3 is decomposed by the dropwise addition of H_2SO_4 and argon carries the evolved H_2Te gas through a solution of $Cd(ClO_4)_2 \cdot 6H_2O$ and the desired thiol. This solution is then heated under reflux.

Figure 3.2 (Left) Photograph of aqueous CdTe TGA QDs of increasing sizes illuminated by UV light. They were synthesised via the method outlined above and refluxed for increasing periods of time (left to right). (Right) Illustration of TGA stabilised CdTe QD.

Figure 3.3 UV-vis absorbance (black) and corresponding emission spectra (red) of CdTe TGA QDs.

Figure 3.4 HRTEM images of CdTe TGA QDs

Figure 3.5 SAXS measurements of CdTe TGA QDs and schematic representation illustrating the results.

Figure 3.6 Zeta potential measurements of CdTe TGA QDs.

Figure 3.7 Lifetime decay curve of CdTe TGA fluorescence decays measured at the maximum of the PL band using a 370 nm "Nanoled".

Figure 3.8 3-D plot of emission decay curves showing the fluorescence *intensity* dependence vs. wavelength.

Figure 3.9 3-D plot of emission decay curves showing the fluorescence *lifetime* dependence vs. wavelength.

Figure 3.10 Nanosecond flash photolysis measurements carried out on CdTe TGA QDs (left) and the instrument response of the laser pulse (right).

Figure 3.11 Scheme showing the binding of the Eu.1 to the surface of a CdTe TGA QD by displacement of two water molecules and coordination of COO^-.

Figure 3.12 Naphthyltrifluoroacetylacetone

Figure 3.13 Scheme outlining sensitised emission of Eu.1 upon titration with nta for determination of concentration via titration

Figure 3.14 (Top) Evolution of the UV-visible spectrum of nta 10^{-5} M in Hepes-buffered solution (0.1 M, pH 7.4) upon addition of 1TA·Eu (0-2 equivalents) at room temperature. (Bottom) The changes observed at 329 nm vs. the number of equivalents 1TA·Eu added.

Figure 3.15 (Top) Evolution of the Eu(III) $^5D_0 \rightarrow {}^7F_2$ transitions of a 10^{-5} M nta solution in Hepes-buffer (0.1 M, pH 7.4) upon addition of 1TA·Eu (0-2 equivalents) at room temperature. (Bottom) The changes in the integrated emission relative to the absorbance at 329 nm vs. the number of equivalents 1TA·Eu added.

Figure 3.16 Absorption spectrum of Eu.1 0.1 M (red) and CdTe TGA QDs (blue), and emission spectrum of CdTe TGA QDs (black) in water. The spectra have been normalized for sake of comparison.

Figure 3.17 Evolution of the fluorescence emission spectrum of CdTe TGA QDs in the presence of increasing concentration of Eu.1. Inset: The changes in the emission integrals of CdTe TGA *vs.* the equivalents of Eu.1 added; [CdTe TGA] = 3.69×10^{-6} M, [Eu.1] = 0 → 3.69×10^{-5} M. λ_{ex} = 420 nm.

Figure 3.18 Fluorescent lifetime decays of CdTe TGA upon addition of Eu.1.

Figure 3.19 Normalised integrated emission (red) and lifetime (blue) intensities

Figure 3.20 The Stern-Volmer plots and their corresponding linear fits of the changes in the fluorescence emission and lifetimes of CdTe TGA in the presence of increasing amounts of Eu.1; [CdTe TGA] = 3.69×10^{-6} M, [Eu.1] = 0 → 3.69×10^{-5} M.

Figure 3.21 The coloured section of the previous Stern-Volmer plot and the corresponding linear fits of the changes in the fluorescence emission and lifetimes of CdTe TGA in the presence of increasing amounts of Eu.1; [CdTe TGA] = 3.69×10^{-6} M, [Eu.1] = 0 → 6×10^{-6} M

Figure 3.22 Linear part of Stern-Volmer plot of the fluorescence emission of CdTe TGA in the presence of increasing amounts of Eu.1; T = 298 K, [CdTe TGA] = 3.69×10^{-6} M, [Eu.1] = 0 → 3.69×10^{-5} M.

Figure 3.23 Evolution of the fluorescence spectrum of CdTe TGA QDs (3.7 μM) in water upon addition of $Eu(CF_3SO_3)_3$ (0→3 equivalents). Inset: The changes in the emission integrals (450-750 nm) *vs.* equivalents of Eu(III) added; T = 298 K and λ_{ex} = 420 nm with Eu.1

Figure 3.24 Evolution of the fluorescence spectrum of CdTe TGA QDs (3.7 μM) in water upon addition of $Tb(CF_3SO_3)_3$ (0→3 equivalents). Inset: The

changes in the emission integrals (450-750 nm) *vs.* equivalents of Tb(III) added; T = 298 K and λ_{ex} = 420 nm.

Figure 3.25 The Stern-Volmer plots of the changes in the fluorescence emission integrals of CdTe TGA QDs in the presence of increasing amounts of Ln(III); [CdTe TGA] = 3.7 μM, [Ln(III)] = 0 → 1.06×10^{-5} M.

Figure 3.26 The Stern-Volmer plots of the changes in the fluorescence emission integrals of TGA-CdTe in the presence of increasing amounts of Ln(III); [CdTe TGA] = 3.7 μM, [Ln(III)] = 0 → 2.74×10^{-5} M.

Figure 3.27 CdTe TGA QDs and 10 equivalents of $Eu(CF_3SO_3)_3$ (left), and Eu.1 (right), respectively.

Figure 3.28 (a) Transient absorption spectra following 400 nm (50 fs) excitation of (a) 3.7 μM CdTe TGA QDs, (b) in the presence of Eu.1 (3 eq.), (c) comparison of kinetics for recovery of bleach at 513 nm in CdTe TGA QDs upon addition of Eu.1.

Figure 3.29 Comparison of the data obtained using two different QDs concentration ([QDs] = 3.7 and 1 μM); Eu.1 = 0 → 10 equivalents; λ_{ex} = 420 n .

Figure 3.30 Evolution of the fluorescence emission spectrum of CdTe TGA in the presence of increasing concentration of Eu.1. ([QDs] = 0.1 μM); Eu.1 = 0 → 10 equivalents; λ_{ex} = 420 nm.

Figure 3.31 Diagram showing the structure of dpa.

Figure 3.32 Scheme illustrating the off-on sensor concept using dpa. Addition of dpa results in removal of the Eu.1 complex from the QD and recovery of emission.

Figure 3.33 Absorption (black), excitation (blue) (λ_{an} = 615 nm) and emission (λ_{ex} = 280 nm, 0.1 ms delay after flash) spectra of a 3.7 μM solution of QDs in the presence of 1eq. Eu.1 and 30eq. dpa. The emission spectrum has

been recorded directly after the addition of dpa (red curve) and 16h later (black curve).

Figure 3.34 Evolution of the fluorescence emission of a 3.7 μM solution of QDs in the presence of 1 eq. Eu.1 upon addition of dpa. The inset shows the changes observed in the integrated emission as a function of the equivalents of dpa added.

Figure 3.35 Evolution of the fluorescence emission of a 1 μM solution of QDs in the presence of 1 eq. Eu.1 upon addition of dpa.

Figure 3.36 Evolution of the Eu(III)-centered emission (λ_{ex} = 280 nm) of CdTe-Eu.1 upon addition of dpa.

Figure 3.37 Evolution of the Eu(III)-centered emission (λex = 280 nm) of CdTe-Eu.1 upon addition of dpa. The inset shows the changes observed in the integrated emission as a function of the equivalents of dpa added.

Figure 3.38 Evolution of the Eu(III) lifetime as a function of the equivalents dpa added.

Figure 3.39 Comparison of the Eu(III) emission (black squares, left y-scale) and lifetime (red circles, right y-scale) changes as a function of dpa equivalents added.

Table 3.1: Quenching constants (K_{SV} and k_q) estimated from the fluorescence quenching experiments (emission and lifetimes) performed on CdTe TGA in the presence of increasing amounts of Eu.1.

Table 3.2: Quenching constants (K_{SV} and k_q) estimated from the fluorescence quenching experiments performed on CdTe TGA in the presence of increasing amounts of Ln(II).

Table 3.3: Lifetimes of the Eu($^5D_0$) excited state in water in the presence of increasing amounts of dpa (λ_{ex} = 280 nm and λ_{an} = 615 nm); each value is the average of at least three different measurements.

Chapter 4: Study of interactions between CdTe QDs and Porphyrin Systems

Figure 4.1 Structures of the free base H_2TMPyP4, zinc coordinated ZnTMPyP4, and platinum coordinated PtTMPyP4 porphyrins respectively.

Figure 4.2 Normalised absorbance (blue) and emission (red) spectra of H_2TMPyP_4 highlighting the Soret band (@ 423 nm) and Q bands, as well as the fluorescence from the triplet state.

Figure 4.3 UV-vis absorbance spectra of CdTe TGA QDs (red) and H_2TMPyP_4 (blue).

Figure 4.4 UV-vis spectrum of the titration of CdTe TGA QDs to H_2TMPyP_4. The rapid decrease in the Soret band at 423 nm and evolution of the peak at 465 nm is clear.

Figure 4.5 UV-vis spectrum of the titration of CdTe TGA QDs to H_2TMPyP_4. There is no signal for the original Soret band at 423 nm, only the peak at 465 nm.

Figure 4.6 UV-vis spectra of H_2TMPyP_4 (black) and following the addition of one equivalent of CdTe TGA QDs (red).

Figure 4.7 UV-vis spectra of CdTe TGA QDs (black) and following the addition of one equivalent of H_2TMPyP_4 (red).

Figure 4.8 UV-vis spectrum showing the Q bands of the free-base porphyrin (black) and after the addition of one equivalent of CdTe TGA QDs (red).

Figure 4.9 UV-vis spectra of H_2TMPyP_4 (black), and after the addition of $Cd(ClO_4)_2$ (red), $MgCl_2$ (blue), $MnCl_2$ (green) and NaCl (pink).

Figure 4.10 UV-vis spectra of H_2TMPyP_4 after the reduction of the pH of solution to pH 2 using HCl.

Figure 4.11 UV-vis spectra of the titration of NaOH to H_2TMPyP_4 pH 7 – 14 showing the entire wavelength range.

Figure 4.12 UV-vis spectra of the titration of NaOH to H_2TMPyP_4 pH 7 – 14 focusing on the Soret band shift.

Figure 4.13 UV-vis spectra of the titration of NaOH to H_2TMPyP_4 pH 7 – 14 focusing on the Q bands.

Figure 4.14 UV-vis spectra of addition of 1.8 nm CdTe TGA QDs to H_2TMPyP_4 showing, (a) the shift in the Soret band and (b) the Q bands at no QDs (black), 0.15 eq. (red), and 1 eq. (blue) of QDs.

Figure 4.15 Schematic representation of binding between H_2TMPyP_4 and TGA capped CdTe QDs.

Figure 4.16 (Top) Emission spectra of the titration of CdTe TGA QDs to H_2TMPyP_4 showing the quenching of the porphyrin emission and (after 1 equivalent) recovery of the QD emission. (Bottom) Change in porphyrin emission intensity at 705 nm.

Figure 4.17 (Top) Emission spectra from the titration of H_2TMPyP_4 to CdTe TGA QDs showing the quenching of the QD emission. (Bottom) Change in QD emission intensity at 555 nm.

Figure 4.18 Normalised absorbance (blue) and emission (red) spectra of ZnTMPyP4 highlighting the Soret band (@ 436 nm) and Q bands, as well as the fluorescence from the singlet state.

Figure 4.19 (a) UV-vis spectrum of the titration of CdTe TGA QDs to ZnTMPyP4 and (b) the Soret band shift on addition of QDs (0 - 0.25 equivalents).

Figure 4.20 UV-vis spectrum of the titration of ZnTMPyP4 to CdTe TGA QDs.

Figure 4.21 Normalized small-angle X-ray scattering (SAXS) curve and size distribution results obtained for (a) CdTe, (b) CdTe:ZnP (4:1), (c) CdTe:ZnP (2:1), (d) CdTe:ZnP (1:1) and (e) CdTe:ZnP (1:2). The CdTe illustrations at different CdTe:ZnP ratios are also shown.

Figure 4.22 Fluorescence spectra showing quenching of ZnTMPyP4 emission and emergence of CdTe-TGA emission.

Figure 4.23 Diagram showing quenching of ZnTMPyP4 emission and emergence of CdTe-TGA emission with increasing CdTe-TGA concentration.

Figure 4.24 Quenching of CdTe emission at increasing ZnTMPyP4 conc. Inset: Corresponding emission spectra of CdTe-TGA.

Figure 4.25 Diagram of the excitation and relaxation of ZnP. Purple arrow denotes heavy atom effect, resulting in increased yield of the triplet state.

Figure 4.26 Scheme illustrating electron transfer from CdTe QD to ZnP after excitation.

Figure 4.27 Nanosecond TA spectra of ZnP (top right) and CdTe:ZnP 2:1 (bottom right). Porphyrin conc. is the same in both cases. Also shown is the comparison of the bleach and transient intensities in the absence (top left) and presence (bottom left) of CdTe. Pump wavelength @ 355 nm.

Figure 4.28 The decays measured over long times showing (left) slow decay of the transient at 485 nm and (right) slow bleach recovery of ZnP in the presence of CdTe, 2:1 (triplet lifetime of free ZnP is 3 μs).

Figure 4.29 Transient absorption spectra of CdTe TGA with (inset) kinetic profiles over the first 15 ps. Pump wavelength @ 400 nm.

Figure 4.30 Transient absorption spectra of CdTe TGA over the first 1 ps. Pump wavelength @ 400 nm.

Figure 4.31 Transient absorption spectra of ZnP with (inset) kinetic profiles over the first15 ps. Pump wavelength @ 400 nm.

Figure 4.32 (a) ps-TA spectrum of 2:1 CdTe-TGA:ZnTMPyP4 up to 10 ps after pump pulse. Inset: spectra at longer time delays up to 3 ns. (b) Kinetics at short times. (c) Kinetics at longer times.

Figure 4.33 Comparison of the ZnP and QD decays at 445 nm and 510 nm respectively.

Figure 4.34 Diagram and scheme of possible electron transfer and quenching mechanism.

Figure 4.35 Normalised absorbance (blue) and emission (red) spectra of PtTMPyP4 highlighting the Soret band (@ 402 nm) and two Q bands, as well as the phosphorescence from the triplet state.

Figure 4.36 UV-vis spectrum of the titration of (a) CdTe TGA QDs to PtP, and (b) PtP to CdTe TGA QDs.

Figure 4.37 (a) Emission spectrum of the titration of CdTe TGA QDs to PtP. (b) Quenching of PtP and (c) recovery of QD emission.

Figure 4.38 (a) Emission spectrum of the titration of PtP to CdTe TGA QDs. (b) Quenching of QD emission.

Chapter 5: Synthesis and Characterisation of New Chiral QDs

Figure 5.1 Illustration comparing heating using microwave irradiation (left) and reflux (right). Adapted from[14].

Figure 5.2 Reaction scheme for the preparation of *D*- and *L*- penicillamine stabilised CdSe nanoparticles

Figure 5.3 Diagram of 2^2 statistical analysis of penicillamine stabilised CdSe nanoparticles. The cadmium concentration is varied in the y direction, penicillamine in the x direction.

Figure 5.4 UV-vis absorbance spectrum of D- (blue), L- (red), Rac- (green) Pen CdSe QDs.

Figure 5.5 Circular dichroism spectra of D- (blue), L- (red), Rac- (green) Pen CdSe QDs.

Figure 5.6 Monitoring the synthesis of *L*-Pen CdSe using CD spectroscopy.

Figure 5.7 Photoluminescence spectra of D- (blue), L- (red), Rac- (green) Pen CdSe QDs.

Figure 5.8 Comparison of the absorbance and emission spectra of *L*-Pen CdSe QDs(black and pink) and CdTe TGA QDs (blue and red).

Figure 5.9 Comparison of the absorbance and emission spectra of *L*-Pen CdSe QDs synthesised via microwave irradiation (blue) and under reflux (red).

Figure 5.10 (a) Transmission Electron Microscopy (TEM) and (b) High Resolution TEM of *L*- Pen CdSe QDs.

Figure 5.11 3-D plot of emission decay curves showing the fluorescence *intensity* dependence vs. wavelength.

Figure 5.12 3-D plot of emission decay curves showing the fluorescence *lifetime* dependence vs. wavelength.

Figure 5.13 3-D plot of emission decay curves focusing of either extremes of the spectrum.

Figure 5.14 Contour plot constructed from the normalized emission decay curves of CdSe L- Pen measured at different wavelengths with step 5nm (PL intensity scale is logarithmic).

Figure 5.15 Plot of chosen decays curves constructed from slices of 450 – 770 nm scan @ 20 nm intervals. Excited with 295 nm "Nanoled".

Figure 5.16 Time resolved emission spectra of CdSe *L*- Pen obtained by PL kinetic tracesslicing (using a moving time window (ca. 48ns) at delays given in the legend.(a) Cumulative log counts measured at constant acquisition time and (b) normalized to unity. The full width half max for these curves are decreasing from 580 (top curve) to 500 meV (bottom curve).

Figure 5.17 UV-vis absorbance spectrum of D- (blue), L- (red), Rac- (green) Cys CdSe QDs.

Figure 5.18 Photoluminescence spectra of D- (blue), L- (red), Rac- (green) Pen CdSe QDs.

Figure 5.19 Circular dichroism spectra of D- (blue), L- (red), Rac- (green) Pen CdSe QDs.

Figure 5.20 Optical spectra (UV-vis absorption - left, and emission – right) of CdTe nanocrystals stabilized with *D*- (blue), *L*- (green) and *Rac*-Cys (red). Excitation wavelength for all emission spectra is 470nm.

Figure 5.21 The observed changes in the QYs are dependent on the ratio of *D*- to *L*-cysteine present on the quantum dots. 0% *L*-Cys corresponds to pure *D*-cysteine, 100% *L*-Cys corresponds to pure *L*-cysteine stabilised dots. The point at 50% is, of course, the racemate. Insert: a photograph of *D*-, *Rac*- and *L*- Cysteine stabilised CdTe QDs under UV light.

Figure 5.22 HRTEM images of *D*-, *L*- and *Rac*- of cysteine stabilised CdTe nanocrystals.

Figure 5.23 CD spectra of *D*- (blue), *L*-(green), and *Rac*-(red) cysteine stabilised CdTe. Despite the clear structure and the mirror imaging of the *D*- and *L*- scans, the signals are extremely weak.

Figure 5.24 CD spectra monitoring the formation of *D*-Cys CdTe QD's. a) *D*-Cys stabiliser absorbs negatively at ~210 nm. b) The addition of Cd ions

forms a Cd-Cys complex and causes the appearance of a new band at ~233nm. c) The clusters after addition of the sodium tellurite before the microwave treatment – new bands from 250 to 405 nm (blue). d) CdTe QD's after the microwave treatment –all signals beyond 255nm have practically disappeared with only the Cd-Cys complex signal remaining strong.

Figure 5.25 UV-Vis and Pl spectra of *D*- (blue) and *L*- (green) Cys/Pen mixed ligand CdTe nanoparticles. Particles were excited at 500nm. The ratio of cysteine to penicillamine used here was 2:3.

Figure 5.26 CD spectra of *D*- (blue) and *L*- (green) Cys/Pen mixed ligand CdTe nanoparticles. The ratio of cysteine to penicillamine is 3:2

Table 5.1 Quantum yields and tri-exponential fitting parameters (lifetimes and relative contributions) for the fluorescence decays measured at the maximum of the PL bands using a 370 nm "Nanoled".

Table 5.2 The fitting parameters (lifetimes and relative contributions) obtained from a tri -exponential fit to PL decay data for *L*- Pen capped CdSe measured at different emission wavelengths and excited with a 295 nm "Nanoled".

Table 5.3 The fitting parameters (lifetimes and relative contributions) obtained from a tri -exponential fit to PL decay data for argon degassed *L*- Pen capped CdSemeasured at different emission wavelengths and excited with a 295 nm "Nanoled".

Table 5.4 The fitting parameters (lifetimes and relative contributions) obtained as a result of a tri -exponential fit to PL decay data for *L*- Pen capped CdSe collected at 450, 560 and 705 nm from excitation at 295, 340 and 370 nm.

Chapter 6: Time Resolved Ultrafast Spectroscopy Studies of Chiral CdSe QDs

Figure 6.1 (a) and (c) Picosecond transient absorption spectra following 400 nm excitation of *L*-Pen CdSe at 100 nJ (0.56 mJ/cm^2) and 5 nJ (28 μJ/cm^2), respectively. Artefact (*) at about 400 nm is due to excitation line. (b) Normalized decay curves of the bleach (422 nm, black) and transient absorption (600 nm, red) following 400 nm excitation of L-Pen CdSe at 100 nJ. The bleach decay curve has been inverted for comparison. (d) Comparison of the normalised bleach decays at 100 nJ (black) and 5 nJ (blue) at 422 nm.

Figure 6.2 TRIR spectra following 400 nm excitation of *L*-Pen CdSe at 50 nJ (0.28 mJ/cm^2) in H_2O.

Figure 6.3 TRIR spectra following 400 nm excitation of (a) *D*-Pen and (b) *Rac*-Pen CdSe at 50 nJ (0.28 mJ/cm^2) in H_2O.

Figure 6.4 (a) The fs growth of the IR transient and (b) triexponential fit of the IR transient absorption decay curve of *L*- Pen CdSe (1837 cm^{-1}). The fitting parameters (baseline parameter A_0, lifetimes τ and percentage contributions) are given in the inset.

Figure 6.5 Triexponential fit of the IR transient absorption decay curve of *D*- and *Rac*- Pen CdSe (1837 cm^{-1}) for comparison.

Figure 6.6 Comparison of bleach (420nm, inverted) and IR kinetics at 1000 ps (50nJ, 1837 cm^{-1}), 400nm excitation.

Figure 6.7 Normalised IR transient absorption decay curves recorded using 10 nJ and 50 nJ, 400 nm excitation.

Figure 6.8 (a) Time resolved absorption spectra of *L*-Pen CdSe obtained by kinetic traces slicing at desired time windows and delays (0, 16, 31, 47, 62, 78,

95, 109, 125, 140 μs)measured at 308 nm excitation (58 mJ/cm^2). Kinetic curves were recorded by averaging 10 laser shots per one wavelength measurement with steps of 10 nm. (b) Transient absorption spectrum of *L*-Pen stabilized CdSe recorded using an ICCD camera over initial 3 μs after excitation (signal was averaged from 60 laser shots).

Figure 6.9 (a) The decay curve of the bleach at 440 nm and (b) transient at 600 nm for *L*-Pen capped CdSe. Red lines represent (a) mono and (b) biexponential fits to the data. Kinetic curves were recorded by averaging 50 laser shots.

Figure 6.10 Suggested electronic structure of chiral CdSe QDs.

Figure 6.11 Uv-vis absorbance spectrum of D-, L- and Rac- Pen CdSe QDs synthesised in D_2O.

Figure 6.12 PL spectrum of D-, L- and Rac- Pen CdSe QDs synthesised in D_2O.

Figure 6.13 TRIR spectra following 400 nm excitation of *L*-Pen CdSe at 100 nJ (0.56 mJ/cm^2) in D_2O. Artefact (*) is due to switching from the 1st to the 2nd IR detector.

Table 6.1 Lifetime parameters obtained from tri- and bi- exponential fitting of ps-TA decay curves for pulse energies of at 100 nJ (0.56 mJ/cm^2) and 5 nJ (28 μJ/cm^2), respectively.

Table 6.2 Lifetime parameters obtained from 3-exponential fitting of ps-TRIR decay curves. Pulse energy at 50 nJ (0.28 mJ/cm^2).

Chapter 7: QD-Nanocomposites as Components of DSSCs

Figure 7.1 SEM of the FTO layer on glass. Thickness is measured to be approximately 330 nm.

Figure 7.2 Sample SEM images of the resulting TiO_2 films obtained after multiple layer deposition and sintering. (a) The entire cell layer, (b) the cracks throughout the film.

Figure 7.3 (a) Side on and (b) top down view profilometer measurements of the resulting TiO_2 films obtained after multiple layer deposition and sintering.

Figure 7.4 Raman spectra of TiO_2 film, showing the characteristic anatase peaks.

Figure 7.5 (a-c) Side on SEM images of four layers TiO_2. The depth of the cracking along with the poor adhesion to the base FTO is obvious. The lack of interface between the TiO2 layers is also clear, compared to (d), reproduced from[16]. Note the top layer seen in (a-c) is larger particulate TiO_2.[15]

Figure 7.6 Sample of SEM images showing the poor resulting layer quality obtained from multi-layer deposition of TiO_2. (a-e) Cracking can be seen throughout the entire layer, (b) there is poor adhesion to the cell base, and (d-f) obvious pitting in the TiO_2 surface.

Figure 7.7 SEM images of single layer (a, b) Dyesol 18NR-T, and (c, d) Dyesol 90T TiO_2 pastes deposited using black tape.

Figure 7.8 Profilometer measurement of single layer Dyesol paste deposited with black electrical tape. The 'squaring' of the image and rise towards the middle is again software related, caused by stitching the map together.

Figure 7.9 SEM images of single layer Dyesol 18NR-T TiO_2 paste deposited using Scotch tape.

Figure 7.10 SEM images of single layer Dyesol 90T TiO_2 pastes deposited using Scotch tape.

Figure 7.11 Profilometer measurement of single layer Dyesol paste deposited with Scotch tape. The 'squaring' of the image and rise towards the middle is again software related, caused by stitching the map together.

Figure 7.12 SEM images of single layer Eternal Company Ti-2105-3 paste deposited using (a-c) black tape, and (d-f) Scotch tape respectively.

Figure 7.13 Profilometer measurement of single layer Eternal Company Ti-2105-3 paste deposited with black tape. The 'squaring' of the image is again software related.

Figure 7.14 SEM images of single layer Solaronix Ti-Nanoxide D paste depositedusing (a -c) black tape, and (d-f) Scotch tape respectively. The presence of the larger scattering TiO_2 particles also present in this paste can be seen in (c) and (f).

Figure 7.15 Profilometer measurement of single layer Solaronix Ti-Nanoxide D paste deposited with Scotch tape. The 'squaring' of the image is again software related.

Figure 7.16 Profilometer map of the SolarPrint electrode made from Eversolar® P-200, 20-50 nm TiO_2 paste via screen printing. The relatively smooth nature of the film is clearly evident.

Figure 7.17 SEM images of SolarPrint electrode made from Eversolar® P-200, 20-50 nm TiO_2 paste via screen printing.

Figure 7.18 (Right) Cysteamine molecule and (left) 11-mercaptoundecanoic acid

Figure 7.19 Reaction scheme for functionalisation of MWNTs with cysteamine.

Figure 7.20 Mechanism illustrating the role of EDC in facilitating the amide coupling reaction

.**Figure 7.21:** TGA analysis of pristine and functionalised MWNTs (derivative graph).

Figure 7.22 Selection of TEM images showing the presence of QDs on the surface of the graphene.

Figure 7.23 Selection of TEM images showing the presence of QDs on the surface of the functionalised graphene.

Figure 7.24 Selection of TEM images showing the presence of QDs on the surface of the functionalised graphene.

Figure 7.25 Selection of TEM images showing the presence of QDs on the surface of the functionalised graphene.

Figure 7.26: Structure of the IL electrolyte, 1-methyl-3-propylimidazolium iodide.

Table 7.1 Results from the various combinations of pastes and tapes used. X = poor quality film with cracks, ✓= good quality film deposited with little to no defects.

Table 7.2 The total combinations of QDs and electrodes brought further for testing

Table 7.3 Efficiencies obtained from the various QD-electrode combination

References

(1) http://publications.nigms.nih.gov/chemhealth/cool.htm

(2) *http://wps.prenhall.com/wps/media/objects/602/616516/MediaAssests/Chapter21/Text_Images/FG21_10.JPG.*

(3) http://www.elec-intro.com/evident-technologies.

(4) Chestnoy, N.; Harris, T. D.; Hull, R.; Brus, L. E. *The Journal of Physical Chemistry* **1986**, *90*, 3393.

(5) Brus, L. *IEEE J. Quant. Elec.* **1986**, *22*, 1909.

(6) *http://gizmodo.com/5514438/quantum-dots-could-make-dark-grainy-cellphone-party-pics-obsolete.*

(7) Eli, Y.; Owen, M.; Optical Society of America: 2010, p SWA1.

(8) Yong-Hang, Z.; Ding, D.; Johnson, S. R.; Lim, S. H.; Optical Society of America: 2010, p SWC4.

(9) Boer, D. K. G. d. *SPIE Newsroom* 2010.

(10) Grätzel, M. *Inorganic Chemistry* 2005, *44*, 6841.

(11) Kamat, P. V. *The Journal of Physical Chemistry C* 2008, *112*, 18737.

(12) R. Reisfeld; Jørgensen, C. K. *Structure and Bonding* 1982, *49*, 1.

(13) Peng, X.; komatsu N.; Bhattacharya, S.; Shimawaki, D.; Aonuma, S.; Kimura, T.; Osuka, A. *Nature Nanotechnology* 2007, 2, 361

(14) D. S. Ginley and D. Cahen, Fundamentals of Materials for Energy and Environmental Sustainability, Cambridge University Press, 2011.

(15) *http://www.biotage.com/DynPage.aspx?id=22052.*

(16) Ito, S.; Kitamura, T.; Wada, Y.; Yanagida, S. *Solar Energy Materials & Solar Cells* 2003, *76*, 3.

Chapter 1: Introduction

1.1 Why Nano? - The Huge Possibilities Offered by Small Things

Nanoscience and nanotechnology are areas focused on the research and development of materials with scales on the nanometre range, i.e. between 1 and 100 nm. To put this into context, one nanometre (nm) is 100,000 times smaller than a full stop (Figure 1.1).

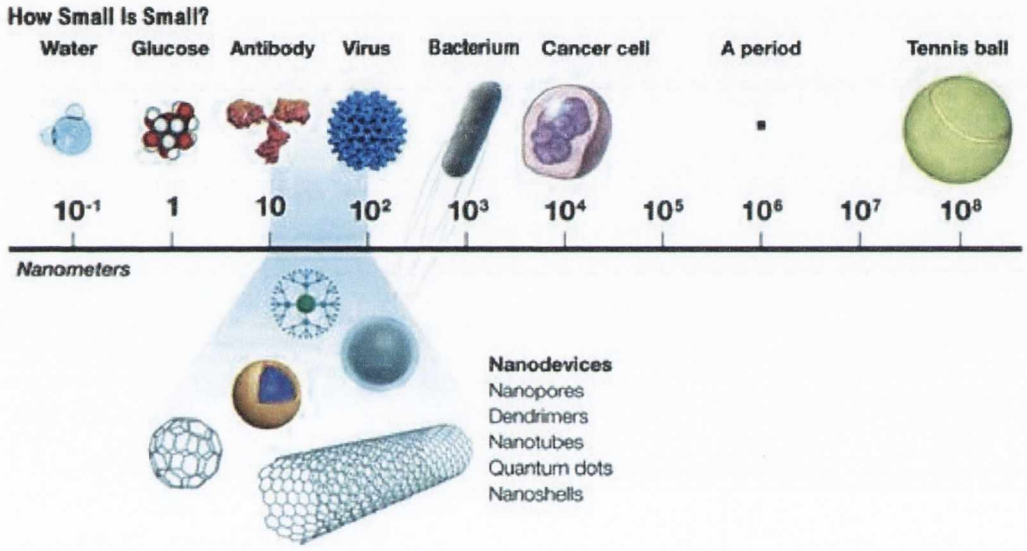

Figure 1.1: Length scale (in nm) showing the nanometer in context. Adapted from literature[1].

The massive growth in interest, research and investment in this area of science is paralleled by the equally large potential offered by these unique materials. Features such as high surface-to-volume ratios, controllable surfaces, improved solubility and multifunctionality make these materials extremely well suited for a range of applications.

The properties exhibited by nanomaterials can also differ greatly from those of their bulk counterparts. Examples include the size dependent optical properties of semiconducting quantum dots[2], the superparamagnetism displayed by magnetic nanomaterials (e.g. nano Fe_3O_4)[3], and the exceptional strength and conductivity of graphene[4] and carbon nanotubes[5,6], to name but a few. The vast array of controllable

features on offer with nano-based materials makes them highly desirable, and theoretically suited to an almost infinite range of potential roles, from biological applications such as drug delivery, antibacterial agents and biological imaging[7], to advanced computing[8], superior catalysts[9], and improved solar technology[10].

This project is focused on the development of new semiconducting nanomaterials, and semiconducting-based-hybrid nanomaterials, for potential applications in biotechnology and solar cell technology.

1.2 Semiconductors

Semiconductors are materials whose name derives from the fact that they are non-conductive when pure or at a low temperature, but when doped with a suitable impurity (dopant) or heated to a higher temperature, exhibit conductivity between that of insulators and most metals[11].

Binary semiconductors are named according to their metallic element's valence number and their non-metallic element's group number. For example, CdS, is a II-VI semiconductor (Cd^{2+} has a valence of II, S^{2-} is in group VI). The ability of these compounds to exhibit properties intermediate to those of conductors and insulators is a result of the overlapping of their atomic orbitals in an ordered crystalline lattice. This creates a continuum of position independent electronic energy levels, called *bands*. A semiconductor possesses not only a valence band but also a conduction band, corresponding to the bonding and antibonding orbitals in a molecule.

The size of the band gap of any semiconductor is dependent on its constituent elements (and temperature) and cannot be altered; consequently a material may be identified by its band energy (Figure 1.2). However, an impurity or dopant, with a smaller band gap, may be used to "bridge" the larger band gap of a material and help facilitate the promotion of an electron to the conduction band.

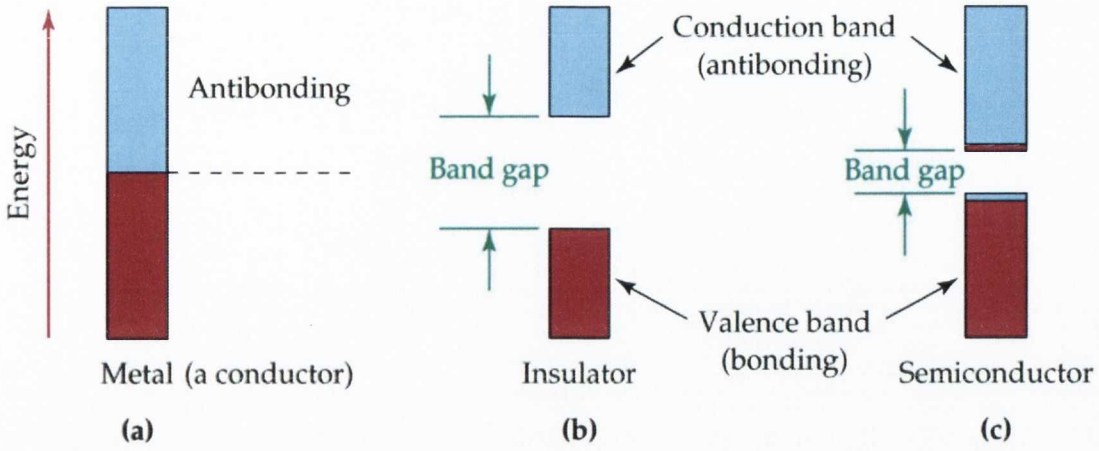

Figure 1.2: Diagram of the energy bands of a) a conductor, b) an insulator, c) a semiconductor[12].

The valence band in an undoped semiconductor is filled, whereas the conduction band is empty. As energy is supplied to the system electrons can be promoted to the conduction band. This energy difference separating the valence and conduction bands from each other is known as the band gap. Energy, such as a photon of light, may be used to promote electrons from the valence to the conduction band (Figure 1.3)[13-16].

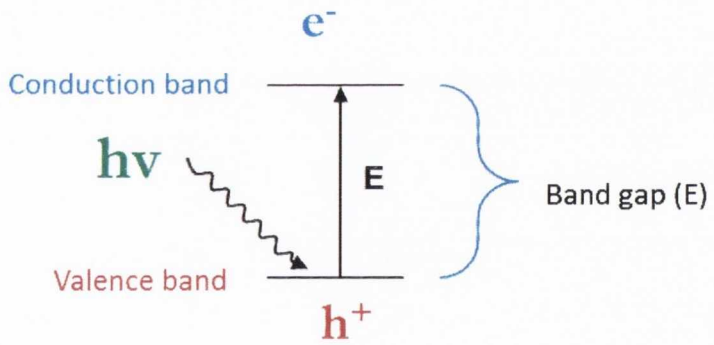

Figure 1.3: Diagram showing energy, in the form of a photon (hv), exciting an electron across the band gap of a semiconductor, from the valence band to the conduction band, and the creation of the positive hole.

Once an electron has been promoted from the valence band to the conduction band a so-called "hole" now exists in the valence band. These holes are considered as point positive charges in direct contrast to the point negative charge of the promoted electron. Both the hole and electron can move within the lattice allowing the crystal to conduct electricity. They also experience coulombic forces and can form a Wannier exciton, a state that is similar to a hydrogen atom. The radius within which such an exciton exists is called its Bohr radius (Figure 1.4).

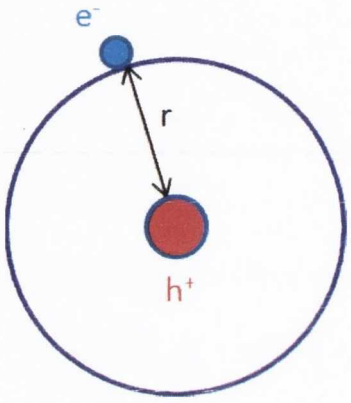

Figure 1.4: Diagram of the exciton and its Bohr radius.

Table 1.1: Mass and mobility properties of the electron and hole in CdSe.

Material: CdSe	Electron	Hole
Effective mass (m^*)	0.13	0.45
Mobility (cm^2/V sec)	650	50

As the effective masses of the electron and hole are very small and the crystals' electrons screen the charge carriers in the exciton from each other, the binding energy of the exciton is small and its Bohr radius large. This intrinsic instability is easily seen using a hydrogen atom as a stable analogous structure and a CdS hole and electron as a typical semiconductor exciton. A CdS exciton has a binding energy of 0.05 eV and a radius of 25 Å, while a hydrogen atom has a much greater binding energy of 13.51 eV over the much smaller radius of 0.53 Å. So although similar, a hydrogen atom is stable

while a semiconductor exciton is much less so. The combination of the exciton's low binding energy and wide radius results in their rapid dissociation into the free charge carriers at higher temperatures[17].

1.3 Quantum Dots (QDs)

While the properties, outlined above, are true of bulk material semiconductors, when dealing with the same material on the nanoscale there are key differences[2,18,19]. One factor to be aware of here is the effect of quantum confinement. This occurs when the radius of the semiconductor crystal is less than the Bohr radius of its exciton. That is to say, if the same CdS as above (which possesses an exciton radius of 25 Å) was prepared in such a way as to exist in a nanocrystalline form with a particle diameter of less than this e.g. 20 Å, its exciton would be too large for the particle in which it exists (Figure 1.5).

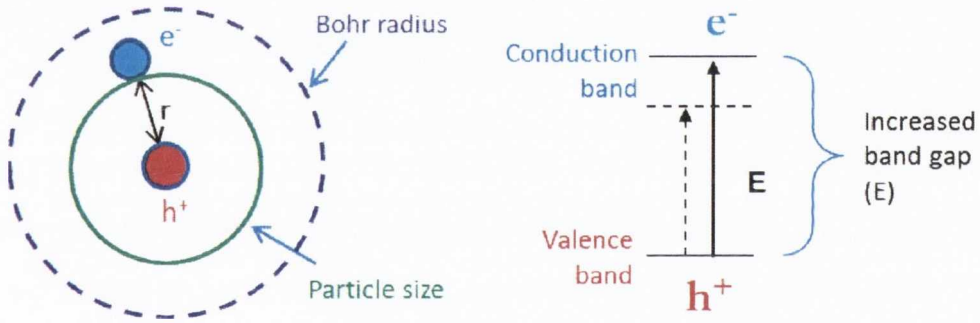

Figure 1.5: Diagram illustrating the quantum confinement of an exciton spatially (left) and energetically (right).

As the exciton cannot leave the particle, it is trapped. However, the charge carriers are linked not only spatially but also energetically and so, to alleviate this situation, a state of higher energy is assumed. The exciton, (the hole and the electron), can now fit inside the nanocrystal. This results in the energy levels splitting into discrete quantised levels and a change in the band gap. Thus as the size of the nanocrystal gets smaller the exciton's energy must increase (Figure 1.5). The band gap,

which was believed to be controlled solely by the constituent elements of the semiconductor, is now observed to increase as the size of the particle decreases and this leads to a decrease in the absorption wavelength[20,21]. So a blue shift in the absorption wavelength of the substance in question is observed once the particle size has been reduced by a sufficient degree i.e. to the nano-range (Figure 1.6).

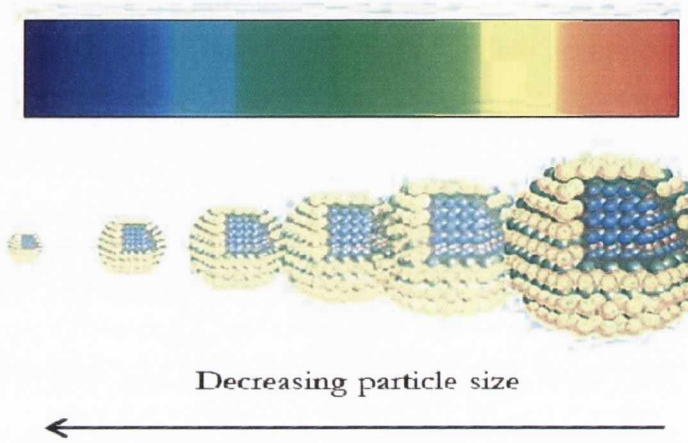

Figure 1.6: Illustration showing the shifting absorbance wavelength a particle as a function of decreasing particle size (right to left). Adapted from literature[22].

Related size effects have also been observed in metallic nanoparticles such as gold, silver and platinum[23-29]. Research has also been conducted which attempts to develop nano-sized semiconducting materials such as the sulphides, selenides and tellurides of cadmium[30-36], lead, mercury and zinc II-VI semiconductors[26,37,38].

After a certain time the exciton will collapse as the charge carriers recombine with each other, losing their energy by emitting a photon. However, as well as this, both the electron and the hole can combine with various traps in the semiconductor. These traps are defects, interstitial atoms, impurities and dislocations in the crystal and the resulting recombinations can be either radiative or non-radiative processes, as illustrated in Figure 1.7. The traps are frequently found on the surface as a result of the disturbed bonding forces there. These effects are even stronger when dealing with nanoparticles, as due to their large surface to volume ratio, the majority of the crystal's atoms may lie at the surface[39-42].

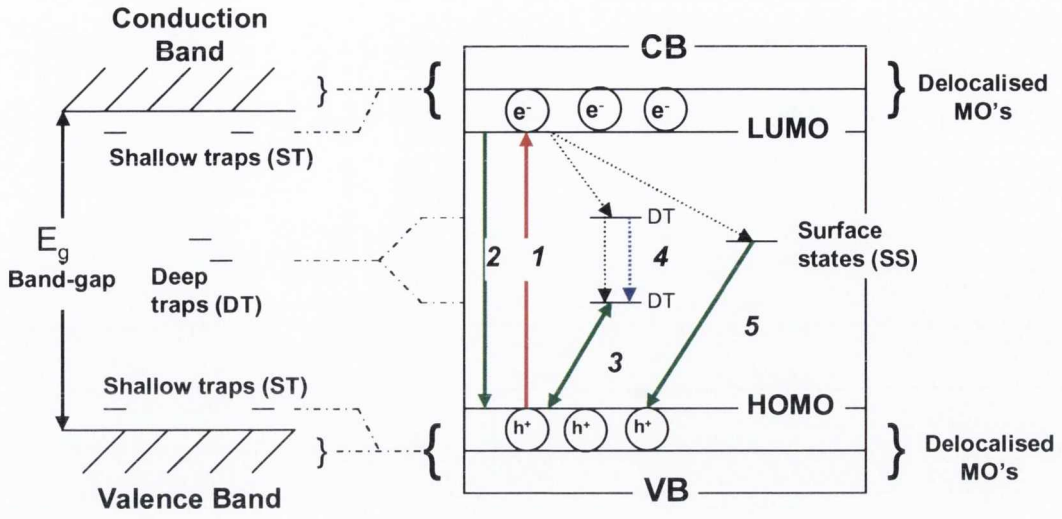

1: hυ induced excitation ($E > E_g$)
2: Exciton recombination: luminescence
3: Deep trap (defect) emission
4: Radiationless transition
5: Surface state emission

Figure 1.7: Schematic representation of the band gap (E_g) structure of a semiconducting material and the change in that structure on going from the bulk to the nanoscale. The absorption and subsequent emission pathways upon excitation by a photon are also shown. Adapted from literature[43,44].

The effect of increasing quantum confinement and increasing band gap thus also results in a change in the emission of these materials, and the emission band in spectra is shifted to higher energies (blue shift) upon recombination of the exciton (Figure 1.8).

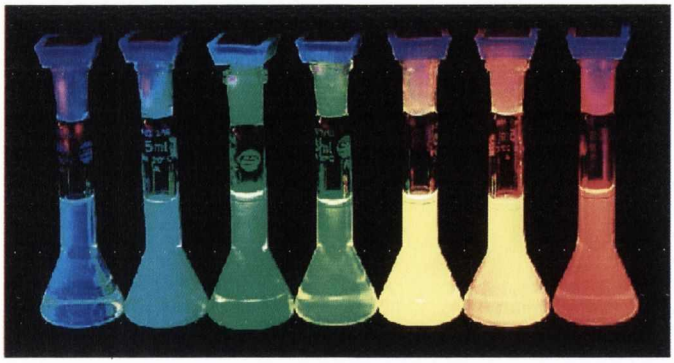

Figure 1.8: Photograph showing the effect of increasing quantum confinement/ decreasing particle size (right to left) and the resulting blue shifted, higher energy emission. Adapted from literature[45].

1.4 Surface Stabilisers

Semiconducting nanoparticles can be produced by a wide variety of different methods. All of these synthetic routes, however, have one crucial thing in common, the use of certain capping molecules as so-called stabilising agents. These are needed in order to coat the surface and stabilise nanocrystals and their colloidal solutions. A wide range of molecules are currently being used for such a role e.g. thiols, amino acids, antibodies, DNA, organic polymers etc[46-48]. These stabilising agents prevent the nanoparticles from aggregation and precipitation. The stabilisers are also essential in preventing the process of Ostwald ripening, in which smaller particles are lost to larger ones, resulting in their growth, and the formation of larger and larger particles. If this continues in a sample, the size of the crystalline particles will grow to exceed the Bohr radius of that material's exciton, thus resulting in the loss of quantum confinement within the crystal and the unique properties this brings with it.

Over time a growing variety of molecules were studied for this purpose, and increasingly effective stabilisers were discovered. It was also found that the hydrophilicity of the surface stabilising molecule was the important factor in governing the relative solubility of the nanoparticles[49,50]. Thus it was possible to make nanoparticles soluble in a wide range of solvents, both aqueous and organic. Also, via ligand exchange, it was achievable to transfer organic based nanoparticles to aqueous solutions and vice versa, simply by changing the stabiliser[50]. However, this often adversely affects the luminescent properties of the nanoparticles. Furthermore, these were not the only effects that these stabilising molecules had. It was also realised that by changing the stabiliser, it was possible to change the shapes of the nanoparticles formed, producing a variety of shapes e.g. spheres, rods etc[51]. Thus, the choice of molecule used to stabilise the nanoparticles is of key importance[49,50].

Largely, over the last decade much attention has been directed towards II-VI type CdS, CdTe and CdSe QDs. It is the ability to fine tune their optical properties by chemical control of their size and shape (i.e. their degree of quantum confinement) which makes quantum dots particularly interesting. This level of optical control combined with QDs resistance to photobleaching and their high level of solubility in

practically any solvent (depending on the stabiliser used) makes these nanomaterials potentially suited for roles as divergent as light emitting diodes,[52] biological sensors[53] and photovoltaic devices.[54-56]. Thiol groups have proved to be excellent stabilisers[57,58] due to their strong affinity for Cd, with thioglycolic acid (TGA) becoming a popular surface capping molecule for CdTe nanoparticles[59-62]. This has the benefit of being a 'greener' aqueous synthesis for QDs, avoiding the use of organic solvents, as well as the all of the above potential uses.

1.5 Lanthanides

The lanthanides (Ln) are a series of fifteen metallic f-block elements with atomic numbers 57 to 71, corresponding to the filling of their 4f electron shell as one goes across the series, from lanthanum ($4f^0$) to lutetium ($4f^{14}$). The element electronic structure generally follows $[Xe]6s^2 4f^n$, and in compounds the 6s electrons are lost and the resulting ions have the $[Xe]4f^n$ configuration. All the lanthanides form trivalent cations, oxidation state Ln^{3+}, and their chemistry is largely determined by their ionic radius, which decreases steadily from lanthanum to lutetium (lanthanide contraction). This is a result of the 4f orbitals being buried inside the 4p and 6s orbitals, and so shielded from external influences and reactions. The large nature of lanthanide ions results in them having high coordination numbers, those early in the series being 9-coordinate, the smaller ones being 8. Because of this, they generally dislike monodentate ligands, but form strong complexes with chelating ligands such as EDTA. With the possibility for a high number of unpaired electrons in their f orbitals, e.g. Gd^{3+} has 7 unpaired electrons, corresponding lanthanide complexes can have very large magnetic moments, resulting in their use as MRI contrast agents.

Transitions by electrons between the f orbitals are forbidden by Laporte rules, and as a consequence lanthanides are characterised by weak absorption spectra with narrow bands. This also means that, once an electron has been excited, its decay to the ground state is very slow, due to the ease with which a population inversion can be achieved they are commonly used in lasers. If a suitable sensitising antenna can be bound to the lanthanide however, excitation of this can activate otherwise disallowed f-f

transitions through energy transfer[63,64]. This will result in lanthanide emission, and sharp well-spaced, line-like emission (~10 nm) in the visible [Eu(III), Tb(III)] and near infrared [Yb(III), Nd(III)] regions are obtained throughout the visible, NIR and IR region, with long emission lifetimes (ms). It is these characteristics which have seen them employed widely for sensing and imaging[65-68] purposes.

Their ability to be sensitised by appropriate antennae, and their long excited state lifetimes has seen them become the focus of research investigating their possibility to act as both donors, and acceptors, in energy transfer processes such as FRET[69-72]. Such work has also explored the use of nanoparticles in these systems, and recently the combined sensing capabilities of a lanthanide complex to a gold nanoparticle surface for the purpose of detection of biologically relevant ions was demonstrated[68]. Reports also exist demonstrating the ability for FRET between lanthanide complexes and QDs[73-75]. It is this avenue of research that we hope to further, and exploit the properties offered by both lanthanides and QDs to develop new QD-hybrid functional materials[74].

1.6 Porphyrins and Their Interactions with QD Systems

Porphyrins are a group of molecules which are heterocyclic macrocycles, organic compounds composed of four pyrrole style units connected to each other through their α carbon atoms via methine bridges (αC=C-αC). The simplest version is porphine, shown in Figure 1.9.

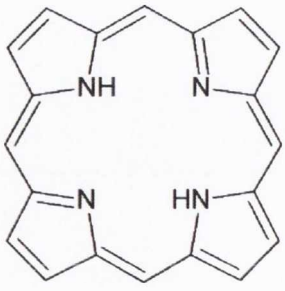

Figure 1.9: Structure of the parent porphine macrocycle.

All other porphyrin molecules share this porphine backbone but differ in their respective substituent groups. These can lie either on the central carbon of the methane bridge or off the pyrrole rings.

Porphyrins can also differ in their coordinated central metal atom. The central protons in the porphyrin macrocycle are very weakly acidic, and so can be substituted by most metals. Depending on the coordination number, metals can acquire axial ligands to change the shape from planar to square pyramidal or octahedral. The porphyrins macrocycle itself is generally planar, although the presence of the large metals or bulky substituents can distort the structure out of plane[76,77]. A porphyrin without a coordinated metal atom at its centre is called a *free base*.

Many porphyrins, especially metal-coordinated ones, are naturally occurring and are well known, playing very important roles in biology. They are involved in a variety of processes, including oxygen transport and storage, light harvesting, electron transport and energy transfer[78]. Examples are the oxygen-binding proteins (hemoproteins), containing iron-coordinated porphyrins that make up the active binding site. The most well-known are haemoglobin, responsible for oxygen transport in the red blood cells of humans and nearly all vertebrates, and the cause of the red pigmentation of blood, and myoglobin, used to store oxygen in the muscles. Other important metalloporphyrin derivatives include chlorophyll (magnesium coordinated), responsible for photosynthesis, and vitamin B_{12} (cobalt coordinated), essential in DNA synthesis and energy production.

Porphyrins are aromatic, obeying Huckel's rule ($4n+2$ π) and having 18 π-electrons which are delocalised over the macrocycle. This conjugated system results in porphyrins having intense colours, due to the highly allowed π to π^* transitions in the visible region. These transitions give rise to the characteristic signals in the absorbance spectra. The primary absorptions come from transitions between two HOMOs and two LUMOs on the macrocycle. The so called 'Q-bands' lie to the lower energy region of the absorption spectrum and are due to single π to π^* e_g <- a_u transitions. The characteristic Soret band is the single strong peak at higher energy to the Q-bands and arises from a double transition to the second excited state (2 e_g <- a_{2u}). The number of Q-bands in a porphyrins absorbance spectrum is related to the degree of symmetry in

the porphyrin. Our free base porphyrin H_2TMPyP4 has four Q-bands, due to its D_{2h} symmetry. The coordination of a metal atom lifts the porphyrin's symmetry, resulting in fewer Q-bands than the free base's four e.g. D_{4h} for PtTMPyP4. It also results in a shifting of the Soret band from that of our free base H_2TMPyP4, which lies at 423 nm. This can be a red or blue shift, depending on the nature of the metal atom.

The presence of the metal atom also affects the deactivation of the π^* excited states[78]. For example, both the free base and Zn(II) coordinated porphyrins exhibit fluorescence, Pt(II) and Pd(II) coordinated versions display room temperature phosphorescence due to efficient intersystem crossing to the triplet state, non-radiative decay through low-lying d-d states is dominant in the Ni(II)[79], and exciplex formation is caused by coordination of Cu(II)[80]. A general energy diagram for porphyrins is shown in Figure 1.10.

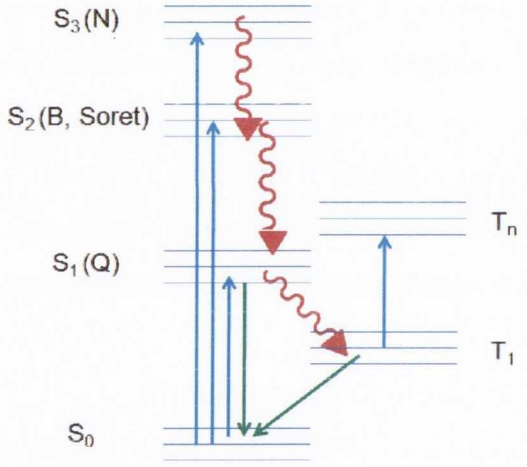

Figure 1.10: Generalised Jablonski diagram for common transitions in porphyrins.

Due to their high yields of singlet-triplet intersystem crossing, porphyrins are very effective type 2 sensitisers. One such molecule that can interact with porphyrin is molecular oxygen, as it has a triplet ground state. When an excited porphyrin and an oxygen molecule are in close proximity, an energy transfer can take place that allows the porphyrin to relax to its ground singlet state, and create an excited singlet state oxygen molecule, so called singlet oxygen. Several studies have shown a variety of porphyrins to be successful generators of singlet oxygen in aqueous solution via this photosensitised process of energy transfer. Singlet oxygen is a highly reactive species

and has been shown to react rapidly with nearby biomolecules, a feature that is utilised in photodynamic anti-cancer therapy. This has subsequently led to numerous investigations into the potential of porphyrins as anti-cancer agents[81-86].

Quantum dots, with their controllable size-dependant optical properties, coupled with water solubility and biocompatibility when coated with the correct stabilisers, also hold promise for applications is this field[87]. Their wide absorption bands and narrow emission make them ideal candidates for energy transfer such as FRET[88-91], and QDs in their own right are the subject of research into their potential as generators of singlet oxygen[92]. These properties also make them attractive as indirect producers of singlet oxygen, if coupled together with a suitable sensitiser. Reports are already available of using QD-based FRET to facilitate the excitation of a photosensitiser, increasing the triplet state yield and resulting in enhanced generation of singlet oxygen[92-94]. One of the benefits of this system is the wide spectral range over which it is effective, due to the wide absorption band of the QD. In these systems, for the reasons outlined above, porphyrins are a popular choice of photosensitser, with a variety of porphyrin and QD combinations already being investigated. It is this line of research that we will attempt to develop further.

1.7 Chirality and Chiral QDs

Amino acids containing a Thiol group have proven to be excellent stabilisers, with *L*-cysteine becoming one of the popular surface capping molecules for CdX (X = S, Se, Te) nanoparticles.[95-102]. In addition, this use of stereospecific chiral stabilising molecules opened another avenue of interest in the area of quantum dot research, as chirality is a key factor in biological and biochemical interactions.

A molecule is chiral if it contains one or more chiral centres. This often occurs when there is a carbon atom in the molecule which has four different groups attached. These can be arranged differently in space, giving rise to molecules that are chemically identical but due to the spatial arrangement of their substituents, are not superimposable on each other.

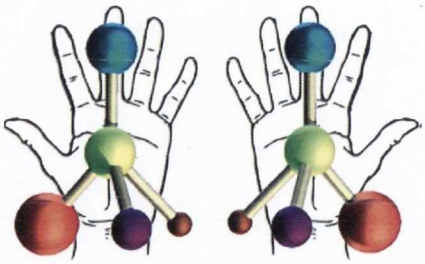

Figure 1.11: Illustration demonstrating the nature of chirality.

In circularly polarized light, the electric field vector has a constant length, but rotates about its propagation direction. Hence it forms a helix in space while propagating. If this is a left-handed helix, the light is referred to as left circularly polarized, and *vice versa* for a right-handed helix. The electric field of a light beam causes a linear displacement of charge when interacting with a molecule, whereas the magnetic field of it causes a circulation of charge. These two motions combined result in a helical displacement when light impinges on a molecule. When the molecule is chiral, the two types of circularly polarized light are absorbed to different extents. In a CD experiment, equal amounts of left and right circularly polarized light of a selected wavelength are alternately radiated into a (chiral) sample. One of the two polarizations is absorbed more than the other one. If a molecule is in the dextrorotary or *D*- form then it will absorb right handed circularly polarised light, while if it absorbs left handed circularly polarised light then the molecule is said to be in the levorotary or *L*- conformation. If the two enantiomers are present in equal amounts then the sample is said to be racemic and the two cancel each other out. This wavelength-dependent difference of absorption is measured, yielding the CD spectrum of the sample. This can be measured in delta absorbance ΔA (where $\Delta A = A_L - A_R$, the difference between absorbance of left and right circularly polarized light), $\Delta\epsilon$ ($\Delta\epsilon = \epsilon_L - \epsilon_R$) or ellipticity [$\theta$] in degrees[103].

Chirality is a common occurrence in the natural world and chiral compounds are very important in chemistry, biology, pharmacology and medicine. It has also been envisaged that chirality could play an important role in nanotechnology[104,105]. The majority of existing research in this field has been focused on chiral organic, metallorganic and biological molecules and their supramolecular structures[106], while research in the area of chiral inorganic nanoparticles is still in the very early stage of its

development[107]. For example, there has been some work involving chiral optically active metallic gold[108,109] and silver[110,111] nanoparticles, as well as carbon nanotubes[112,113]. However, there currently few publications dealing with chiral light emitting semiconducting nanocrystals (quantum dots)[114-119].

Due to their unique photophysical properties (tuneable, strong characteristic spectral emission, chirality), it is expected that chiral QDs will have a range of potential applications in photonics and biochemistry as light emitting devices, fluorescent sensors and bioassays, among others[117,120,121].

1.8 Transient Absorption Spectroscopy

All of the above mentioned systems are to be studied using a range of steady state and time resolved spectroscopic techniques, such as UV-vis absorption spectroscopy (UV-vis), photoluminescence spectroscopy (PL), and time correlated single photon counting (TCSPC), the basics of which are not detailed here. One particular method to be used extensively in this work is ultrafast picosecond-Transient Absorption (TA), and relatedly, ps-Time Resolved Infrared (TRIR) spectroscopy. Use of these techniques is still relatively rare due to their limited availability, consequently, an outline of the principles underlying them is pertinent here.

Transient absorption spectroscopy involves two pulses of light, hence it is called a pump-probe technique. In contrast to steady state absorption, TA allows for monitoring of both excited state absorption and ground-state emission and it enables the study of emissive and non-emissive excited states (Figure 1.12). It should thus shed light on the excited state dynamics and energy/electron transfer mechanisms at play in our QDs and QD-based conjugate systems outlined above.

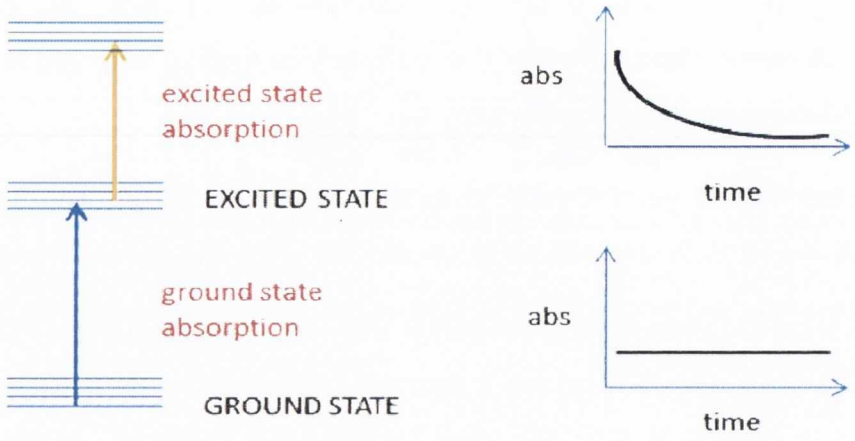

Figure 1.12: Diagram showing the different regions probed by steady state and transient absorption spectroscopy.

Steady state spectroscopy measures ground state absorption via irradiation using a continuous wave beam. Excited states are created and eliminated and eventually a steady-state is obtained where their concentration is constant, with the fraction of light absorbed measured. There is no probe beam in this technique and thus no kinetic information obtained.

Time resolved spectroscopy measures the evolution and decay of excited states as a function of time via a pump-probe technique. Laser pulses excite the sample, and probe beams (either pulsed lamp or continuous wave) interrogate the sample before and after excitation from the laser pulse. The measured parameter is the change in sample absorbance (ΔA) obtained from the change in transmitted light intensity of the probe beam before and after laser excitation.

TA spectra are measured by the following sequence of events outlined below and illustrated in Figure 1.13;

1) The first 'pump' pulse of light hits the sample
2) This results in the sample absorbing the light, causing the population of excited states (so-called *bleaching* of the sample)

3) Rapid intraband relaxation to lowest excited state (1S) occurs. These transitions can often be seen in the NIR when using appropriate detectors (TRIR)
4) Relaxation of the electron back toward ground state may occur directly or via interspacing energy levels – so called defect states. The timescale for these transitions is typically associated with luminescence (ns), though may be much longer e.g. phosphorescence from triplet states
5) Before the electron reaches the ground state, the sample is hit with a second 'probe' pulse. This is fired at different delay times
6) This re-excites the electron and time related absorbance spectra of these excited states are obtained

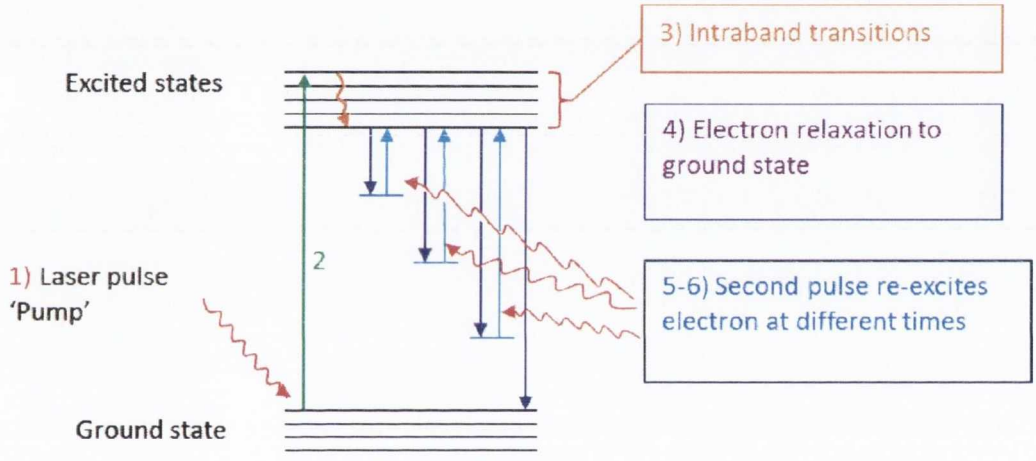

Figure 1.13: Diagram illustrating transient absorption spectroscopy

1.9 Solar Cells and Related Problems

With the increasing scarcity of fossil fuels, along with the negative impact on the environment and the acceleration of climate change, to the detriment of the world, there is a greater need for cleaner, more renewable energy resources. Sunlight is a completely carbon neutral, environmentally friendly, free and endless potential source of energy and is thus the focus of much interest and research, aimed at maximising and harnessing this energy through solar or photovoltaic (PV) cell development. These have the potential to solve the growing energy crisis the world will undoubtedly face in the near future.

The vast majority of solar cells available today are based on single and poly-crystalline silicon, the so called first generation of cells.

A completely pure semiconductor is called an intrinsic semiconductor and has an equal proportion of electron holes to free electrons when stoichiometric, the population of which increases relative to temperature. Intrinsic semiconductors normally have low conductivity values unless heated to high temperatures or possess a small E_g. This low conductivity is greatly increased through the introduction of dopants creating crystal defects that introduce energy levels within E_g These crystal defects are categorised with respect to their origins either as extrinsic, due to impurities or intrinsic due to the crystal structure itself.

Extrinsic crystal defects due to aliovalent substitution are termed extrinsic doping. While intrinsic defects produce intrinsic doping due to the pure substance being non-stoichiometric. Both types of dopants can produce an excess of either holes termed p-type or free electrons termed n-type, which dominate the conductivity behaviour. N-type Si can be produced by aliovalent substitution through the introduction of group-15 elements (P, As, Sb) ,resulting in excess electrons in a lattice position due to it possessing one electron more in its valence shell than Si. These excess electrons will introduce a donor level in the E_g, near the CB and allow electrons to be easily excited into the CB and so shifting the Femi level towards the CB. This imbalance in charge carriers allows the term majority charge carrier to be assigned to electrons and minority charge carrier to electron holes. P-type Si can be produced by aliovalent substitution through the introduction of group-13 elements (B, Al, Ga) resulting in hole production in the lattice due to it possessing one electron less in its valence shell than Si. These holes will introduce an acceptor level in E_g just above the VB. This allows electrons to be excited into these levels from the VB, producing holes in the VB, and causing the Fermi-level to shift towards the VB. Therefore, in p-type-semiconductors the majority charge carrier are electron holes and electrons are the minority carrier.

P-N junctions are the basis for semiconductors integral role in modern day electronics, finding applications in transistors, photovoltaic cells and a large range of diodes, including light emitting diodes (LEDs). The simplest device, the diode, allows current flow in one direction more readily than the other direction (rectification) and

can be made using a p-n junction. A p-n junction is formed at the point of contact between an n-type and p-type semiconductor and is described as a p-n homojunction when both semiconductors utilised are the same or a p-n heterojunction when two different semiconductors are used. When these two materials are brought together electrons flow from the n-type to the p-type semiconductor and holes flow the p-type to the n-type. These charge carriers then undergo recombination with majority carriers in the respective materials leaving behind in both materials charged ions. This charge transfer therefore leaves a net positive charge on the n-type material and a net negative charge on the p-type material and so setups an electric field across the p-n junction in the order of 0.6 to 0.7 V for Si. This charging pushes the down the n-type band levels and pushes up the p-type band levels until the Fermi-levels of the two materials are equal. The area in which charge carrier transfer has taken place is called the space charge layer or depletion zone, due to lack of charge carriers in this region and the presence of an electric field.

Another important diode is the Schottky junction, a junction created between a metal and a semiconductor. The semiconductor used can be either n-doped or p-doped and any metal can be used. When the metal is brought into contact with the semiconductor, its majority charge carriers near the junction are injected into the metal, creating a depletion region in the semiconductor called a Schottky Barrier (SB). The height of the Schottky junction is given by SB = E_g + (electron affinity) – (work function) while p-type is given by SB = (work function) – (electron affinity).

The use of silicon itself has led to the drive to find alternatives, as rapid escalation in the cost of high purity silicon by almost an order of magnitude has made this form of photovoltaic technology increasingly expensive, leading to the development of the second and third generation of solar cells. First generation cells also have other drawbacks. One of the main concerns or problems in relation to solar cells, particularly these first generation cells is efficiency, and key to this is the Shockley–Queisser limit[122]. This is a theoretical barrier to the maximum attainable solar conversion efficiency from a solar cell under the illumination of one sun and illustrates some of the main problems facing us in increasing solar cell efficiency. It is measured to be 33.7% for a single p-n junction with a band gap of 1.1 eV, typical for silicon. This means that

from all the power in sunlight falling directly on such a silicon-based cell (approx. 1000 W/m^2), only 33.7% of this energy can ever be converted into electricity (337 W/m^2). Losses in efficiency are due to a wide number of factors. The main three reasons are as follows;

1) Loss of absorbed energy through blackbody radiation.

This is estimated to be around 7% of the available incoming sunlight energy at room temperature. This effect is also dependent on the cell temperature. As any energy lost by the cell is most likely to be turned into heat, inefficiency increases the cell's temperature as it is placed in sunlight. This in turn increases the amount of blackbody radiation and thus further energy loss. This process continues until the cell reaches equilibrium, usually at temperatures as high as 45°C. Solar cells therefore operate at lower efficiencies than they would typically at room temperature.

2) Recombination of photoexcited electrons with other holes.

Upon photoexcitation, an electron and a positive 'hole' are created. These charged species will attempt to neutralise themselves through recombination with a member of the opposite charge. Thus the photoelectrons will travel toward the electrode at the front of the cell, while the holes will travel toward the source of electrons at the back electrode. For several reasons, holes move much slower than electrons and so in a given time, an electron created and travelling to the front electrode may encounter a hole generated from a previous photoexcitation event. This will result in recombination and loss of energy, usually as a photon. This places an upper limit on the rate of photogeneration of charge carriers, past a certain rate there are so many holes that electrons never make it to the p-n junction. In the silicon cell, discussed above, this leads to a loss of another 10% on top of the thermal losses outlined already. The effect obviously increases with increasing light intensity, often placing a cell's optimum efficiency rate at well below the power delivered by one sun.

3) Band-gap related spectrum losses.

As the excitation of an electron from the valence to the conduction band requires a certain amount of energy to cross the band gap, only photons from wavelengths with equal and greater energy will result in exciton generation. This means that while any light of greater energy will produce photoelectrons, all lower energy light is lost. In the silicon cell example with a bandgap of 1.1 eV, corresponding to IR light, even though the energy from wavelengths of the visible spectrum are captured, all infrared, microwaves and radio waves are not[123]. As, out of the total 1000 W/m^2 of energy from the sun, only around half of the emitted light is of greater energy than 1.1 eV, this immediately places an upper limit of approximately 50% or less on the cells efficiency, not including the other factors outlined above. Another contributor to loss is that any light energy at much higher energy than that of the bandgap is also lost. So for example while blue light is roughly double the energy of red light, the excess energy after promotion across the bandgap is not captured. Blue light will result in photoexcitation of an electron but the extra energy will be lost, typically as heat[123]. This bandgap related loss is by far one of the greatest sources of low efficiency in solar cells.

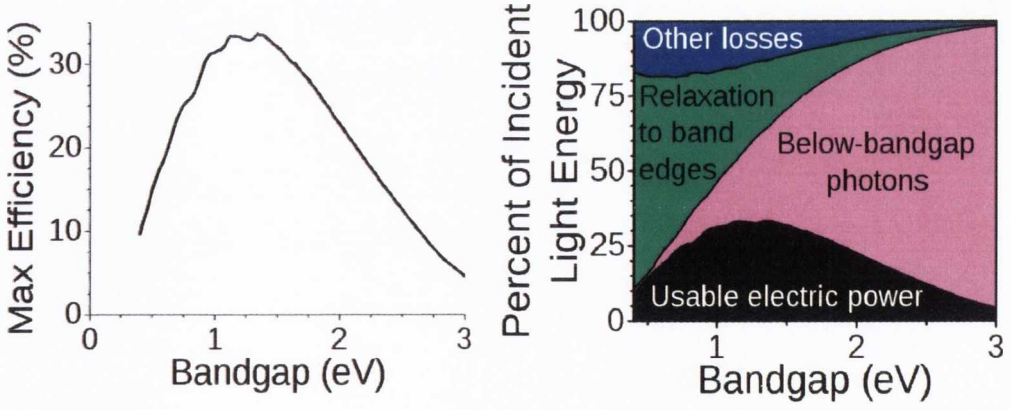

Figure 1.14: Graphs showing (a) the maximum % efficiency and (b) outlining the % energy loss, as a function of the band gap energy. Reproduced from[124,125]

Other losses may be due to trapping by interstitial defects in the crystal lattice, or reemission of the absorbed energy[126]. The interfaces between the various components can act as barriers to the free movement of charge carriers through the cell. All of these factors are critical and must be considered when creating an eventual successful solar cell.

To overcome this low efficiency limit, several approaches have been suggested. One such method is a tandem cell. This device is based on multiple cells stacked like layers on top of one another, each one tuned to a different part of the spectrum by using different materials. If the layers are thin enough they will be almost transparent to lower energy light which can then be harvested in another cell behind the first. Theoretical maximum efficiencies with this set up, when coupled with new materials such as gallium arsenide which have greater electron mobility and more available charge carriers, lie at around 55% for a bilayer cell, 63% for three layers and 86% for infinite layers[127]. Typically three layers are employed covering the visible region, blue, yellow and red.

The use of luminescent solar concentrators (LSCs) is another approach being investigated to increase overall cell efficiency, though it does not affect the cell itself. This is essentially a sheet of high refractive index material permeated with a luminescent species. The plate absorbs the solar energy which is then converted to fluorescence, as illustrated in Figure 1.15. Via total internal reflection, the light is guided to the plate edges where it emerges in a concentrated form[128-130].

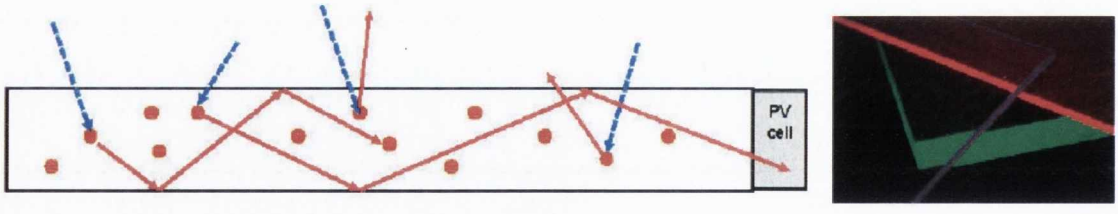

Figure 1.15: (Left) LSC with luminophores (dots) absorbing sunlight (blue) and emitting longer wavelength light (red) that is then harnessed by a PV cell. (Right) example of LSCs showing light guided to the edges. Reproduced from [131]

Theoretically almost 80% of the luminescence can be harnessed to the edges in this manner. Overall, theoretical efficiency of the LSC per cell lies at around 20%[132] (energy reaching solar cell/energy falling on plate) though several cells can be arranged around one LSC. However the best to date is 7% and saves a factor of 2.5 of PV-cell area[133]. This model thus can also result in further cell efficiency when solar cells are arranged around the edges of the LSC, as well as increased efficiencies, in terms of cost per m^2 of available sunlight area, as LSCs are cheaper to make than the equivalent amount of solar cells required to cover the same area. If sufficient solar concentration of the lost IR light can be obtained, this can also increase the probability of two-photon absorption processes[134]. However, as two-photon absorption is a nonlinear third-order process and weaker than normal linear absorption by several orders of magnitude, being dependant on the square of the light intensity, the overall efficiency derived from this route remains low when compared to using normally IR excited materials[135].

With the advent of quantum confinement and the ability to tune the bandgap of semiconducting materials, the use of QD based materials becomes highly attractive. Using QDs allows for manipulation of bandgaps from the UV to the IR and offers wide spectral range without using different materials, thus also reducing overall cost. This is crucial as currently one of the main factors impeding mass production of these next generation cells is cost. The use of materials such as QDs may allow greater electron transport due to their small nature, if created pure there are fewer encountered defects per electron. Capturing the energy from so called 'hot carriers', that is, before they relax to the band edge and the energy is lost as heat through electron-phonon scattering and subsequent phonon emission to the crystal structure, is also possible[136,137]. Other materials such as Pb chalcogenide QDs have very small bandgaps and are able to harvest light even further out into the IR region (the pink region in Figure 1.14 (b)), and while the energy of such photons and thus the efficiency of the individual cell itself is low, when incorporated into a successful tandem arrangement could yield greater overall efficiency. QDs are also capable of multi-exciton generation (MEG), that is, the creation of multiple electron-hole pairs from the absorption of a single photon. MEG has been demonstrated in a wide variety of QDs[138-140]. The exact quantum mechanical process of MEG is still little understood but a solar cell utilising this property could

exceed the Shockley–Queisser limit by utilising the green area as well as the black area in Figure 1.14 (b). These combined aspects make QDs ideal candidates for light harvesting in photovoltaic devices.

1.10 The Third Generation - Dye Sensitised Solar Cells

Pioneered by Professor Michael Grätzel, third generation solar cells are based on the creation of current by the absorption of a photon by a dye molecule[141]. Absorption leads to a photoexcited electron which is injected into the conduction band of an n-type semiconductor such as nanoporous titanium dioxide TiO_2. The oxidised dye molecule is regenerated by an electrolyte which contains some form of redox couple such as I^-/I_3^-. The oxidised species of the couple is reduced at the counter electrode. This is usually platinum, which is an excellent electrocatalyst for the reduction of the triiodide, increasing the rate of electron transfer back into the electrolyte from the external circuit, and also providing good light reflectance. The working electrode (front) is made of a transparent conducting oxide, typically either indium tin oxide (ITO) or fluorine doped tin oxide FTO, coated onto glass. In terms of efficiencies, dye-sensitised solar cells (DSSCs) stand at best at around 11%[141], which is substantially less than current silicon cells (30%). This is somewhat compensated by their steady performance in various weather conditions and diffused light such as a cloudy day, with little drop in efficiency, compared to their silicon counterparts which are more heavily affected by light incidence, angle and temperature. DSSCs are not without their problems however, with the photobleaching and degradation of the dye, along with leakage of the electrolyte over time being some of the main issues.

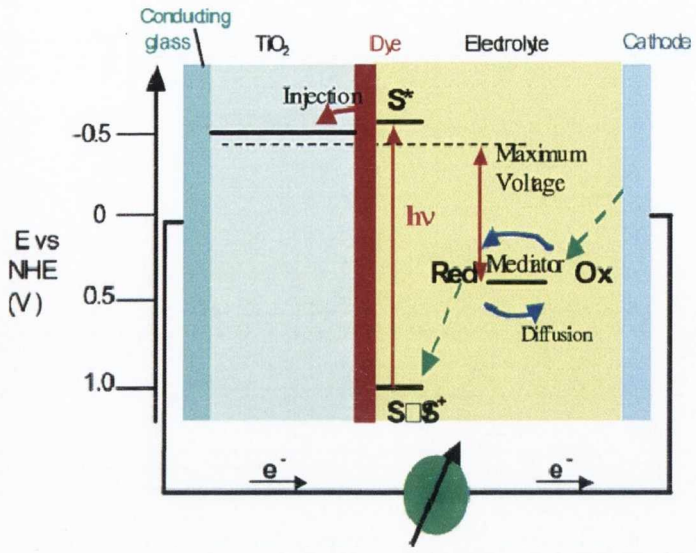

Figure 1.16: Representation of the DSSC structure. Reproduced from[142].

There are several possible approaches already outlined in the current literature for the incorporation of QDs into a solar cell[143]. One popular and relatively straightforward method is to use QDs in solar cells that are based on the DSSC platform. This involves replacing the typical light harvesting dye molecule (e.g Ru complex) with QDs (QDSSC), adsorbing them onto the working electrode/ photo anode, in this case, nano-particulate TiO_2. Current efficiencies for such QDSSC based solar cells stand at around 4%[144]. The possible benefits of QDs in solar applications are already well established (outlined above). Recent developments have also shown that MEG is possible in QDs in a QDSSC style solar cell, with internal conversion efficiencies of 100% and greater, meaning the conversion of every absorbed photon to at least one photoexcited electron[145,146]. These combined aspects make QDs very promising candidates for light harvesting in photovoltaic devices. Consequently, the use of QDs, and the development of QDSSCs, is an obvious avenue for further future solar cell research. It is, therefore, this line of research that we will attempt to develop; testing of our novel chiral QDs as replacements for organic dyes in a QDSSC style set up. The principle of QDSSC with CdSe is outlined in Figure 1.17.

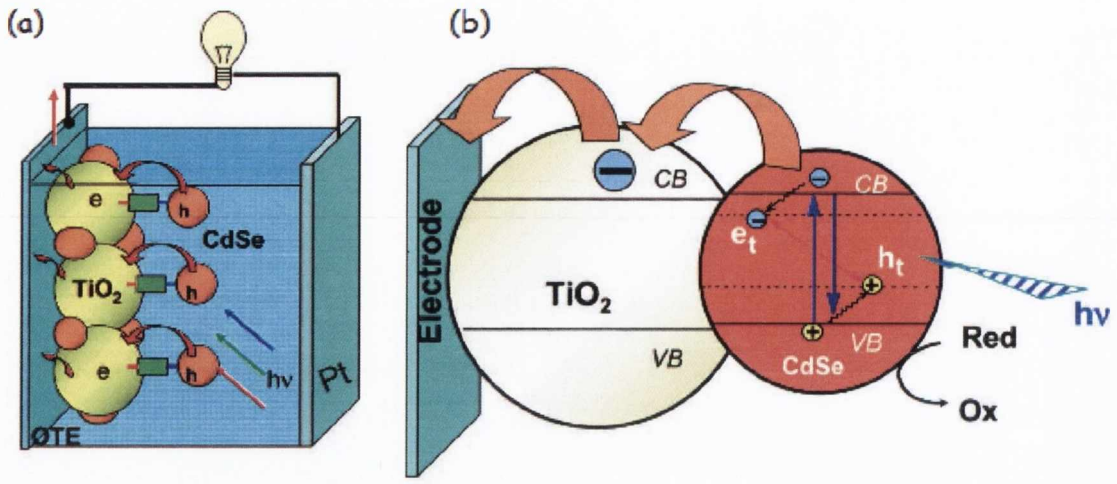

Figure 1.17: Schematic representation of light harvesting by CdSe QDs showing the movement of photogenerated electrons and holes. Reproduced from[143].

1.11 Carbon Nanomaterials

Graphene and carbon nanotubes (CNTs) are allotropes of carbon. Examples of other carbon allotropes are diamond and graphite. In graphene, each carbon atom sits at a vertex of a planar hexagonal honeycomb lattice, separated from three nearest neighbours by a bond distance of 0.142 nm. The bonds are composed of σ-like molecular orbitals arising from the interaction of sp^2 hybrid orbitals on the nearest neighbouring carbon atoms. A fourth orbital from each carbon lies perpendicular to the plane and overlaps with its neighbours, giving rise to delocalized π-like molecular orbitals. Normally, strong atomic potentials and covalent bonding imply the existence of a large band-gap. However, due to the hexagonal array of the sp^2-bonded carbon atoms and the resulting potential, the structure cannot distinguish between the π and π^* states at the Fermi level[147]. Thus, they remain equal in energy and the two bands formed, from the $2p_z$ orbitals, touch at the Fermi level. A graphene sheet can therefore be described as a semi-metal[148]. The interest in graphene cannot be understated and this is for several reasons; both experimental and theoretical studies show that graphene and gaphene based materials demonstrated unique mechanical and electrical properties[149], it is an incredibly resistant material to chemical and mechanical stress, and has extraordinary properties when in bi- and multi-layer form[150].

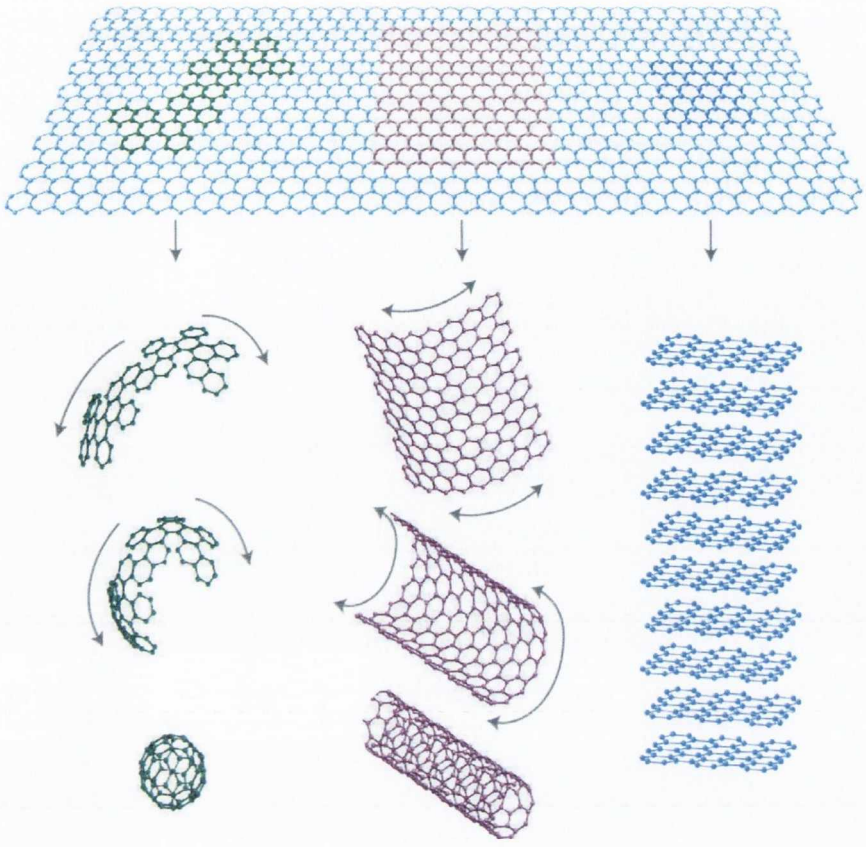

Figure 1.18: Illustration of graphene as a 2D building block for carbon materials of all other dimensions such as 0D fullerenes (left), 1D nanotubes (middle) and stacked to form 3D graphite. Reproduced from[151].

Sumio Iijima is credited with elucidating the carbon nanotube structure in 1991[152]. The tip of a nanotube is structurally similar to a C_{60} molecule known as a buckminsterfullerene. The molecular orbitals in carbon nanotubes are sp^2 hybridised, therefore, their properties are to some extent similar to graphene and a fullerene. Since a CNT is cylindrical rather than a flat sheet, an admixture of sp^3 hybrid orbitals is required to facilitate this curvature, with the amount increasing as the radius of the nanotube decreases[153,154]. There are two main types of carbon nanotubes, single-walled nanotubes (SWNT) and multi-walled nanotubes (MWNT). MWNT are simply several SWNT of different diameters packed inside each other, a tube within a tube type structure. The structure of a CNT is one dimensional with axial symmetry, and generally exhibit a spiral conformation called chirality[155]. The crucial point about the structure of a CNT is the orientation of the six-membered carbon ring in the honeycomb

lattice relative to the axis of the nanotube. Depending on how one imagines rolling a graphene sheet to construct a tube, achiral and chiral CNTs result, Figure 1.19.

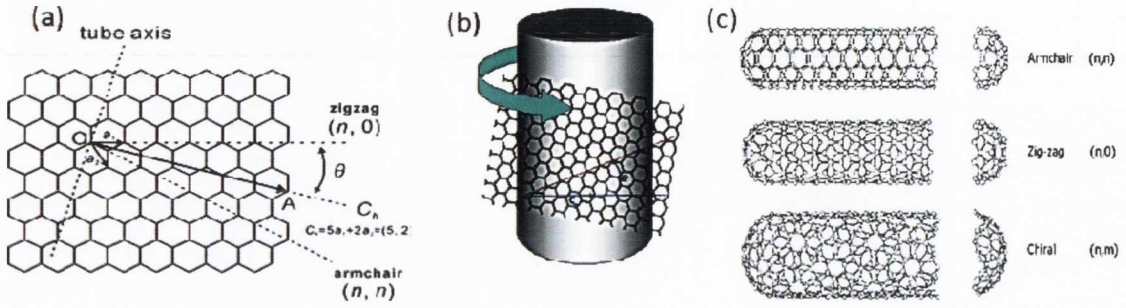

Figure 1.19: (a) The unrolled honeycomb lattice of a SWNT. The chiral vector, C_h, is defined by OA and is expressed in terms of integers (n,m). (b) Pictorial representation of the various ways a graphene sheet can be rolled to form a SWNT. (c) The resulting SWNT (adapted from[132]).

The structure of a SWNT can be classified according to a pair (n,m) integers that define the rolling or chiral vector, C_h[152]. The chiral vector can be expressed in terms of the real space vectors $\mathbf{a}_1$ and $\mathbf{a}_2$ of the hexagonal lattice.

$$C_h = n\mathbf{a}_1 + m\mathbf{a}_2 \equiv (n,m)$$

SWNTs can be metallic or semiconducting, depending on their diameter and chirality. Those with the specifications (n,0) and (n,n) are achiral and are labelled as *zigzag* and *armchair* respectfully. These correspond to a chiral angle value, θ, of 0° and 30° respectfully. Both these types of nanotubes are metallic. All other (n.m) chiral vectors, for $0^\circ < \theta < 30^\circ$, correspond to chiral SWNTs which can be metallic or semiconducting. In a MWNT, the various tubes can each have any of these structures.

One of the primary reasons that these materials have attracted such attention is because of their conductance, calculated to be be 1/12.9 $k\Omega^{-1}$ for and average CNT[156]. This corresponds to an ability to carry 1000 times more current than copper wire[157]. The reason for this is that as an electron travels through a carbon nanotube it is governed by the laws of quantum mechanics because of the nano dimensions of the CNT. This gives rise to in ballistic conductance within the tube and quantum tunnelling between the tubes. Ballistic conductance results in very high electrical conductance

along the length of the tube but poor conductance through the side of the tube. This phenomenon is observed because an electron travelling through a defect-free carbon nanotube experiences no resistance, due to the extended network of delocalised π-bonds from the carbon atoms in the graphene.

1.12 Chirality in Carbon Nanotubes

As previously mentioned, carbon nanotubes also possess an element of chirality, depending on the direction in which the graphene sheet is rolled on itself. Research has been done using chiral diporphyrin as a type of nanotweezers, separating carbon nanotubes according to their chirality[113], Figure 1.20.

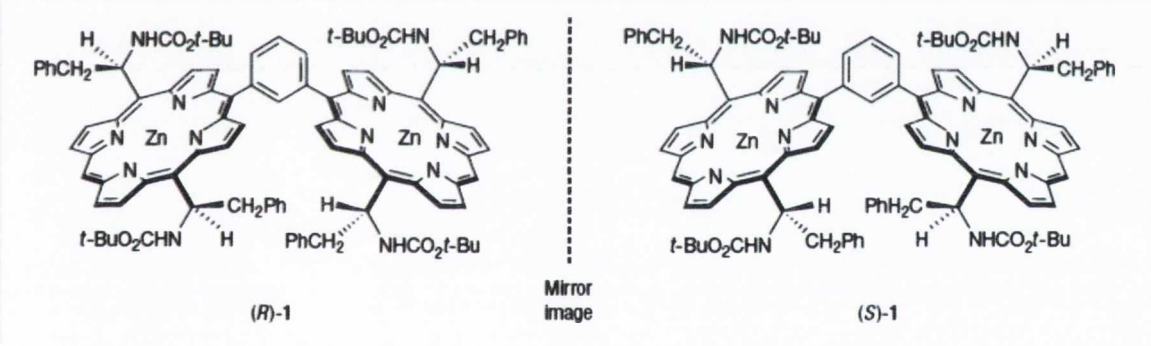

Figure 1.20: Pictorial representation of both enantiomers of the chiral diporphyrin. Adapted from literature[158].

This has opened up the area of possible chiral-chiral interaction based nanotube systems such as recognition-based assemblies of functionalised nanotubes with complementary DNA. Since DNA is not only an excellent chiral template when growing optically active metallic nanoparticles, it can also be used to produce a chiral response in racemic mixtures of single walled carbon nanotubes. These could further be used as possible biological sensors[159]. This opens up the possibility that carbon nanotubes and chiral quantum dots may exhibit chiral interactions, opening new avenues of interest for further research and investigation.

1.13 Carbon Nanomaterials Functionalization

In order to use carbon allotropes, it is often necessary to adapt or functionalise them. This is carried out for a variety of reasons: to increase their solubility in a given solution, to help prevent bundling of the nanotubes (a serious problem when working with tubes, particularly in aqueous solutions), to increase their mechanical or electronic properties, or to improve their reactivity. All of the above are obtained through modification of the nanotubes surface and a wide variety of methods have been developed to achieve these goals. However, we will stick to just one method of surface functionalisation for this research. We will also only focus on MWNTs and graphene.

Sainsbury and Fitzmaurice have previously reported covalently binding organic molecules to a nanotube surface, and it is a variation of this method we will use for our work[160]. The functionalisation is based on a simple amide coupling reaction, catalysed by EDC. One can attach a wide range of molecules containing an NH_2 group using this method. For our work, the molecules we will attach are cysteamine and 11-mercaptoundecanoic acid.

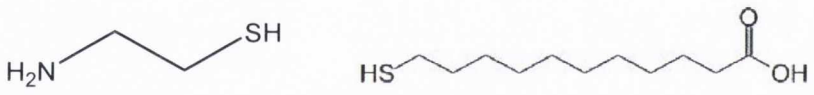

Figure 1.21: (Right) Cysteamine molecule and (left) 11-mercaptoundecanoic acid.

These particular molecules were chosen as they are simple alkyl chains which possess a terminal thiol group, thus making it chemically similar to the stabilising molecules being used to make quantum dots. The approach is to synthesise quantum dots in the presence of these functionalised MWNTs and graphene. This in-situ approach has already been demonstrated successfully for the attachment of QDs to the surface of CNTs[161]. The cysteamine/ 11-mercaptoundecanoic acid will act in a similar manner to the amino acid stabiliser in solution (indeed cysteamine is often used itself as a stabiliser for nanoparticles), binding via the thiol group to cadmium atoms on the surface of the nanoparticle. This would yield covalently bound carbon-quantum dot composites. Covalent bonding of the two species via the linker molecule is important

as it should allow for charge transfer to occur from one nanomaterial to the other through the linker.

1.14 Carbon Nanomaterials and Their Potential for Solar Cells

The use of CNT and graphene based materials in a solar energy application is already the focus of much diverse research, as outlined in one of the reviews from our group[10]. Due to their unique and superior properties, CNTs and graphene materials may be ideal candidates for improvement of, or even complete substitution of, almost any part of a current solar cell, from supplementing or replacing both the photoanode and photocathode electrodes[162-165], to additives in the electrolyte[166-168], increasing charge mobility across the cell and thus the efficiency of the cell.

Coupled with the use of carbon nanomaterials in solar cells, has been the growing use of ionic liquids.

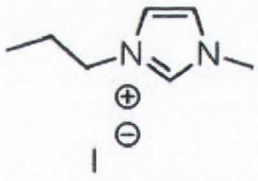

Figure 1.22: Structure of the IL electrolyte, 1-methyl-3-propylimidazolium iodide.

Ionic liquids (ILs) are receiving a great deal of attention as possible alternative electrolytes to the organic solvent based ones used in third generation DSSCs[169]. For an electrolyte to work efficiently in a cell, it must have certain characteristics. These include high viscosity, low vapour pressure, excellent thermal stability and high conductivity, as well as being non-corrosive to the PV-cell sealant. The current range of organic electrolytes, while delivering efficiencies of around 11%[141,142], also have low vapour pressures, viscosities and high diffusion coefficients. This leads to several problems such as degradation of the electrolyte, poor temperature stability and

corrosion of the cell sealant and leakage over time. The various properties displayed by IL's, namely their negligible vapour pressure, tuneable viscosity, non-volatility and superior thermal stability at both very low and elevated temperatures[150,170], coupled with their high ionic conductivities and a broad electrochemical potential window[171,172], circumvent a lot of the issues around organic solvent based electrolytes, making them ideal candidates for use as electrolytes in DSSCs. One of the drawbacks to IL's is that they result in lower efficiencies in DSSCs than their solvent counterparts. The main reason for this is due to their extremely high viscosities which impedes the diffusion of the redox couple through the device[173]. The incorporation of carbon materials in the IL have shown to increase cell efficiency[166,167,174]. This is attributed to the carbon nanomaterial providing an extended electron transfer surface (EETS) which catalyses the reduction of the I_3^- ions[175-178].

It is this area of research that the final part of our work aims to develop, creating improved DSSCs using an IL incorporating our QD-carbon composites. Choosing an IL electrolyte should suspend the G-QD and MWNT-QD composites in solution as well as acting as a good electrolyte, setting up the necessary redox couple. The attachment of our QDs to the carbon allotropes should facilitate electron transport, while also acting as secondary light harvesters.

1.15 Aims of this Project

The main aims of this project were to develop various new II-VI QD based materials and investigate their properties and energy/electron transfer processes in relevant systems using various spectroscopic techniques. We also planned to utilise some of our QD systems as potential light harvesting components for solar cells.

Initially we planned to prepare aqueous CdTe TGA-capped QDs and analyse them fully using a range of both steady state and time resolved techniques. These QDs were then used in the subsequent studies, covered by the first two results chapters of this thesis.

We aimed to investigate aqueous lanthanide-QD systems based on an Eu(III) cyclen complex and CdTe TGA capped QDs.

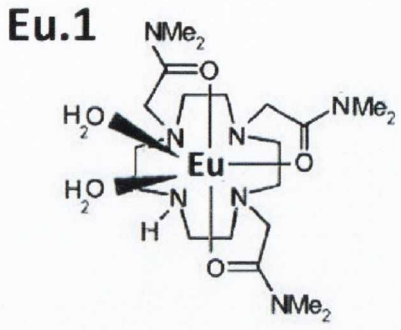

Figure 1.23: Structure of the Eu(III) cyclen complex, Eu.1.

We expected that there would be the coordination of a europium complex to the COOH groups of the TGA. A thorough photophysical investigation was then undertaken using steady state absorption and emission spectroscopy, as well as time correlated single photon counting (TCSPC). Ultrafast ps-transient absorption spectroscopy was also employed in an effort to elucidate the excited state dynamics of this system. The potential of this hybrid system to act as a sensor for a biologically relevant molecule was also investigated.

Further, we aimed to study the interaction of CdTe TGA QDs with three different porphyrins. The first was tetracationic *meso*-tetrakis(4-N-methylypyridyl) porphyrin (H_2TMPyP4). The other two were metalloporphyrins of this, coordinated with zinc(II) ($ZnTMPyP_4$) and platinum(II) ($PtTMPyP_4$) respectively.

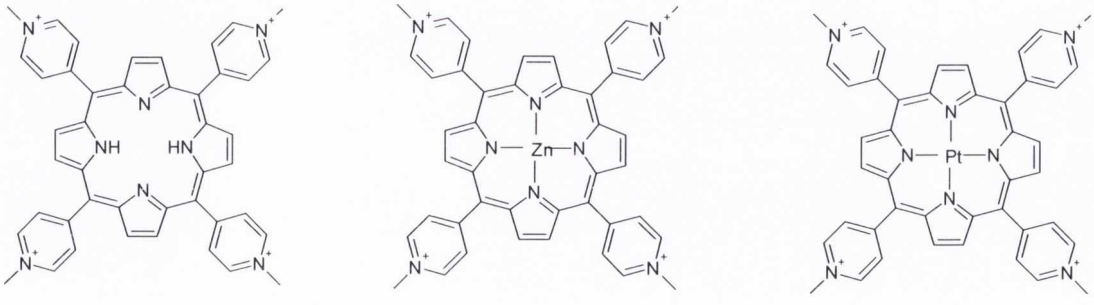

Figure 1.24: Structures of the free base H_2TMPyP4, zinc coordinated ZnTMPyP4, and platinum coordinated PtTMPyP4 porphyrins respectively.

The transfer processes (energy or electron transfer) displayed by these systems were studied using both steady state absorbance and photoluminescence spectroscopy. To probe in more detail, ultrafast time resolved ps-transient absorption spectroscopy was again employed in an effort to elucidate the excited state dynamics of the system. It was expected that in using these combined spectroscopic measurements, the exciton and transfer processes of our porphyrin-QD systems could be studied in depth, leading to a further understanding of the mechanisms at work. This could in turn be used to develop new complexes for use in, among other things, enhanced singlet oxygen generation, photodynamic therapy, and improved light harvesting devices.

Another of the principle aims of this work was to develop novel chiral CdSe and CdTe based QDs by using chiral stabilisers and to investigate the properties of these materials. By using the dextrorotary (D-), levorotary (L-) enantiomers, as well as the racemate (Rac-) of two chiral molecules, 2-amino-3-mercapto-3-methylbutanoic acid and 2-amino-3-mercaptopropionic acid (more commonly known as penicillamine and cysteine respectively), in all their enantiomeric forms as nanoparticle stabilisers, it was hypothesised that they will retain their chirality.

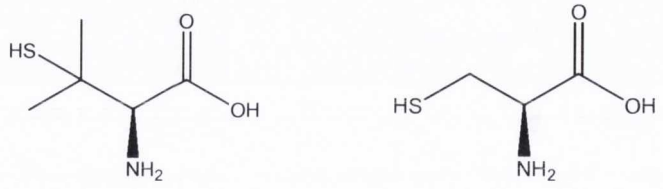

Figure 1.25: The *L*- forms of penicillamine left), and cysteine (right).

These semiconducting nanocrystals would thus have all the benefits of quantum confinement, be stable in aqueous media and highly luminescent, as well as optically active. These chiral QDs could ultimately find an application as fluorescent assays and sensors (or probes) in asymmetric synthesis, catalysis, enantioseparation, biochemical analysis and medical diagnostics.

We also planned to study our chiral QDs as potential components in a DSSC model, utilising the unique chiral CdSe and CdTe QDs as a replacement for the typical dye molecule, to create novel QDSSCs. This initially required the fabrication and

optimisation of the TiO_2-based working electrode. This was to be followed by attaching the QDs directly onto the TiO_2 surface, and the subsequent fabrication of a complete solar cell.

Also, we planned to prepare and investigate new QD–carbon composites using the novel chiral CdSe and CdTe QDs outlined previously, bound to MWNTs or graphene. As the QDs are stabilised by chiral amino acids there was the added possibility of a chiral-chiral interaction. The MWNTs and graphene were modified with appropriate functional groups that facilitated the covalent binding of the chiral CdSe and CdTe QDs to their surface.

Finally, we aimed to use these new QD-carbon nanomaterials as components in a solar cell. This was to be achieved by incorporating these QD-carbon composites into an ionic liquid (IL) based electrolyte. A typical DSSC style cell was used to test these additives, again fabricated in-house, using the electrodes developed earlier. These materials were expected to increase the transport of charge carriers through the cell, while also acting as a secondary light harvester, thus yielding improved solar efficiency.

In summary, our major scientific goals were to:

- Synthesise aqueous CdTe TGA QDs;
- Investigation of the interaction of these CdTe TGA QDs with an Eu(III) complex and testing of this QD-Eu conjugate as a biological sensor;
- Study of the interaction of CdTe TGA QDs with three porphyrin molecules;
- Synthesise entirely novel chiral CdSe and CdTe QDs using chiral amino acid stabilisers;
- Study all of the above systems using a range of steady state (UV-vis and PL) and time resolved (TCSPC, ultrafast ps-transient absorption spectroscopy, time resolved infrared spectroscopy) methods;
- Optimise the fabrication of a TiO_2 electrode for a DSSC;
- Test the chiral QDs as dye replacements in a QDSSC using the above electrode;
- Develop QD-carbon composite nanomaterials from our chiral QDs and MWNTs/ graphene, and test these in a DSSC as combined charge carriers/light harvesters.

Overall, we expect that the new nanomaterials developed in this project will also find a broader range of potential applications. We believe that our research will contribute to further progress of relevant areas of nanotechnology, chemistry, biosciences and solar technology.

References

(1) *http://publications.nigms.nih.gov/chemhealth/cool.htm.*

(2) Alivisatos, A. P. *Science* **1996**, *271*, 933.

(3) R.H, K. *Journal of Magnetism and Magnetic Materials* **1999**, *200*, 359.

(4) Geim, A. K. *Science* **2009**, *324*, 1530.

(5) Baughman, R. H.; Zakhidov, A. A.; de Heer, W. A. *Science* **2002**, *297*, 787.

(6) Ebbesen, T. W.; Lezec, H. J.; Hiura, H.; Bennett, J. W.; Ghaemi, H. F.; Thio, T. *Nature* **1996**, *382*, 54.

(7) Gao, J.; Xu, B. *Nano Today* **2009**, *4*, 37.

(8) Tseng, G. Y.; Ellenbogen, J. C. *Science* **2001**, *294*, 1293.

(9) Gellman, A. J.; Shukla, N. *Nature Materials* **2009**, *8*, 87.

(10) Brennan, L. J.; Byrne, M. T.; Bari, M.; Gun'ko, Y. K. *Advanced Energy Materials* **2011**, *1*, 472.

(11) Weller, H. *Angewandte Chemie International Edition in English* **1993**, *32*, 41.

(12) *http://wps.prenhall.com/wps/media/objects/602/616516/Media_Assests/Chapter21/Text_Images/FG21_10.JPG.*

(13) Smith, R. A. *Semiconductors*; Cambridge University Press, 1978.

(14) Reed, E. M. *Semiconductors and Semimetals*; Academic Press, 1992; Vol. 35.

(15) Seiler, E. D. G.; Littler, C. L. *Semiconductors and Semimetals*; Academic Press, 1992; Vol. 36.

(16) Zanio, E. K. *Semiconductors and Semimetals*; Academic Press, 1978; Vol. 13.

(17) Kumar, S.; Nann, T. *Small* **2006**, *2*, 316.

(18) Alivisatos, A. P. *The Journal of Physical Chemistry* **1996**, *100*, 13226.

(19) Nenadovic, M. T.; Rajh, T.; Micic, O. I. *The Journal of Physical Chemistry* **1985**, *89*, 397.

(20) Brus, L. *The Journal of Physical Chemistry* **1986**, *90*, 2555.

(21) Efros, A. L. *Soviet Physics: Semiconductors* **1982**, *16*, 772.

(22) http://www.elec-intro.com/evident-technologies.

(23) Yao, H.; Fukui, T.; Kimura, K. *The Journal of Physical Chemistry C* **2007**, *111*, 14968.

(24) Gautier, C.; Bürgi, T. *Journal of the American Chemical Society* **2006**, *128*, 11079.

(25) Nishida, N.; Yao, H.; Ueda, T.; Sasaki, A.; Kimura, K. *Chemistry of Materials* **2007**, *19*, 2831.

(26) Shimada, T.; Ookubo, K.; Komuro, N.; Shimizu, T.; Uehara, N. *Langmuir* **2007**, *23*, 11225.

(27) Chen, S.; Ferreira, P. J.; Sheng, W.; Yabuuchi, N.; Allard, L. F.; Shao-Horn, Y. *Journal of the American Chemical Society* **2008**, *130*, 13818.

(28) Qiu, L.; Liu, F.; Zhao, L.; Yang, W.; Yao, J. *Langmuir* **2006**, *22*, 4480.

(29) Zhao, S.-Y.; Chen, S.-H.; Wang, S.-Y.; Li, D.-G.; Ma, H.-Y. *Langmuir* **2002**, *18*, 3315.

(30) Qu, L.; Peng, X. *Journal of the American Chemical Society* **2002**, *124*, 2049.

(31) Peng, Z. A.; Peng, X. *Journal of the American Chemical Society* **2001**, *123*, 1389.

(32) Yu, Z.; Li, J.; O'Connor, D. B.; Wang; Barbara, P. F. *The Journal of Physical Chemistry B* **2003**, *107*, 5670.

(33) Santra, S.; Yang, H.; Holloway, P. H.; Stanley, J. T.; Mericle, R. A. *Journal of the American Chemical Society* **2005**, *127*, 1656.

(34) Gaponik, N.; Talapin, D. V.; Rogach, A. L.; Hoppe, K.; Shevchenko, E. V.; Kornowski, A.; Eychmüller, A.; Weller, H. *The Journal of Physical Chemistry B* **2002**, *106*, 7177.

(35) Wuister, S. F.; Driel, F. V.; Meijerink, A. *Journal of Luminescence* **2003**, *102*, 327.

(36) Wuister, S. F.; Driel, F. V.; Meijerink, A. *Physical Chemistry Chemical Physics* **2003**, *5*, 1253.

(37) Qian, H.; Dong, C.; Peng, J.; Qiu, X.; Xu, Y.; Ren, J. *The Journal of Physical Chemistry C* **2007**, *111*, 16852.

(38) Murphy, J. E.; Beard, M. C.; Norman, A. G.; Ahrenkiel, S. P.; Johnson, J. C.; Yu, P.; Mićić, O. I.; Ellingson, R. J.; Nozik, A. J. *Journal of the American Chemical Society* **2006**, *128*, 3241.

(39) Majetich, S. A.; Carter, A. C. *The Journal of Physical Chemistry* **1993**, *97*, 8727.

(40) Nirmal, M.; Murray, C. B.; Bawendi, M. G. *Physical Review B* **1994**, *50*, 2293.

(41) Wang, Y.; Herron, N. *The Journal of Physical Chemistry* **1991**, *95*, 525.

(42) Katari, J. E. B.; Colvin, V. L.; Alivisatos, A. P. *The Journal of Physical Chemistry* **1994**, *98*, 4109.

(43) Chestnoy, N.; Harris, T. D.; Hull, R.; Brus, L. E. *The Journal of Physical Chemistry* **1986**, *90*, 3393.

(44) Brus, L. *IEEE Journal of Quantum Electronics* **1986**, *22*, 1909.

(45) *http://gizmodo.com/5514438/quantum-dots-could-make-dark-grainy-cellphone-party-pics-obsolete.*

(46) Abel, K. A.; Shan, J.; Boyer, J.-C.; Harris, F.; van Veggel, F. C. J. M. *Chemistry of Materials* **2008**, *20*, 3794.

(47) Chen, X.; Hutchison, J. L.; Dobson, P. J.; Wakefield, G. *Journal of Colloid and Interface Science* **2008**, *319*, 140.

(48) Wuister, S. F.; Meijerink, A. *Journal of Luminescence* **2003**, *102–103*, 338.

(49) Xue, P.; Lu, R.; Huang, Y.; Jin, M.; Tan, C.; Bao, C.; Wang, Z.; Zhao, Y. *Langmuir* **2004**, *20*, 6470.

(50) Lin, W.; Fritz, K.; Guerin, G.; Bardajee, G. R.; Hinds, S.; Sukhovatkin, V.; Sargent, E. H.; Scholes, G. D.; Winnik, M. A. *Langmuir* **2008**, *24*, 8215.

(51) Wang, W.; Banerjee, S.; Jia, S.; Steigerwald, M. L.; Herman, I. P. *Chemistry of Materials* **2007**, *19*, 2573.

(52) Achermann, M.; Petruska, M. A.; Koleske, D. D.; Crawford, M. H.; Klimov, V. I. *Nano Letters* **2006**, *6*, 1396.

(53) Zhang, Q.; Russell, T. P.; Emrick, T. *Chemistry of Materials* **2007**, *19*, 3712.

(54) Liu, J.; Tanaka, T.; Sivula, K.; Alivisatos, A. P.; Frechet, J. M. J. *Journal of the American Chemical Society* **2004**, *126*, 6550.

(55) Locklin, J.; Patton, D.; Deng, S.; Baba, A.; Millan, M.; Advincula, R. C. *Chemistry of Materials* **2004**, *16*, 5187.

(56) Querner, C.; Benedetto, A.; Demadrille, R.; Rannou, P.; Reiss, P. *Chemistry of Materials* **2006**, *18*, 4817.

(57) Rogach, A. L.; Kornowski, A.; Gao, M.; Eychmüller, A.; Weller, H. *The Journal of Physical Chemistry B* **1999**, *103*, 3065.

(58) Medintz, I. L.; Uyeda, H. T.; Goldman, E. R.; Mattoussi, H. *Nature Materials* **2005**, *4*, 435.

(59) Byrne, S. J.; Corr, S. A.; Rakovich, T. Y.; Gun'ko, Y. K.; Rakovich, Y. P.; Donegan, J. F.; Mitchell, S.; Volkov, Y. *Journal of Materials Chemistry* **2006**, *16*, 2896.

(60) Byrne, S. J.; Williams, Y.; Davies, A.; Corr, S. A.; Rakovich, A.; Gun'ko, Y. K.; Rakovich, Y. P.; Donegan, J. F.; Volkov, Y. *Small* **2007**, *3*, 1152.

(61) Jan, E.; Byrne, S. J.; Cuddihy, M.; Davies, A. M.; Volkov, Y.; Gun'ko, Y. K.; Kotov, N. A. *ACS Nano* **2008**, *2*, 928.

(62) Chen, J.-Y.; Lee, Y.-M.; Zhao, D.; Mak, N.-K.; Wong, R. N.-S.; Chan, W.-H.; Cheung, N.-H. *Photochemistry and Photobiology* **2010**, *86*, 431.

(63) Weissman, S. I. *The Journal of Chemical Physics* **1942**, *10*, 214.

(64) Sabbatini, N.; Guardigli, M.; Lehn, J.-M. *Coordination Chemistry Reviews* **1993**, *123*, 201.

(65) dos Santos, C. M. G.; Harte, A. J.; Quinn, S. J.; Gunnlaugsson, T. *Coordination Chemistry Reviews* **2008**, *252*, 2512.

(66) Poole, R. A.; Kielar, F.; Richardson, S. L.; Stenson, P. A.; Parker, D. *Chemical Communications* **2006**, 4084.

(67) McMahon, B.; Mauer, P.; McCoy, C. P.; Lee, T. C.; Gunnlaugsson, T. *Journal of the American Chemical Society* **2009**, *131*, 17542.

(68) Massue, J.; Quinn, S. J.; Gunnlaugsson, T. *Journal of the American Chemical Society* **2008**, *130*, 6900.

(69) Bunzli, J.-C. G.; Piguet, C. *Chemical Society Reviews* **2005**, *34*, 1048.

(70) Steemers, F. J.; Verboom, W.; Reinhoudt, D. N.; van der Tol, E. B.; Verhoeven, J. W. *Journal of the American Chemical Society* **1995**, *117*, 9408.

(71) Xiao, M.; Selvin, P. R. *Journal of the American Chemical Society* **2001**, *123*, 7067.

(72) Torelli, S.; Imbert, D.; Cantuel, M.; Bernardinelli, G.; Delahaye, S.; Hauser, A.; Bünzli, J.-C. G.; Piguet, C. *Chemistry – A European Journal* **2005**, *11*, 3228.

(73) Hildebrandt, N.; Charbonniere, L.; Lohmannsroben, H.-G. *Journal of Biomedicine and Biotechnology* **2007**, *2007*.

(74) Charbonnière, L. J.; Hildebrandt, N. *European Journal of Inorganic Chemistry* **2008**, *2008*, 3241.

(75) Charbonnière, L. J.; Hildebrandt, N.; Ziessel, R. F.; Löhmannsröben, H.-G. *Journal of the American Chemical Society* **2006**, *128*, 12800.

(76) Horváth, O.; Huszánk, R.; Valicsek, Z.; Lendvay, G. *Coordination Chemistry Reviews* **2006**, *250*, 1792.

(77) Borek, C.; Hanson, K.; Djurovich, P. I.; Thompson, M. E.; Aznavour, K.; Bau, R.; Sun, Y.; Forrest, S. R.; Brooks, J.; Michalski, L.; Brown, J. *Angewandte Chemie International Edition* **2007**, *46*, 1109.

(78) Kalyanasundaram, K. *Photochemistry of polypyridine and porphyrin complexes*; Academic Press: London; San Diego, 1992.

(79) Galievsky, V. A.; Chirvony, V. S.; Kruglik, S. G.; Ermolenkov, V. V.; Orlovich, V. A.; Otto, C.; Mojzes, P.; Turpin, P.-Y. *The Journal of Physical Chemistry* **1996**, *100*, 12649.

(80) Kruglik, S. G.; Galievsky, V. A.; Chirvony, V. S.; Apanasevich, P. A.; Ermolenkov, V. V.; Orlovich, V. A.; Chinsky, L.; Turpin, P.-Y. *The Journal of Physical Chemistry* **1995**, *99*, 5732.

(81) Praseuth, D.; Guaudemer, A.; Verlhac, J.; Kraljic, I.; Sissoeff, I.; Guille, E. *Journal of Photochemistry and Photobiology* **1986**, *44*, 717.

(82) Benstead, K.; Moore, J. V. *British Journal of Cancer* **1990**, *62*, 48.

(83) Cohen, L.; Schwartz, S. *Cancer Research* **1966**, *26*, 1769.

(84) Krasnovsky, A. A. *Biochemistry (Moscow)* **2007**, *72*.

(85) Schweitzer, C.; Schmidt, R. *Chemical Reviews* **2003**, *103*, 1685.

(86) Schaffer, M.; Schaffer, P. M.; Corti, L.; Gardiman, M.; Sotti, G.; Hofstetter, A.; Jori, G.; Dühmke, E. *Journal of Photochemistry and Photobiology B: Biology* **2002**, *66*, 157.

(87) Eichkorn, K.; Ahlrichs, R. *Chemical Physics Letters* **1998**, *288*, 235.

(88) Sapsford, K. E.; Berti, L.; Medintz, I. L. *Angewandte Chemie International Edition* **2006**, *45*, 4562.

(89) Willard, D. M.; Carillo, L. L.; Jung, J.; Van Orden, A. *Nano Letters* **2001**, *1*, 469.

(90) Raymo, F. M.; Yildiz, I. *Physical Chemistry Chemical Physics* **2007**, *9*, 2036.

(91) Michalet, X.; Pinaud, F. F.; Bentolila, L. A.; Tsay, J. M.; Doose, S.; Li, J. J.; Sundaresan, G.; Wu, A. M.; Gambhir, S. S.; Weiss, S. *Science* **2005**, *307*, 538.

(92) Samia, A. C. S.; Chen, X.; Burda, C. *Journal of the American Chemical Society* **2003**, *125*, 15736.

(93) Rakovich, A.; Savateeva, D.; Rakovich, T.; Donegan, J. F.; Rakovich, Y. P.; Kelly, V.; Lesnyak, V.; Eychmüller, A. *Nanoscale Research Letters* **2010**, *5*, 753.

(94) Juzenas, P.; Chen, W.; Sun, Y.-P.; Coelho, M. A. N.; Generalov, R.; Generalova, N.; Christensen, I. L. *Advanced Drug Delivery Reviews* **2008**, *60*, 1600.

(95) Gaponik, N.; Talapin, D. V.; Rogach, A. L.; Hoppe, K.; Shevchenko, E. V.; Kornowski, A.; Eychmuller, A.; Weller, H. *The Journal of Physical Chemistry B* **2002**, *106*, 7177.

(96) Chen, J.; Gao, Y.; Guo, C.; Wu, G.; Chen, Y.; Lin, B. *Spectrochimica Acta Part A: Molecular and Biomolecular Spectroscopy* **2008**, *69*, 572.

(97) Chen, Y.; Rosenzweig, Z. *Analytical Chemistry* **2002**, *74*, 5132.

(98) Bao, H.; Wang, E.; Dong, S. *Small* **2006**, *2*, 476.

(99) Huang, F.; Chen, G. *Spectrochimica Acta Part A: Molecular and Biomolecular Spectroscopy* **2008**, *70*, 318.

(100) Liu, F.-C.; Cheng, T.-L.; Shen, C.-C.; Tseng, W.-L.; Chiang, M. Y. *Langmuir* **2008**, *24*, 2162.

(101) Liu, W.; Choi, H. S.; Zimmer, J. P.; Tanaka, E.; Frangioni, J. V.; Bawendi, M. *Journal of the American Chemical Society* **2007**, *129*, 14530.

(102) Zhang, Y.-h.; Zhang, H.-s.; Guo, X.-f.; Wang, H. *Microchemical Journal* **2008**, *89*, 142.

(103) Berona, N.; Nakanishi, K.; Woody, R. W. *Circular Dichroism*; Wiley, 2000.

(104) Kitaev, V. *Journal of Materials Chemistry* **2008**, *18*, 4745.

(105) Govorov, A. O.; Fan, Z.; Hernandez, P.; Slocik, J. M.; Naik, R. R. *Nano Letters* **2010**, *10*, 1374.

(106) Zhang, J.; Albelda, M. T.; Liu, Y.; Canary, J. W. *Chirality* **2005**, *17*, 404.

(107) Govorov, A. O.; Gun'ko, Y. K.; Slocik, J. M.; Gerard, V. A.; Fan, Z.; Naik, R. R. *Journal of Materials Chemistry* **2011**, *21*, 16806.

(108) Schaaff, T. G.; Whetten, R. L. *The Journal of Physical Chemistry B* **2000**, *104*, 2630.

(109) Yao, H.; Miki, K.; Nishida, N.; Sasaki, A.; Kimura, K. *Journal of the American Chemical Society* **2005**, *127*, 15536.

(110) Shemer, G.; Krichevski, O.; Markovich, G.; Molotsky, T.; Lubitz, I.; Kotlyar, A. B. *Journal of the American Chemical Society* **2006**, *128*, 11006.

(111) Lieberman, I.; Shemer, G.; Fried, T.; Kosower, E. M.; Markovich, G. *Angewandte Chemie-International Edition* **2008**, *47*, 4855.

(112) Dukovic, G.; Balaz, M.; Doak, P.; Berova, N. D.; Zheng, M.; McLean, R. S.; Brus, L. E. *Journal of the American Chemical Society* **2006**, *128*, 9004.

(113) Peng, X.; Komatsu, N.; Bhattacharya, S.; Shimawaki, T.; Aonuma, S.; Kimura, T.; Osuka, A. *Nat Nano* **2007**, *2*, 361.

(114) Moloney, M. P.; Gun'ko, Y. K.; Kelly, J. M. *Chemical Communications* **2007**, 3900.

(115) Elliott, S. D.; Moloney, M. c. l. P.; Gun'ko, Y. K. *Nano Letters* **2008**, *8*, 2452.

(116) Nakashima, T.; Kobayashi, Y.; Kawai, T. *Journal of the American Chemical Society* **2009**, *131*, 10342.

(117) Carrillo-Carrión, C.; Cárdenas, S.; Simonet, B. M.; Valcárcel, M. *Analytical Chemistry* **2009**, *81*, 4730.

(118) Zhou, Y.; Yang, M.; Sun, K.; Tang, Z.; Kotov, N. A. *Journal of the American Chemical Society* **2010**, *132*, 6006.

(119) Govan, J. E.; Jan, E.; Querejeta, A.; Kotov, N. A.; Gun'ko, Y. K. *Chemical Communications* **2010**, *46*, 6072.

(120) Alivisatos, P. *Nat Biotech* **2004**, *22*, 47.

(121) Bruchez, M., Jr.; Moronne, M.; Gin, P.; Weiss, S.; Alivisatos, A. P. *Science* **1998**, *281*, 2013.

(122) Shockley, W.; Queisser, H. J. *Journal of Applied Physics* **1961**, *32*, 510.

(123) Shalav, A.; Richards, B. S.; Trupke, T.; Kramer, K. W.; Gudel, H. U. *Applied Physics Letters* **2005**, *86*, 013505.

(124) Eli, Y.; Owen, M.; Optical Society of America: 2010, p SWA1.

(125) Yong-Hang, Z.; Ding, D.; Johnson, S. R.; Lim, S. H.; Optical Society of America: 2010, p SWC4.

(126) Landsberg, P. T.; Baruch, P. *Journal of Physics A: Mathematical and General* **1989**, *22*, 1911.

(127) De Vos, A. *Journal of Physics D: Applied Physics* **1980**, *13*, 839.

(128) Renata, R. *Optical Materials* **2010**, *32*, 850.

(129) Goetzberger, A.; Greube, W. *Applied Physics A: Materials Science & Processing* **1977**, *14*, 123.

(130) Grätzel, M.; Jørgensen, C.; Kalyanasundaram, K.; Kiwi, J.; Reisfeld, R.; Tributsch, H.; Reisfeld, R.; Jørgensen, C.; Springer Berlin / Heidelberg: 1982; Vol. 49, p 1.

(131) Boer, D. K. G. d. *SPIE Newsroom* **2010**.

(132) R. Reisfeld; Jørgensen, C. K. *Structure and Bonding* **1982**, *49*, 1.

(133) Slooff, L. H. *Phys. Status Solidi Rapid Res. Lett.* **2008**, *2*, 257.

(134) Jalali, B.; Fathpour, S.; Tsia, K. *Optics and Photonics News* **2009**, *20*, 18.

(135) Shcherbatyuk, G. V.; Inman, R. H.; Wang, C.; Winston, R.; Ghosh, S. *Applied Physics Letters* **2010**, *96*, 191901.

(136) Nozik, A. J. *Annual Review of Physical Chemistry* **2001**, *52*, 193.

(137) Tisdale, W. A.; Williams, K. J.; Timp, B. A.; Norris, D. J.; Aydil, E. S.; Zhu, X.-Y. *Science* **2010**, *328*, 1543.

(138) Stubbs, S. K.; Hardman, S. J. O.; Graham, D. M.; Spencer, B. F.; Flavell, W. R.; Glarvey, P.; Masala, O.; Pickett, N. L.; Binks, D. J. *Physical Review B* **2010**, *81*, 081303.

(139) Beard, M. C.; Knutsen, K. P.; Yu, P.; Luther, J. M.; Song, Q.; Metzger, W. K.; Ellingson, R. J.; Nozik, A. J. *Nano Letters* **2007**, *7*, 2506.

(140) Kim, S. J.; Kim, W. J.; Sahoo, Y.; Cartwright, A. N.; Prasad, P. N. *Applied Physics Letters* **2008**, *92*, 031107.

(141) Grätzel, M.; O'Regan, B. *Nature* **1991**, *353*, 737.

(142) Grätzel, M. *Inorganic Chemistry* **2005**, *44*, 6841.

(143) Kamat, P. V. *The Journal of Physical Chemistry C* **2008**, *112*, 18737.

(144) Wang, X.; Koleilat, G. I.; Tang, J.; Liu, H.; Kramer, I. J.; Debnath, R.; Brzozowski, L.; Barkhouse, D. A. R.; Levina, L.; Hoogland, S.; Sargent, E. H. *Nat Photon* **2011**, *5*, 480.

(145) Fuke, N.; Hoch, L. B.; Koposov, A. Y.; Manner, V. W.; Werder, D. J.; Fukui, A.; Koide, N.; Katayama, H.; Sykora, M. *ACS Nano* **2010**, *4*, 6377.

(146) Semonin, O. E.; Luther, J. M.; Choi, S.; Chen, H.-Y.; Gao, J.; Nozik, A. J.; Beard, M. C. *Science* **2011**, *334*, 1530.

(147) Ventra, M. D. *Academic Publishers* **2004**.

(148) Loiseau, A.; Launois, P.; Petit, P.; Roche, S.; J., S. *Springer* **2006**.

(149) Stankovich, S. D., D. A.; Dommett, G. H. B.; Kohlhaas, K. M.; Zimney, E. J.; Stach, E. A.; Piner, R. D.; Nguyen, S. T.; Ruoff, R. S. *Nature* **2006**, *442*, 282.

(150) Ferrari, A. C. M., J. C.; Scardaci, V.; Casiraghi, C.; Lazzeri, M.; Mauri, F.; Piscanec, S.; Jiang, D.; Novoselov, K. S.; Roth, S.; Geim, A. K. *Physical Review Letters* **2006**, *97*, 187401.

(151) Geim, A. K. N., K. S. *Nature Materials* **2007**, *6*, 183.

(152) Iijima, S.; Ichihashi, T. *Nature* **1993**, *363*, 603.

(153) Viswanathan, G.; Chakrapani, N.; Yang, H.; Wei, B.; Chung, H.; Cho, K.; Ryu, C. Y.; Ajayan, P. M. *J. Am. Chem. Soc.* **2003**, *125*, 9258.

(154) Gersten, J. I.; Smith, F. W. *Wiley* **2001**.

(155) Saito, R. D. *Imperial College Press* **2001**.

(156) Frank, S. P., P.; Wang, Z. L.; Heer, W. A. n. d. *Science* **1998**, *280*, 1744.

(157) Collins, P. G. A., P. *Scientific American* **2000**, *283*, 62.

(158) Peng, X.; Komatsu, N.; Bhattacharya, S.; Shimawaki, T.; Aonuma, S.; Kimura, T.; Osuka, A. *Nature Nanotechnology* **2007**, *2*, 361.

(159) Williams, K. A.; Veenhuizen, P. T. M.; de la Torre, B. G.; Eritja, R.; Dekker, C. *Nature* **2002**, *420*, 761.

(160) Sainsbury, T.; Fitzmaurice, D. *Chemistry of Materials* **2004**, *16*, 2174.

(161) Li, X.; Liu, Y.; Fu, L.; Cao, L.; Wei, D.; Y., W. *Advanced Functional Materials* **2006**, *16*, 2431.

(162) Byrne, M. T.; Gun'ko, Y. K. *Advanced Materials* **2010**, *22*, 1672.

(163) Sgobba, V.; Guldi, D. M. *Journal of Materials Chemistry* **2008**, *18*, 153.

(164) Wang, X.; Zhi, L.; Mullen, K. *Nano Letters* **2007**, *8*, 323.

(165) Kazaoui, S.; Minami, N.; Nalini, B.; Kim, Y.; Hara, K. *Journal of Applied Physics* **2005**, *98*, 084314.

(166) Chen, P. Y.; Lee, C. P.; Vittal, R.; Ho, K. C. *J. Power Sources* **2010**, *195*, 3933.

(167) Lee, C.-P.; Chen, P.-Y.; Vittal, R.; Ho, K.-C. *Journal of Materials Chemistry* **2010**, *20*, 2356.

(168) Usui, H.; Matsui, H.; Tanabe, N.; Yanagida, S. *Journal of Photochemistry and Photobiology A: Chemistry* **2004**, *164*, 97.

(169) Papageorgiou, N.; Athanassov, Y.; Armand, M.; Bonhote, P.; Pettersson, H.; Azam, A.; Gratzel, M. *Journal of The Electrochemical Society* **1996**, *143*, 3099.

(170) Rogers, R. D.; Seddon, K. R. *Science* **2003**, *302*, 792.

(171) Gratzel, M. *Nature* **2001**, *414*, 338.

(172) Fukushima, T.; Aida, T. *Chemistry – A European Journal* **2007**, *13*, 5048.

(173) Kubo, W.; Kambe, S.; Nakade, S.; Kitamura, T.; Hanabusa, K.; Wada, Y.; Yanagida, S. *The Journal of Physical Chemistry B* **2003**, *107*, 4374.

(174) Noda, A.; Hayamizu, K.; Watanabe, M. *The Journal of Physical Chemistry B* **2001**, *105*, 4603.

(175) Murakami, T. N.; Ito, S.; Wang, Q.; Nazeeruddin, M. K.; Bessho, T.; Cesar, I.; Liska, P.; Humphry-Baker, R.; Comte, P.; Pechy, P.; Gratzel, M. *Journal of The Electrochemical Society* **2006**, *153*, A2255.

(176) Imoto, K.; Takahashi, K.; Yamaguchi, T.; Komura, T.; Nakamura, J. i.; Murata, K. *Solar Energy Materials and Solar Cells* **2003**, *79*, 459.

(177) Suzuki, K.; Yamaguchi, M.; Kumagai, M.; Yanagida, S. *Chemistry Letters* **2003**, *32*, 28.

(178) Saito, Y. K., W.; Kitamura, T.; Wada, Y.; Yanagida, S. *Journal of Photochemistry and Photobiology a-Chemistry* **2004**, *164*, 153.

Chapter 2: Experimental

2.1 Starting Materials

Cadmium Perchlorate, Sodium Tellurite, Sodium Borohyride, Coumarin 153, Rhodamine 6G, *D*-Penicillamine, *L*- Penicillamine, Sodium Sulphite, elemental Selenium, 11 Mercaptoundecanoic Acid, Dimethylaminopyridine (DMAP), Graphite, Deuterium Oxide, and Sephadex G25 were all supplied by Aldrich.

The stabilisers *D*-Cysteine and *L*-Cysteine, as well as Cysteamine and 1-Ethyl-3-(3-dimethylaminopropyl) Carbodiimide (EDC), were purchased from Fluka.

Aluminium Telluride was purchased from Cerac Inc.

Multi-walled nanotubes were purchased from MER Corporation (Tucson, Arizona 85706).

Titanium dioxide pastes, platinum paste, electrolytes and FTO coated glass were all supplied by Dyesol unless otherwise specified.

Millipore water obtained from a Millipore filtration system operating at 18.2 MΩ was used throughout. This was deoxygenated by sonicating under high vacuum for 30 minutes and then bubbling argon through it for 20 minutes.

2.2 Synthesis for Chapter 3

2.2.1 Preparation of aqueous CdTe nanoparticles by heating under reflux

CdTe QDs were synthesised using our modification of the method published by Gaponik and co-workers[1]. $Cd(ClO_4)_2 \cdot 6H_2O$ and the stabiliser TGA were added to 150 mL degassed Millipore water in 1:1.4 ratio. The pH of the solution was adjusted to 11 by dropwise addition of a 2 M NaOH solution. To a known weight of Al_2Te_3 (molar ratio of 0.25 compared to Cd) was added 15 mL of H_2SO_4 to generate H_2Te gas which was then bubbled through the Cd/thiol solution. The resulting non-luminescent solution was then heated under reflux. Once the QDs reached the desired size, the reflux was

stopped and different fractions were obtained *via* size-selective precipitation using isopropanol. The final samples were further purified on a Sephadex-G25 column.

2.3 Synthesis for Chapter 5

2.3.1 Preparation of aqueous Selenium stock solution (Na_2SeSO_3)

This water soluble selenium salt was prepared by dissolving 0.0947 g of Na_2SO_3 in 50 mL (1.5×10^{-2} M) of degassed Millipore water. Once dissolved, 0.0315 g (4×10^{-4} M) of Se powder was then added. The apparatus was set up for reflux and put under a constant flow of argon. The mixture was stirred vigorously to ensure the insoluble Se did not stick to the sides of the round bottom flask. The mixture was refluxed at 110 °C overnight. The resulting clear colourless solution was used immediately.

2.3.2 Microwave preparation of aqueous chiral CdSe nanoparticles

2 mL of an aqueous 1×10^{-2} M solution of *D*-, *L*- or *Rac*- penicillamine was added to degassed Millipore water (40 mL) in a 100 mL flask, under a constant flow of Ar. The pH was adjusted to 11.5 by the dropwise addition of 5 M NaOH. 1×10^{-2} M $Cd(ClO_4)_2.xH_2O$ (2 mL) and 1×10^{-2} M of Na_2SeO_3 (2 mL) were then added and the solution was stirred vigorously. The resulting homogeneous solution was then transferred to a CEM Star System 6 microwave and irradiated for 40 seconds at 1500W. The resulting clear, yellow, solution was then stored in the dark for at least one day. The volume of the colloid was then reduced to ~3 mL using the rotary evaporator and propan-2-ol was added to precipitate out the nanoparticles. The particles were isolated by centrifugation. The particles were washed several times with a propan-2-ol water mixture (9:1) and finally re-dispersed in Millipore water. UV-vis, CD and fluorescence spectroscopy measurements were carried out on the stable suspensions in water.

2.3.3 Microwave preparation of aqueous chiral CdTe nanoparticles

CdTe nanoparticles were prepared similarly to the CdSe nanoparticles, however the selenium source was replaced with 2 mL of a 1×10^{-2} M Na_2TeO_3 aqueous solution. 2 mL of 1×10^{-1} M $NaBH_4$ was also added before the solution was microwaved. The

resulting clear, orange solution was stored in the dark for at least one day. The volume of the colloid was then reduced to ~3 mL using the rotary evaporator and propan-2-ol was added to precipitate out the nanoparticles. These were collected by centrifugation. The nanoparticles were washed several times with a propan-2-ol, water mixture, (9:1), and finally re-dispersed in Millipore water. UV-Vis, CD and fluorescence spectroscopy was carried out on the stable suspensions in water.

2.4 Synthesis for Chapter 7

2.4.1 Functionalisation of MWNTs with cysteamine and 11-mercaptoundecanoic acid

15 mL of conc. nitric acid was added to 10 mg of MWNTs (MER, ~2 μm length) in a 25 mL round bottomed flask. The solution was sonicated for 15 minutes and then refluxed for 48 hours at 135°C. After cooling, the solution was then sonicated again for 10 minutes and filtered using Millipore PTFE 0.45μm membrane filters. The MWNTs were washed with Millipore water and removed from the PTFE filter by sonication in 20 mL water. 30 mg $KMnO_4$ (1.9×10^{-4} moles) were added and the solution stirred at 0 °C. 10 mL (70%, 0.1 moles) perchloric acid was added dropwise and the solution stirred at 0 °C for 30 minutes. Solution was removed from the ice bath and 0.62 g (0.0032 moles) citric acid was added. The solution was stirred until the purple colour disappeared. The resulting mixture was filtered as before and washed with Millipore water. MWNTs were removed from the PTFE filter and dried in an oven @ 70°C. The MWNTs were then sonicated in 20 mL thionyl chloride and refluxed @ 70°C under argon for 24 hrs. The MWNTs were then dried first on a rotovap and then under high vacuum on a shlenk line. 20 mL 100% pure ethylenediame was then added and sonicated for 15 minutes to ensure dispersion. The solution was stirred overnight, then filtered and washed with Millipore water. MWNTs were removed from the PTFE filter by sonication in 30 mL Millipore water. 0.2 g (1.3×10^{-3} moles) EDC (1-ethyl-3-(3-dimethylaminopropyl) carbodiimide) and 0.538 g (4.4×10^{-3} moles) DMAP (4-Dimethylaminopyridine) were added to the solution and stirred for 10 minutes.

To functionalise with cysteamine or 11-mercaptoundecanoic acid, either 50 mg (6.4×10^{-4} moles) of cysteamine, or 140 mg (6.4×10^{-4} moles) of 11-mercaptoundecanoic acid, were added to this solution and stirred overnight. The resulting mixture was filtered as before and washed with Millipore water. The EDC coupling reaction with 11-mercaptoundecanoic acid was repeated to ensure better coverage of the MWNTs.

2.4.2 Preparation of Graphene Oxide

1 g (0.08 moles) of graphite was added to a 500 mL round bottom flask. To this 0.5 g (0.007 moles) of sodium nitrite and 25mL of sulphuric acid were added. This solution was then stirred on ice and 3 g (0.019 moles) of $KMnO_4$ were added very slowly (over 10-15 minutes) while stirring on ice. The solution was then stirred for 1 hour at 35°C. 200 mL of Millipore water were then added and the resulting solution was centrifuged @ 3,500 rpm for 10 minutes. The graphene oxide precipitate was washed with a 10% HCl: 90% Millipore water solution repeatedly until the supernatant was clear, centrifuging each time. The graphene oxide was then washed with ethanol five times and dried in as oven at 70°C overnight.

2.4.3 Functionalisation of Graphene Oxide with cysteamine and 11-mercaptoundecanoic acid

10 mg of graphene oxide, obtained as outlined above, were sonicated in 20 mL of Millipore water. To this 30 mg (1.9×10^{-4} moles) of $KMnO_4$ was added and the solution stirred at 0 °C. 10 mL (70%, 0.1 moles) of perchloric acid was added dropwise and the solution stirred at 0 °C for 30 minutes. The solution was removed from the ice bath and 0.62 g (0.0032 moles) citric acid was added. The solution was stirred until the purple colour disappeared. The resulting mixture was filtered using Millipore PTFE 0.45μm membrane filters and washed with Millipore water. The graphene oxide was removed from the PTFE filter by sonication in 30 mL Millipore water. 0.2 g (1.3×10^{-3} moles) EDC (1-ethyl-3-(3-dimethylaminopropyl) carbodiimide) and 0.538 g (4.4×10^{-3} moles) DMAP (4-Dimethylaminopyridine) were added to solution and stirred for 10 minutes.

To functionalise with cysteamine or 11-mercaptoundecanoic acid, either 50 mg (6.4×10^{-4} moles) of cysteamine, or 140 mg (6.4×10^{-4} moles) of 11-mercaptoundecanoic acid, was added to this solution and stirred overnight. The resulting mixture was filtered as before and washed with Millipore water. The EDC coupling reaction with was repeated to ensure better coverage of the MWNTs.

2.4.4 Microwave preparation of aqueous chiral CdSe-carbon nanocomposites

Approximately 0.5 mg of the functionalised carbon allotrope (either QD-MWNT or QD-G) prepared previously were sonicated in Millipore water. Using this water as the reaction solvent, CdSe nanoparticles stabilised with *Rac*- Penicillamine and *Rac*- Cysteine were prepared as outlined previously. A basic aqueous (1×10^{-2} M) solution of stabiliser *Rac*- Penicillamine or Cysteine was prepared and 2 mL (2×10^{-5} moles) was added to 45 mL of Millipore water (containing functionalised MWNTs or GO) in a 100 mL round bottomed flask. The pH was adjusted to 11 by the dropwise addition of 1M NaOH. 1×10^{-2} M $Cd(ClO_4)_2.xH_2O$ (2 mL) and 1×10^{-2} M of Na_2SeO_3 (2 mL) respectively were then added and the resulting solution was stirred vigorously. This homogeneous solution was then transferred to a conventional microwave and irradiated for 40 seconds at 1500 W. The resulting clear solution was stored in the dark for at least one day to allow the nanoparticles to grow. The solutions were then filtered using Millipore PTFE 0.22 μm membrane filters in order to isolate the carbon composite. The volume of the filtered solution was then reduced to ~2 mL using the rotary evaporator and propan-2-ol was added to precipitate out the nanoparticles. These were collected by centrifugation. The nanoparticles were washed several times with a propan-2-ol, water mixture, (9:1), and finally re-dispersed in Millipore water.

2.4.5 Microwave preparation of aqueous chiral CdTe-carbon nanocomposites

This synthesis was carried out similar to above except CdTe nanoparticles were prepared in the presence of functionalised carbon composite. The method of CdTe preparation follows that described earlier (Section 2.4.4). Again the solutions were then filtered using Millipore PTFE 0.22 μm membrane filters in order to isolate the carbon composite.

2.4.6 TCO coated glass; specifications and preparation

The working electrode was produced onto sheets of non-conductive glass. These were 3.2 mm thick, coated on one side with a layer of transparent conducting oxide (TCO), in this case fluorine-doped tin oxide (FTO) and obtained from Pilkington Group Ltd. (glass specification: NSC TEC™ C15). These glass sheets were then cut into approx. 2 cm x 2 cm square slides. The slides were cleaned by sonication in Millipore water with detergent for 30 minutes, and then washed thoroughly by first rinsing, and then sonicating in Millipore water, followed by sonicating in ethanol. The slides were then dried in an oven (approx. 75°C, 30 minutes) after which they were allowed to cool. The presence of the FTO layer was confirmed through SEM and sheet resistance measurements.

2.4.7 Working electrode fabrication; TiO_2 deposition using the doctor blade method

Before deposition of the TiO_2 paste, the slides were first treated by immersing them in an aqueous TiO_2 sol solution at 70°C for 30 minutes, created by the hydrolysis of $TiCl_4$ (1.1 mL) in Millipore water (200 mL, 0.05 M). After this the slides were washed with Millipore water and ethanol and then dried (approx. 75°C, 30 minutes) after which they were allowed to cool. The presence of this initial TiO_2 layer was confirmed however by an increase in the sheet resistance.

To create templates for the fabrication of the solar cells, circular holes measuring 6 mm in diameter were cut out of sticky tape using a standard hole punch. The tape was then cut out into square segments large enough to cover the 2 cm x 2 cm slide surface. These templates were stuck onto the FTO coated surface of the slides as a mask, thus leaving a 6 mm diameter hole exposed. The tapes used were standard black electrical tape (thickness 125 μm) and Scotch Magic 3M tape, (thickness 60 μm). Using a razor blade, a layer of one of the TiO_2 nanoparticle pastes was then applied across the open hole of the mask onto the surface of the FTO-slide placing a small amount of the paste in front of the hole and swiping a razor blade across the hole, thus depositing a film of paste onto the substrate. The resulting thickness of the deposited layer thus depends on the tape thickness, as well as the composition and concentration

of the paste. This layer was allowed to dry in air for a day. The mask was then removed and the slides were further dried in an oven at 75°C. For the deposition of further layers of TiO_2, the tape template was then reapplied to the slide, taking care to align the hole with the previous layer, and another layer was applied as outlined above.

These were then sintered using the following heating profile; 1) a heating phase from room temperature to 200°C at a rate of 8°C per minute, 2) a dwell time of 15 minutes at 200°C, 3) a second heating ramp stage to 450°C at a rate of 12°C per minute, 4) a dwell time of 30 minutes at 400°C, 5) a slow cooling phase back to room temperature, no faster than 10°C per minute.

Following sintering, the resulting TiO_2-FTO-slides were then treated again by immersing them in a solution of $TiCl_4$ in Millipore water (0.05 M, 70°C, 30 minutes). After this the slides were washed with Millipore water and ethanol and then dried. The slides were then sintered for a second time using the same heating profile and washed again with Millipore water and ethanol and then dried. These were analysed using SEM and profilometry.

2.4.8 Counter electrode fabrication; Pt deposition using the doctor blade method

This was created in much the same manner as the working electrode outlined above, using 2 mm x 2 mm slides of the same FTO coated NSC TEC™ C15 glass. A film of platinum containing paste (Dyesol, PT1) was applied via the doctor blade method. The mask was removed and the glass slides were then sintered at 450°C for 30 minutes after which they were allowed to cool to room temperature.

2.4.9 Solar cell fabrication

The above working electrodes were soaked overnight in a solution of the desired QDs, removed and washed with water. These were then allowed to dry in air. 10 μL of the acetonitrile based electrolyte (Dyesol EL-141) was pipetted onto the QD doped TiO_2 surface of the working electrode and then the Pt counter electrode was placed on top. This arrangement was held in place using crocodile clips and measured for photovoltaic activity.

2.5 Instrumental Techniques and Procedures

2 .5.1 UV-Vis Absorption spectroscopy

UV-Vis absorption spectra were recorded at room temperature using a SHIMADZU UV2101 PC UV-Vis scanning spectrometer. All samples were examined in a 1 cm quartz cell. The solvent used was Millipore water.

2.5.2 PL spectroscopy

Emission spectra were recorded using a Varian Cary Eclipse Fluorescence Spectrophotometer working in fluorescence mode. Fluorescence was detected at right angles to excitation. All samples were measured in a 1 cm quartz fluorescent cell with excitation and emission monochromators set to 5 nm.

2.5.3 Fluorescence Lifetime measurements

The photoluminescence lifetime and time resolved emission spectra measurements were performed using a time correlated single photon counting (TCSPC) spectrometer (Fluorolog 3 Horiba Jobin Yvon) and different semiconductor diode lasers (295 nm, 340 nm, and 370 nm ''Nanoled''- HORIBA Jobin Yvon) with pulse duration shorter than 1 ns for excitation.

Analysis of the relaxation behaviour, in both fluorescence lifetime decay measurements, and transient absorption measurements, was achieved by fitting the rate of decays to an exponential model. The equation used to fit the data is as follows:

$y(t) = A + B1\exp(-k1t) + B2\exp(-k2t)$ biexponential fitting

$y(t) = A + B1\exp(-k1t) + B2\exp(-k2t) + B3\exp(-k3t)$ triexponential fitting

with $\tau_1 = 1/k1$, $\tau_2 = 1/k2$ and $\tau_3 = 1/k3$

where the B terms are the pre-exponential factors or amplitude factors. This fitting results in two (or three) lifetimes, τ_1, τ_2 (and τ_3) and the contribution from these lifetimes is directly proportional to the magnitude of the B terms.

This method of fit uses a non-linear least squares fit, a nonlinear regression based on the Levenberg-Marquardt algorithm. The quality of fit of the model to the decay curve is determined statistically with the R^2 and X^2 (chi squared) coefficients. R^2 is a measure of the variability of the data with the model and looks at how the residuals (residual sum of squares) vary with respect to the total sum. Graphing the residuals should result in a random set of values with no trends. X^2 is the sum of the differences between the observed and expected outcome frequencies, each squared and divided by the expectation. A coefficient value approaching 1 is desired for both R^2 and X^2 and represents a good fit of the model with the given data set.

Average lifetimes were calculated using the following equation:

B1T1(sqr) + B2T2(sqr)}/{B1T1 + B2T2}

2.5.4 Quantum Yields

These were calculated from the absorption and integrated emission data of the nanoparticles compared to that of an organic dye using the following formula:

(Dye Abs/Sample Abs) x (Sample integration/Dye integration) x (Sample refractive index/Dye refractive index)^2 x Standard Quantum Yield of Dye

2.5.5 Circular Dichroism measurements

CD activity measurements were made on a JASCO J-810 CD/UV spectrometer. All samples were measured in a 1 cm quartz fluorescent cell.

2.5.6 Sonication

The GEX-600 ultrasonic processor used was operated at 120 W with a tapered tip. A Grant Ultrasonic Bath (single power setting) was also used.

2.5.7 Microwave

The microwave used in these experiments was a CEM Star System 6.

2.5.8 Transmission electron microscopy

All low resolution Transmission electron microscopy (TEM) images were taken with the help of Mr Neal Leddy, (Centre for Microscopy and Analysis-TCD) using a Jeol 2100 TEM. High resolution TEM images were taken with the help of Dr. Marcus Bose (Advanced Microscopy Laboratory) using an FEI-Titan TEM. Samples for TEM were prepared by deposition and drying of a drop of the powder dispersed in Millipore water onto a formvar coated 400 mesh copper grid.

2.5.9 Zeta Potential

Zeta potentials of nanoparticles were measured on a Malvern Zetasizer Nano Series V5.10. The concentration of samples used for these measurements was typically corresponding to an absorbance around 0.2 in the band edge. Three measurements were usually taken for each sample, each made of 10 to 20 accumulations as optimised by the machine.

2.5.10 Small-Angle X-ray Scattering (SAXS)

SAXS measurements were taken with the help of Dr. Miguel Magno. These were performed on a SAXSess high-flux small-angle X-ray scattering instrument (Anton Paar, Austria), attached to a PW3830 X-ray generator (PANalytical) with a sealed-tube anode (Cu Kα wavelength of 0.1542 nm).

The size and shape of colloidal structures was investigated by SAXS. However, neighbouring particles can influence the scattering curve considerably, leading to interparticle effects represented by the so-called structure factor S(q) while the intraparticle effects are described by the form factor P(q). The effect of structure factor on scattering curves depends on the preferred ordering of the particles, which is a result of the interaction between the particles. In the case of monodisperse, homogeneous, globular particles, the total scattering intensity can be expressed by $I(q) = NS(q)P(q)$ with the number of particles N. This factorization allows a separation of inter- and intraparticle effects by means of the generalized indirect Fourier transformation GIFT technique, which is an extension of the indirect Fourier transformation IFT. The IFT technique transforms the scattering curve into real space resulting in a pair distance

distribution function (PDDF) including corrections for instrumental broadening. This transformation is model free and there are no constraints except the maximum dimension of the particle. The model for the structure factor is assumed for use in the GIFT technique. There are several ways to calculate the structure factors of charged particles that consist in using different closure relations of the Ornstein–Zernike equation. Here we used the rescaled mean spherical approximation RMSA model (charged spheres model) that appears to be the most accurate model for this thesis.

2.5.11 Ultrafast Time-Resolved UV-Vis and Infrared Absorption Spectroscopy – ULTRA system (RAL)

The samples for UV-Vis transient absorption measurements were prepared in water as follows; a known volume of solution (typically 100 µL and 50 µL for CdSe and CdTe measurements respectively) was dropped between two CaF_2 (25 mm diameter) windows (Crystan Ltd., UK), separated by a Teflon spacer of known length (typically 100 µm and 56 µm for CdSe and CdTe respectively), in a demountable solution IR cell (Harrick Scientific Products Inc., New York). The picosecond transient absorption pump-probe experiments were carried out by using the high-sensitivity ULTRA apparatus at the Central Laser Facility of the Science & Technology Facilities Council in the Rutherford Appleton Laboratory.

Briefly, a titanium sapphire chirped pulse amplifier (custom developed by Thales Laser) is seeded with the <20 fs oscillator to generate 10 kHz, 50 fs, 1 mJ pulses at 800 nm. The part of the Ti:Sapphire laser output beam was used to generate white light continuum (WLC) in LiF2 crystal. The crystal plate was continuously rotated to avoid colour centre formation and to improve pulse-to-pulse stability in the probe. The WLC was dispersed through the grating monochromator and detected using linear silicon array from Quantum Detectors. Pump excitation light was generated by second harmonic upconversion of the 800 nm laser to 400 nm. Excitation pulse energy was monitored before each experiment and set to either 100 nJ (0.56 mJ/cm2) or 5 nJ (28 µJ/cm2) using a circular variable neutral density filter. In front of the monochromator, a 400 nm interference filter was placed in order to remove scatter from the excitation beam. The samples for transient measurements were prepared by placing a small

volume of solution between two quartz windows of a standard solution IR cell of 500 μm path length (Harrick Scientific). During pump-probe experiments samples were rastered to minimize photodecomposition effects and to avoid eventual re-excitation. Samples were also frequently checked for decomposition by using standard UV-visible spectroscopy.

2.5.12 Laser flash photolysis spectroscopy

Transient absorption spectroscopy at longer time scales was performed in a 1 cm quartz cell using Edinburgh Instruments (model LP920) flash photolysis spectrometer. The samples were excited using a 308 nm line (pulse duration about 20 ns, 58 mJ/cm^2) from GAM excimer laser (model EX100). Xenon arc lamp (450 W) working in pulsed mode were used as a probe. One of the main advantages of this spectrometer is the possibility to work in both kinetic and spectral mode. Standard R 928 photomultiplier and Andor ICCD (model DH501-18F-13) camera were used for signal detection in kinetic and spectral mode respectively. As expected, spectra obtained by data slicing were consistent with an ICCD recorded spectrum.

2.5.13 Profilometer

Profilometer measurements were taken with the help of Mr Neal Leddy, (Centre for Microscopy and Analysis-TCD) using an Omniscan MicroXamWhite light interferometer.

2.5.14 Solar PCE Measurements

These were performed using a 150 W Xe-short arc lamp with an "Ozone free" coating from Ushio(uxl-150SO), powered in a Oriel Instruments 50-500 W arc lamp housing injunction with a AM1.5D filter. The resulting illumination intensity was determined using a SP-110 Apogee silicon-cell pyronometer. IV curve measurements were taken using a two-probe setup, with a Keithley 2400 sourcemeter. The active area of the cell was determined to be 3.6 x 10^{-7} m^2 and cell testing was performed at room temperature under an ambient atmosphere.

Current-Voltage (IV) Curve

To characterise a PV cell, the cell is illuminated with a light source, then using a sourcemeter, an increasing voltage is applied across the cell and the current is recorded, the resulting graph is called an IV curve and contains a large amount of information related to the cells performance.

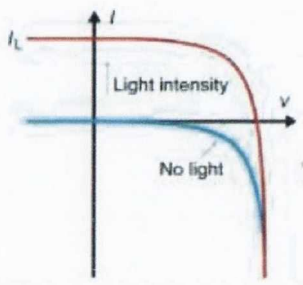

Figure 2.1: I-V curve of a solar cell under illumination and darkness.[2]

Power In (P_{in})

This is the total amount of solar energy applied to the cell, and so is a function of the cell size and the solar irradiance.

Short Circuit Current (I_{sc})

This is the current produced when a PV cell's cathode and anode are connected with zero resistance wire while being illuminated and corresponds to the maximum current a cell can produce. I_{sc} is related to the amount of charge carriers produced under illumination, and therefore the E_g of material. Since as E_g in a PV cell is reduced, more of the photons in the solar illumination will be able to produce charge carriers in the cell and so I_{sc} is increased.

Open Circuit Voltage (V_{oc})

The open circuit voltage describes the voltage generated by a solar cell when it is irradiated without the two terminals of the device being connected; allowing the charge carriers to build up on each terminal and corresponds to the maximum voltage the cell can produce. If in the cell design there exists no potential drop, the V_{oc} maximum possible out of a PV cell is related to the E_g of the material by $V_{oc}= E_g/q$ (where q is

electron charge).[84] In reality, all solar cells require a potential drop to enable charge separation; therefore, the real V_{oc} is always smaller than the absorber material's E_G/q but V_{oc} still shows a strong relation to the E_g.

Maximum Power Point (MPP) ,Maximum Power (P_{max})and Theoretical power (P_t)

This refers to the voltage and current combination that delivers the maximum power from a PV cell (P_{max}) and corresponds to the knee of the cell's I-V curve. The theoretical power (P_t) is the power calculated using the V_{oc} and I_{sc}.

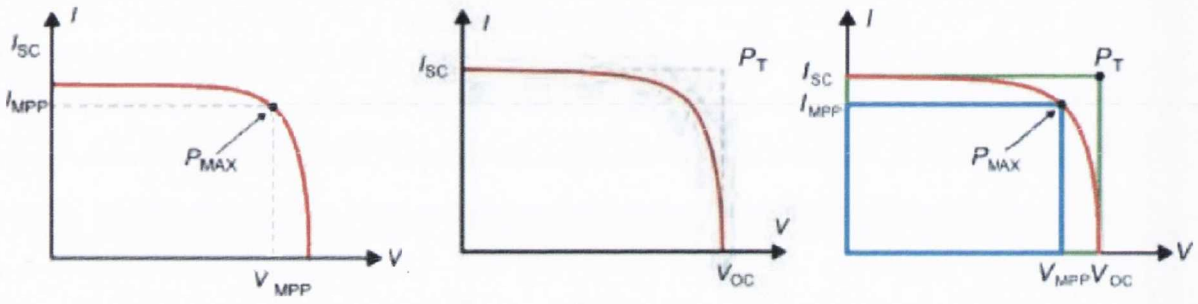

Figure 2.2: I-V curves showing P_{max} , I_{mpp} , V_{mpp} on left, I_{sc} , V_{oc} P_t,in middle and FF on right.[2]

Fill Factor (FF)

Fill Factor (FF) describes the shape of the I-V curve of a PV cell; specifically it's squareness and relates to the resistive losses of the cell. An ideal FF of 100% describes a right angle between the V_{oc} and the I_{sc} where $P_{max}=P_t$. Unfortunately, a FF of 100% is not possible in a solar since resistive losses always exist, but an efficient cell will achieve a FF over 80%.

$$FF = \left(\frac{P_{max}}{P_t}\right) = \left(\frac{V_{MPP}*I_{MPP}}{V_{oc}*I_{sc}}\right) (1)$$

Series Resistance (R_s) and Shunt Resistance (R_{sh})

Series Resistance refers to the combined resistance of the cell's components that lie in the currents path including semiconductor material, metal wire and semiconductor-metal contact resistance. R_s should be as low as possible for an efficient cell (below 10mΩ per cm^2), as R_s increases the I-V curve graph changes , with current beginning to

drop at a lower applied voltage. At very high R_s the I-V curve becomes a straight line from I_{sc} to V_{oc} with I_{sc} being reduced in overall value.

The Shunt Resistance (R_{sh}) is the resistance across the junction, and has its origin in current leakage across the charge separation area, and is a sign of pure rectification in the cell. R_{sh} should be as high as possible so that current travels the correct route around the circuit through the load instead of short circuiting across the junction. The effect of low R_{sh} is that V_{oc} is decreased while the I_{sc} is maintained. Also the R_s and R_{sh} can be estimated by using the inverse of the IV-curve slope at I_{sc} and V_{oc} respectively.

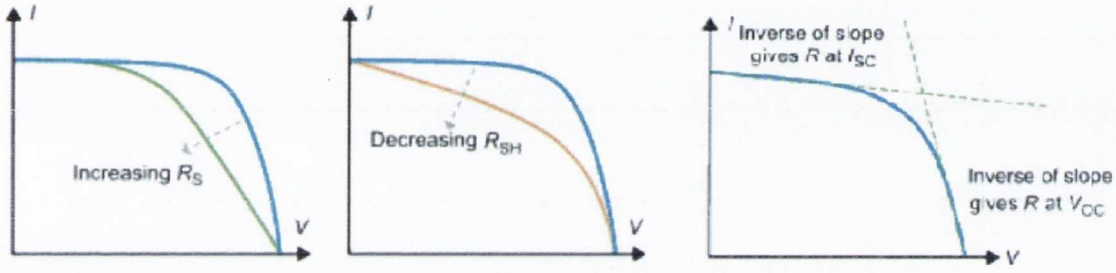

Figure 2.3: IV curves showing the effects of increasing R_s (left graph), increasing R_{sh} (middle graph) and how to estimate the magnitude of R_s and R_{sh} from the inverse of the slope at I_{sc} and V_{oc} (right).[2]

Power Conversion Efficiency (PCE)

The PCE is the power conversion efficiency and is dependent upon the FF, V_{oc} , I_{sc} and the P_{in} and can be calculated using equation 2.

$$PCE = \left(\frac{V_{oc} I_{sc} FF}{P_{in}}\right) \quad (2)$$

2.6 Calculations [3,4]

Laser energy: Nanosecond: beam size area 10x6 mm = 0.6cm^2, about 35 mJ/0.6 cm^2 = 58.3 mJ/cm^2

Picosecond: beam size 150 μm diameter, area = 1.767x10^{-4}cm^2,
50 nJ/1.767x10^{-4} cm^2 = 2.8297x10^{-4} J/cm^2 = 0.28297 mJ/cm^2
10 nJ/1.767x10^{-4} cm^2 = 5.6593x10^{-5} J/cm^2 = 0.056593 mJ/cm^2

N = the average number of e-h pairs excited per QD,

N = pump fluence (photons/cm^2) x absorption cross section^2

Size 4.2nm, abs coef = $1.6x10^5$ cm^{-1}

Nanosecond (308nm): N = 1122.2 e-h pairs per QD

Picosecond 50 nJ (400nm) N = 7.0735 e-h pairs per QD

Picosecond 10 nJ (400nm) N = 1.4147 e-h pairs per QD

To Calculate N_{e-h}: the Average Number of electron-hole pairs excited per QD for **CdSe**.

$N_{e-h} = j_p \times \sigma_a$

j_p = Pump Fluence σ_a = Absorption Cross-section

N_{e-h} = Pump Fluence (photons/cm^2) x Absorption Cross-section

j_p (Pump Fluence) = $\frac{\textbf{Laser energy}}{(1239.8/\lambda) \times 1.60217653 \times 10^{-19}}$ cm^{-2}

- **Laser energy** = $\frac{\text{Pulse energy (J)}}{\text{Beam size area (cm}^2\text{)}}$ Pulse energies = 0.035 J for ns

= $5x10^{-8}$ and $1x10^{-8}$ J for ps

(50 and 10 nJ respectively)

Beam areas: - ns = 10 x 6 mm = 0.6 cm^2

- ps = 150 μm diameter = 1.767×10^{-4} cm^2

=> **Laser energy** = 5.833×10^{-2} J/cm^2 for ns laser

= 2.8297×10^{-4} J/cm^2 for 50 nJ ps laser

= 5.6593×10^{-5} J/cm^2 for 10 nJ ps laser

λ = laser wavelength λ = 308 nm for ns laser (308 nm = 4.03 eV)

$(1239.8/\lambda) \times 1.60217653 \times 10^{-19} = 4.0253 \times 1.60217653 \times 10^{-19} = 6.4493 \times 10^{-19}$

λ = 400 nm for ps laser (400 nm = 3.1 eV)

$(1239.8/\lambda) \times 1.60217653 \times 10^{-19} = 3.0995 \times 1.60217653 \times 10^{-19} = 4.9659 \times 10^{-19}$

j_p = **9.0441×10^{16}** for ns laser

5.6983×10^{14} for 50 nJ ps laser

1.1396×10^{14} for 10 nJ ps laser

σ_a (Absorption Cross-section) = $\frac{4\pi}{3} \cdot [f]^2 \cdot \alpha_b \cdot r^3$

α_b = bulk absorption coefficient at pump wavelength — $\alpha_b = 1.6 \times 10^5$ cm^{-1}

f = coefficient accounting for local field effects — **f** = 0.25

r = QD radius. QD size = 4.2 nm (4.2×10^{-7} cm) — **r** = 2.1×10^{-7} cm

$r^3 = 9.261 \times 10^{-21}$

$\sigma_a = \frac{4\pi}{3} \cdot 0.25 \cdot 1.6 \times 10^5 \cdot 9.261 \times 10^{-21}$

$\sigma_a = 1.5517 \times 10^{-15}$

$N_{e\text{-}h} = j_p \times \sigma_a$ $= 9.0441 \times 10^{16} \times 1.5517 \times 10^{-15}$ => **N** = 1.40337 e-h pairs for ns

$= 5.6983 \times 10^{14} \times 1.5517 \times 10^{-15}$ => **N** = 0.8842 e-h pairs 50nJ

$= 1.1396 \times 10^{14} \times 1.5517 \times 10^{-15}$ => **N** = 0.1768 e-h pairs 10 nJ

References

(1) N.Gaponik, D.V., Talapin, A. L., Rogach, K. Hoppe, E. V., Shevchenko, A., Kornowski, A. Eychmuller, H. Weller, *The Journal of Physical Chemistry B* **2002**, *106*, 7177-7185.

(2) D. S. Ginley and D. Cahen, Fundamentals of Materials for Energy and Environmental Sustainability, Cambridge University Press, 2011.

(3) Klimov, V. I.; McBranch, D. W.; Leatherdale, C. A.; Bawendi, M. G. *Physical Review B*, **1999**, 60, 13740.

(4) Lide, D.R. *CRC handbook of chemistry and physics: a ready-reference book of chemical and physical data*, CRC Press, **2004**.

Chapter 3: Investigation of the Interactions between CdTe QDs and a Lanthanide Cyclen System

3.1 Introduction

The unique properties of cadmium chalcogenide quantum dots, in particular their highly luminescent nature, render them attractive for a range of applications including optoelectronics, biological imaging and biosensing[1-10]. One example, CdTe QDs, are attractive for luminescence sensing and other fluorescence based applications as they possess a single narrow emission band and can be prepared with high quantum yields[7]. Laser excitation of such QDs generates exciton (electron hole pair) excited states which can subsequently recombine through a number of processes. These processes occur over varying timescales with fast carrier trapping known to happen on the picosecond timescale while electron-hole recombination occurs over much longer times, which makes the study of these particles challenging[11]. Surface phenomena are especially important as the majority of the atoms lie at the surface and defects in the lattice can contribute significantly to excited state dynamics. QDs are highly sensitive to the chemical environment and surface events[12,13] and controlled surface modification can both tune and enhance the QDs properties[14]. QD-hybrids are attractive materials for imaging, sensing, and light harvesting. Numerous systems have been prepared by surface assembly of species capable of energy transfer (ET) and electron transfer (eT), such as metal complexes, organic molecules and nanomaterials[15-19].

Their ability to be sensitised by appropriate antennae, and their long excited state lifetimes has seen lanthanides become the focus of research investigating their possibility to act as both donors, and acceptors, in energy transfer processes such as Förster Resonance Energy Transfer (FRET)[20-23]. Such work has also explored the use of nanoparticles in these systems, and recently the combined sensing capabilities of a lanthanide complex to a gold nanoparticle surface for the purpose of detection of biologically relevant ions was demonstrated[24]. There are also reports demonstrating the ability for FRET between lanthanide complexes and QDs[25-27]. It is this avenue of

research that we aim to further explore, and exploit the properties offered by both lanthanides and QDs to develop new QD-hybrid functional materials[26].

In this work we focus on the investigation of interactions in an aqueous lanthanide compound -QD system based on an Eu(III) cyclen complex and thioglycolic acid (TGA) capped CdTe QDs. This is to be assembled *via* the coordination of a europium complex to the carboxylic acid groups of the TGA. A thorough photophysical investigation will then be undertaken using steady state absorption and emission spectroscopy, as well as time correlated single photon counting (TCSPC) and ultrafast ps-transient absorption spectroscopy. The potential for this system to act as a sensor for a biologically relevant molecule is also explored.

3.2 Synthesis and Characterisation of CdTe TGA QDs

The initial aim of this line of research was to investigate the interaction between aqueous cadmium telluride quantum dots (CdTe TGA QDs) and a Eu(III) cyclen complex, to do this the synthesis and detailed characterisation of CdTe TGA QDs needed to be firstly carried out.

The well-established route to aqueous CdTe QDs developed by Gaponik et al.[28] was used in this work to synthesis our TGA stabilised CdTe quantum dots (CdTe TGA QDs). A schematic representation of the experimental set-up is shown in Figure 3.1.

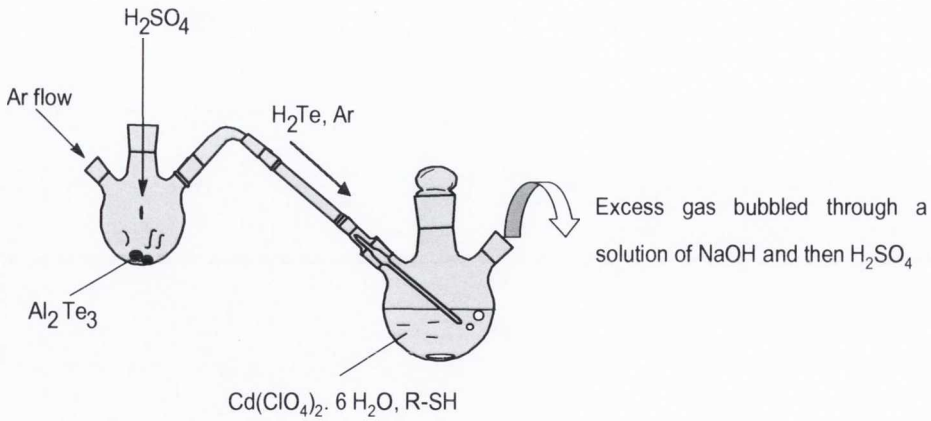

Figure 3.1: Illustration of the setup used to produce water soluble CdTe QDs. Al_2Te_3 is decomposed by the dropwise addition of H_2SO_4 and argon carries the evolved H_2Te gas through a solution of $Cd(ClO_4)_2 \cdot 6H_2O$ and the desired thiol. This solution is then heated under reflux.

Briefly, $Cd(ClO_4)_2 \cdot 6H_2O$ and TGA stabiliser were dissolved in degassed Millipore water and the pH was adjusted to 11 by the addition of a 2M NaOH solution. H_2Te gas, generated from the reaction of 0.5 M H_2SO_4 with Al_2Te_3, was bubbled through the stirred solution under a slow argon flow for approximately 10 minutes. This process initially results in non-luminescent CdTe-based clusters, which are then heated under reflux at 100°C over time to result in a crude solution of CdTe QDs. The size of the QDs can be tuned by altering the reflux time, with elongated reflux times resulting in larger QDs, accompanied by a red shift of both the absorption and emission peaks (Figure 3.2). The crude solution was then fractioned through size-selective precipitation using small amounts of isopropanol in order to produce samples of narrow size distributions and therefore narrow emission.

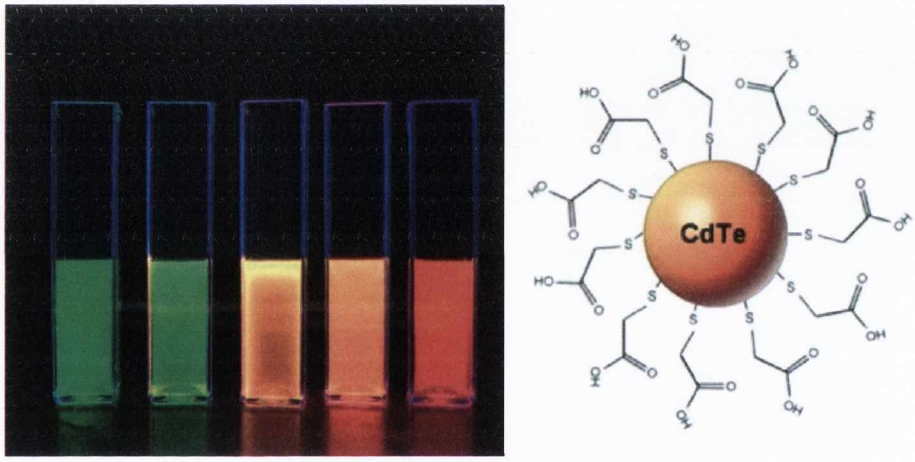

Figure 3.2: (Left) Photograph of aqueous CdTe TGA QDs of increasing sizes illuminated by UV light. They were synthesised via the method outlined above and refluxed for increasing periods of time (left to right). (Right) Illustration of TGA stabilised CdTe QD.

Previous work carried out by our group, aimed at optimising this procedure, showed that stable CdTe TGA QDs with good luminescence can be obtained after refluxing for 40 minutes. A selected batch had a quantum yield of 27%, calculated using the dye rhodamine 6G as a reference[29]. The absorbance and emission spectra for these QDs are shown in Figure 3.3.

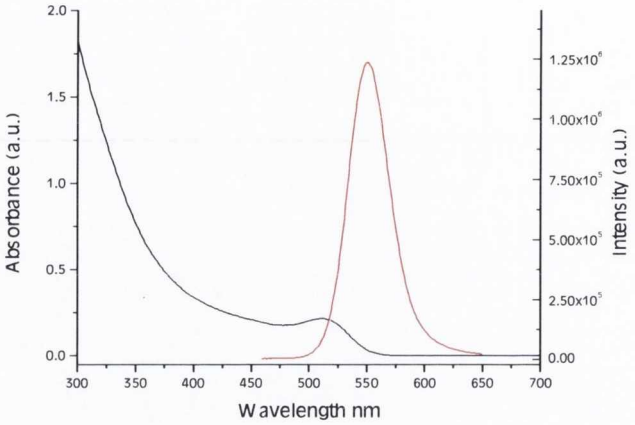

Figure 3.3: UV-vis absorbance (black) and corresponding emission spectra (red) of CdTe TGA QDs.

These QDs show strong characteristic intrinsic emission, with a narrow full-width half maximum of 39 nm and a Stokes shift of 41 nm. The size of these QDs was determined spectroscopically to be 2.3 nm in diameter[30] and the number of TGA molecules on the surface of these particles was calculated to be approximately 128[30,31]. Their size was corroborated using high resolution transmission electron microscopy (HRTEM), as seen in Figure 3.4.

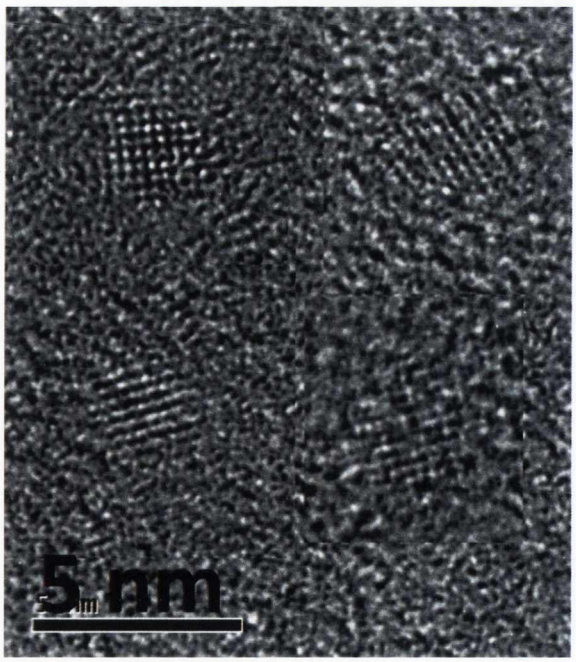

Figure 3.4: HRTEM images of CdTe TGA QDs

Small-angle X-ray scattering measurements (SAXS), carried out in collaboration with Dr. Luis Magno in UCD, showed that these particles were slightly oblong instead of perfectly spherical, with a width of approximately 3.1 nm, and a length of 3.8 nm (Figure 3.5). These values are in good agreement with our HRTEM and spectroscopic determination of size, given the added hydrodynamic radius and ligand shell also incorporated in these measurements.

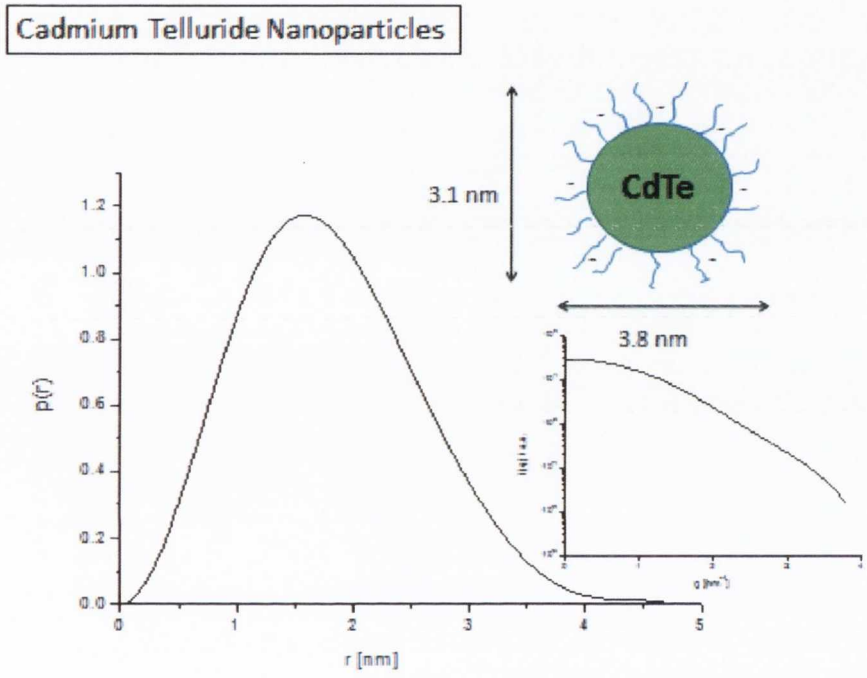

Figure 3.5: SAXS measurements of CdTe TGA QDs and schematic representation illustrating the results.

The surface charge of these CdTe QDs was also investigated by zeta potential measurements. As the thiol group is the terminal group that binds to the Cd atoms of the nanoparticle, the carboxyl group is exposed. The pKa for the COOH of TGA is 3.67[32], thus in a pH neutral aqueous solution (achieved after separation and purification of the QDs) this should exist in its deprotonated COO^- form, giving a negatively charged surface to the QD. Zeta potential measurements of these CdTe QDs (Figure 3.6) demonstrate that this is indeed the case.

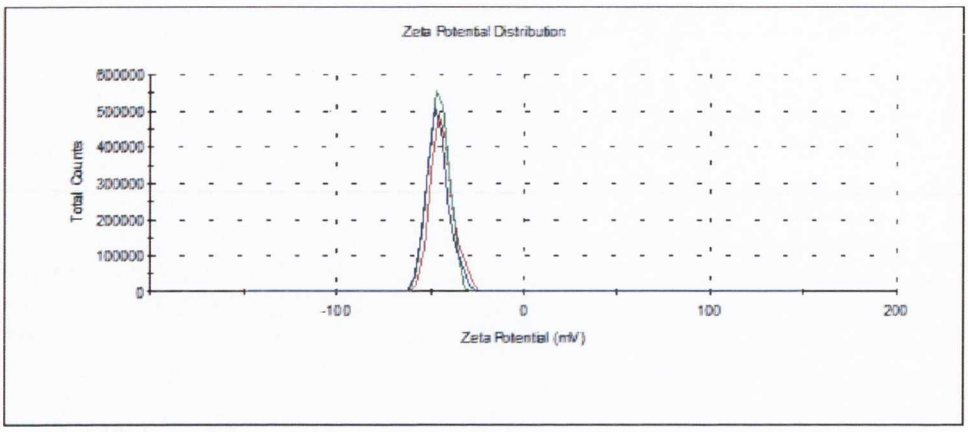

Figure 3.6: Zeta potential measurements of CdTe TGA QDs.

The luminescence lifetimes of these QDs were determined using time correlated single photon counting (TCSPC) technique (Figure 3.7). The luminescence decay of the CdTe TGA particles was measured at the maximum of their emission using a 370 nm "Nanoled" as the excitation source. It was found that the decay curve was best fit using a bi-exponential function (based on satisfactory χ^2 values of between 0.9 and 1.1), with lifetimes of 6 and 20 ns for τ_1 and τ_2 respectively.

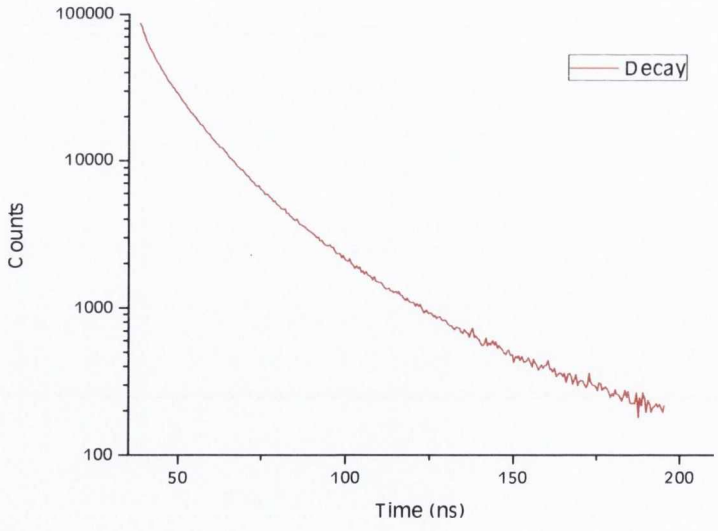

Figure 3.7: Lifetime decay curve of CdTe TGA fluorescence decays measured at the maximum of the PL band using a 370 nm "Nanoled".

A more detailed analysis of this emission decay was also undertaken. Firstly the photoluminescence decay curves of CdTe TGA were measured as a function of the emission wavelength in the spectral range from 500 nm to 650 nm (in 5 nm steps), resulting in a 3-dimensional (3-D) map of the emission decay curves (Figure 3.8). In this experiment the acquisition was limited to 300 seconds at each particular wavelength, and therefore it showed the dependence of signal intensity on the emission wavelength.

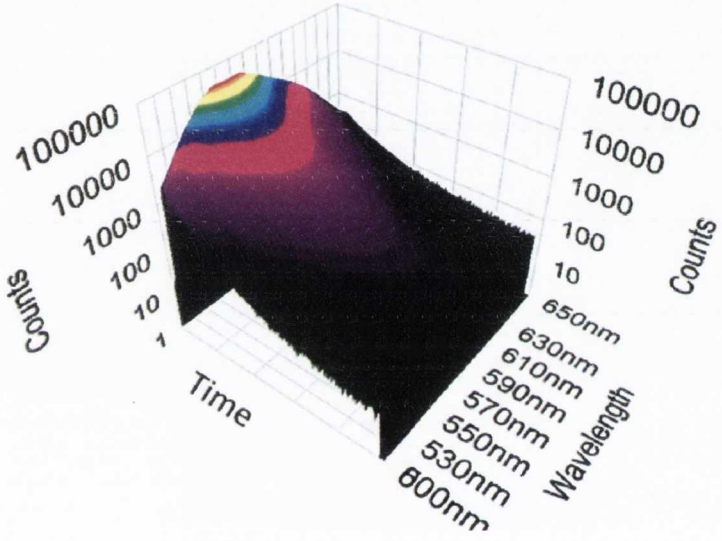

Figure 3.8: 3-D plot of emission decay curves showing the fluorescence *intensity* dependence vs. wavelength.

The shape of this 3-D curve illustrates the dependence of the luminescence intensity on the emission wavelength, and matches the obtained PL spectra shown earlier. This result is to be expected with a time limited acquisition spectrum. Even more information was obtained in a similar manner, with time resolved scans of the photoluminescence decay curves measured again as a function of the emission wavelength, in the spectral range from 450 nm to 770 nm (in 5 nm steps), resulting in a 3-D plot of normalized emission decay curves (Figure 3.9). In this experiment however, the acquisition was limited to 5000 counts at each particular wavelength, which naturally erased any intensity discrepancy and showed there to be no dependence of the fluorescence lifetime on the emission wavelength.

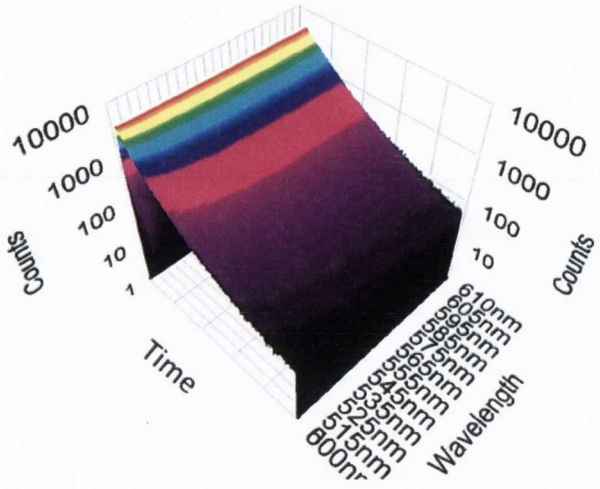

Figure 3.9: 3-D plot of emission decay curves showing the fluorescence *lifetime* dependence vs. wavelength.

It is clear that there is no dependence of the emission lifetime on the wavelength. This is in agreement with these QDs exhibiting intrinsic emission, with little interference on the exciton recombination from defect states.

An attempt was also made to study these QDs using nanosecond flash photolysis. However it was found that signals corresponding to the bleach and transient decay of these QDs upon excitation could not be elucidated. This was due to the short timescale on which complete recombination of the exciton occurs, corresponding to the emission decay lifetime (due to the low interference from defect states there are no longer lived processes), being on a par with the instrument response itself (Figure 3.10).

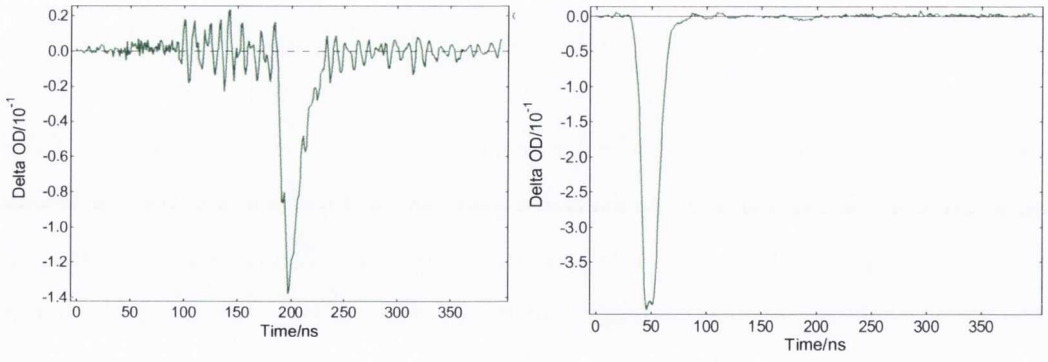

Figure 3.10: Nanosecond flash photolysis measurements carried out on CdTe TGA QDs (left) and the instrument response of the laser pulse (right).

These CdTe QDs were then used for the next part of this study, investigating the interactions between these CdTe QDs and the Eu(III) cyclen complex.

3.3 CdTe QD – Eu Cyclen Interactions

The results obtained from titrating CdTe QDs against the Eu(III) cyclen complex are detailed below. These systems were studied using steady state UV-vis and fluorescence spectroscopy. The high degree of emission quenching of both species upon titration is seen as an indication of their binding. To probe the mechanism of quenching in more detail, ultrafast ps-transient spectroscopy was also employed.

The Eu(III) complex used, Eu.1 was synthesised using a tri-acetamide substituted cyclen ligand according to previously reported procedures[33] in collaboration with Dr. Steve Combys in TCD.

Eu.1 possesses two labile water molecules which are known to be readily displaced in the presence of a carboxylate ion. Consequently, Eu.1 can coordinate to the terminal COOH groups of the CdTe TGA QDs to form the Eu.1-CdTe conjugate as shown in Figure 3.11. The water soluble nature of the two species allows for the study of quenching effects in aqueous solution.

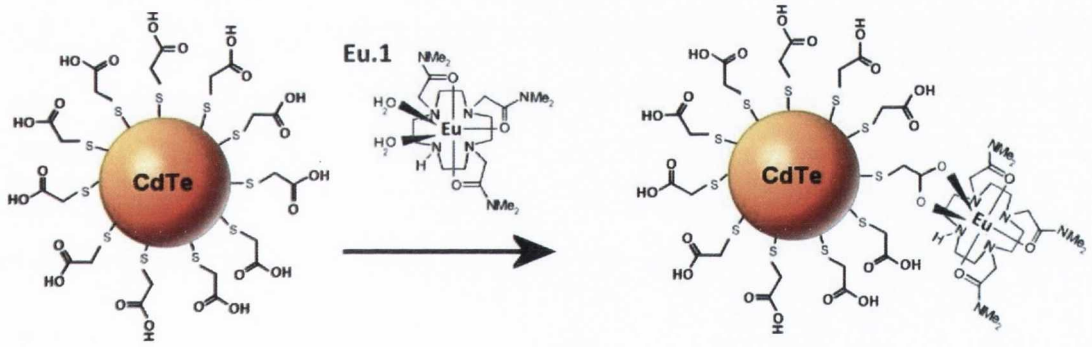

Figure 3.11: Scheme showing the binding of the Eu.1 to the surface of a CdTe TGA QD by displacement of two water molecules and coordination of COO^-.

It is important to note that the strongly forbidden f-f electronic transitions of Eu(III), coupled with the nature of the cyclen ligand, result in a very small molar absorption coefficient for Eu.1. Thus, accurate concentration of the complex was

determined using a displacement titration. This was achieved by the addition of 2-naphthoyltrifluoroacetone (nta), a beta-diketonate (Figure 3.12), which binds in a 1:1 fashion to the Eu.1, resulting in sensitised emission from the europium (Figure 3.13).

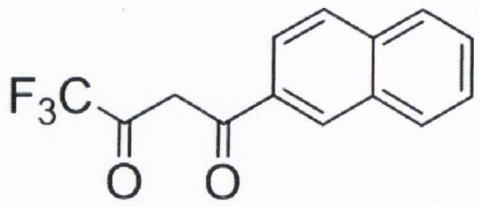

Figure 3.12: 2-naphthoyltrifluoroacetone

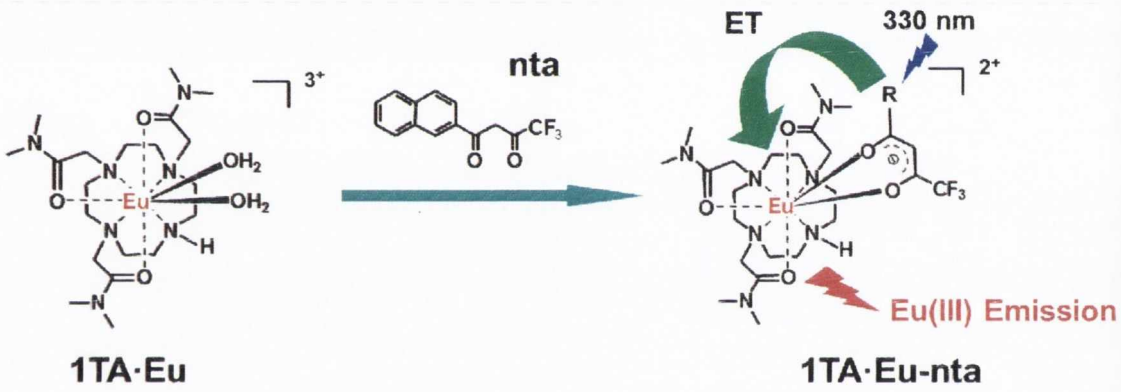

Figure 3.13: Scheme outlining sensitised emission of Eu.1 upon titration with nta for determination of concentration via titration

Measurement of the displacement titration using UV-vis and PL spectroscopy allows for the concentration of Eu.1 to be calculated from the changing slope in the growth of both the absorption of the nta, and the emission of the Eu.1 (Figure 3.14 and 3.15).

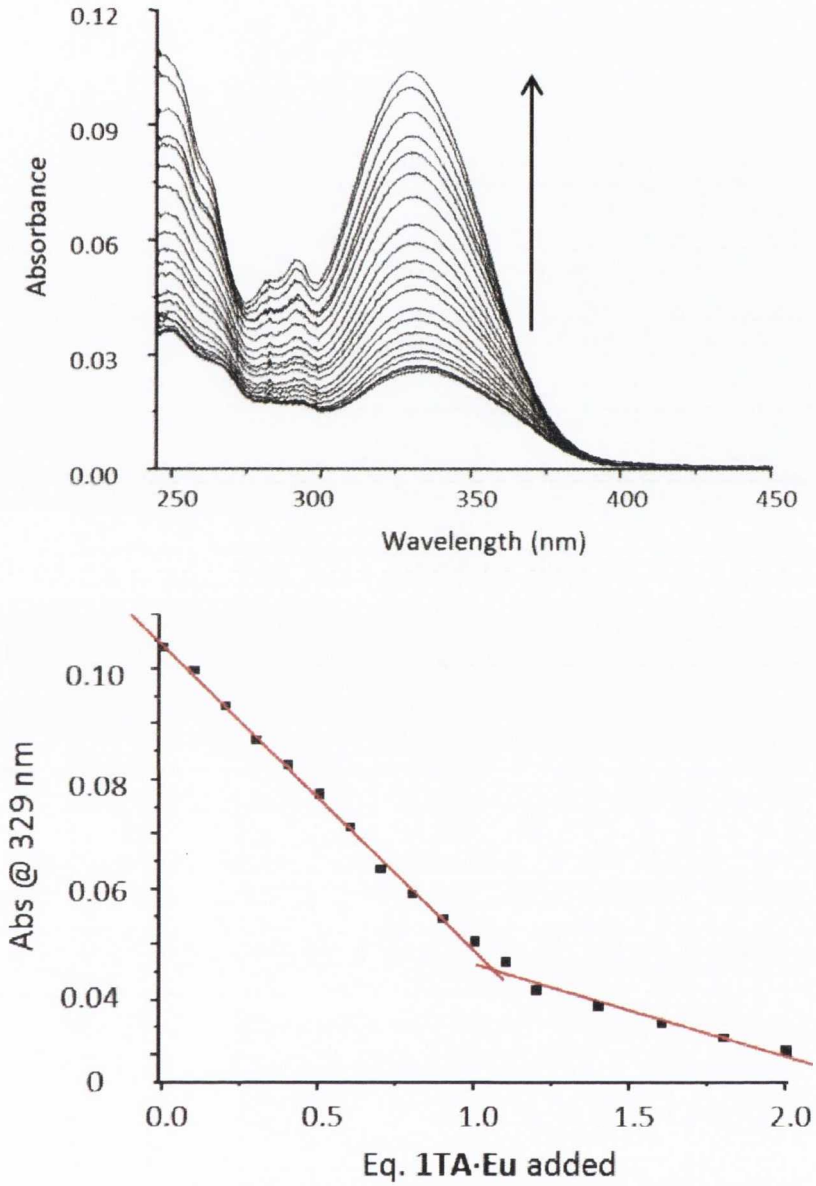

Figure 3.14: (Top) Evolution of the UV-visible spectrum of nta 10^{-5} M in Hepes-buffered solution (0.1 M, pH 7.4) upon addition of Eu.1 (0-2 equivalents) at room temperature. (Bottom) The changes observed at 329 nm vs. the number of equivalents Eu.1 added.

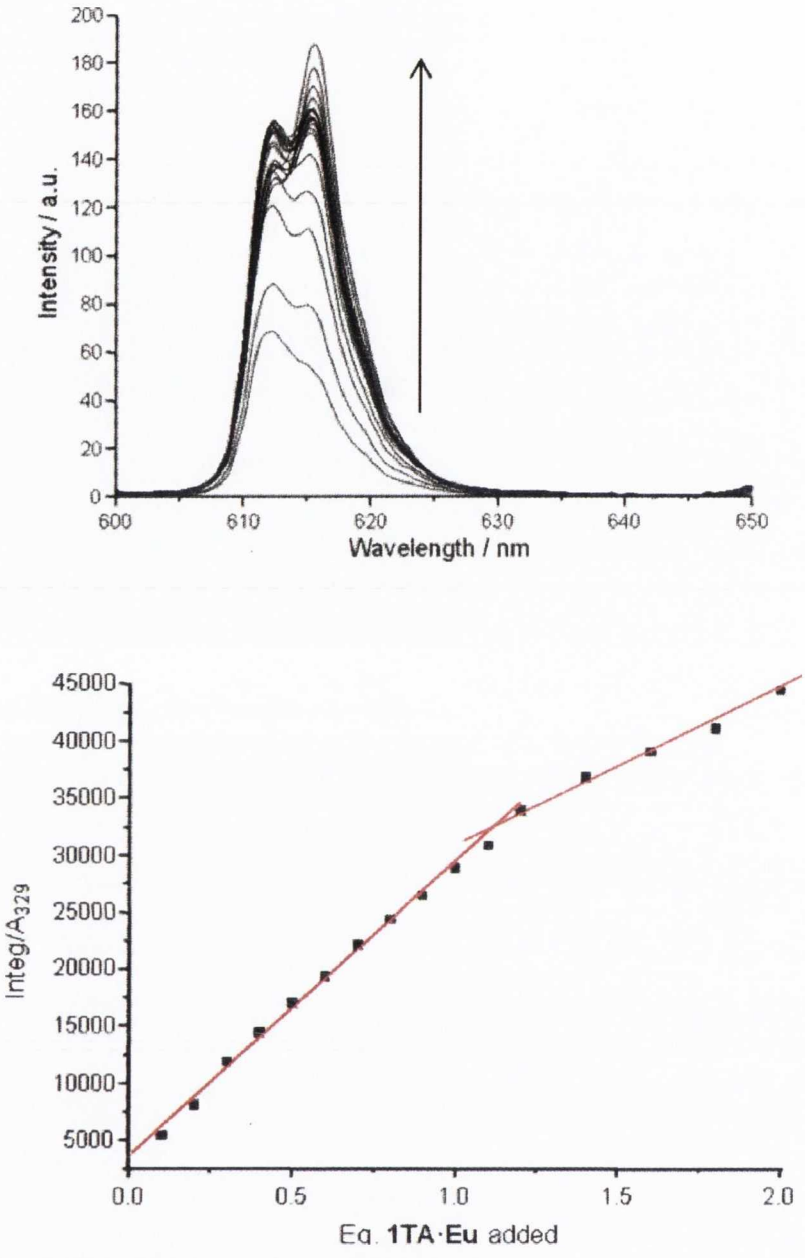

Figure 3.15: (Top) Evolution of the Eu(III) $^5D_0 \rightarrow {}^7F_2$ transitions of a 10^{-5} M nta solution in Hepes-buffer (0.1 M, pH 7.4) upon addition of Eu.1 (0-2 equivalents) at room temperature. (Bottom) The changes in the integrated emission relative to the absorbance at 329 nm vs. the number of equivalents Eu.1 added.

The comparison of the Eu.1 absorption spectrum and the CdTe TGA QD fluorescence spectrum are shown in Figure 3.16.

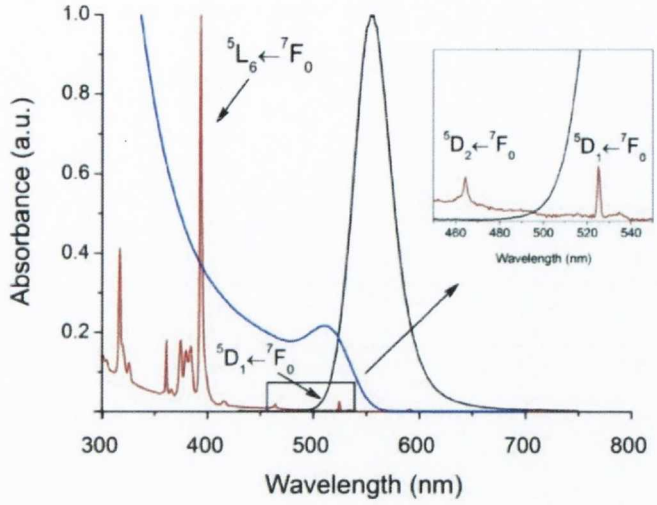

Figure 3.16: Absorption spectrum of Eu.1 0.1 M (red) and CdTe TGA QDs (blue), and emission spectrum of CdTe TGA QDs (black) in water. The spectra have been normalized for sake of comparison.

The addition of the Eu.1 to the QDs resulted in no significant change in the UV-visible absorption of the QDs. However, a dramatic effect was observed on the steady state emission of the QDs upon titration of the Eu.1 (Figure 3.17), with strong quenching of 75% on the titration of one equivalent (eq.) of Eu.1 and almost complete quenching (~96%) reached with two equivalents.

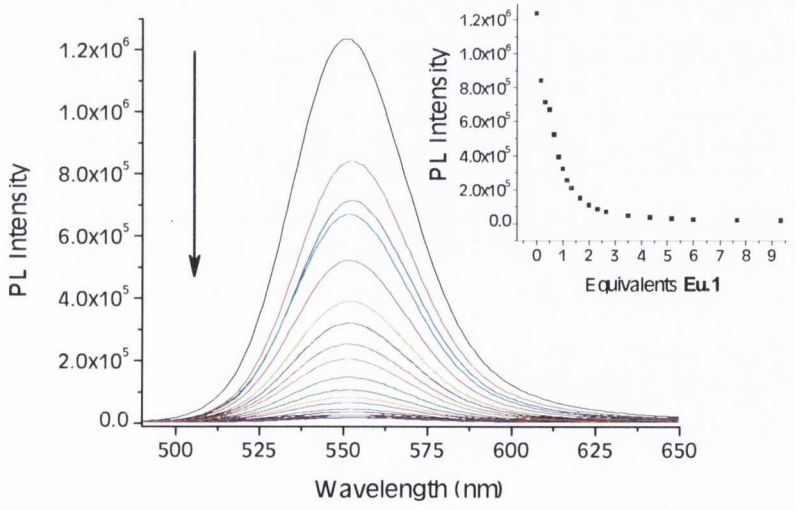

Figure 3.17: Evolution of the fluorescence emission spectrum of CdTe TGA QDs in the presence of increasing concentration of Eu.1. Inset: The changes in the emission integrals of CdTe TGA *vs.* the equivalents of Eu.1 added; [CdTe TGA] = 3.69×10^{-6} M, [Eu.1] = 0 → 3.69×10^{-5} M. λ_{ex} = 420 nm.

The efficient quenching of emission in the presence of low concentrations of Eu.1 is taken as strong evidence for coordination of the europium centre to the TGA at the particle surface by displacing the labile water bound molecules. There is a significant driving force to form the coordinative bonds with the available carboxylate sites on the nanoparticle (~128 COOH groups).

The fluorescent lifetime of the CdTe TGA QDs was measured in the presence of increasing concentrations of Eu.1 using TCSPC (HORIBA Jobin Yvon Fluorolog), see Figure 3.18. In the absence of europium the QD emission was found to decay biexponentially with τ values of 6 ns (25%) and 20 ns (75%) respectively. However, upon successive additions of Eu.1, a reduction in both the signal amplitude and lifetime was observed which correlates extremely well with the steady state fluorescence measurements (Figure 3.19).

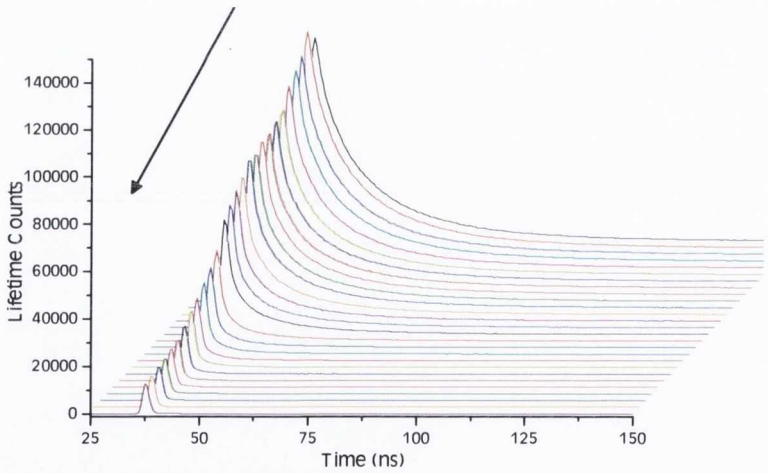

Figure 3.18: Fluorescent lifetime decays of CdTe TGA upon addition of Eu.1.

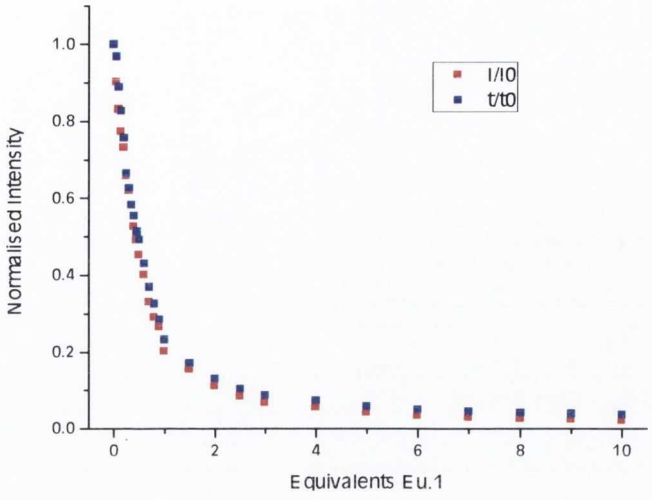

Figure 3.19: Normalised integrated emission (red) and lifetime (blue) intensities.

3.4 Stern-Volmer Analysis and Quenching Dynamics

From an initial analysis of the data, based on a comparison of the integrated intensities of both the emission and lifetime spectra from the titration of Eu.1 to QDs, it would appear that they give remarkably similar results. To investigate whether a donor-acceptor style system had been formed with this Eu.1-CdTe conjugate, the presence of phosphorescence arising from a sensitised Eu.1 was also investigated. However, no phosphorescence was observed, indicating that, although binding of the two species was occurring, as shown by the steady state measurements performed on the QDs, the Eu.1 was not becoming sensitised.

To probe the quenching dynamics in more detail, the quenching of both the CdTe TGA QD emission and lifetime upon the addition of Eu.1 were fitted using the Stern-Volmer equation (1):

$$\frac{I_0}{I} = \frac{\tau_0}{\tau} = 1 + K_{SV} \cdot [Q] = 1 + k_q \cdot \tau_0 \cdot [Q] \qquad (1)$$

where K_{SV} represents the Stern-Volmer quenching constant, which is defined as the product of k_q, the bimolecular quenching constant and τ_0, the CdTe TGA QDs

fluorescence lifetime in the absence of quencher. I and I_0 are the fluorescence of the CdTe TGA QDs in the presence and absence of the quencher, respectively.

It must be noted that in the case of pure collisional quenching, a bimolecular quenching constant of approximately 1×10^{10} $M^{-1}s^{-1}$ may be considered as the largest possible value in aqueous solution. Moreover, many quenchers are larger than molecular oxygen and thus smaller diffusion-limited quenching constants are to be expected.

The resulting Stern-Volmer plots, obtained when I_0/I and τ_0/τ are plotted against [Eu.1], are shown in Figure 3.20. Both displayed linear behaviour upon first inspection.

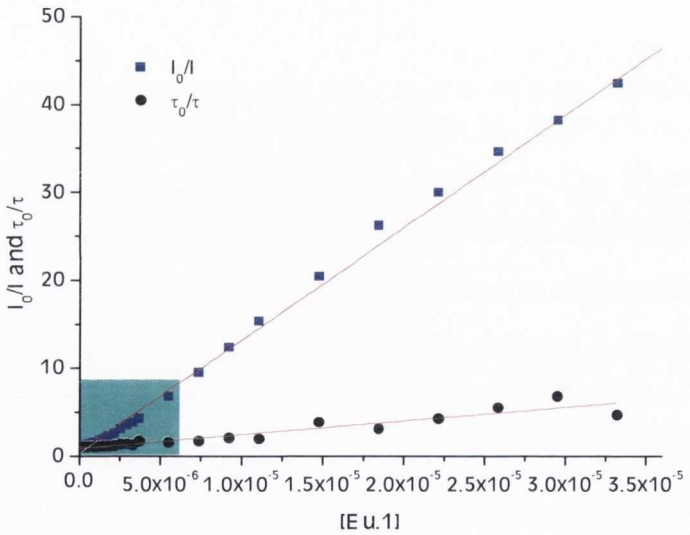

Figure 3.20: The Stern-Volmer plots and their corresponding linear fits of the changes in the fluorescence emission and lifetimes of CdTe TGA in the presence of increasing amounts of Eu.1; [CdTe TGA] = 3.69 x 10^{-6} M, [Eu.1] = 0 → 3.69 x 10^{-5} M.

However, on closer examination, the data gathered at low concentrations of Eu.1 clearly demonstrated that the plot for the fluorescence emission exhibited a more complex behaviour, with a linear evolution only at the start of the titration, between 0 and 0.4 equivalents of Eu.1 added (see Figure 3.21). To the contrary, the plot obtained from the average lifetimes remains perfectly linear throughout.

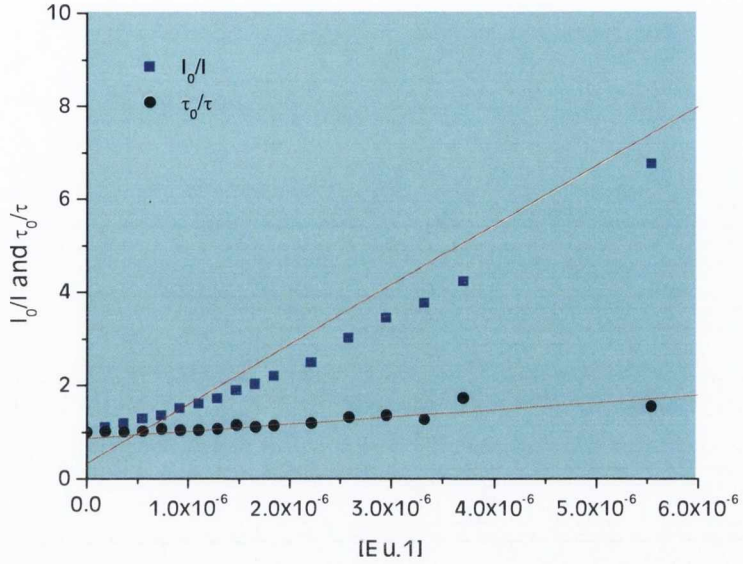

Figure 3.21: The coloured section of the previous Stern-Volmer plot and the corresponding linear fits of the changes in the fluorescence emission and lifetimes of CdTe TGA in the presence of increasing amounts of Eu.1; [CdTe TGA] = 3.69×10^{-6} M, [Eu.1] = 0 → 6×10^{-6} M.

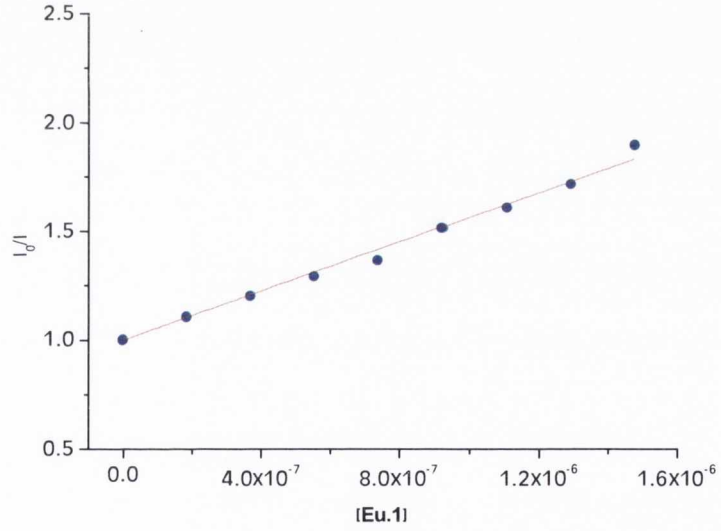

Figure 3.22: Linear part of Stern-Volmer plot of the fluorescence emission of CdTe TGA in the presence of increasing amounts of Eu.1; T = 298 K, [CdTe TGA] = 3.69×10^{-6} M, [Eu.1] = 0 → 3.69×10^{-5} M.

Since the average lifetime of the CdTe TGA QDs in the absence of Eu.1 has been measured (τ_{avg} = 13.5 ns), the quenching constants K_{SV} and k_q can be determined from equation (1) based on the full concentration range for the lifetime data, and only the 0 → 5.16×10^{-6} M range for the fluorescence emission (where the Stern-Volmer plot

remained linear, Figure 3.22). The calculated quenching constants are summarized in Table 3.1.

Table 3.1: Quenching constants (K_{SV} and k_q) estimated from the fluorescence quenching experiments (emission and lifetimes) performed on CdTe TGA in the presence of increasing amounts of Eu.1.

Method	K_{SV} / M^{-1}	k_q / $M^{-1}.s^{-1}$
Fluorescence emission	564022 ± 11676	4.2 (± 0.2)×10^{13}
Fluorescence lifetimes	147603 ± 7583	1.1 (± 0.1)×10^{13}

The quenching process is considered to be 'dynamic' when the external environmental influence (quencher) interferes with the behaviour of the excited state after its formation, and thus includes phenomenon such as collisional quenching, energy transfer, and electron transfer. On the other hand, 'static' quenching occurs when the environmental influence inhibits the process of excited state formation, for instance through the formation of a non-luminescent ground-state complex between the molecule and the quencher.

Keeping these definitions in mind, the decrease observed in the average lifetimes (reduction in τ_{avg} from 13.5 ns to 7.8 ns for one equivalent Eu.1) confirms the presence of dynamic quenching for our system and the constant determined by fitting the lifetime changes gives us the dynamic quenching constant. Furthermore, the value calculated for k_q is higher (by three orders of magnitude) than the diffusion-limited quenching constant expected in aqueous solution, and therefore provides evidence for the presence of other mechanisms (electron transfer or energy transfer) than collisional quenching.

The possibility for an energy transfer between the CdTe TGA QDs and the Eu.1 complex can be reasonably discarded for two main reasons:

1) Energy transfer to Ln(III) ions has been demonstrated to take place in the majority of cases from the triplet state of organic molecules and very rarely

from the singlet state[20]. This is because the deactivations (radiative or nonradiative) of this singlet state occur very fast (on the order of 10^{12} - $10^{9}s^{-1}$) and thus compete efficiently against other pathways, preventing an efficient sensitization of the Ln(III) ion through energy transfer. As deactivation of the 1st exciton state of the CdTe TGA QDs occurs on a similar timescale to that of a singlet state, evidenced by its ns emission lifetime, it can be assumed that the energy transfer will be non-existent, or at least very poor. This assumption was confirmed by measuring the phosphorescence spectrum of Eu.1 in the presence of CdTe TGA QDs, which did not exhibit the characteristic red emission of the Eu(III) in the 570-720 nm range.

2) The possibility of fluorescence resonance energy transfer (FRET), where the TGA-CdTe QDs would act as donor and the Eu.1 cyclen complex as acceptor, can also be ruled out as the Ln(III) ions are characterized by very low extinction coefficients as a result of the Laporte-forbidden *f-f* transitions. The only transition in the emission range of the QDs (500-650 nm) is located at 525 nm and is attributed to the $^5D_1 \leftarrow {}^7F_0$ transition, characterized by a $\epsilon < 1$ M^{-1} cm^{-1} ($\epsilon_{525} = 0.06$ M^{-1} cm^{-1}, see Figure 3.16). This specific transition has an oscillator strength almost 2 orders of magnitude weaker than the main Eu(III) transition at 394 nm ($^5L_6 \leftarrow {}^7F_0$, $\epsilon_{394} < 5$ M^{-1} cm^{-1}).

As energy transfer from the CdTe TGA QDs to the Eu.1 complex is thus unlikely to take place (discussion above), there is a good probability that an electron transfer process is the cause of the significant quenching observed in the QDs emission on addition of Eu.1. The close proximity of the surface coordinated Eu.1 can facilitate electron transfer from the QD to the complex[34,35]. Such quenching has been recently observed for a series of organic molecules[36-38]. Furthermore, a reduction of the Eu(III) to Eu(II) would explain the absence of the red Eu(III)-centred emission, as Eu(II) is not emissive in solution, and indeed Eu(II) would emit in the blue region.

Coming back to Table 3.1, we can see that the K_{SV} constant determined for the fluorescence emission (in the concentration range where the plot remains linear) is much higher than the one calculated from the lifetimes (dynamic quenching constant), and thus suggests the presence of static quenching in addition to the dynamic process.

This is not surprising as it was expected that the Eu.1 complex would bind to the carboxylate groups of the TGA capped QDs. This also suggests that the Eu.1 complex is able to quench a precursor to the exciton by sub-nanosecond processes which are too fast to measure with the SPC instrument.

3.5 CdTe QD – $Ln(CF_3SO_3)_3$ Interactions

To provide further evidence for the electron transfer process, two experiments were planned. These were based on the following reasoning:

1) If electron transfer to the Eu(III) is the main pathway for the quenching of the exciton emission, then the cyclen ligand should not be essential and the same titration can be performed with a Eu(III) triflate salt [$Eu(CF_3SO_3)_3$], expecting the emission to behave in a similar way as observed with Eu.1.
2) Depending on the results obtained in the first experiment 1), the same titration would be performed again, but this time with the $Tb(CF_3SO_3)_3$. As the Tb(III) ion cannot be reduced to Tb(II), but only oxidized to Tb(IV), it thus cannot accept the electron from the TGA capped QDs.

Using the exact same conditions as before, the titration of adding $Eu(CF_3SO_3)_3$ to the CdTe TGA QDs was carried out. UV-vis spectroscopy again showed no significant changes in the absorption spectrum, however results from the fluorescence measurements demonstrated remarkably similar quenching behaviour to that seen previously with Eu.1 (Figure 3.23).

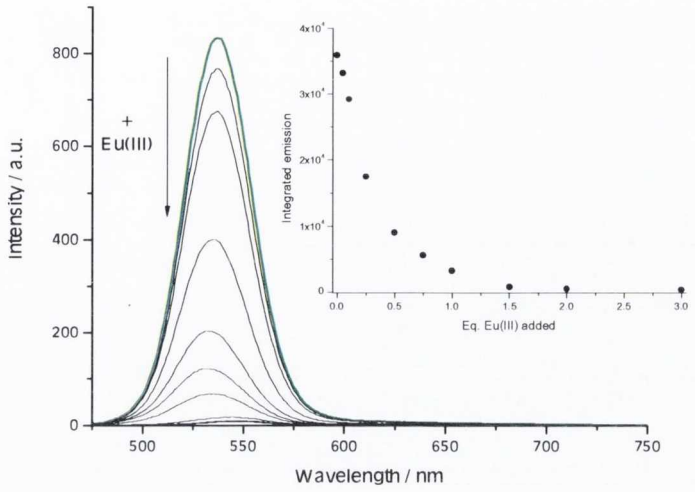

Figure 3.23: Evolution of the fluorescence spectrum of CdTe TGA QDs (3.7 μM) in water upon addition of $Eu(CF_3SO_3)_3$ (0→3 equivalents). Inset: The changes in the emission integrals (450-750 nm) *vs.* equivalents of Eu(III) added; T = 298 K and λ_{ex} = 420 nm

Based on this result and the similar levels of quenching achieved with $Eu(CF_3SO_3)_3$ as with Eu.1, the second experiment was also undertaken, this time titrating $Tb(CF_3SO_3)_3$ against our CdTe TGA QDs. Again, little was observed by way of changes in the absorption spectra. The PL results are shown in Figure 3.24.

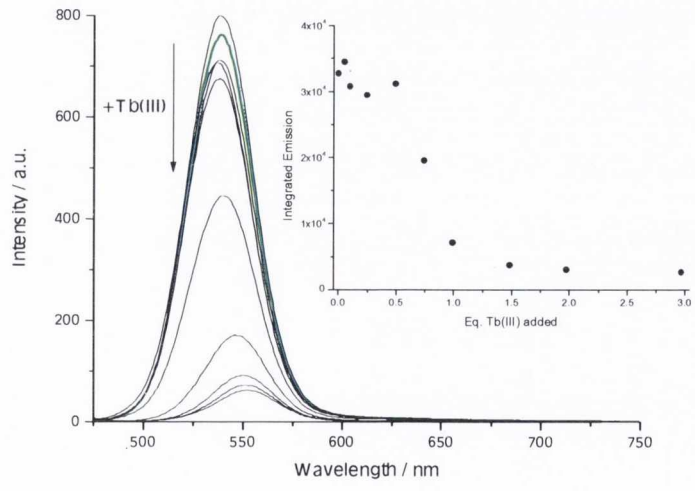

Figure 3.24: Evolution of the fluorescence spectrum of CdTe TGA QDs (3.7 μM) in water upon addition of $Tb(CF_3SO_3)_3$ (0→3 equivalents). Inset: The changes in the emission integrals (450-750 nm) *vs.* equivalents of Tb(III) added; T = 298 K and λ_{ex} = 420 nm.

It can be seen in the second titration, using $Tb(CF_3SO_3)_3$, that the same high rate of quenching is not achieved within one equivalent. This supports our premise that quenching is due to electron transfer from our CdTe TGA QDs to the Eu(III) ion. Its ability to be reduced to Eu(II), unlike the Tb(III), results in the quenching of our emission. This point is clarified on comparison of the Stern-Volmer plots of the data for these two systems (Figure 3.25).

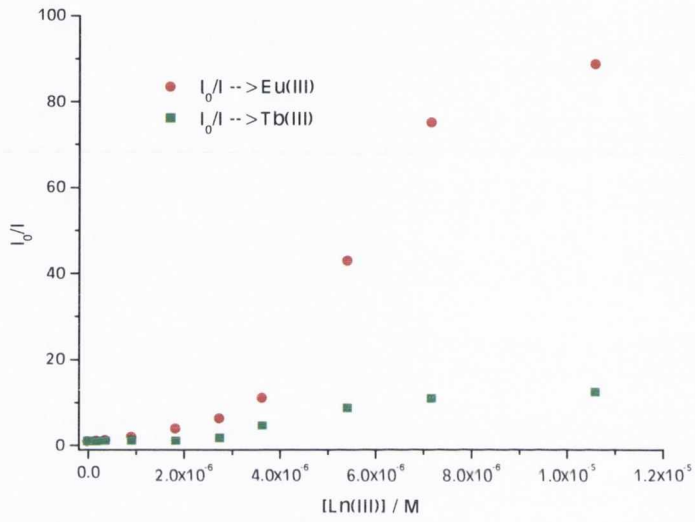

Figure 3.25: The Stern-Volmer plots of the changes in the fluorescence emission integrals of CdTe TGA QDs in the presence of increasing amounts of Ln(III); [CdTe TGA] = 3.7 μM, [Ln(III)] = 0 → 1.06×10^{-5} M.

As before, the results obtained for the Eu(III) show a non-linearity over the range of the titration, with only addition of the first equivalent giving a relatively linear result. By comparison, the Stern-Volmer of the Tb(III) titration shows reasonable linearity throughout. Analysis of only this linear section (Figure 3.26) allows determination of the quenching constants K_{SV} and k_q from equation (1) as before (Table 3.2).

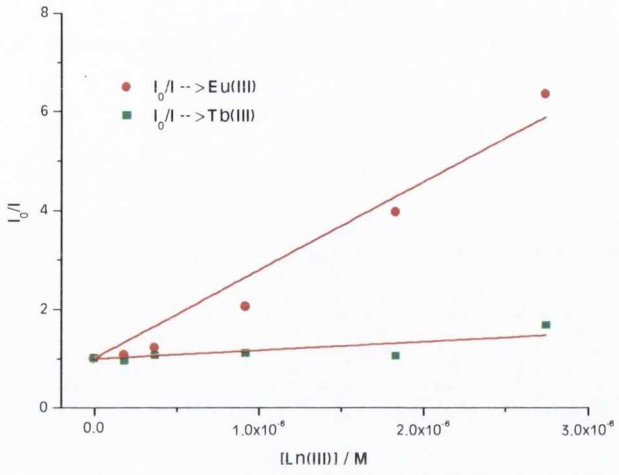

Figure 3.26: The Stern-Volmer plots of the changes in the fluorescence emission integrals of TGA-CdTe in the presence of increasing amounts of Ln(III); [CdTe TGA] = 3.7 μM, [Ln(III)] = 0 → 2.74×10^{-5} M.

Table 3.2: Quenching constants (K_{SV} and k_q) estimated from the fluorescence quenching experiments performed on CdTe TGA in the presence of increasing amounts of Ln(II).

Method	K_{SV} / M^{-1}	k_q / $M^{-1}.s^{-1}$
Fluorescence emission Eu(III)	$1.78 (\pm 0.12)\times10^{6}$	$1.3 (\pm 0.2)\times10^{14}$
Fluorescence emission Tb(III)	172485 ± 44908	$1.3 (\pm 0.7)\times10^{13}$

The interactions between the CdTe TGA QDs and the Eu(III) triflate did show one substantial difference compared to those with the cyclen complex, Eu.1. There was obvious aggregation and precipitation of the QD-$Eu(CF_3SO_3)_3$ system over time at higher equivalents. This is demonstrated in Figure 3.27, which directly compares a solution of CdTe TGA QDs with 10 equivalents of $Eu(CF_3SO_3)_3$ and Eu.1 respectively.

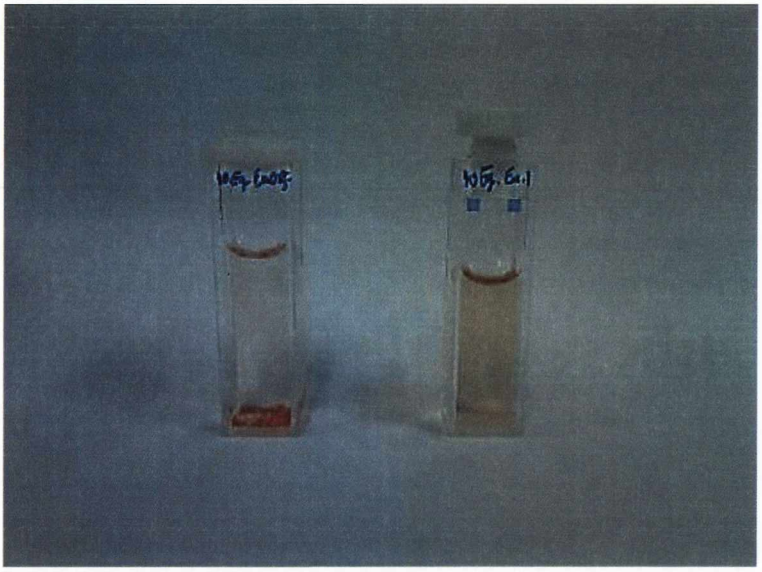

Figure 3.27: CdTe TGA QDs and 10 equivalents of $Eu(CF_3SO_3)_3$ (left), and Eu.1 (right), respectively.

This indicates that the Eu.1-CdTe conjugate is far more stable than its triflate version, which is to be expected given that the Eu.1 complex is for the most part protected, having only two labile water molecules that can be displaced. On the other hand the Eu(III) ion in $Eu(CF_3SO_3)_3$, has 9 coordinated water molecules in aqueous solution, and so is much less protected. This means it can bind four carboxylates, and thus more than one QD, resulting in eventual aggregation and precipitation. This is a key point of importance if this system is to be used further, for example, as a sensor, as investigated later.

The findings so far show that the addition of Eu.1 to CdTe TGA QDs results in coordination of the Eu.1 to the surface of the QD through displacement of two water molecules by the carboxylate. This binding results in rapid quenching of the QD emission. Previously studied systems e.g. between QDs and a Ru complex[39], have shown quenching of the QD emission but only at higher equivalents, and in non-aqueous solvents, and analysis has shown this to be due to purely static quenching. Thus, not only is our system here more efficient, it has the added benefit of being in aqueous solution, opening up the possibility of biological use. The rate of quenching is higher than that for a purely static system, as shown by Stern-Volmer analysis, indicating the presence of a dynamic quenching process, as further ascertained by the

shortening of the QDs lifetime. The quenching behaviour was also found to be specific to the lanthanide ion, with only Eu(III), and not Tb(III), exhibiting this strong effect. This all indicates (albeit indirectly) that the mechanism of quenching is due to electron transfer from the CdTe TGA exciton to the Eu(III) ion, resulting in reduction of the Eu(III) ion to Eu(II) which is non-emissive. This is further evidenced by the lack of Eu based phosphorescence from our system.

3.6 Transient Absorption Spectroscopy Studies of CdTe QD-Eu.1 cyclen systems

It was recently demonstrated that electron transfer from QDs to fullerenes (C60) is responsible for the decrease in the first exciton lifetime of the QDs upon addition of fullerene, using transient spectroscopy[40]. It was shown that, in the presence of fullerene, the QDs 1st exciton bleach displayed a faster recovery on the nanosecond timescale than the free QDs. The faster bleach recovery in the QD-C60 system was attributed to an additional decay pathway for the 1s electron taking place; by electron transfer to the C60 molecule. To this end, and to elucidate the mechanism of quenching in the Eu.1-CdTe system, ultrafast ps-transient absorption spectroscopy was performed on our structure (Figure 3.28), with delays from 0 to 3 ns.

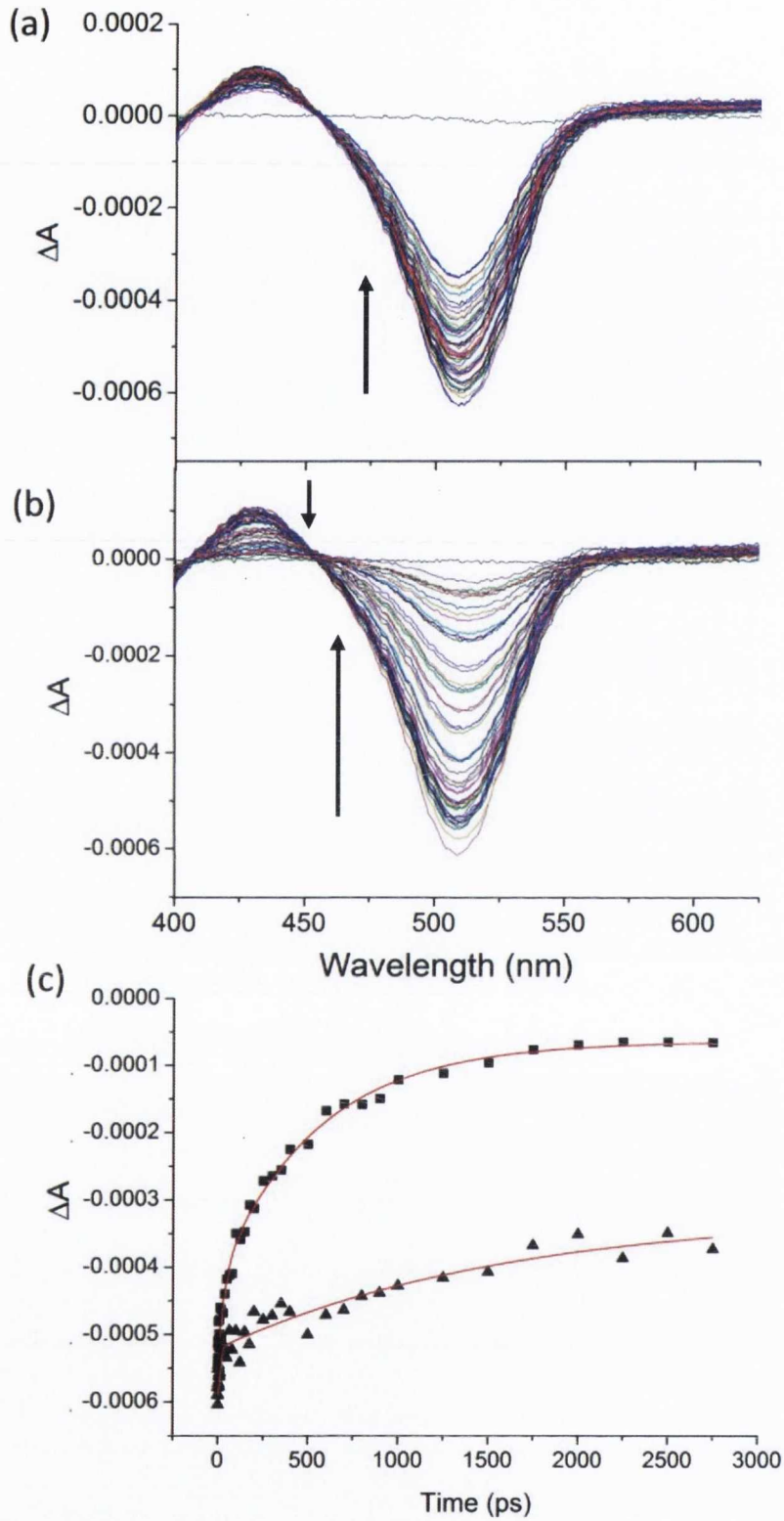

Figure 3.28: (a) Transient absorption spectra following 400 nm (50 fs) excitation of (a) 3.7 μM CdTe TGA QDs, (b) in the presence of Eu.1 (3 eq.), (c) comparison of kinetics for recovery of bleach at 513 nm in CdTe TGA QDs upon addition of Eu.1.

The quenching phenomenon was investigated by picosecond transient absorption spectroscopy at a range of Eu.1 concentrations. Care was taken to avoid multiphoton effects by ensuring that the excitation energy was below 100 nJ. The ps-transient absorption spectra of the CdTe TGA QDs on their own following excitation at 400 nm (50 fs) is shown in Figure 3.28 (a). The dominant feature is that of a strong bleached band around 515 nm, which corresponds to the depletion of the ground state, and correlates well with the QD band edge absorption band (Figure 3.3). Multicomponent analysis was needed to determine the kinetics of recovery of the bleach band and, assuming a biexponential model, lifetimes of 8 ± 3 ps (40 %) 1.6 ± 0.5 ns (60 %) were determined (Figure 3.28 (c)), the latter state results in incomplete recovery (44 %) of the bleach on the timescale of the experiment, 3.1 ns. These times are in agreement with recent ps-TA observations for similar QDs[15].

Figure 3.28 (b) shows the transient absorption of CdTe TGA QDs recorded in the presence of three equivalents of Eu.1. In this case we see almost complete signal recovery of the bleach band at 513 nm. The transient absorption data clearly reveal the quenching effect of the complex on the CdTe excited states. Analysis of the recovery kinetics for the bleach again required multicomponent fitting. The recovery of the bleach at 515 nm had associated lifetimes of 16 ± 4 ps (23 %) and 475 ± 42 ps (77 %) and essentially no longer-lived species (Figure 3.28 (c)). In the presence of Eu.1-CdTe, a 475 ps component dominates, indicating that the principle recovery pathway is due to surface interactions[16]. The efficient quenching of the emission in the presence of low concentrations of Eu.1 is taken as strong evidence for coordination of the europium centre to the TGA at the particle surface. This contrasts with studies that employ hole and electron trapping agents in large excess. There exists significant driving force to form the coordination bonds with the available carboxylate sites on the nanoparticle (~128 COOH groups) which results in the release of two water molecules. Importantly, the steady state quenching phenomena are mirrored in the transient experiments.

3.7 Low Concentration CdTe QD – Eu Cyclen Interactions

As can be seen above, highly efficient quenching, specific to Eu, was obtained with this system. This opened up the potential of using these QDs and this complex as a chemosensor. In order to test this, titrations were initially carried out at lower concentrations, to investigate the sensitivity of the QDs to quenching by the Eu.1 complex. Titrations of CdTe TGA QDs and Eu.1 were done as outlined previously, but starting with a QD concentration of 1 μM, adding Eu.1 from 0 to 10 equivalents. As can be seen in Figure 3.29, similar behaviour was observed for both concentrations.

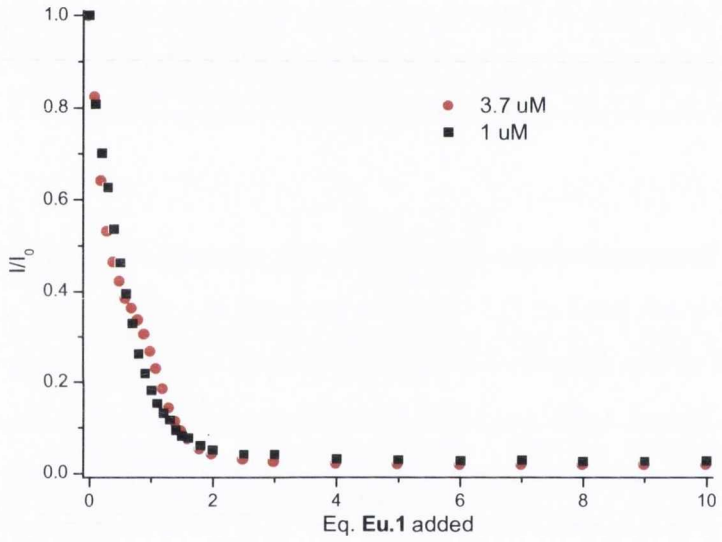

Figure 3.29: Comparison of the data obtained using two different QDs concentration ([QDs] = 3.7 and 1 μM); Eu.1 = 0 → 10 equivalents; λ_{ex} = 420 nm.

Going even further, similar efficient quenching behaviour was observed at a QD starting concentration of 0.1 μM (Figure 3.30 (a)). The appearance that only 80% quenching is achieved in this is due to interference from the growing Raman peak (around 490 nm), and not caused by residual QD emission (Figure 3.30 (b)).

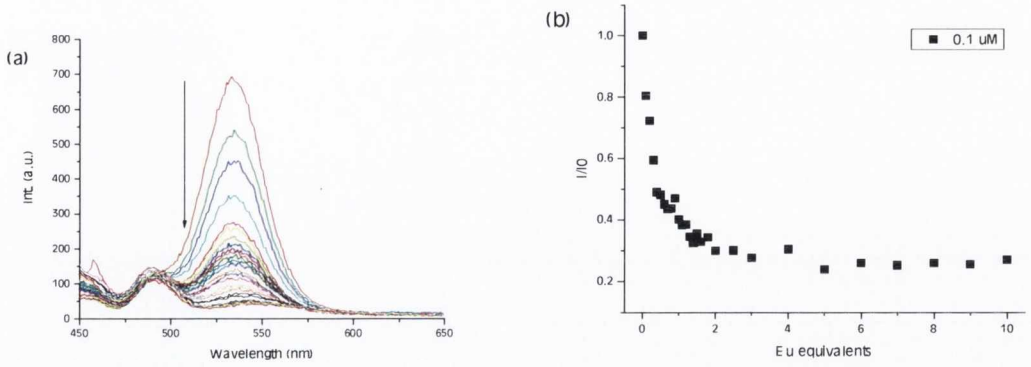

Figure 3.30: Evolution of the fluorescence emission spectrum of CdTe TGA in the presence of increasing concentration of Eu.1. ([QDs] = 0.1 μM); Eu.1 = 0 → 10 equivalents; λ_{ex} = 420 nm.

The above titrations showed that QD emission is extremely sensitive to the addition of Eu.1, with results in the nanomolar range correlating well with those previously at higher concentrations. The sensitivity shown here for detection at such extremely low concentration levels was promising for using this system as a sensor.

3.8 Investigation into Possible Sensing Using QD- Eu Cyclen Systems

To develop this concept, and investigate further the interaction taking place between the QDs and Eu.1, a suitable, as well as relevant, molecule had to be chosen for testing. 2,6-Pyridinedicarboxylic acid (dipicolinic acid, dpa, Figure 3.31) was decided upon as the molecule to examine, and the approach was to monitor the behaviour of a CdTe TGA QD solution (3.7 μM) in the presence of one equivalent of Eu.1 upon addition of dpa (0→30equivalents).

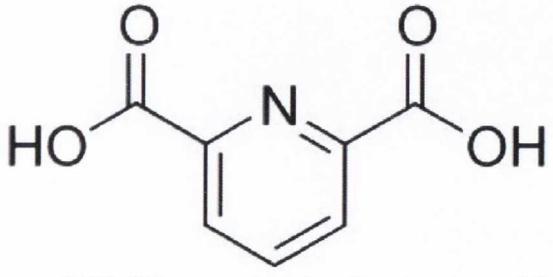

Figure 3.31: Diagram showing the structure of dpa.

Dpa is a tridentate molecule and can act as a chelating ligand to form complexes with lanthanide ions in the form $Ln(dpa)_3$[41,42]. Dpa is also of significance in biology, composing up to 10% of the dry weight of bacterial endospores[43,44]. Endospores are dormant forms of bacteria, able to survive in harsh conditions for decades, even centuries. Two genera of bacteria produce endospores, *Bacillus* and *Clostridium*. Within these genera are several species of bacteria that are of significant importance in the area of human health and disease. Examples include *C.botulinum* and *C.tetani* of the *Clostridium* genus which are responsible for botulanism and tetanus respectively. Spores of *bacillus anthracis* are the cause of anthrax, an infectious disease affecting humans and animals, most forms of which are lethal. The use of anthrax spores as a biological warfare weapon has been actively researched (and used) by several nations. They have also successfully been used in bioterrorism, with attacks on two US Democratic senators and several news media offices resulting in five deaths in the United States in 2001. Thus, the growing threat of international terrorism, and particularly bioterrorism, coupled with the danger posed by anthrax (and other) spores, makes research into methods that facilitate the fast, easy detection of bacterial endospores at low concentrations of great interest and importance to both the scientific and global community[45]. The significant percentage of dpa present in these spores means that detection of this biomarker could allow an easy route for detection, and the ability of lanthanides to bind to dpa is currently been exploited to create possible dpa-based anthrax sensors. Such research is only in the early stages of development with few examples. These include systems using lanthanides on their own[46-48], and well as coupling them to carbon nanotubes to create hybrid materials[49].

Here our aim was to use our novel QD-Eu.1 conjugate to sense dpa. The addition of dpa to the CdTe-Eu.1 solution should result in displacement of the cyclen complex from the QDs surface and hence possible recovery of the QD emission. This would be coupled with the simultaneous appearance of the characteristic Eu(III) emission between 570 and 720 nm arising from the 1:1 ternary complex (Eu.1-dpa) formed between dpa and Eu.1. This concept is represented in the following scheme (Figure 3.32) and such a system would serve as an off/on sensor for dpa.

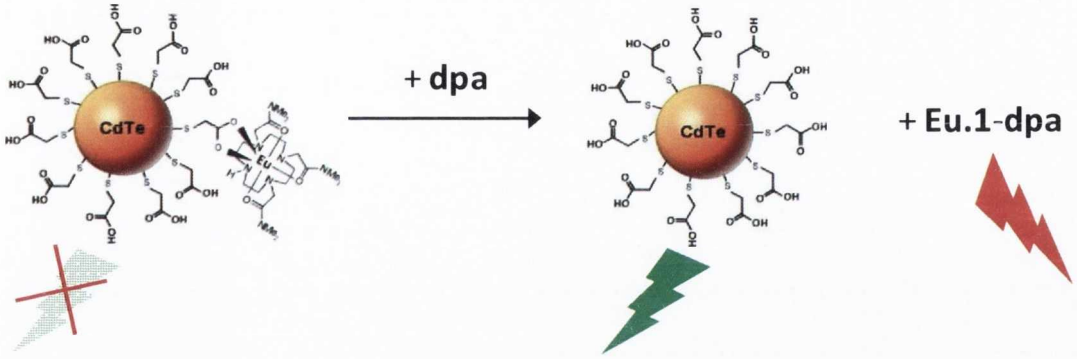

Figure 3.32: Scheme illustrating the off-on sensor concept using dpa. Addition of dpa results in removal of the Eu.1 complex from the QD and recovery of emission.

Titration of up to thirty equivalents dpa was carried out against one equivalent of the CdTe-Eu.1 conjugate. This resulted in the characteristic Eu(III)-centered emission upon excitation of the dpa antenna at 280 nm (Figure 3.33). Unfortunately, no fluorescence recovery was observed for the QDs. To the contrary, the QDs emission was further quenched upon addition of dpa (see Figure 3.34).

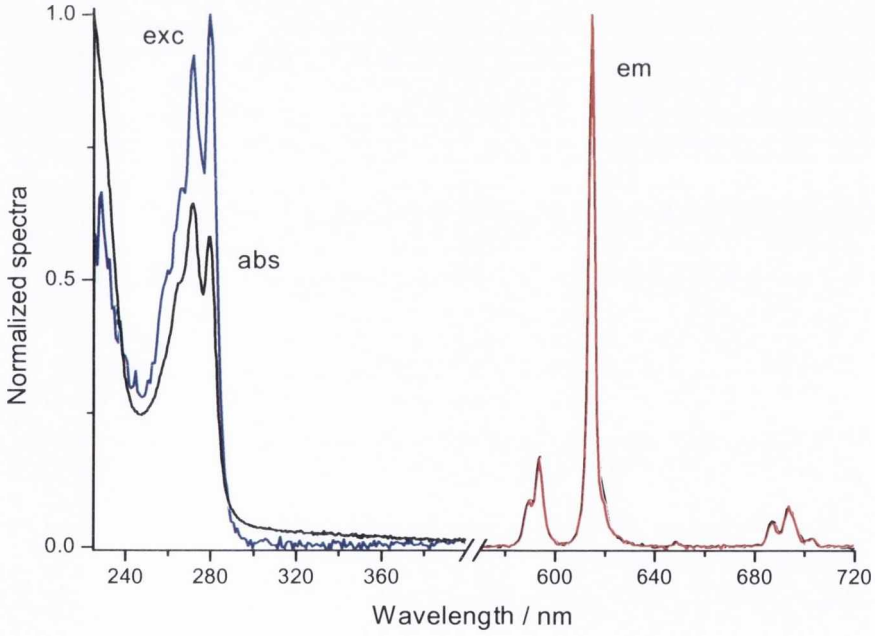

Figure 3.33: Absorption (black), excitation (blue) (λ_{an} = 615 nm) and emission (λ_{ex} = 280 nm, 0.1 ms delay after flash) spectra of a 3.7 μM solution of QDs in the presence of 1eq. Eu.1 and 30eq. dpa. The emission spectrum has been recorded directly after the addition of dpa (red curve) and 16h later (black curve).

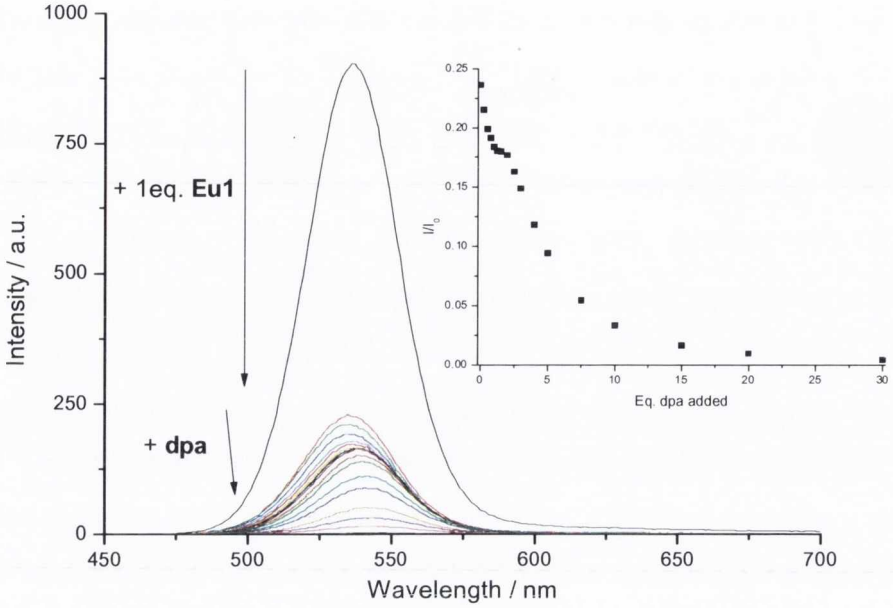

Figure 3.34: Evolution of the fluorescence emission of a 3.7 μM solution of QDs in the presence of 1 eq. Eu.1 upon addition of dpa. The inset shows the changes observed in the integrated emission as a function of the equivalents of dpa added.

This titration was also carried out with a starting QD concentration of 1 μM with similar quenching behaviour achieved (Figure 3.35 and 3.36).

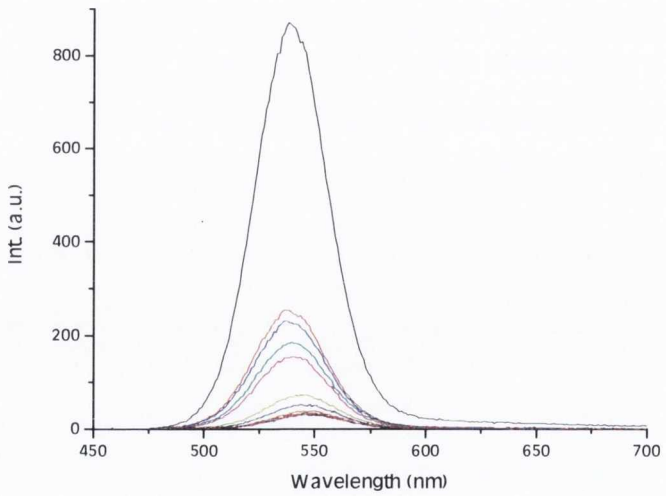

Figure 3.35: Evolution of the fluorescence emission of a 1 μM solution of QDs in the presence of 1 eq. Eu.1 upon addition of dpa.

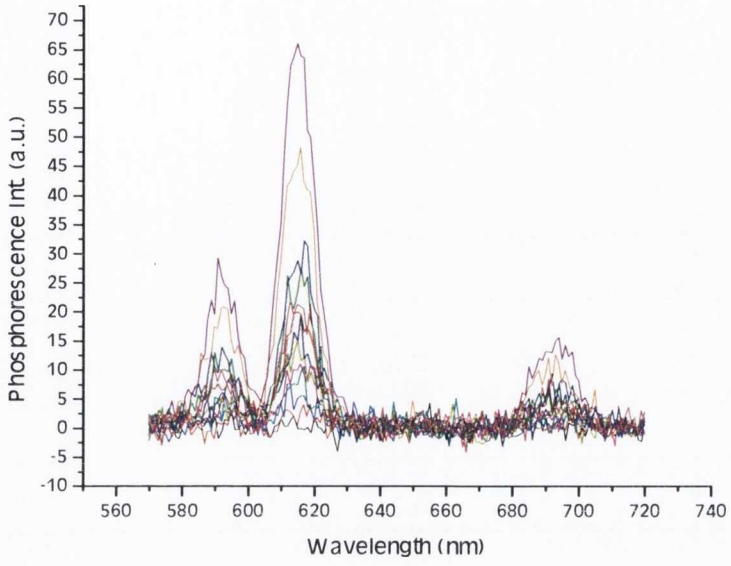

Figure 3.36: Evolution of the Eu(III)-centered emission (λ_{ex} = 280 nm) of CdTe-Eu.1 upon addition of dpa.

The sensitization of the Eu(III) emission by the dpa antenna was ascertained by the good correlation between the excitation and absorption spectra of the solution (see Figure 3.33). These results demonstrate that the interaction taking place between Eu.1 and the thioglycolic groups at the surface of the QDs can be affected by the addition of dpa. The system also showed remarkable stability, with no change occurring over a period of 16 hours (Figure 3.33). However, we also observed that the QD emission did not recover. The reason for this irreversible quenching is still to be explored, as the addition of dpa alone has also been shown to result in quenching of the QDs emission (13%).

Having observed the Ln-centered emission (after the addition of 30eq. dpa) in our previous experiment, the titration was repeated and the Eu(III) phosphorescence emission as well as the Eu($^5D_0$) excited state lifetime were monitored after each dpa addition. The Eu(III) emission showed very little changes from 0 to 5 equivalents of dpa. However, further addition (5 to 30eq.) led to a switching on of the emission, with a *ca.* 300-fold enhancement after the addition of 30eq. dpa (Figure 3.37). The slow response at the start, even if dpa is expected to form a 1:1 complex with Eu.1, can be

explained by the fact that there is a binding equilibrium and a certain amount of dpa is needed to compete with the interaction taking place between the TGA of the QDs and the cyclen complex. Once the threshold is reached, each addition of dpa results in a sizeable enhancement of the overall emission.

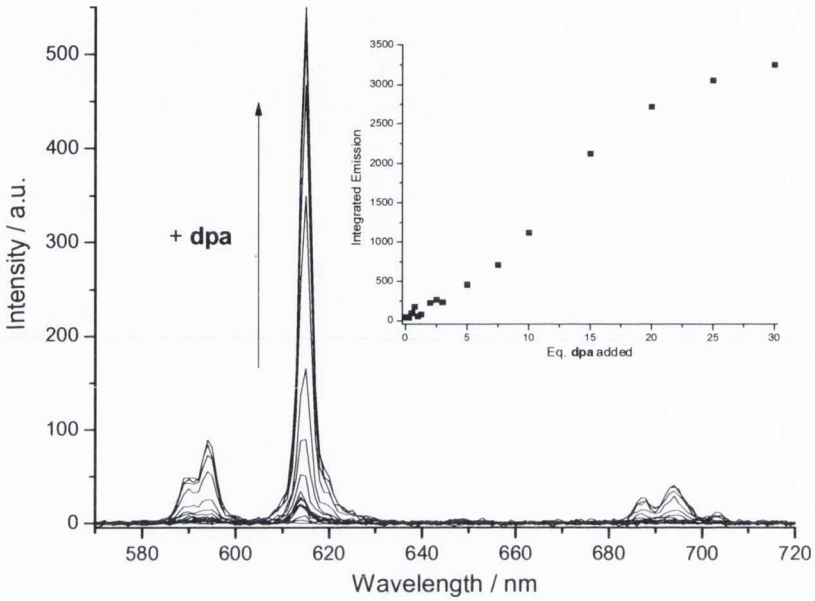

Figure 3.37: Evolution of the Eu(III)-centered emission (λex = 280 nm) of CdTe-Eu.1 upon addition of dpa. The inset shows the changes observed in the integrated emission as a function of the equivalents of dpa added.

As already stated above, the lifetimes of the Eu($^5D_0$) excited state have been monitored and are summarized in Table 3.3. The luminescence decays were best-fitted to monoexponential function of time from 0 to 5eq. dpa, after which the presence of the Eu·1-dpa ternary complex becomes predominant in solution resulting in the observed biexponential decays, with the short-lived species corresponding to Eu·1 and the long-lived one, to Eu·1-dpa. When 25 and 30eq. dpa were added, the luminescence decays could be fitted using both mono- and biexponential functions, the percentage of the long-lived ternary complex reaching values higher than 95%. As a result of the increase in the percentage of the luminescent species, Eu.1-dpa, the average lifetimes $<\tau_{av}>$ increased significantly after 5 equivalents (Figure 3.38) similarly to what was observed previously for the Eu(III) emission (Figure 3.37 and Figure 3.39).

Table 3.3: Lifetimes of the Eu($^5D_0$) excited state in water in the presence of increasing amounts of dpa (λ_{ex} = 280 nm and λ_{an} = 615 nm); each value is the average of at least three different measurements.

QDs-Eu·1 +x eq. **dpa**	τ_1 (±2σ) / ms	% species 1	τ_2 (±2σ) / ms	% species 2
0.25	0.32(2)	-	-	-
0.5	0.34(1)	-	-	-
0.75	0.34(2)	-	-	-
1	0.32(2)	-	-	-
2	0.325(9)	-	-	-
2.5	0.32(1)	-	-	-
3	0.321(1)	-	-	-
5	0.345(9)	-	-	-
7.5	0.32(4)	60±7	1.6(2)	40±7
10	0.29(1)	35±2	1.45(1)	65±2
15	0.3(1)	12±2	1.52(4)	88±2
20	0.3(1)	7±2	1.53(5)	93±2
25	0.3(1)	5±2	1.52(4)	95±2
	-	-	1.39(1)	100
30	0.2(2)	3±1	1.52(3)	97±1
	-	-	1.43(2)	100

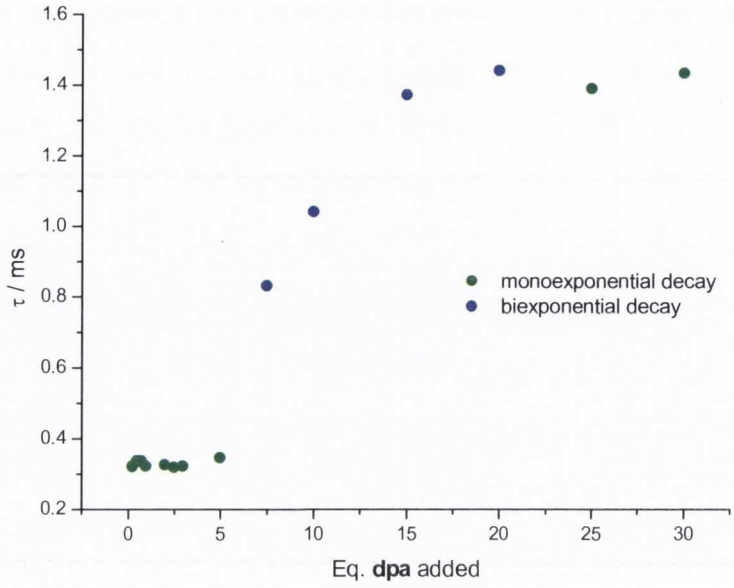

Figure 3.38: Evolution of the Eu(III) lifetime as a function of the equivalents dpa added.

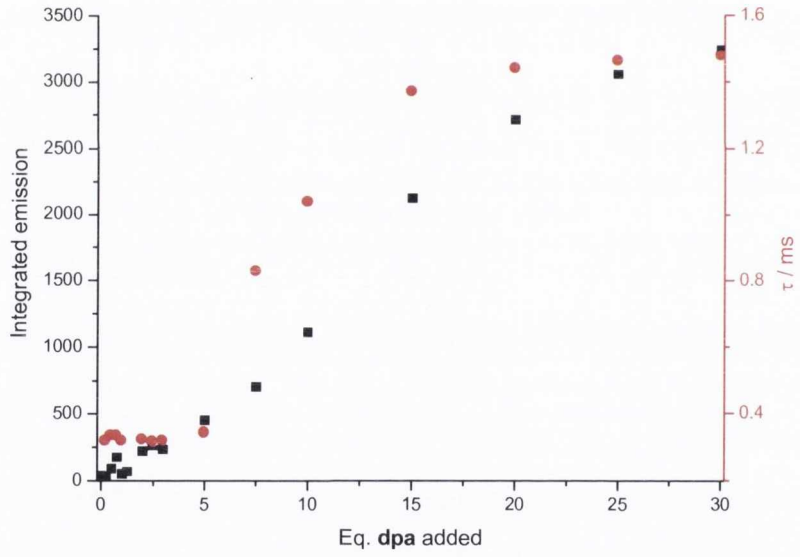

Figure 3.39: Comparison of the Eu(III) emission (black squares, left y-scale) and lifetime (red circles, right y-scale) changes as a function of dpa equivalents added.

These results prove unequivocally that the Eu.1 is being removed from the surface of the QDs, and then becoming sensitised.

3.9 Conclusions

In conclusion, we have demonstrated that the QDs are extremely sensitive to the presence of the Eu.1 complex, with quenching obtained in the nanomolar concentration range (100 nM), which correlated well with those titrations carried out at higher concentrations. Similar quenching was achieved with using just $Eu(CF_3SO_3)_3$, however this did not display any long-term stability. The mechanism of quenching was studied using Stern-Volmer plots, and shown to be more complex than a simple static quenching system, though static quenching does play a role. It is strongly believed from the evidence outlined that there is electron transfer from the QD to the Eu.1, shown by the lack of phosphorescence due to a non-emissive Eu(II), and the lower quenching rate achieved with $Tb(CF_3SO_3)_3$, which unlike Eu, cannot be reduced to Tb(II). An investigation into the use of this QD-lanthanide conjugated system as a potential sensor for bacterial spores was undertaken. This was demonstrated with moderate success, with addition of dpa resulting in sensitised emission from the Eu, indicating that the cyclen complex can be displaced from the QD surface by the addition of a strong Ln(III) chelator such as dpa. This was achieved at concentrations as low as 1 μM. However, even though the displacement was confirmed using several techniques (emission, excitation and lifetimes), the QDs initial emission could not be recovered. This lack of recovery is to be investigated in the future, as well as lower concentration titrations for the dpa sensing experiments in order to test the limits of this sensing behaviour.

References

(1) Byrne, S. J.; Corr, S. A.; Rakovich, T. Y.; Gun'ko, Y. K.; Rakovich, Y. P.; Donegan, J. F.; Mitchell, S.; Volkov, Y. *Journal of Materials Chemistry* **2006**, *16*, 2896.

(2) Byrne, S. J.; le Bon, B.; Corr, S. A.; Stefanko, M.; O'Connor, C.; Gun'ko, Y. K.; Rakovich, Y. P.; Donegan, J. F.; Williams, Y.; Volkov, Y.; Evans, P. *ChemMedChem* **2007**, *2*, 183.

(3) Alivisatos, A. P.; Gu, W.; Larabell, C. *Annual Review of Biomedical Engineering* **2005**, *7*, 55.

(4) Nabiev, I.; Mitchell, S.; Davies, A.; Williams, Y.; Kelleher, D.; Moore, R.; Gun'ko, Y. K.; Byrne, S.; Rakovich, Y. P.; Donegan, J. F.; Sukhanova, A.; Conroy, J.; Cottell, D.; Gaponik, N.; Rogach, A.; Volkov, Y. *Nano Letters* **2007**, *7*, 3452.

(5) Elliott, S. D.; Moloney, M. P.; Gun'ko, Y. K. *Nano Letters* **2008**, *8*, 2452.

(6) Rogach, A. L.; Gaponik, N.; Lupton, J. M.; Bertoni, C.; Gallardo, D. E.; Dunn, S.; Pira, N. L.; Paderi, M.; Repetto, P.; Romanov, S. G.; O'Dwyer, C.; Torres, C. M. S.; Eychmuller, A. *Angewandte Chemie-International Edition* **2008**, *47*, 6538.

(7) Susha, A. S.; Javier, A. M.; Parak, W. J.; Rogach, A. L. *Colloids and Surfaces A: Physicochemical and Engineering Aspects* **2006**, *281*, 40.

(8) Byrne, S. J.; Williams, Y.; Davies, A.; Corr, S. A.; Rakovich, A.; Gun'ko, Y. K.; Rakovich, Y. P.; Donegan, J. F.; Volkov, Y. *Small* **2007**, *3*, 1152.

(9) Jan, E.; Byrne, S. J.; Cuddihy, M.; Davies, A. M.; Volkov, Y.; Gun'ko, Y. K.; Kotov, N. A. *Acs Nano* **2008**, *2*, 928.

(10) Govan, J. E.; Jan, E.; Querejeta, A.; Kotov, N. A.; Gun'ko, Y. K. *Chem. Commun.* **2010**, *46*, 6072.

(11) Burda, C.; Link, S.; Green, T. C.; El-Sayed, M. A. *The Journal of Physical Chemistry B* **1999**, *103*, 10775.

(12) Klimov, V. I.; Schwarz, C. J.; McBranch, D. W.; Leatherdale, C. A.; Bawendi, M. G. *Physical Review B* **1999**, *60*, R2177.

(13) Pandey, A.; Guyot-Sionnest, P. *Science* **2008**, *322*, 929.

(14) Baker, D. R.; Kamat, P. V. *Langmuir* **2010**, *26*, 11272.

(15) Idowu, M.; Nyokong, T. *Journal of Luminescence* **2009**, *129*, 356.

(16) Wu, H.; Liang, J.; Han, H. *Microchimica Acta* **2008**, *161*, 81.

(17) Harris, C.; Kamat, P. V. *ACS Nano* **2009**, *3*, 682.

(18) Neuman, D.; Ostrowski, A. D.; Mikhailovsky, A. A.; Absalonson, R. O.; Strouse, G. F.; Ford, P. C. *Journal of the American Chemical Society* **2007**, *130*, 168.

(19) Ma, Q.; Su, X. *Analyst* **2011**, *136*, 4883.

(20) Bunzli, J.-C. G.; Piguet, C. *Chemical Society Reviews* **2005**, *34*, 1048.

(21) Steemers, F. J.; Verboom, W.; Reinhoudt, D. N.; van der Tol, E. B.; Verhoeven, J. W. *Journal of the American Chemical Society* **1995**, *117*, 9408.

(22) Xiao, M.; Selvin, P. R. *Journal of the American Chemical Society* **2001**, *123*, 7067.

(23) Torelli, S.; Imbert, D.; Cantuel, M.; Bernardinelli, G.; Delahaye, S.; Hauser, A.; Bünzli, J.-C. G.; Piguet, C. *Chemistry – A European Journal* **2005**, *11*, 3228.

(24) Massue, J.; Quinn, S. J.; Gunnlaugsson, T. *Journal of the American Chemical Society* **2008**, *130*, 6900.

(25) Hildebrandt, N.; Charbonniere, L.; Lohmannsroben, H.-G. *Journal of Biomedicine and Biotechnology* **2007**, *2007*.

(26) Charbonnière, L. J.; Hildebrandt, N. *European Journal of Inorganic Chemistry* **2008**, *2008*, 3241.

(27) Charbonnière, L. J.; Hildebrandt, N.; Ziessel, R. F.; Löhmannsröben, H.-G. *Journal of the American Chemical Society* **2006**, *128*, 12800.

(28) Gaponik, N.; Talapin, D. V.; Rogach, A. L.; Hoppe, K.; Shevchenko, E. V.; Kornowski, A.; Eychmuller, A.; Weller, H. *J. Phys. Chem. B* **2002**, *106*, 7177.

(29) Fery-Forgues, S.; Lavabre, D. *Journal of Chemical Education* **1999**, *76*, 1260.

(30) Yu, W. W.; Qu, L.; Guo, W.; Peng, X. *Chemistry of Materials* **2003**, *15*, 2854.

(31) Zhang, H.; Zhou, Z.; Yang, B.; Gao, M. *The Journal of Physical Chemistry B* **2002**, *107*, 8.

(32) Edsall, J. T.; Wyman, J. *Biophysical Chemistry*; Academic Press, Inc., New York, 1958.

(33) Leonard, J.; Gunnlaugsson, T. *Journal of Fluorescence* **2005**, *15*, 585.

(34) dos Santos, C. M. G.; Harte, A. J.; Quinn, S. J.; Gunnlaugsson, T. *Coordination Chemistry Reviews* **2008**, *252*, 2512.

(35) Poole, R. A.; Kielar, F.; Richardson, S. L.; Stenson, P. A.; Parker, D. *Chem. Commun.* **2006**, 4084.

(36) Uematsu, T.; Waki, T.; Torimoto, T.; Kuwabata, S. *The Journal of Physical Chemistry C* **2009**, *113*, 21621.

(37) Boulesbaa, A.; Huang, Z.; Wu, D.; Lian, T. *The Journal of Physical Chemistry C* **2009**, *114*, 962.

(38) Gadenne, B.; Yildiz, I.; Amelia, M.; Ciesa, F.; Secchi, A.; Arduini, A.; Credi, A.; Raymo, F. M. *Journal of Materials Chemistry* **2008**, *18*, 2022.

(39) Amelia, M.; Font, M.; Credi, A. *Dalton Transactions* **2011**, *40*, 12083.

(40) Song, N.; Zhu, H.; Jin, S.; Zhan, W.; Lian, T. *Acs Nano* **2010**, *5*, 613.

(41) Bleaney, B.; Dobson, C. M.; Levine, B. A.; Martin, R. B.; Williams, R. J. P.; Xavier, A. V. *Journal of the Chemical Society, Chemical Communications* **1972**, 791b.

(42) Donato, H.; Martin, R. B. *Journal of the American Chemical Society* **1972**, *94*, 4129.

(43) Slieman, T. A.; Nicholson, W. L. *Appl. Environ. Microbiol* **2001**, *67*, 1274.

(44) Madigan, M. T.; Martinko, J. M.; Stahl, D.; Clark, D. P. *Brock Biology of Microorganisms* 13 ed.; Benjamin Cummings, 2010.

(45) Hurtle, W.; Bode, E.; Kulesh, D. A.; Kaplan, R. A.; Garrison, J.; Bridge, D.; House, M.; Frye, M. S.; Loveless, B.; Norwood, D. *Journal of Clinical Microbiology* **2004**, *42*, 179.

(46) Cable, M. L.; Kirby, J. P.; Levine, D. J.; Manary, M. J.; Gray, H. B.; Ponce, A. *Journal of the American Chemical Society* **2009**, *131*, 9562.

(47) Cable, M. L.; Kirby, J. P.; Sorasaenee, K.; Gray, H. B.; Ponce, A. *Journal of the American Chemical Society* **2007**, *129*, 1474.

(48) Rosen, D. L.; Sharpless, C.; McGown, L. B. *Analytical Chemistry* **1997**, *69*, 1082.

(49) Tan, C.; Wang, Q.; Zhang, C. C. *Chem. Commun.* **2011**, *47*, 12521.

Chapter 4: Study of interactions between CdTe QDs and Porphyrin Systems

4.1 Introduction

The main aim of this piece of work was to investigate energy or charge transfer processes in QD-porphyrin systems. Our work focused on the study of the aqueous interaction of CdTe stabilised with thioglycolic acid (TGA) and three selected porphyrin complexes. These systems were investigated using a range of steady state and time resolved spectroscopic techniques. It is expected that using these combined spectroscopic measurements the exciton and transfer processes of our porphyrin-QD systems can be studied in depth, leading to a further understanding of the mechanisms at work. This understanding can in turn be employed to develop new complexes for use in, among other things, enhanced singlet oxygen generation and photodynamic therapy, or electron transfer systems for solar energy conversion.

The porphyrins used are all derivatives of the parent porphine macrocycle, however each of the methane bridge's hydrogen atoms have been replaced with a cationic methylated pyridinium moiety. The free base form is tetracationic *meso*-tetrakis(4-N-methylypyridyl)porphyrin (H_2TMPyP4), the counterion being tosylate. The other two are metalloporphyrins of this, coordinated with zinc(II) (ZnTMPyP4) and platinum(II) (PtTMPyP4) respectively. These both have chloride counterions. Their structures are shown in Figure 4.1.

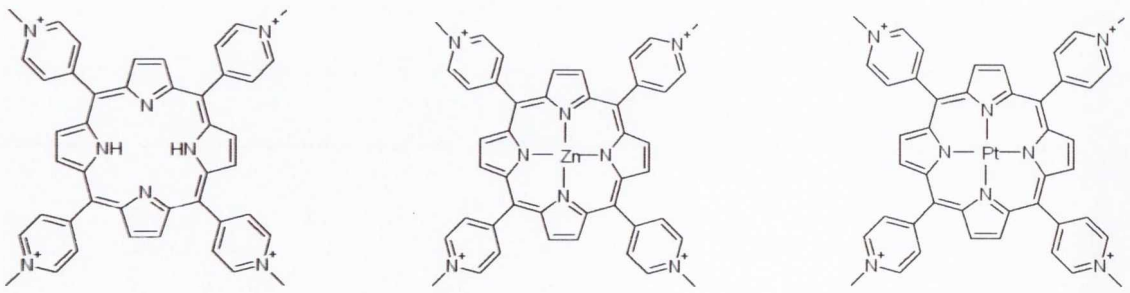

Figure 4.1: Structures of the free base H_2TMPyP4, zinc coordinated ZnTMPyP4, and platinum coordinated PtTMPyP4 porphyrins respectively.

The quantum dots used in this study are the same as those detailed previously in this work (Chapter 3). These are aqueous cadmium telluride QDs stabilised with thioglycolic acid (TGA). The absorbance and emission spectra for these QDs are shown in Chapter 3, Figure 3.3. The steady state absorption spectrum of CdTe TGA QDs in water shows a band at 513 nm, which is assigned to first excitonic transition ($1S_e$-$1S_h$). The excitation of the QDs at 450 nm resulted in band edge photoluminescence centred at 550 nm, with a quantum yield of 27%, calculated using the dye Rhodamine 6G as a reference[1]. Using this information the size of these QDs was determined spectroscopically to be 2.3 nm in diameter[2] and the number of TGA molecules at the surface of these particles was calculated to be approximately 128[2,3].

These CdTe QDs were subsequently used for the next part of this study, investigating the interactions between these CdTe QDs and three porphyrin molecules. It was believed that they would interact strongly with these porphyrins given their oppositely charged natures.

The results obtained from titrating CdTe QDs against three types of porphyrin are detailed below. These systems were studied using steady state UV-vis and fluorescence spectroscopy. The high degree of emission quenching of both species upon titration is seen as an indication of their binding and allows for the determination of their ratios. To probe the mechanism of quenching in more detail, small-angle X-ray scattering and ultrafast transient spectroscopy were also employed.

4.2 Free-base Porphyrin (H_2TMPyP4) and CdTe QDs system

The first porphyrin studied in this work was tetracationic *meso*-tetrakis(4-N-methylypyridyl)porphyrin (H_2TMPyP4), so called *free-base* as it lacks a coordinated metal atom at its centre. The normalised absorbance and emission spectra of the free-base is shown in Figure 4.2, highlighting the Soret band (at 423 nm) and four Q bands, as well as the fluorescence from the singlet state.

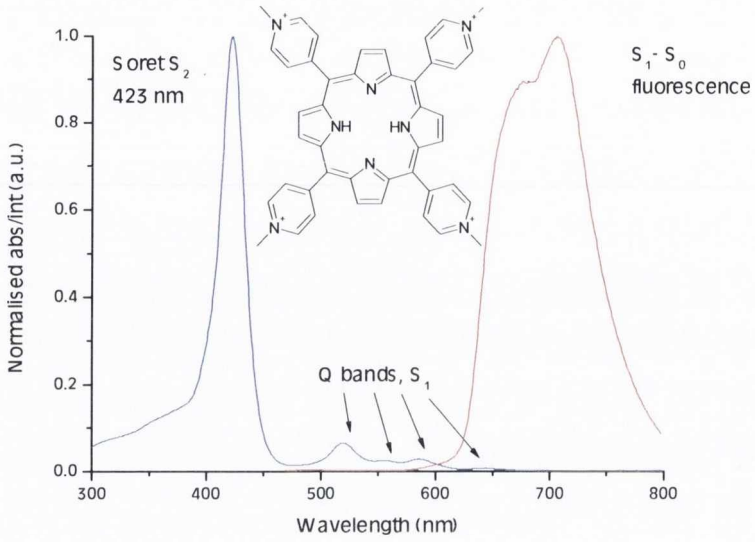

Figure 4.2: Normalised absorbance (blue) and emission (red) spectra of H_2TMPyP4 highlighting the Soret band (@ 423 nm) and Q bands, as well as the fluorescence from the triplet state.

4.2.1 Steady State Absorption Spectroscopy

The titration of CdTe TGA QDs and H_2TMPyP4 was carried out in both directions. A comparison of their respective UV-vis absorption profiles is shown in Figure 4.3.

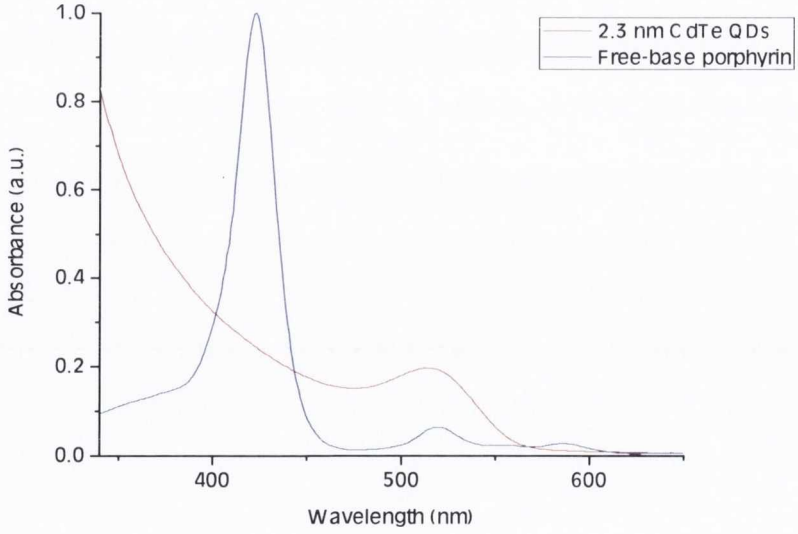

Figure 4.3: UV-vis aborbance spectra of CdTe TGA QDs (red) and H_2TMPyP4 (blue).

In the first instance, our CdTe QDs were titrated into an aqueous solution of H_2TMPyP4. This resulted in rapid hypochromism (decrease) in the Soret band at 423 nm, coupled with the evolution of another, red-shifted band, at 465 nm. This signal does not correspond to the QD band edge, as their absorbance can be seen unchanged at 513 nm (Figure 4.4).

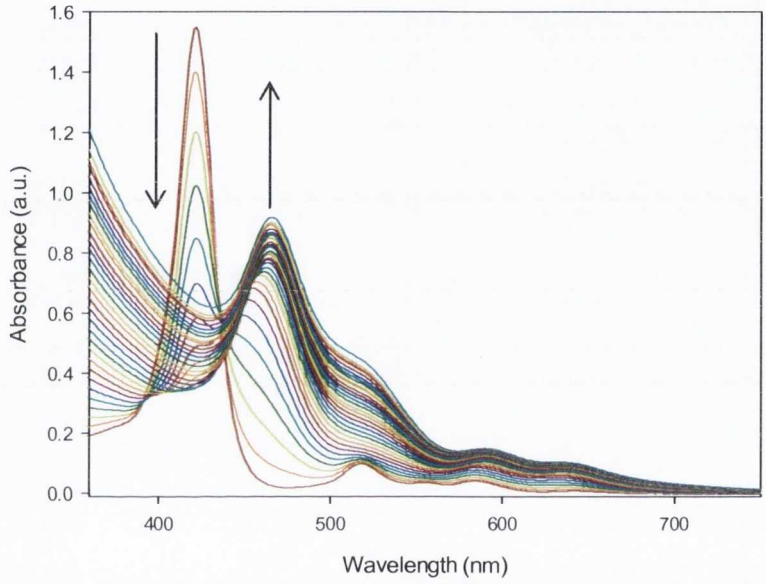

Figure 4.4: UV-vis spectrum of the titration of CdTe TGA QDs to H_2TMPyP4. The rapid decrease in the Soret band at 423 nm and evolution of the peak at 465 nm is clear.

Titration in the opposite direction (adding H_2TMPyP4 to CdTe QD) also resulted in the formation of this new peak at 460 nm, with no evidence remaining of the original Soret band at 423 nm (Figure 4.5). The QD band edge contribution again appears to remain unchanged, though it loses its fine structure with addition of the H_2TMPyP4 due to the overlapping absorbance.

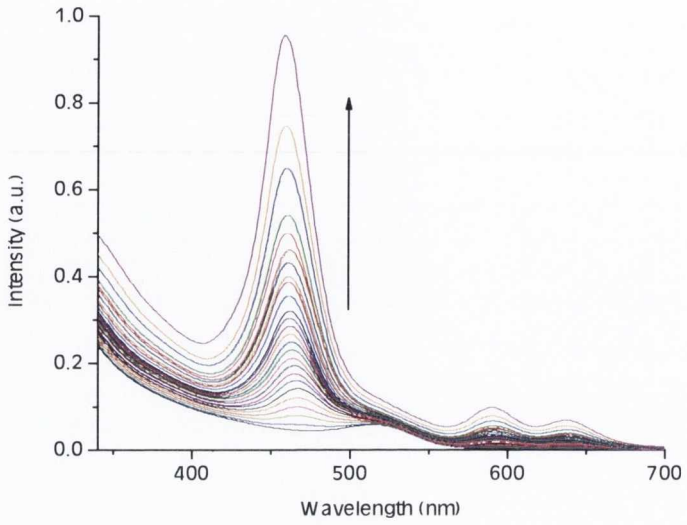

Figure 4.5: UV-vis spectrum of the titration of CdTe TGA QDs to H_2TMPyP4. There is no signal for the original Soret band at 423 nm, only the peak at 465 nm.

This new signal at approximately 465 nm indicates a strong red-shift (of 43 nm) of the Soret band, caused by the addition of these QDs to the H_2TMPyP4. Figure 4.6 shows the free-base porphyrin spectrum, and the resulting spectrum after the addition of one equivalent of CdTe TGA QDs. Figure 4.7 shows the result of titrating one equivalent of porphyrin into a solution of QDs.

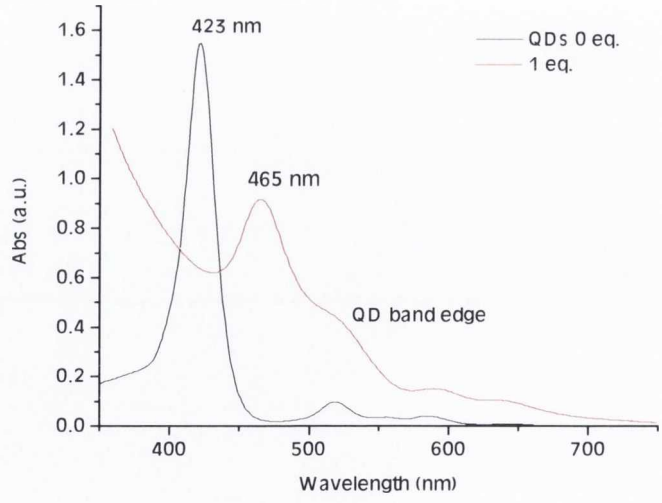

Figure 4.6: UV-vis spectra of H_2TMPyP4 (black) and following the addition of one equivalent of CdTe TGA QDs (red).

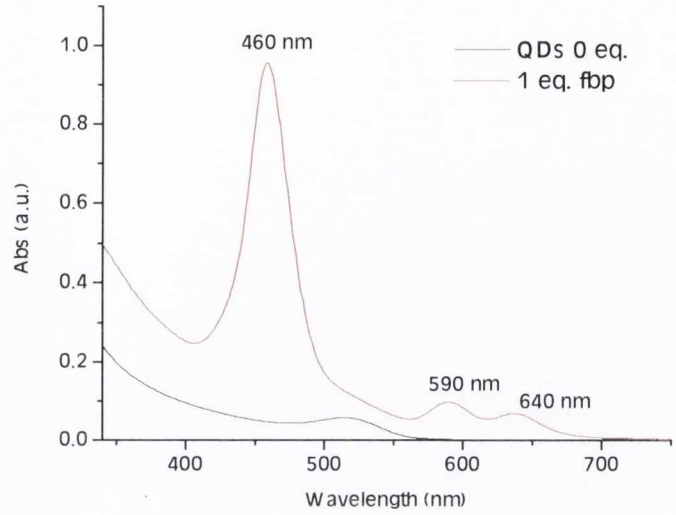

Figure 4.7: UV-vis spectra of CdTe TGA QDs (black) and following the addition of one equivalent of H_2TMPyP4 (red).

This shift in the porphyrin Soret band was also coupled with a change in the Q bands (Figure 4.8). This result was again indifferent to the direction of the titration (QD to porphyrin or vice versa). It appears that there is a reduction in the number of Q bands, from an initial four to an apparent two, though the band at 520 nm may be lost under the QD absorption.

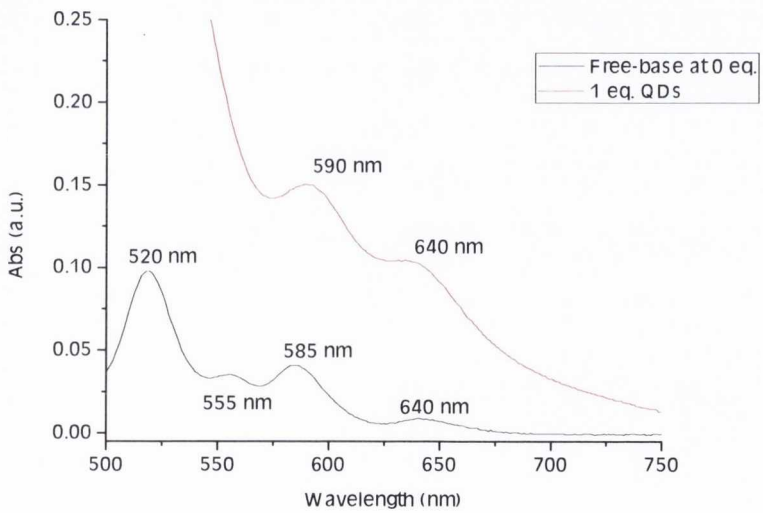

Figure 4.8: UV-vis spectrum showing the Q bands of the free-base porphyrin (black) and after the addition of one equivalent of CdTe TGA QDs (red).

An explanation for the cause of this effect was necessary and therefore several experiments were devised in order to further investigate this phenomenon.

4.2.1.1 Investigation of potential metal co-ordination

The initial line of investigation explored the apparently most obvious explanation is that the shift in the Soret band was caused by the coordination of a metal atom to the centre of the free-base porphyrin. Coordination of a metal centre is known to result in a shifting of the Soret band. This can be a red or blue shift, depending on the nature of the metal atom[4]. It also causes a reduction in the number of Q bands, as the number of Q-bands in a porphyrins' absorbance spectrum is related to the degree of symmetry in the porphyrin. Our free base porphyrin H_2TMPyP4 has four Q-bands, due to its D_{2h} symmetry. The coordination of a metal atom lifts the porphyrin's symmetry, resulting in fewer Q-bands than the free base's four e.g. D_{4h} for PtTMPyP4. It also results in a shifting of the Soret band from that of our free base H_2TMPyP4, which lies at 423 nm.

Consequently, an investigation was undertaken as to whether coordination of a variety of metals to H_2TMPyP4 is possible under such ambient conditions. Several titrations of H_2TMPyP4 were carried out, studying the effect of the addition of various concentrated metal salt solutions to H_2TMPyP4, to establish if this resulted in similar shifts in the absorbance spectrum. The first metal tested was cadmium, as this is the most obvious possibility, being present in abundance on the QDs surface (though it should be capped by TGA molecules). It was found however that, even after the addition of 100 equivalents of cadmium perchlorate, no significant spectral changes were observed. Titrations with other metal salts ($MgCl_2$, $MnCl_2$ and NaCl) showed a similar result, with the porphyrin exhibiting a resistance to metal coordination, even at high concentrations of metal ions (Figure 4.9).

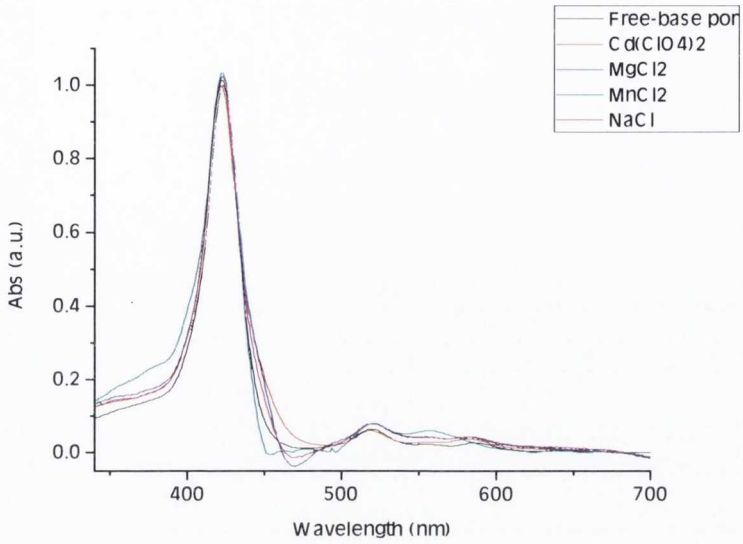

Figure 4.9: UV-vis spectra of H_2TMPyP4 (black), and after the addition of $Cd(ClO_4)_2$ (red), $MgCl_2$ (blue), $MnCl_2$ (green) and NaCl (pink).

4.2.1.2 Investigation of a potential acid effect

The next approach was to add an acid to a solution of the porphyrin to establish if this resulted in the same spectral shifts. However, as can be seen in Figure 4.10, titration of HCl into a solution of H_2TMPyP4 and reduction of the pH from neutral to pH2 had little effect on either the Soret or Q bands.

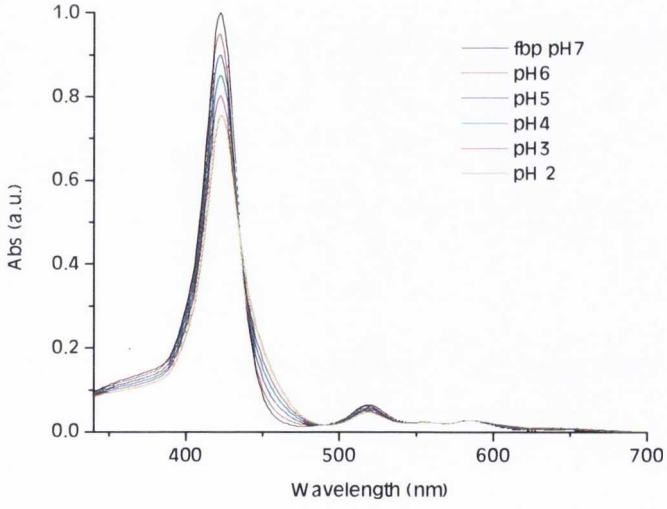

Figure 4.10: UV-vis spectra of H_2TMPyP4 after the reduction of the pH of solution to pH 2 using HCl.

4.2.1.3 Investigation of a potential base effect

Having ruled out the these potential explanations, as outlined, and in light of the negative values obtained from the zeta potential measurements (Chapter 3, Figure 3.6), which suggest that the carboxyl groups of the TGA are already deprotonated, it seemed possible that the COO^-s could result in deprotonation of the central protons in the porphyrin macrocycle. It has been shown that the acid-base equilibrium between the free base and the mono-deprotonated form ($H_2TMPyP4$ to $HTMPyP4^-$) is characterised by a pKa of 12.9 ± 0.2[5]. An exploration of the literature also showed that deprotonation of a free-base porphyrin can result in a shift in the Soret band[6], similar to that observed here for our system, and that other COO^- containing species (e.g. ferrocenecarboxylate[7]) have previously demonstrated this behaviour. To investigate whether this was occurring in our system, deprotonation of the $H_2TMPyP4$ was attempted by addition of NaOH. The pH of a $H_2TMPyP4$ solution was increased to 14 by addition of a 1 M solution of NaOH, monitoring the titration using UV-vis spectroscopy, as before (Figure 4.11-4.13).

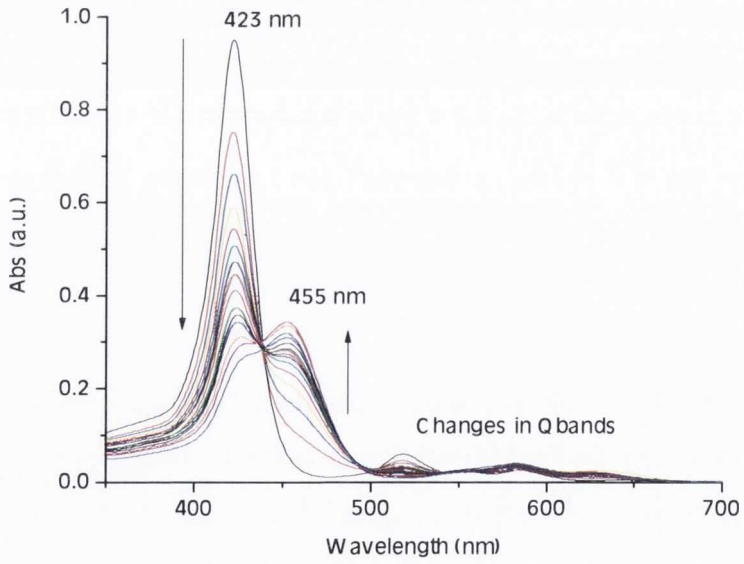

Figure 4.11: UV-vis spectra of the titration of NaOH to $H_2TMPyP4$ pH 7 – 14 showing the entire wavelength range.

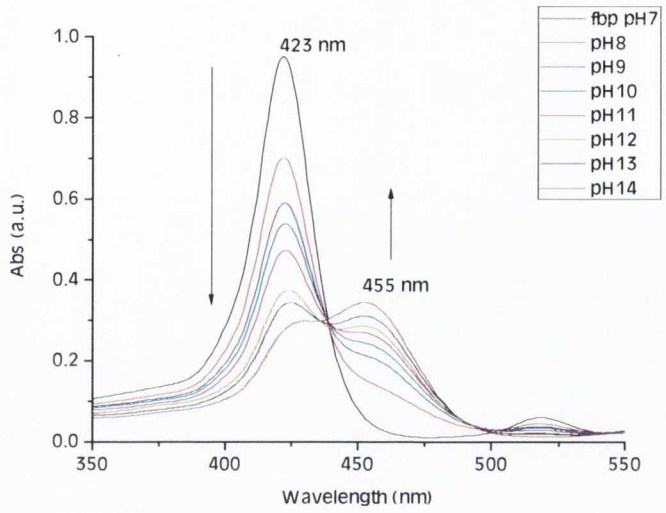

Figure 4.12: UV-vis spectra of the titration of NaOH to H_2TMPyP4 pH 7 – 14 focusing on the Soret band shift.

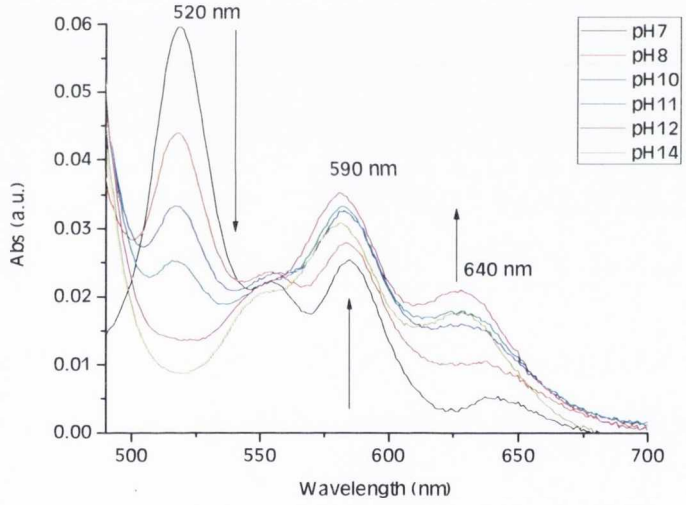

Figure 4.13: UV-vis spectra of the titration of NaOH to H_2TMPyP4 pH 7 – 14 focusing on the Q bands.

The results showed a remarkable similarity to those obtained from the addition of CdTe QDs, with a rapid decrease in the original Soret band at 423 nm, coupled with the formation of a peak at 455 nm, very close to our own result (460nm). The slight variation may result from the overlapping absorbance of our QDs, the contribution from its band edge absorption shifting this band more to the red. There were also substantial changes in the Q bands, from the initial four to only two, situated at 590 nm and 640 nm

respectively. These correlated extremely well with the results of ~ 585 nm and 640 nm obtained from our own titration with CdTe QDs, establishing that this is indeed the cause of our shifting Soret and Q bands.

To ensure that this result was not anomalous or due to the presence of remaining NaOH in solution, these H_2TMPyP4 - QD titrations were repeated three times with QDs thoroughly purified using Sephadex G25 columns, always with the same result. The effect of using QDs of different sizes was also briefly investigated. These were synthesised as before but with shorter reflux duration. As an example, the results from using 1.8 nm CdTe TGA QDs are shown in Figure 4.14.

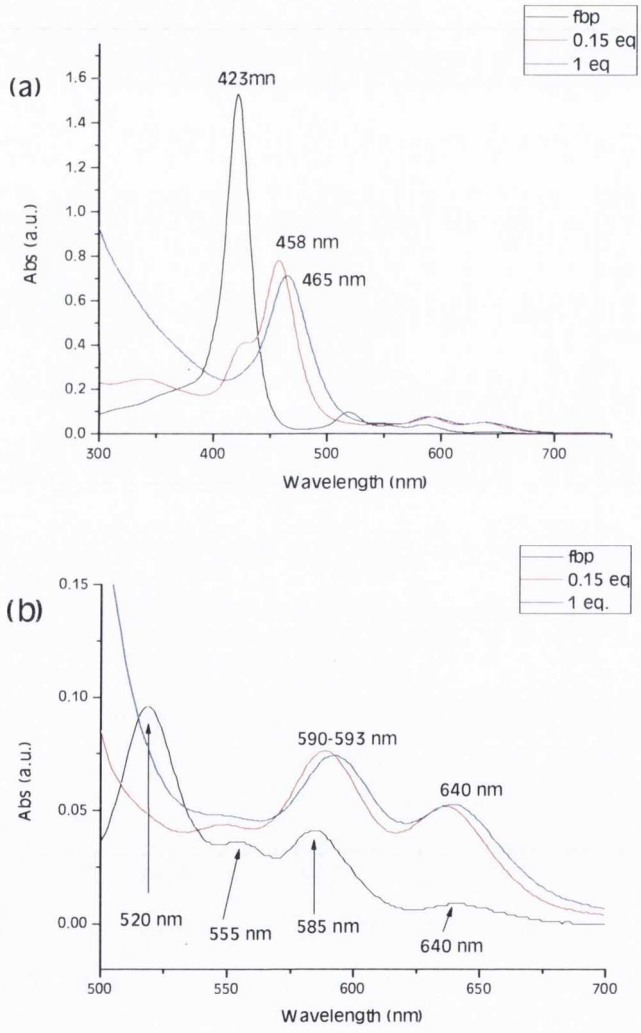

Figure 4.14: UV-vis spectra of addition of 1.8 nm CdTe TGA QDs to H_2TMPyP4 showing, (a) the shift in the Soret band and (b) the Q bands at no QDs (black), 0.15 eq. (red), and 1 eq. (blue) of QDs.

Results obtained using these smaller QDs showed no significant variation from those obtained earlier and so this size dependant investigation was not pursued further.

4.2.1.4 Interim Findings

The significance of these results are quite substantial, and not to be understated. Such TGA stabilised QDs are currently the subject of much research and scrutiny because of their potential roles in a wide range of possible applications, even in our own group, not least in biology, for example in biological imaging, drug delivery and diagnostic agents[8-11]. Thus, this aspect of these particular QDs and their readiness to deprotonate is a key factor to be aware of when designing viable QD based systems for such roles. As similar shifts in the bands were only achieved at very high pH (pH 13-14), their potential strength in acting as deprotonating agents cannot be overlooked. It must also be highlighted that deprotonation of nearly all the porphyrin in solution (measured by the degree of Soret band shift) occurs at very low equivalents of QDs (e.g. Figure 3.24 a), indicating the binding of multiple porphyrin molecules to each QD. It is postulated that electrostatic interactions draw the two species together in solution and that subsequent binding is face on, and not edge on, evidenced by the deprotonation of the central proton by the QD (Figure 4.15).

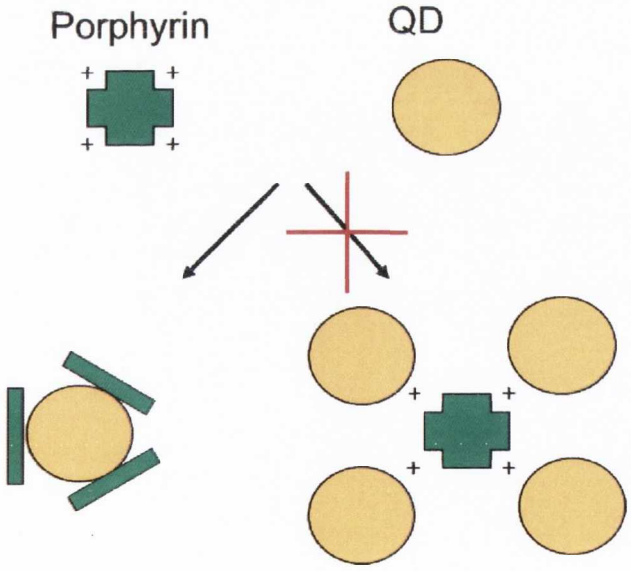

Figure 4.15: Schematic representation of binding between H_2TMPyP4 and TGA capped CdTe QDs.

4.2.2 Steady State Photoluminescence

Following on from this, fluorescence spectroscopy was used to examine this porphyrin-QD system in more detail. Again these titrations were carried out in the forward and back directions. Given the strong evidence for binding of the two species, it was expected that this would affect the emission spectra. Figure 4.16 shows the PL result from the titration of CdTe TGA QDs to H_2TMPyP4. There is an immediate decrease in the porphyrin fluorescence; with 90% quenching achieved upon the addition only 0.25 equivalents of QDs. 100% quenching is reached at approximately 0.45%. This again indicates a ground state binding interaction, and that these QDs can bind and quench multiple porphyrin molecules. The binding to porphyrin clearly also quenches the QD emission. Further addition of QDs past 0.5 equivalents results in no change and the QD luminescence is only seen to recover beyond 1 equivalent.

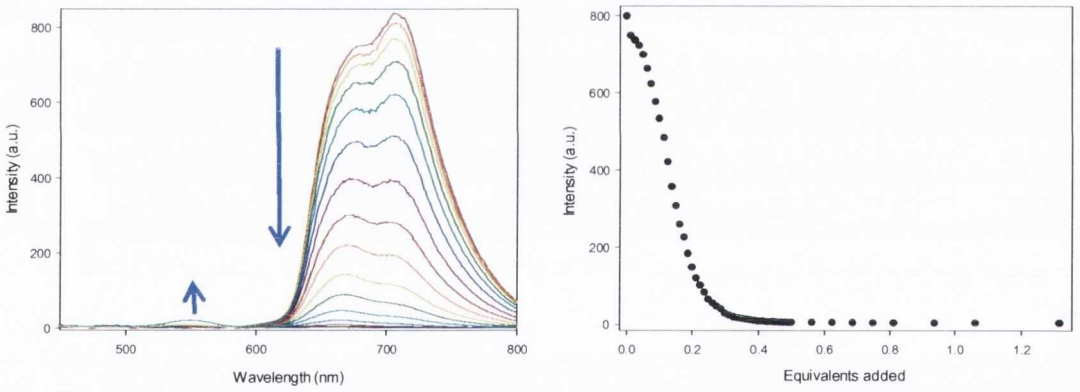

Figure 4.16: (Top) Emission spectra of the titration of CdTe TGA QDs to H_2TMPyP4 showing the quenching of the porphyrin emission and (after 1 equivalent) recovery of the QD emission. (Bottom) Change in porphyrin emission intensity at 705 nm.

The reverse titration, adding H_2TMPyP4 to CdTe TGA QDs causes rapid quenching of the QD emission, with 90% quenching from 0.3 equivalents of porphyrin and 100% at 0.5 equivalents (Figure 4.17). Porphyrin recovery is only seen after the addition of 1.5 equivalents (not shown).

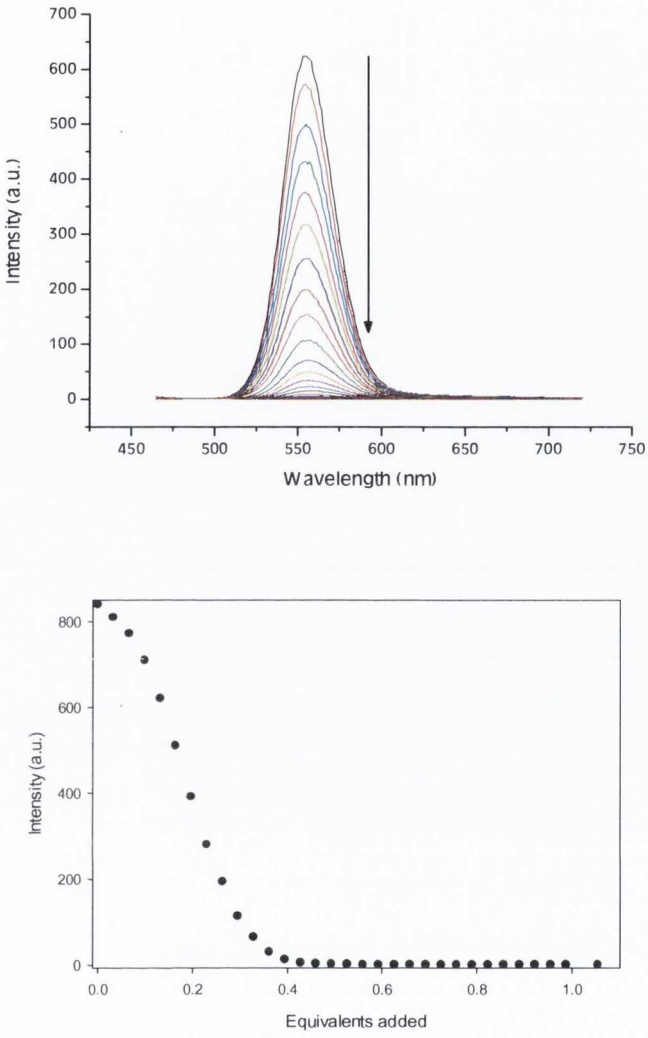

Figure 4.17: (Top) Emission spectra from the titration of H_2TMPyP4 to CdTe TGA QDs showing the quenching of the QD emission. (Bottom) Change in QD emission intensity at 555 nm.

The ratio of quenching seems almost invariant with regard to the order of addition, with 90% quenching achieved in both directions with approximately 0.3 equivalents and 100% by 0.5 equivalents. This indicates a dynamic binding equilibrium between mono-bound and multi-bound porphyrin-QDs. Also to be taken into consideration here is the fact that, the porphyrin complex, being planar, may also bind more than one QD. The system is further complicated by the dramatic shifting of the porphyrin absorption bands as a result of deprotonation. Due to these issues this system was thus not investigated further, Small Angle X-Ray Scattering (SAXS) measurements

still need to be undertaken to determine the actual nature of the bound species. The mechanism of quenching also requires further elucidation.

4.3 Zinc porphyrin Complex (ZnTMPyP4) and CdTe TGA QDs

A similar study was then undertaken with the Zn coordinated version of this porphyrin (Zn(II)-meso-tetrakis(4-N-methlypyridyl)porphyrin, ZnTMPyP4, ZnP). This does not possess two labile protons in its centre and so the deprotonation effects seen above are not expected to be present in this system. The normalised absorbance and emission spectra of ZnTMPyP4 is shown in Figure 4.18, highlighting the relative Soret (at 436 nm) and Q bands, as well as the fluorescence from the singlet state. ZnTMPyP4 is not planar, as the Zn atom sits slightly out of the porphyrin macrocycle. The metal can also be coordinated by a fifth species, usually with a solvent molecule when in solution, though this may be replaced by a carboxyl group on our QDs, facilitating binding.

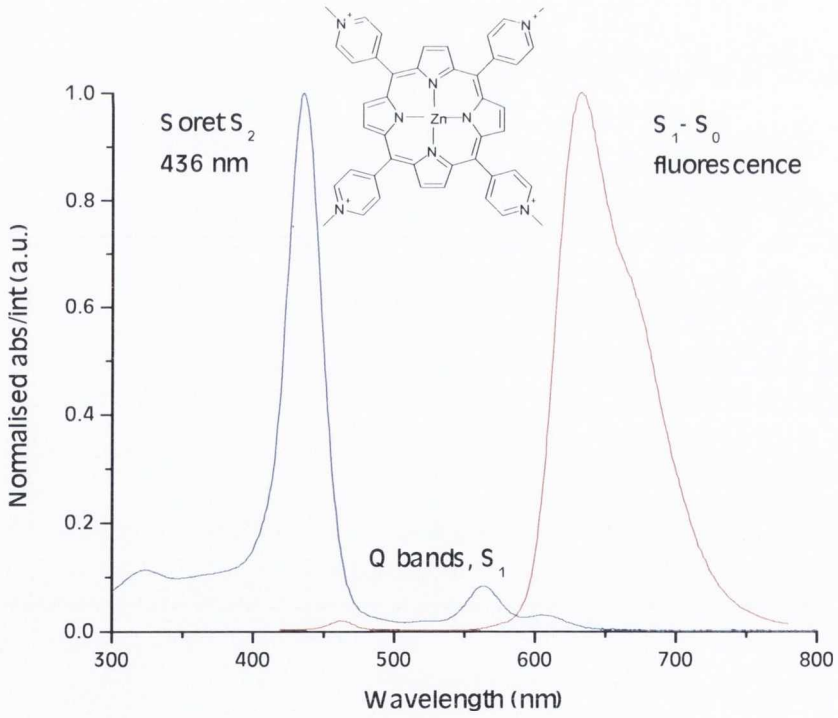

Figure 4.18: Normalised absorbance (blue) and emission (red) spectra of ZnTMPyP4 highlighting the Soret band (@ 436 nm) and Q bands, as well as the fluorescence from the singlet state.

4.3.1 Steady State Absorption Spectroscopy

The titration of CdTe QDs with ZnTMPyP4 was again monitored in the steady state using UV-vis and PL spectroscopy. Figure 4.19 shows the changing absorption spectrum of the porphyrin upon the addition of QDs.

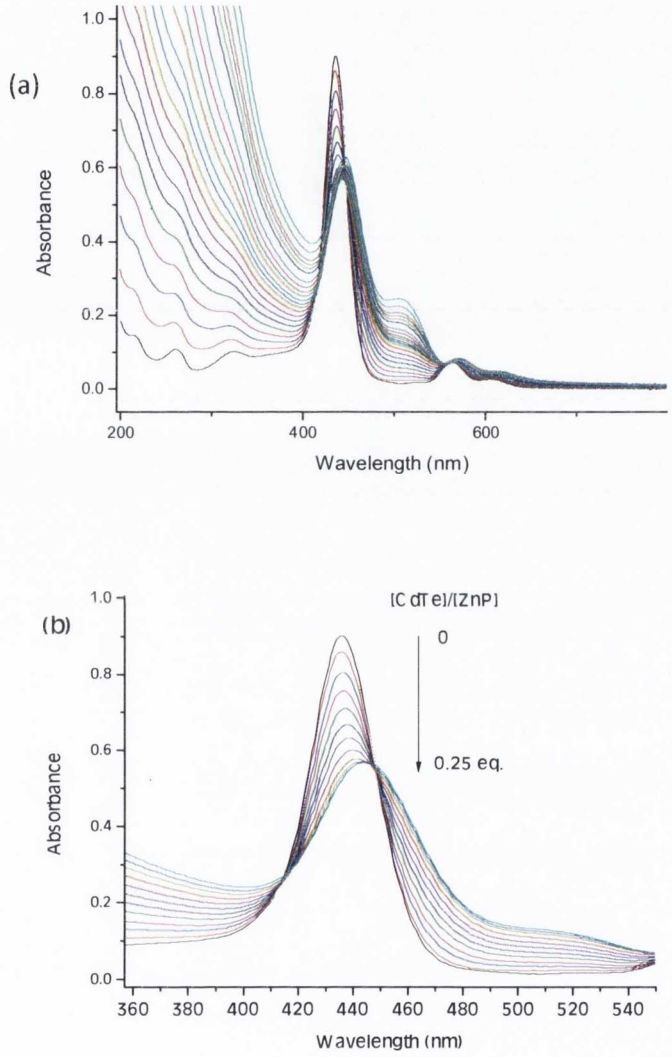

Figure 4.19: (a) UV-vis spectrum of the titration of CdTe TGA QDs to ZnTMPyP4 and (b) the Soret band shift on addition of QDs (0 - 0.25 equivalents).

It was seen that there was again strong hypochromism of the Soret band, coupled with a red shift of 8 nm. This indicates a non-covalent ground-state binding interaction with CdTe QDs. The changes in the Soret band reach a limit on the addition of 0.25 equivalents, indicating that all the porphyrin is bound to QDs at this stage.

Thus, the QDs can clearly bind more than one porphyrin and, from the limit reached at 0.25 equivalents, the ratio of bound porphyrins was estimated at four to one.

The reverse titration, in which the porphyrin is added to the QD was also studied in the steady state. As the QD absorption spectrum is less sensitive to binding interactions, the absorption plots in this case are not as informative as the previous titration (Figure 4.20).

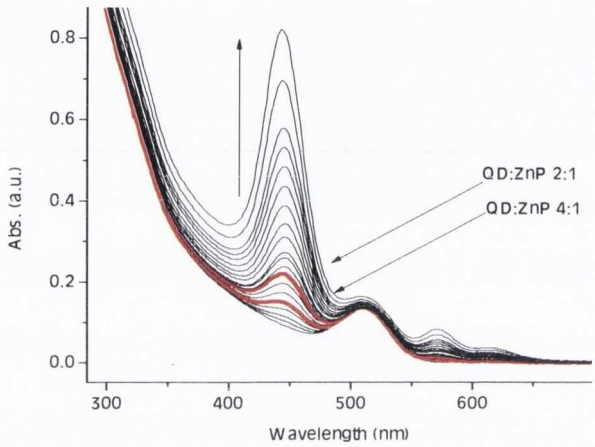

Figure 4.20: UV-vis spectrum of the titration of ZnTMPyP4 to CdTe TGA QDs.

4.3.2 Small-Angle X-ray Scattering

To clarify this simplified binding ratio and determine the actual nature of the complexes formed, small angle X-ray scattering (SAXS) measurements were carried out on this system at a range of ratios during the titration. Figure 4.21 details the results obtained for; (a) just CdTe TGA QDs, (b) CdTe:ZnP (4:1), (c) CdTe:ZnP (2:1), (d) CdTe:ZnP (1:1) and (e) CdTe:ZnP (1:2), along with suggested association schemes that best fit the data.

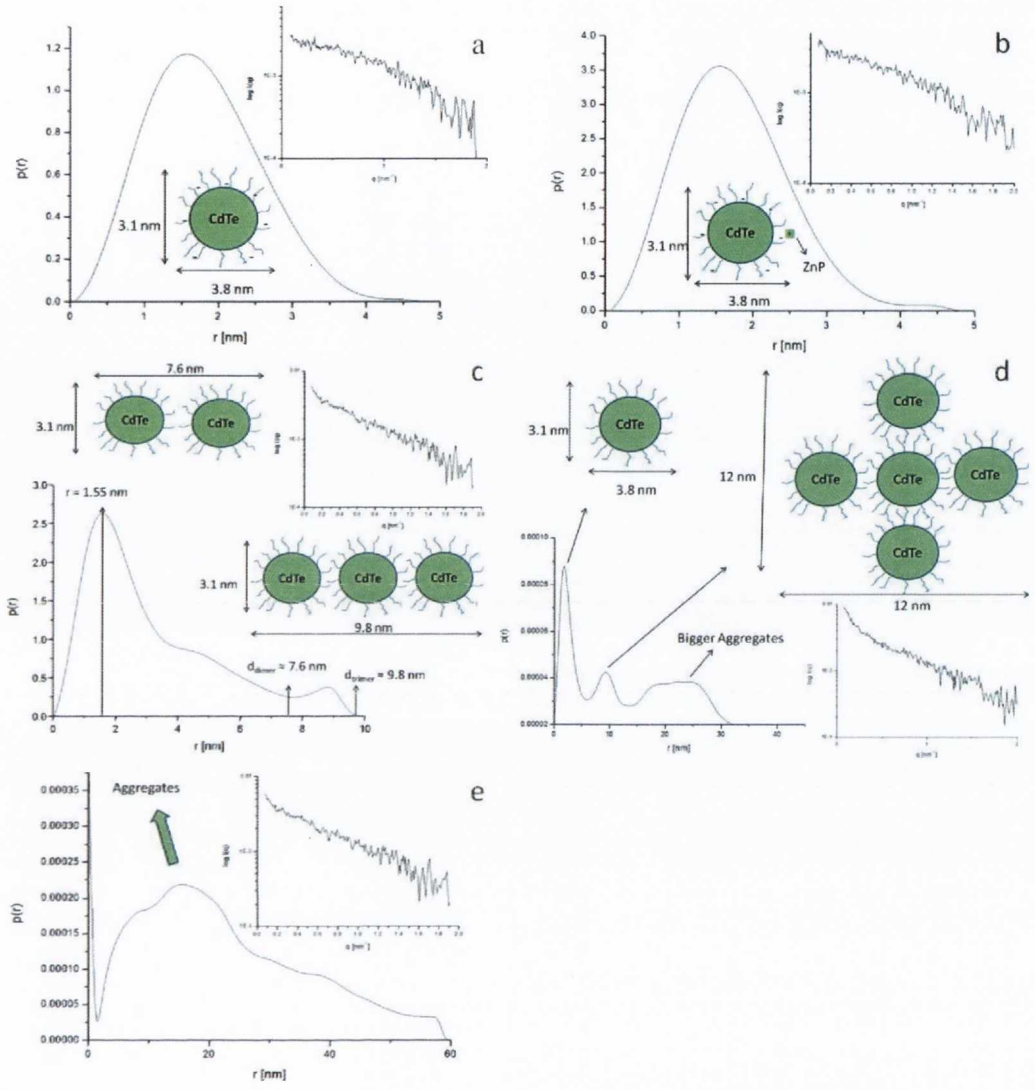

Figure 4.21: Normalized small-angle X-ray scattering (SAXS) curve and size distribution results obtained for (a) CdTe, (b) CdTe:ZnP (4:1), (c) CdTe:ZnP (2:1), (d) CdTe:ZnP (1:1) and (e) CdTe:ZnP (1:2). The CdTe illustrations at different CdTe:ZnP ratios are also shown.

The results for the pure CdTe TGA QDs (a) are as before, showing QDs of monodisperse size and a slight ellipsoid shape (3.1 x 3.8 nm). The same is observed for (b) CdTe:ZnP (4:1), when high QD ratios result in the binding of only one ZnP to a QD. At a 2:1 ratio of CdTe:ZnP (c) the formation of dimers (d = 7.6 nm) and trimers (9.8 nm) is observed, as well as the presence of monomers. A 1:1 ratio of CdTe:ZnP (d) shows that the presence of CdTe:ZnP monomers was still evident. However, the formation of some spherical aggregates (diameter ~12 nm) and other even larger higher order structures also occurs. At an excess of ZnP (1:2 ratio of CdTe:ZnP (e)) only large

aggregates are observed. This shows that the stoichiometry for binding is rarely fixed, but that a mixture of various species can exist at a given ratio.

4.3.3 Steady State Photoluminescence

The titration of QDs and ZnP was also studied in both directions using PL spectroscopy. For the addition of QDs to ZnP, quenching of the porphyrin emission occurred, followed by re-emergence of the QD emission as the concentration of QDs is increased (Figure 4.22 and 4.23).

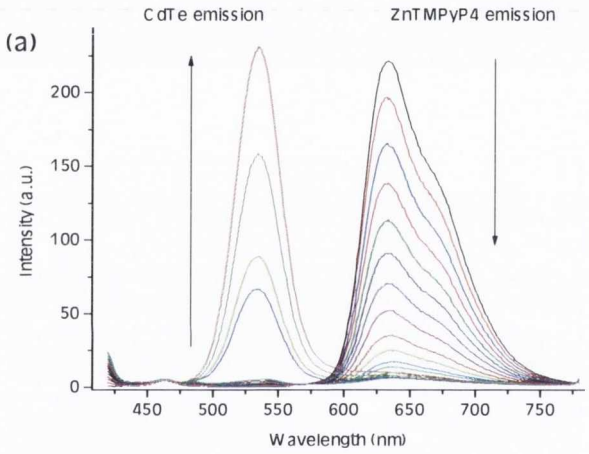

Figure 4.22: Fluorescence spectra showing quenching of ZnTMPyP4 emission and emergence of CdTe-TGA emission.

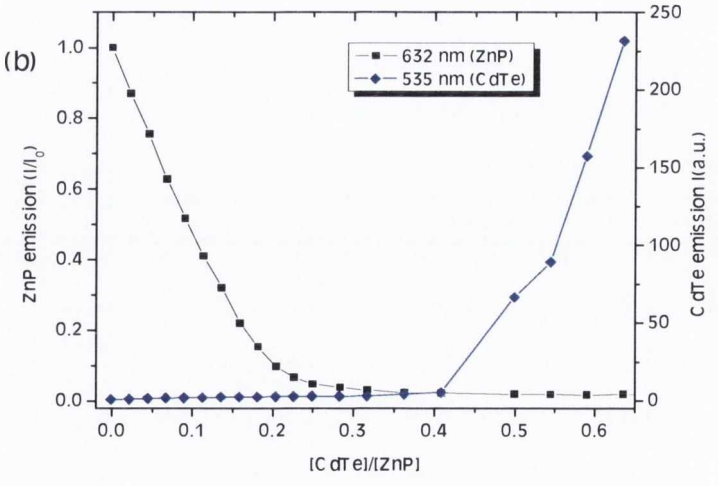

Figure 4.23: Diagram showing quenching of ZnTMPyP4 emission and emergence of CdTe-TGA emission with increasing CdTe-TGA concentration.

The fluorescence plots show how much CdTe QD is required to quench ZnP, and how much is needed to allow the unbound form of the QD (recovery of QD emission). This is important for correlating any conclusions regarding the stoichiometry of binding. The results show full quenching of the ZnP emission occurring at 0.25 equivalents, correlating well with the obtained earlier from the UV-vis data and the SAXS measurements.

In the reverse direction, efficient quenching is again observed, although full quenching of the QD emission is only achieved at higher equivalents of ZnP (Figure 4.24). However, Poisson statistics decree that maximum quenching should not be achieved at equal concentrations, if the association is 1:1. Therefore we can say that the presence of a porphyrin can result in the quenching of more than one QD.

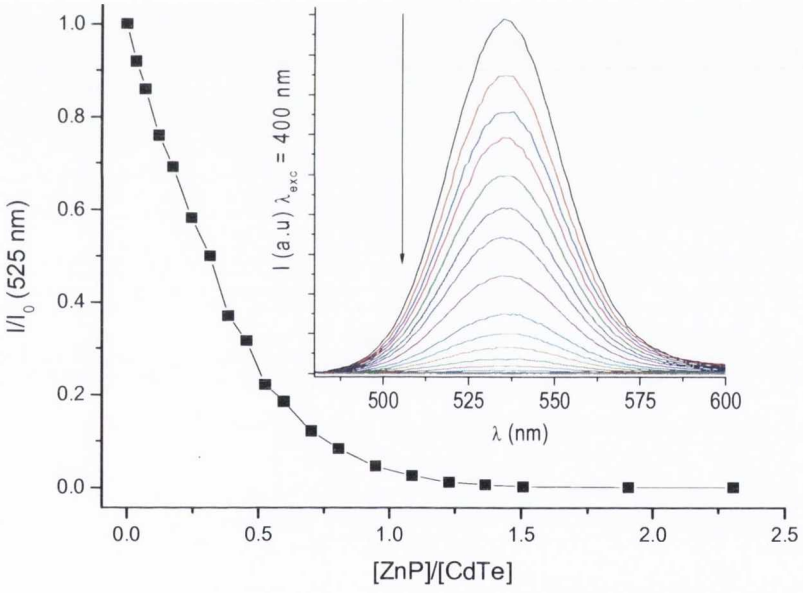

Figure 4.24: Quenching of CdTe emission at increasing ZnTMPyP4 conc.
Inset: Corresponding emission spectra of CdTe-TGA.

It can be seen that the fluorescence of both species is quenched by the addition of the other. Quenching is a competing mechanism of deactivation. Possible explanations for this may be a heavy atom effect e.g. caused by Cd or Te, or electron transfer (ET) from the QD to the porphyrin.

The heavy atom effect is the enhancement of the rate of a spin-forbidden process by the presence of an atom of high atomic number, which is either part of, or external to, the excited molecular entity. The heavy-atom effect has been invoked to explain both luminescence enhancement[12,13], and quenching[14-16]. A heavy atom effect from Cd on the porphyrin would result in an increase in the rate of S1-T1 intersystem crossing (increasing the triplet yield from 90 % to ~100%). This would mean that no fluorescence from S1-S0 would be observed because all of the S1 state is crossing over to T1. Figure 4.25 outlines this possible scenario.

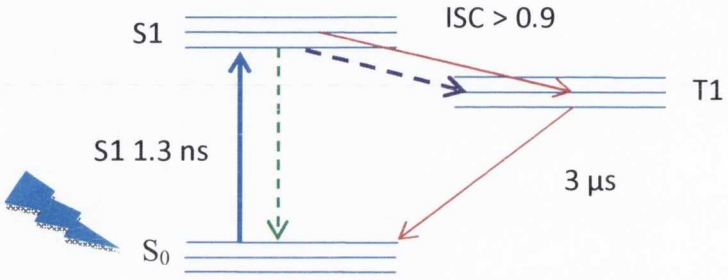

Figure 4.25: Diagram of the excitation and relaxation of ZnP. Purple arrow denotes heavy atom effect, resulting in increased yield of the triplet state.

Another possibility is electron transfer from the CdTe TGA QD to the porphyrin, after the creation of an exciton in the QD following excitation (Figure 4.26). This has been shown to be thermodynamically feasible, at least in the case of the free base[17].

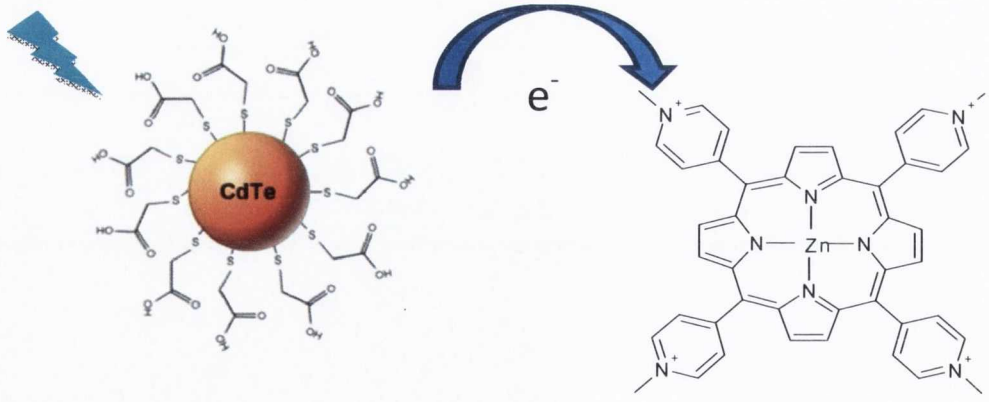

Figure 4.26: Scheme illustrating electron transfer from CdTe QD to ZnP after excitation.

4.3.4 Transient Absorption Spectroscopy Studies

In order to try to elucidate the possible mechanism of quenching, transient absorption (TA) spectroscopy was carried out on this system. This should show the absorption of excited states and intermediates – and how they change with time.

Nanosecond flash photolysis measurements were carried out on the free porphyrin, and the ratio of 2:1 CdTe QD – ZnP examined earlier (Figure 4.27 and 4.28). The free QDs, shown previously (Chapter 3, Figure 3.10), do not have a long lived signal on this timescale (i.e. >~30 ns).

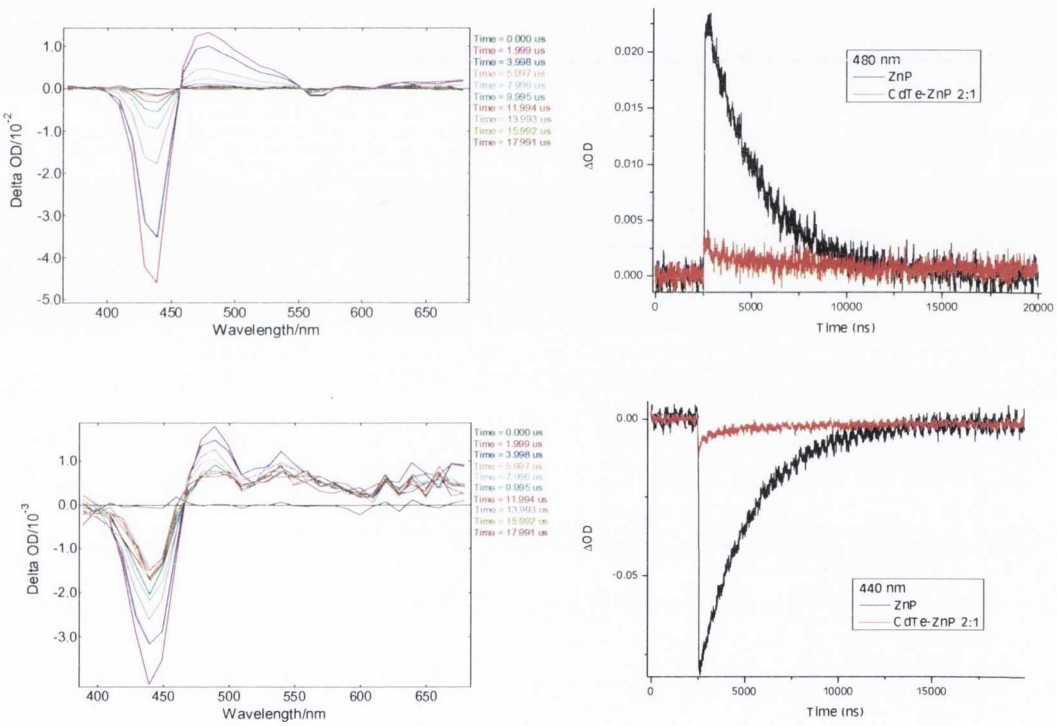

Figure 4.27: Nanosecond TA spectra of ZnP (top right) and CdTe:ZnP 2:1 (bottom right). Porphyrin conc. is the same in both cases. Also shown is the comparison of the bleach and transient intensities in the absence (top left) and presence (bottom left) of CdTe. Pump wavelength @ 355 nm.

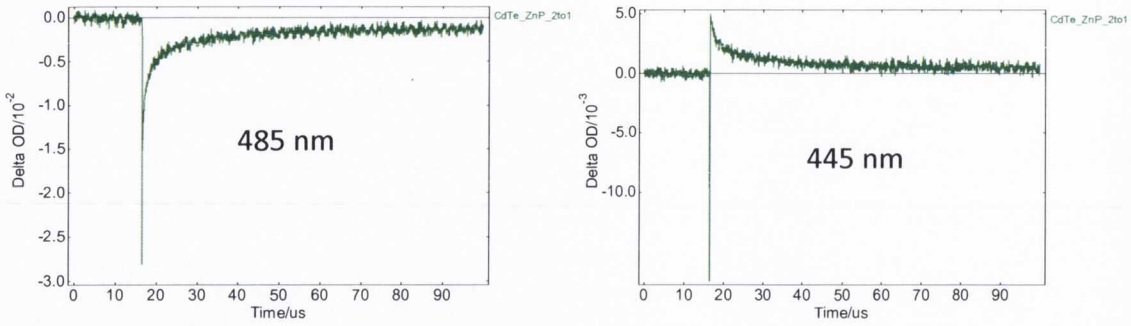

Figure 4.28: The decays measured over long times showing (left) slow decay of the transient at 485 nm and (right) slow bleach recovery of ZnP in the presence of CdTe, 2:1 (triplet lifetime of free ZnP is 3 μs).

Nanosecond flash photolysis of the free ZnP shows a bleach band at approximately 445 nm, correlating well with the absorption spectrum. Transient features are visible above 470 nm, corresponding to the triplet state, as shown by the long decay lifetime (~3 μs, Figure 4.27). Comparison of this with the results obtained in the presence of QDs (CdTe:ZnP 2:1) shows that the yield of the porphyrin excited state and bleaching is significantly lower compared to free ZnP. This possibly indicates a very fast initial decay/recovery occurring within the laser pulse. It may be indicative of efficient quenching of the ZnP singlet state, and subsequent lower yields of the triplet state. It is also possible that the triplet is formed via a porphyrin radical. Interestingly, both the triplet state, and bleach recovery, seem longer lived in CdTe:ZnP than in free ZnP. A similar observation with a zinc phthalocyanine has been reported, where it is believed energy transfer is occurring[18].

Ultrafast picosecond-transient spectroscopy was carried out on the unbound CdTe TGA QDs and Zn porphyrin, along with the 2:1 QD:ZnP ratio examined earlier. Figure 4.29 shows the transient absorption spectra of the free CdTe TGA QDs.

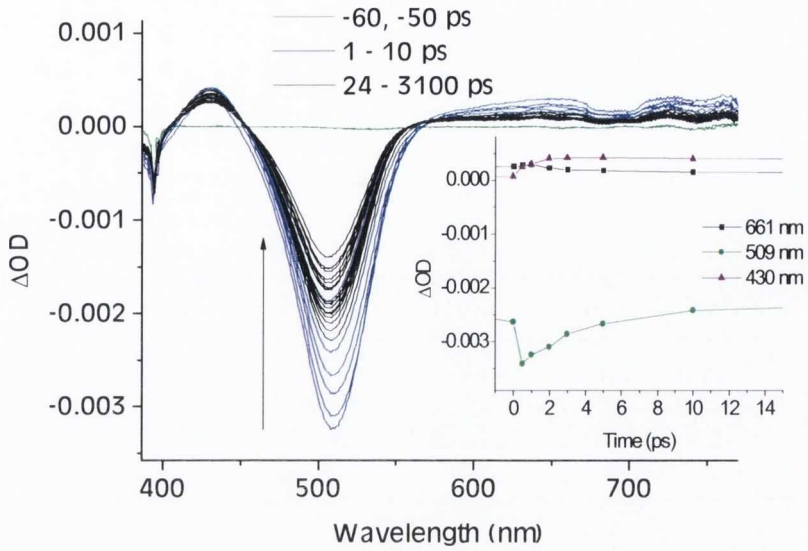

Figure 4.29: Transient absorption spectra of CdTe TGA with (inset) kinetic profiles over the first 15 ps. Pump wavelength @ 400 nm.

The QDs show a strong bleach band in the region of 513 nm, corresponding to their band edge absorption, and transient absorption at lower energies. The formation of this bleach occurs rapidly (within the response of the machine) as shown in Figure 4.30.

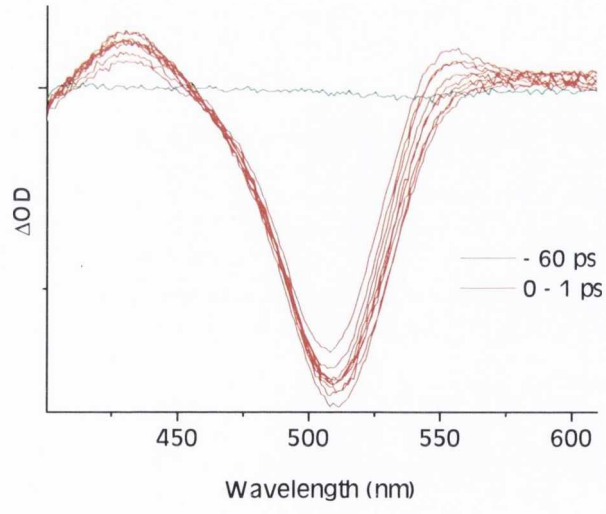

Figure 4.30: Transient absorption spectra of CdTe TGA over the first 1 ps. Pump wavelength @ 400 nm.

The bleach was found to decay biexponentially from ~ 1 ps to > 1 ns, with concurrent decay of the transient, indicating that these represent the same process.

The TA of free ZnP is shown below in Figure 4.31.

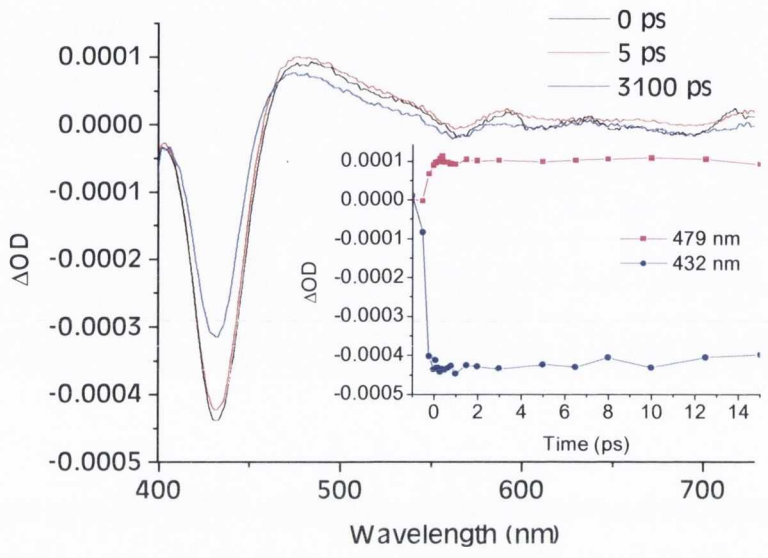

Figure 4.31: Transient absorption spectra of ZnP with (inset) kinetic profiles over the first 15 ps. Pump wavelength @ 400 nm.

Again, almost instantaneous bleaching occurs in the region of the Soret band (436 nm). The obvious transient around 480 nm initially represents the ZnP singlet state (τ = 1.3 ns) which is rapidly formed, followed by conversion to long-lived triplet (Φ_{ISC} ~ 90 %, τT = 3 μs). The singlet and triplet states of porphyrins have very similar transient spectra. The initial transient (red) is the S1 state, and over ca. 1 ns this gives way to the T1 state (blue).

The TA spectra were then obtained of the CdTe:ZnP (2:1) system (Figure 4.32).

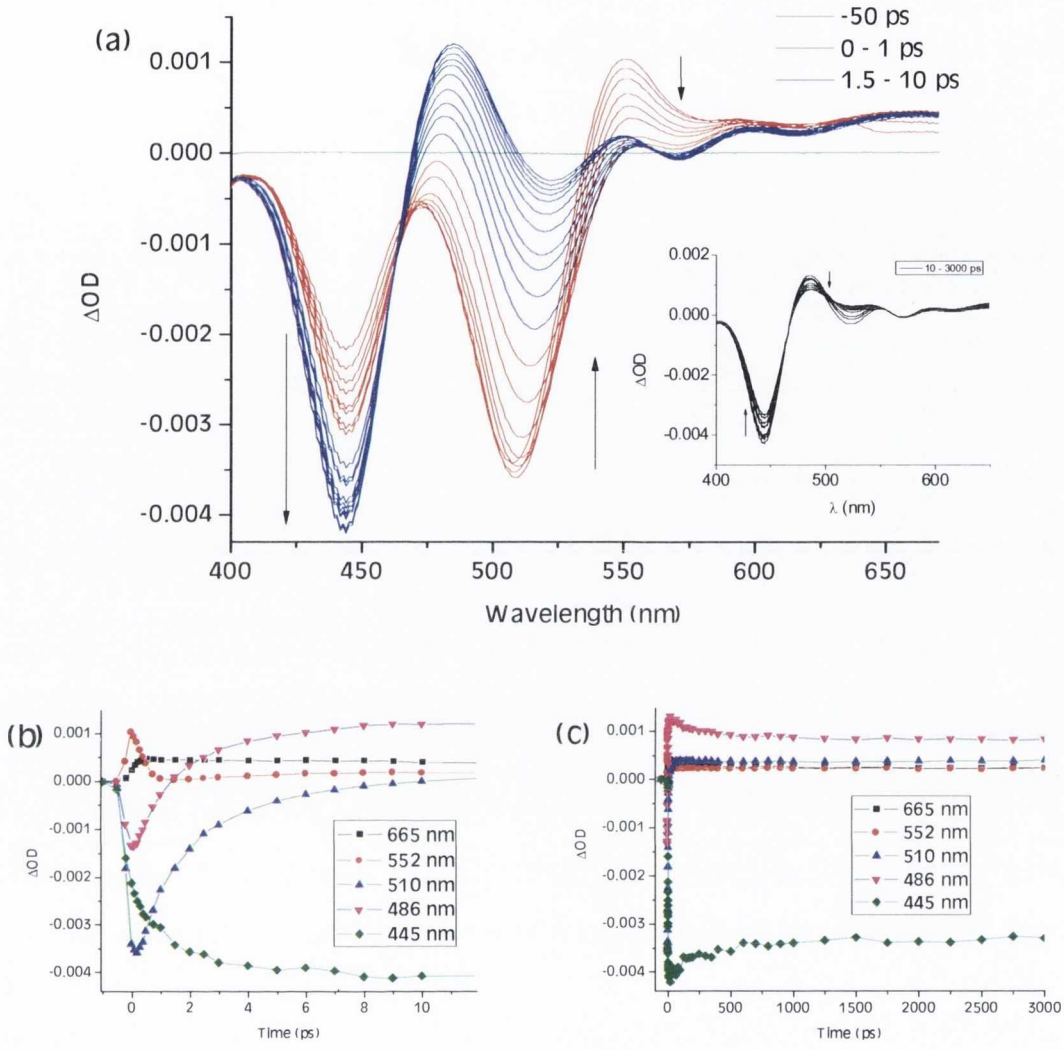

Figure 4.32: (a) ps-TA spectrum of 2:1 CdTe-TGA:ZnTMPyP4 up to 10 ps after pump pulse. Inset: spectra at longer time delays up to 3 ns. (b) Kinetics at short times. (c) Kinetics at longer times.

The results obtained from the kinetic analysis showed that much of the QD-ZnP decay remained unchanged from those of their individual counterparts, as there was a lot of unbound CdTe QD at this ratio. There was however an obvious slowing of the porphyrin bleach growth in the presence of the QDs (Figure 4.32 (a)), unlike the instantaneous bleach formation seen previously in the ZnP only situation. Focusing on the bleach decays of the Zn porphyrin and the CdTe QDs, at 445 nm and 510 nm respectively (Figure 4.32 (b), green and blue), there is a clear correlation between the

slow grow-in of the ZnP bleach, observed over 10 ps, and the decay of the QD bleach over the same time period. Comparison of their kinetics is shown in Figure 4.33.

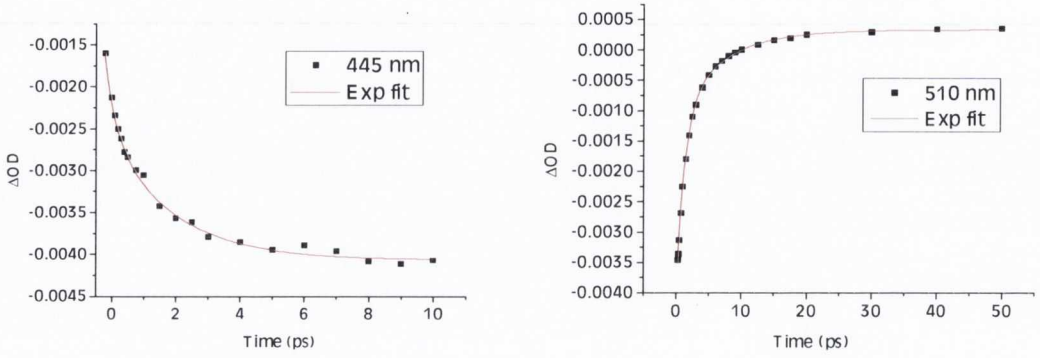

Figure 4.33: Comparison of the ZnP and QD decays at 445 nm and 510 nm respectively.

The 'twinned' evolution of the slow grow-in of the porphyrin bleach and the QD bleach decay (i.e. the fact that porphyrin grows in as the QD recovers) observed over 10 ps in the TA indicated a sensitised process occurring, such as electron transfer. The features seen at longer times (Figure 4.32 (c)) are associated with the porphyrin 'triplet' at 485 nm and the very short feature at 550 nm is associated with the CdTe QD, as it is present in the QD only spectra (Figure 4.29, 4.30). It has previously been reported as a metastable state[19] and seems to be coupled to the bleaching on the blue edge of the exciton bleach, correlating with the transient decay recorded at 510 nm. The cause of such a band may be intraband relaxation or the result of carrier-induced Stark effects[20]

The overall result obtained from the TA indicated that there appears to be a picosecond timescale sensitised process. The presence of the QD prevents ZnP ground-state absorption and instead, ZnP bleach is a result of QD decay, strongly indicating an electron transfer process from the excited QD state to the porphyrin. Figure 4.34 illustrates one possible photophysical scheme. The QD absorbs the light, generating an exciton. The photogenerated electron is transferred to the ZnP S_1 excited state, resulting in a porphyrin radical anion. The electron then populates the triplet excited state which then decays slowly in a non-radiative fashion. Reverse ET may occur from the ZnP S_0 ground state to the QD as the triplet state is populated.

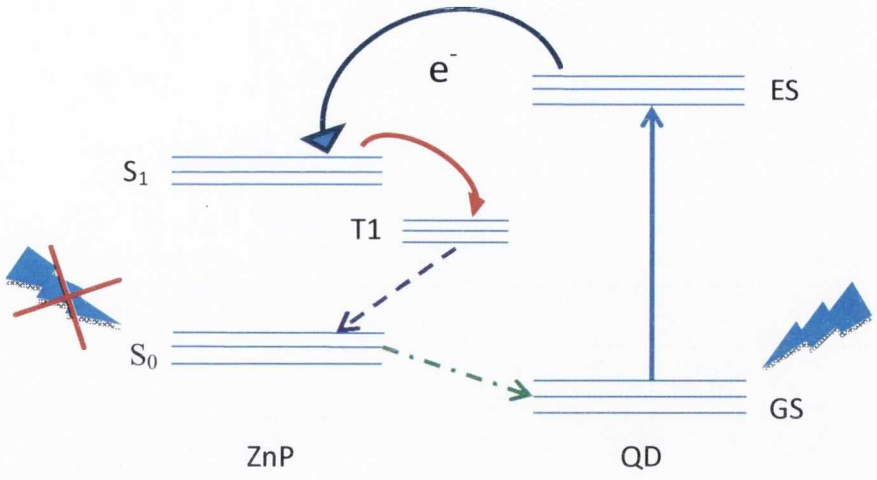

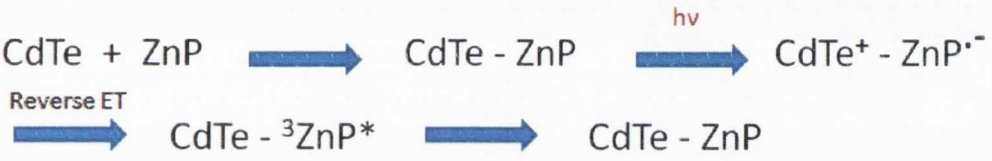

Figure 4.34: Diagram and scheme of possible electron transfer and quenching mechanism.

Interestingly, a number of TA studies on TMPy porphyrins in photo-induced electron transfer systems have failed to observe any reduced porphyrin. This suggests that there may be an intrinsically rapid reverse ET with these porphyrins[21,22].

The exact mechanism of the quenching seen in this system is however very difficult to determine. Two issues complicating the analysis of the TA results are;

1) There is substantial overlap of the signals from the two species, e.g. the ZnP triplet and the QD bleach, at 485 nm and 510 nm respectively. This makes separation of the data and determination of the respective kinetics difficult.

2) Both the QDs and the ZnP absorb at the laser excitation wavelength of 400 nm, and while the absorption of the QDs is much greater, ZnP absorption cannot simply be ruled out. This makes it hard to separate out the resulting spectroscopic features obtained.

Thus, further detailed analysis and spectroscopic studies, such as investigation of the lifetimes of these bound species, is essential.

4.4 Platinum Porphyrin Complex and CdTe TGA QDs

Similar work was also carried out on the platinum coordinated version of our porphyrin (PtTMPyP4). The normalised absorbance and emission spectra is shown in Figure 4.35, highlighting the Soret band (at 405 nm) and two Q bands, as well as the phosphorescence from the triplet state.

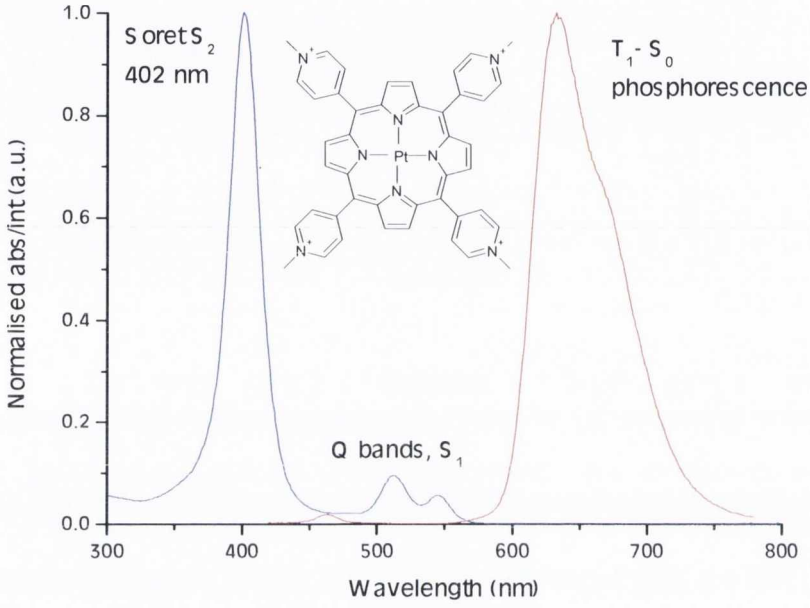

Figure 4.35: Normalised absorbance (blue) and emission (red) spectra of PtTMPyP4 highlighting the Soret band (@ 402 nm) and two Q bands, as well as the phosphorescence from the triplet state.

4.4.1 Steady State Absorption Spectroscopy

These titrations were again carried out in both directions. The steady state absorption results of the titrations are displayed in Figure 4.36.

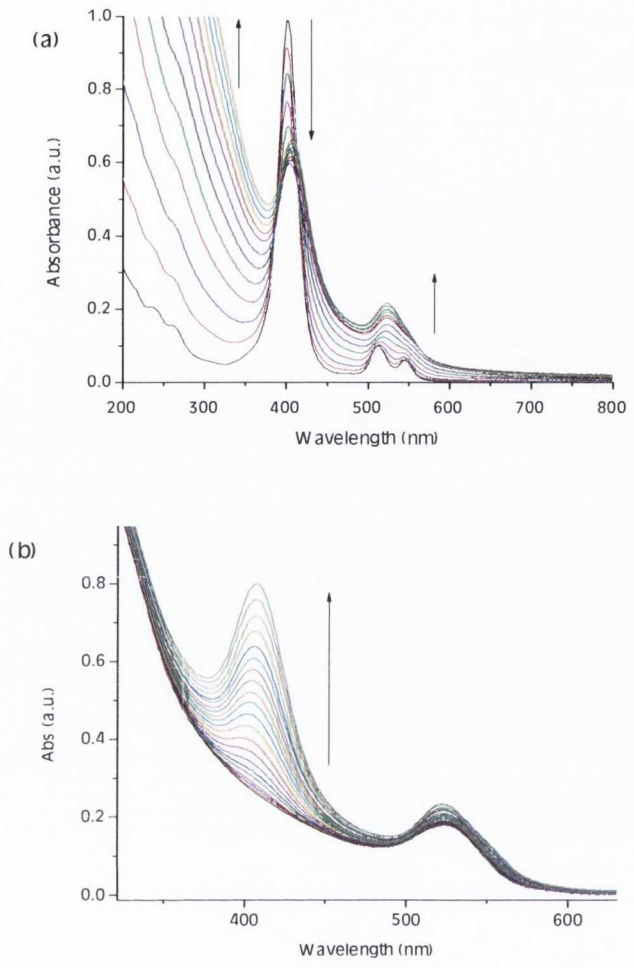

Figure 4.36: UV-vis spectrum of the titration of (a) CdTe TGA QDs to PtP, and (b) PtP to CdTe TGA QDs.

It can clearly be seen that there is an absence of a large red shift in the Soret band, helping to corroborate our position that this was the result of deprotonation of the free-base. There is still substantial hypochromism however, coupled with a red shift of 5 nm, indicating the presence of a ground state binding interaction between our QDs and the porphyrin. The hypochromism of the Soret band reaches a minimum with the addition of 0.25 equivalents of QDs and does not change upon further subsequent additions, indicating that all the PtP is bound at this stage. This infers a rough coordination number of four porphyrin molecules to one QD, although SAXS measurements have previously shown in the case of the Zn-porphyrin, that this is a simplification of a much more complicated system, with higher order structures also present (Figure 4.21).

4.4.2 Steady State Photoluminescence

PL monitoring of the titrations showed again quenching of both species in solution. However, with the forward titration (QDs to PtP, Figure 4.37) recovery of the QD emission was substantially quicker than before, occurring after 0.25 equivalents, indicating that there are unbound QDs in solution after this point. This may indicate that the PtP is more tightly bound than its Zn and free-base counterparts, which showed QD recovery only at higher ratios.

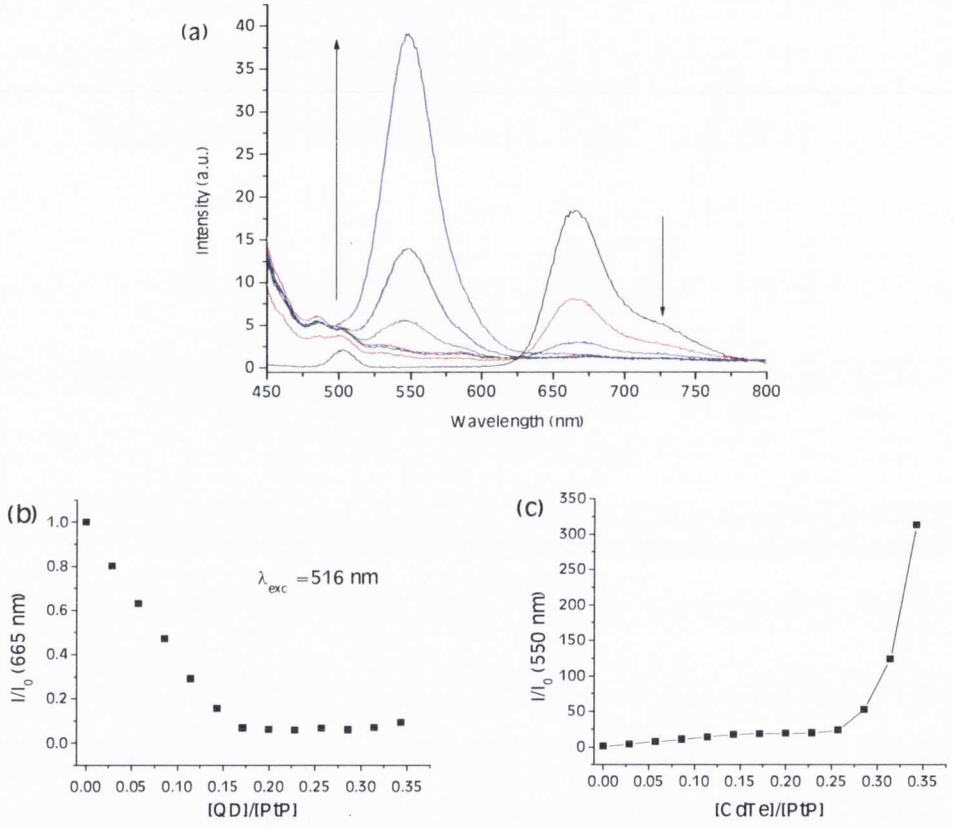

Figure 4.37: (a) Emission spectrum of the titration of CdTe TGA QDs to PtP. (b) Quenching of PtP and (c) recovery of QD emission.

The reverse titration, studying the effect of addition of PtP to QDs was also carried out (Figure 4.38). Similarly to the previous results, the QDs show remarkable resistance to quenching from the PtP, with 2 equivalents of porphyrin needed to achieve 100% quenching.

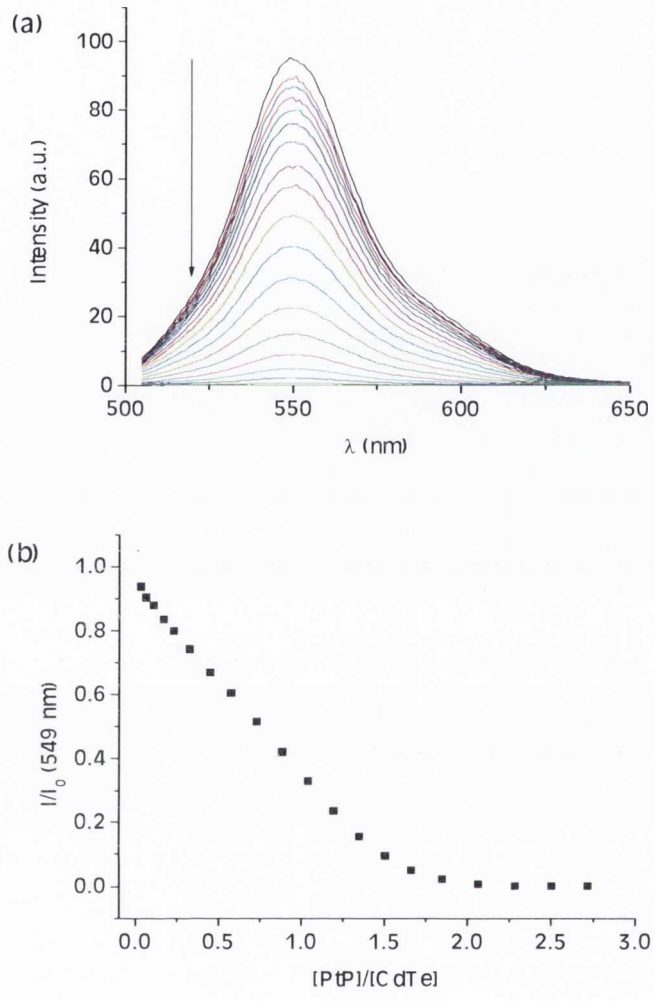

Figure 4.38: (a) Emission spectrum of the titration of PtP to CdTe TGA QDs. (b) Quenching of QD emission.

Investigation of the above PtP-QD system using ultrafast transient spectroscopy was not carried out as it was deemed unsuitable given the position of the PtP Soret band at 402 nm. This overlaps strongly with the 400 nm excitation wavelength of the laser pulse, which would result in masking the contributing signals from CdTe QDs, making the system even more difficult to analyse.

4.5 Conclusions

Thus in this work we have investigated the systems based on CdTe TGA QDs and three separate porphyrin molecules, using a range of steady state and time resolved techniques.

We have found that in the case of the free-base porphyrin, H_2TMPyP4, addition of the QDs resulted in strong hypochromism and a dramatic red-shifting of the porphyrin Soret band, coupled with a reduction in the number of Q bands. Quenching of both the porphyrin and the QD emission occurred on the addition of these two species together, indicating that binding was occurring. However, unfortunately there was no evidence for sensitised emission. A rough coordination ratio that one QD can bind approximately four porphyrin molecules was determined from the steady state measurements. Several tests elucidated that the Soret band shift was due to deprotonation of a central proton in the porphyrin macrocycle, caused by the COO^- groups of the TGA. It was thus inadvertently discovered that these QDs can act as strong deprotonating agents, a key finding if these QDs are to be used in future systems.

The system of CdTe TGA QDs and ZnTMPyP4 porphyrin was studied in depth. Binding was again inferred from the steady state absorption measurements, and coordination numbers were again estimated to be approximately four porphyrins to one QD. Using small-angle X-ray scattering, this was shown to be an oversimplification of a much more complex system, with multiple binding variations and higher order structures shown to exist at a range of QD:ZnP ratios. It was demonstrated that sensitised emission again did not occur, with quenching of both emissions evident. The mechanism of quenching was then studied using ultrafast ps-transient absorption spectroscopy, and it was demonstrated that the presence of the QD prevents ZnP ground state binding. Instead, ZnP excitation and bleach growth was a function of QD decay, with comparable kinetics highlighting the dependence of the former on the latter. This appears to indicate an electron transfer process from the QD to the porphyrin, which then decays slowly through the triplet state in a non-radiative fashion. However further work is necessary to unambiguously elucidate if this is the case.

Studies of these QDs and the platinum porphyrin, PtTMPyP4, showed similar results to those found earlier. Quenching of emission of both was seen, as was the binding ratio of four to one.

Future work in this area would involve studies both of the free-base-QD and PtP-QD systems using transient absorption, in an attempt to further determine the mechanism of emission quenching and corroborate the findings from our work with QD-ZnP. As has been shown, the electron transfer process here is highly efficient, and these conjugate systems may potentially be used for charge separation in light harvesting devices for solar technology.

References

(1) Fery-Forgues, S.; Lavabre, D. *Journal of Chemical Education* **1999**, *76*, 1260.

(2) Yu, W. W.; Qu, L.; Guo, W.; Peng, X. *Chemistry of Materials* **2003**, *15*, 2854.

(3) Zhang, H.; Zhou, Z.; Yang, B.; Gao, M. *The Journal of Physical Chemistry B* **2002**, *107*, 8.

(4) Kalyanasundaram, K. *Photochemistry of polypyridine and porphyrin complexes*; Academic Press: London; San Diego, 1992.

(5) P. Hambright, P.; Fleischer, E. B. *Inorg. Chem.* **1970**, *9*, 1757.

(6) Kruk, N. N. *Journal of Applied Spectroscopy* **2006**, *73*, 686.

(7) Honda, T.; Nakanishi, T.; Ohkubo, K.; Kojima, T.; Fukuzumi, S. *J. Am. Chem. Soc.* **2010**, *132*, 10155.

(8) Conroy, J.; Byrne, S. J.; Gun'ko, Y. K.; Rakovich, Y. P.; Donegan, J. F.; Davies, A.; Kelleher, D.; Volkov, Y. *Small* **2008**, *4*, 2006.

(9) Byrne, S. J.; le Bon, B.; Corr, S. A.; Stefanko, M.; O'Connor, C.; Gun'ko, Y. K.; Rakovich, Y. P.; Donegan, J. F.; Williams, Y.; Volkov, Y.; Evans, P. *ChemMedChem* **2007**, *2*, 183.

(10) Byrne, S. J.; Corr, S. A.; Rakovich, T. Y.; Gun'ko, Y. K.; Rakovich, Y. P.; Donegan, J. F.; Mitchell, S.; Volkov, Y. *Journal of Materials Chemistry* **2006**, *16*, 2896.

(11) Gerard, V.; Maguire, C. M.; Bazou, D.; Gun'ko, Y. K. *Journal of Nanobiotechnology* **2011**, *9*.

(12) Wirz, D. R.; Wilson, D. L.; Schenk, G. H. *Analytical Chemistry* **1974**, *46*, 896.

(13) White, W.; Seybold, P. G. *The Journal of Physical Chemistry* **1977**, *81*, 2035.

(14) Hofeldt, R. H.; Sahai, R.; Lin, S. H. *The Journal of Chemical Physics* **1970**, *53*, 4512.

(15) Sahai, R.; Hofeldt, R. H.; Lin, S. H. *Transactions of the Faraday Society* **1971**, *67*, 1690.

(16) Tomita, G.; Kim, S. S. *Nature* **1965**, *207*, 975.

(17) Jhonsi, M. A.; Renganathan, R. *Journal of Colloid and Interface Science* **2010**, *344*, 596.

(18) Moeno, S.; Idowu, M.; Nyokong, T. *Inorganica Chimica Acta* **2008**, *361*, 2950.

(19) Guldi, D. M.; Rahman, G. M. A.; Sgobba, V.; Kotov, N. A.; Bonifazi, D.; Prato, M. *Journal of the American Chemical Society* **2006**, *128*, 2315.

(20) Kobayashi, Y.; Pan, L.; Tamai, N. *The Journal of Physical Chemistry C* **2009**, *113*, 11783.

(21) Chirvony, V. S.; Galievsky, V. A.; Kruk, N. N.; Dzhagarov, B. M.; Turpin, P.-Y. *Journal of Photochemistry and Photobiology B: Biology* **1997**, *40*, 154.

(22) Steenkeste, K.; Tfibel, F.; Perrée-Fauvet, M.; Briandet, R.; Fontaine-Aupart, M.-P. *The Journal of Physical Chemistry A* **2010**, *114*, 3334.

Chapter 5: Synthesis and Characterisation of New Chiral QDs

5.1 Introduction

Chirality is a common occurrence in the natural world and chiral compounds are very important in chemistry, biology, pharmacology and medicine. It has also been envisaged that chirality could play an important role in nanotechnology[1,2]. The majority of existing research in this field has been focused on chiral organic, metallorganic and biological molecules and their supramolecular structures[3], while research in the area of chiral inorganic nanoparticles is still in the very early stage of its development. For example, there has been some work involving chiral optically active metallic gold[4,5] and silver[6,7] nanoparticles, as well as carbon nanotubes[8,9]. However, there are currently only a few papers dealing with chiral light emitting semiconducting nanocrystals (quantum dots)[10-14].

In general over the last decade much attention has been directed towards II-VI type CdS, CdTe and CdSe quantum dots (QDs)[15-19]. It is the ability to fine tune their optical properties by chemical control of their size and shape (i.e. their degree of quantum confinement) which makes quantum dots particularly interesting. This level of optical control combined with QDs resistance to photobleaching and their high level of solubility in practically any solvent (depending on the stabiliser used) makes these nanomaterials potentially suited for roles as divergent as light emitting diodes[20], biological sensors[21] and photovoltaic devices[22-24]. Amino acids containing thiol groups have proven to be excellent stabilisers, with *L*-cysteine becoming one of the popular surface capping molecules for CdX (X = S, Se, Te) nanoparticles[18,25-31]. In addition this use of stereospecific chiral stabilising molecules opened another avenue of interest in the area of quantum dot research, as chirality is a key factor in biological and biochemical interactions. Due to their unique photophysical properties, we believe that chiral QDs have a range of potential applications in photonics and biochemistry[13,32,33].

The main aim of this part of our work is to develop novel chiral CdSe based QDs by using chiral stabilisers and to investigate the properties of these materials. Here

we report the synthesis and detailed spectroscopic studies of new penicillamine stabilised CdSe QDs, which have been prepared using the dextrorotary (*D*-), levorotary (*L*-) enantiomers, as well as the racemate (*Rac*-) of the amino acid. This research also involved in-depth spectroscopic study of their unique optical and luminescent properties to understand the fundamental principles influencing the structure and properties of chiral QDs. This work was then expanded to develop new CdSe and CdTe QDs stabilised with *D*-, *L*- and *Rac*- cysteine (2-amino-3-mercaptopropionic acid).

5.2 Synthesis of Chiral Penicillamine Stabilised CdSe QDs

A schematic description of the preparation of CdSe nanoparticles is shown in Figure 5.1. The preparation of CdSe quantum dots was carried out similarly to penicillamine (Pen)-stabilised CdS quantum dots[10], which is itself a variation of a previous method[34], substituting Na_2SeSO_3 for CH_3CSNH_2[35,36]. Na_2SeSO_3 was prepared by the method reported and used immediately[37]. All reactions were carried out under an atmosphere of argon, as the selenium precursor is air sensitive.

For the synthesis of these chiral QDs, microwave irradiation was used instead of heating under reflux. The benefits of this method over refluxing are numerous. The energy is deposited directly into the reaction mixture and not the surrounding vessel, which leads to rapid uniform heating throughout the sample and avoids localised hotspots that cause byproducts and decomposition products (Figure 5.1). This also results in greatly reduced reaction times, as well as the potential for scalability[38].

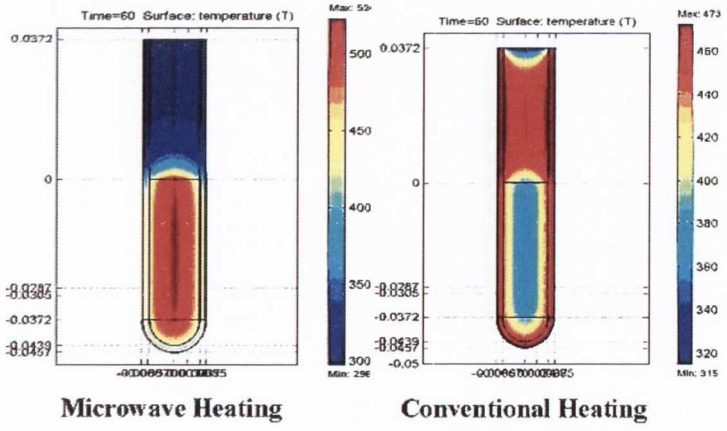

Figure 5.1: Illustration comparing heating using microwave irradiation (left) and reflux (right). Adapted from[39].

The advantage of this technique here is that, being initiated by microwave irradiation, decomposition of the precursors results in the fast and uniform formation of ions in the solution, which promotes the simultaneous creation of numerous nucleation centres and, therefore, the formation of particles with a relatively narrow size distribution[40]. Briefly, the penicillamine, cadmium and selenium precursors were mixed together under argon in deoxygenated Millipore water which was made to pH 11.5 with a solution of 5 M NaOH. The solution was the irradiated with microwave radiation using a CEM Star system 6 microwave.

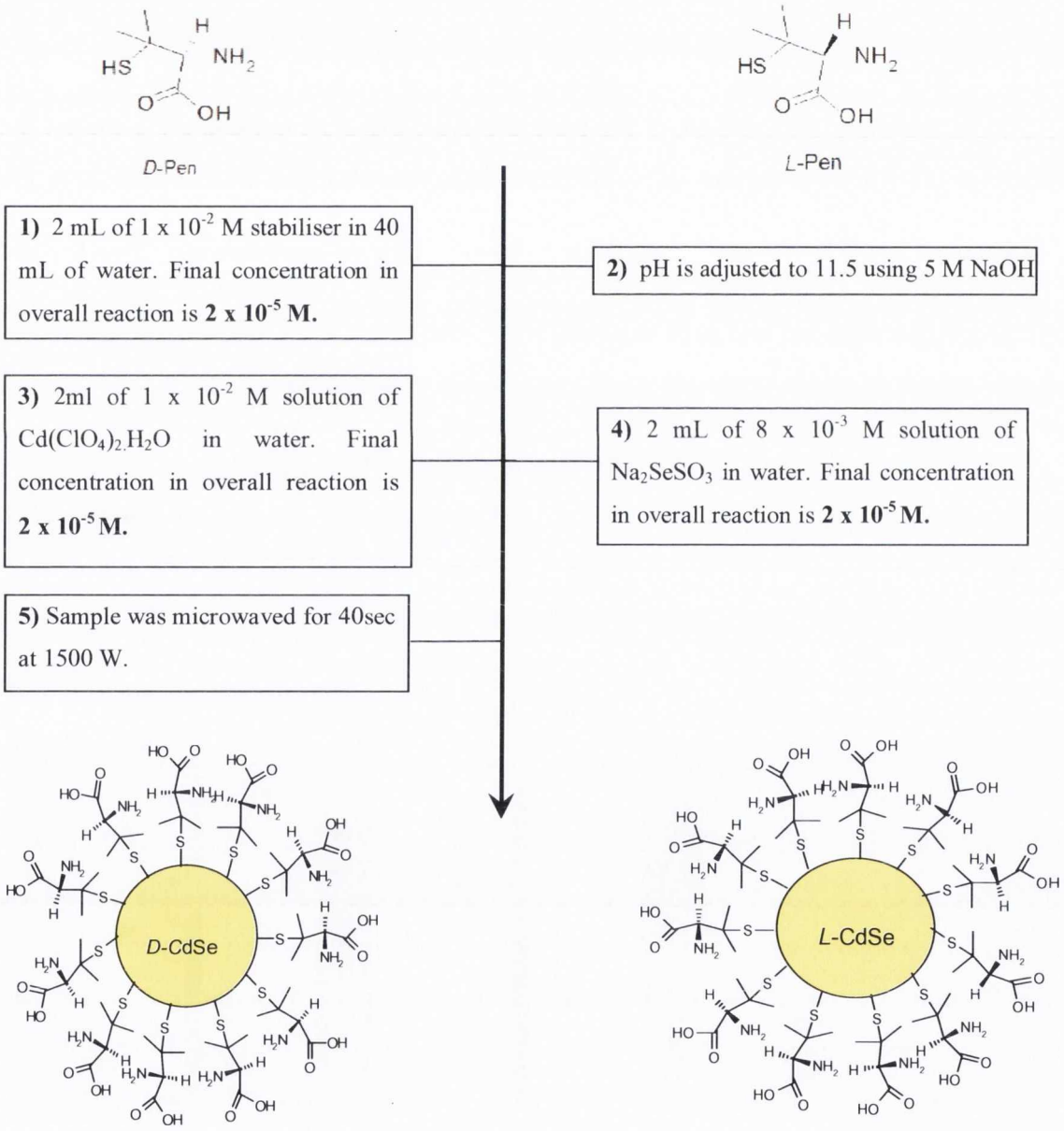

Figure 5.2: Reaction scheme for the preparation of *D*- and *L*- penicillamine stabilised CdSe nanoparticles.

In the synthesis of nanoparticles, a 2^2 statistical analysis based factorial study was initially employed to optimise the preparation process and identify what ratios of cadmium and penicillamine stabiliser resulted in the best nanoparticles (Figure 5.2). This was achieved by keeping the selenium concentration constant and varying the concentrations of cadmium and penicillamine precursors in the reaction solution. To obtain *Rac*- nanoparticles, equal amounts of *D*- and *L*- forms were used in the reaction.

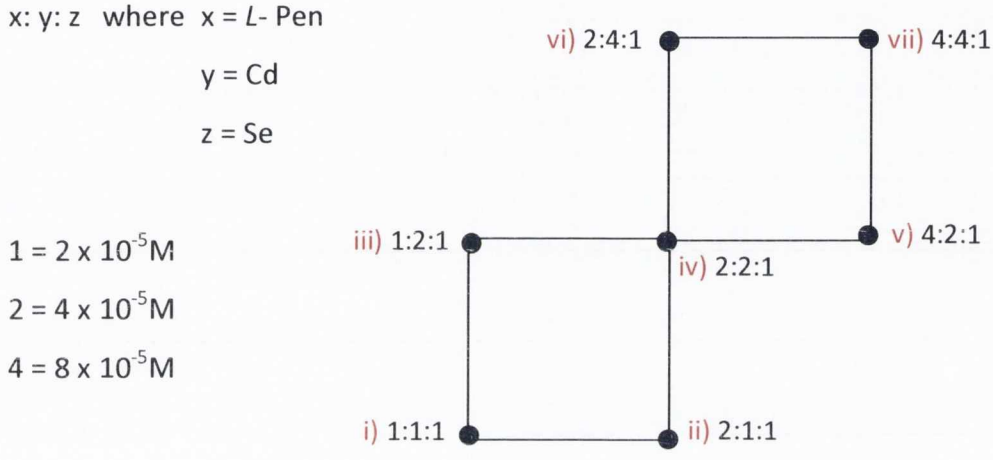

Figure 5.3: Diagram of 2^2 statistical analysis of penicillamine stabilised CdSe nanoparticles. The cadmium concentration is varied in the y direction, penicillamine in the x direction.

All seven reactions from the factorial study were examined using UV-Vis and PL spectroscopy. Both optical activity and photoluminescence quantum yield were used in conjunction as the response factor for the optimised nanoparticles. The results obtained indicated that reactions at points (i), (iv) and (viii) gave the best results i.e. when the molar concentration of all three components is equal. Of these, point (i) gave particles with both the highest quantum yield (see below), and good optical activity, from the least starting material, and so it was this ratio that was used to make *D*-, *L*- and *Rac*- penicillamine stabilised CdSe nanoparticles. The quantum yield of these QDs was calculated in order to evaluate the strength of the luminescence more precisely. This was done in accordance with a reported procedure[41]. The quantum yield was measured by comparing the luminescent intensity of the nanoparticles excited at a certain wavelength with that of an organic dye (Coumarin153) in methanol at the same wavelength, factoring in the relative absorbencies and the refractive indices of the two.

The quantum yields obtained for *D*-, *L*- and *Rac* Penicillamine CdSe were 10%, 10% and 15% respectively, close to those already reported in the literature for other water soluble CdSe particles[42].

5.3 UV- Visible Absorbance Spectroscopy studies

The first step in nanoparticle analysis is invariably investigating their absorbance profile, as this gives immediate useful information on the particles, namely it allows easy, rapid determination of the degree of quantum confinement. The UV-Vis absorbance spectra of the three *D*-, *L*-, and *Rac*- Pen stabilised CdSe nanoparticles are presented in Figure 5.4. It can be seen that QDs have near identical absorption profiles, independent of the enantiomeric composition of the surface stabiliser. There is a clear local maximum in the absorption bands, a so called 'band edge', corresponding to the lowest-energy allowed exciton transition, promoting an electron from a ground state to the first excited state ($1S_{3/2}(h)$–$1S_{1/2}(e)$). For these Pen-stabilised CdSe QDs this was observed at around 420 nm. This is our first indication that our particles are not only of nanometre size but are also quantum confined i.e. they are of a size that is smaller than the Bohr radius of the exciton for bulk CdSe material. This can be deduced by simple comparison with the first excitonic ($1S_{3/2}(h)$–$1S_{1/2}(e)$) transition of bulk CdSe which has an energy gap of approximately 1.7 electron volts. This corresponds to a spectral absorption local maximum at 717 nm and a particle size of approximately 7 nm in diameter. As our transition lies at higher energy, this indicates that our particles are of a smaller size than this limit, and quantum confinement is occurring, as expected. The secondary hump at 360 nm may be attributed to a second exciton transition, commonly observed in these aqueous CdSe nanoparticles.

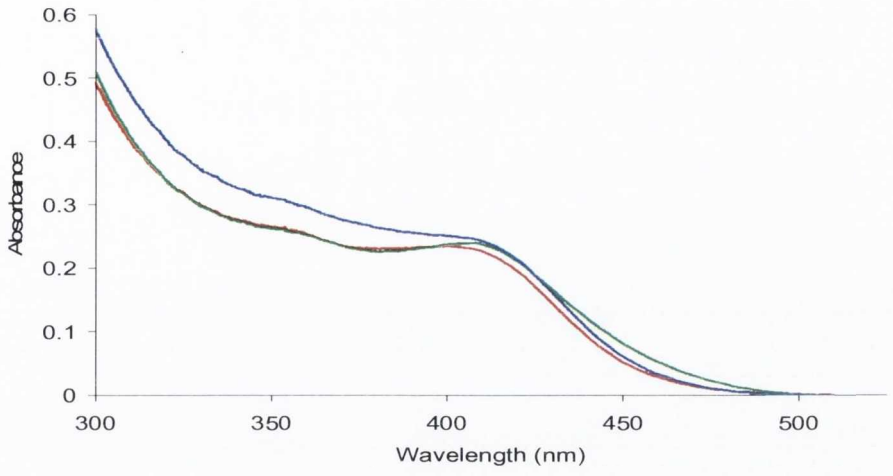

Figure 5.4: UV-vis absorbance spectrum of D- (blue), L- (red), Rac- (green) Pen CdSe QDs.

5.4 Investigation of CD properties

As mentioned earlier, one of the aims of this work it towards a biological application, specifically, to couple the properties of nanoparticles and chirality into one single entity. It is for that reason that chiral amino acids were chosen as surface stabilisers for these particles. Thus, in order to ascertain whether these nanoparticles possess any degree of chirality, Circular Dichroism (CD) spectroscopy was carried out on aqueous solutions of these nanoparticles. The results of this investigation are quite striking and unequivocal. The corresponding CD spectra of *D*-, *L*-, and the racemic stabilised penicillamine CdSe are shown in Figure 5.5. It is clear that both the *D*- and *L*- enantiomerically stabilised QDs demonstrate optical activity, rotating the plane of circular polarised light. What is more, the *D*- and *L*- QDs have complementary signals, being mirror images of each other, as would be expected for oppositely handed stabilisers. The racemic stabilised particles show no CD signal, again as expected, as a 50:50 ratio of *D*- and *L*- enantiomers cancel each other out and have no net overall effect on optical activity. It should be noted that the CD signal observed is quite different from that of the original free *D*- and *L*- penicillamine which shows, as expected, a near symmetrical image only in the far UV with the strongest dichroism signal at 234 ± 2 nm.[10] Here the key feature is that the CD signal originates near 500 nm and is strongest in the region corresponding to the lowest-energy allowed exciton transition, close to the band edge of the nanoparticles. This indicates that it is not

simply a chiral stabiliser around an achiral crystal but that something more complex is occurring. The stabiliser directly 'imprints', as it were, its chirality onto the nanoparticle in some manner.

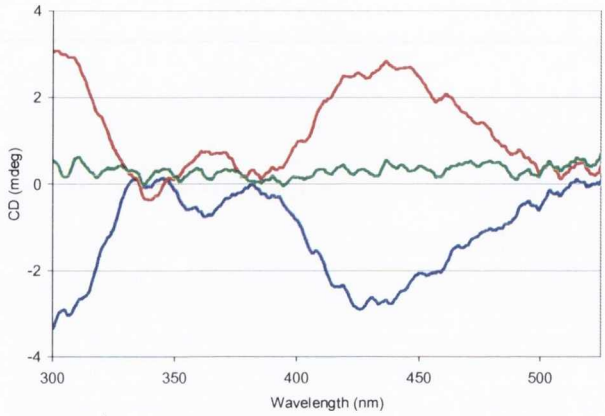

Figure 5.5: Circular dichroism spectra of D- (blue), L- (red), Rac- (green) Pen CdSe QDs.

In order to investigate this optical behaviour in further detail and to improve our understanding of its origins, the synthesis of the CdSe QDs was monitored using CD spectroscopy (Figure 5.6).

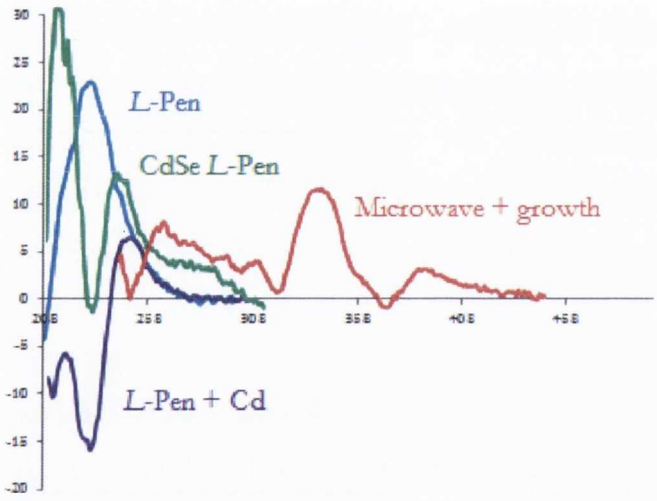

Figure 5.6: Monitoring the synthesis of *L*-Pen CdSe using CD spectroscopy.

As shown in Figure 5.6, the initial free penicillamine stabiliser (*L*-Pen) in water has a CD band at 240 nm. With the addition of cadmium (*L*-Pen + Cd), there is a dramatic change in the signal, with inversion of the initial penicillamine peak and the presence of a new band at 250 nm. This is caused by complexation of the cadmium and

penicillamine. Indeed, penicillamine is often perscribed in cases of cadmium metal poisoning for this very reason, as its chelating nature results in strong binding of the metal ion. As the selenium is added (CdSe *L*-Pen), further shifting of the bands occurs. This is a result of the formation of clusters of CdSe *L*-Pen, which are the non-luminescent precursors to our QDs. After microwave irradiation (microwave and growth) these CD bands red shift in accordance with the red shifting exciton band, as the clusters reform and grow into nanocrystals.

A more in-depth study of this effect was required in order to ascertain how this chirality is 'imprinted' or translated onto the nanocrystals. This was undertaken by our group in collaboration with Dr. Simon Elliott of the Tyndall Institute, Cork[11]. CdS was chosen as the model to study, as it has previously shown by our group to exhibit similar chiral behaviour. Ab initio quantum mechanical calculations using Density Functional Theory (DFT) were carried out on the interaction of penicillamine with CdS surfaces and clusters of various sizes. At the pH of these reactions (approximately pH 12) the amino acid stabiliser is in its dianion form and this was the nature of the ligand used in the calculations. The crystal phase used for CdSe was wurtzite, as clusters in a wurtzite form showed greater cohesive energy to those of zinc blende.

Calculation of the binding in CdS shows that the topmost sulphur atom caps three cadmium atoms, and this was extrapolated to the sulphur of the penicillamine stabiliser. The basic amine nitrogen and carboxylate oxygen are also available for coordination with other Cd atoms and tests indicated a preference for Cd-N. Unlike the sulphur, neither the N or O atoms bridge two or more cadmiums, though the two oxygens from the carboxylate as a whole may bind two separate cadmium atoms individually. The overall result was the binding of three cadmium atoms by the penicillamine's sulphur atom, one of which is also coordinated to the penicillamine's amine nitrogen. Further coordination of an oxygen atom to a fourth Cd surface atom is asymmetric and this changes the mirror symmetry of the surface. This leads to an enantiomeric arrangement of a monolayer of ligands on the surface of the nanocrystal. Further calculations on $Cd_{19}S_{17}$ clusters with penicillamine showed that as well as the above asymmetry, there are several other factors involved as follows;

1) The penicillamine molecule is bigger than the interatomic distances of cadmium in the CdS crystal structure
2) The binding between the nanoparticle CdS surface and the penicillamine is relatively strong
3) The CdS crystal structure is relatively flexible.

The net overall effect is that strain is induced in the crystal and transmitted to the outer layers of the CdS cluster, with the direction of the distortion being opposite for the two enantiomeric stabilisers. This explains how the molecule imprints its chirality onto the nanocrystal, resulting in the optical CD bands in the exciton region.

It can also be seen that the intensity of the CD band decreases as it red shifts with QD growth. This is explained by the fact that in these cluster calculations, the core CdS atoms remained unaffected and achiral; the effect of distortion falls away with increasing distance from the surface. Thus, as more and more chiral precursor is used up to make larger QDs and the core expands, the ratio of surface to core decreases and there is an overall reduction in signal intensity.

We propose that, due to the similarity between the calculated CdS clusters and our CdSe system here (same stabiliser and crystal structure), the above reasoning can also be applied to explain the origin of our CD bands in these CdSe nanoparticles. Indeed, this has shown to be the most probable scenario, with initial DFT calculations on CdSe showing similar distortion of the surface CdSe atomic arrangement, caused by the penicillamine stabiliser.

5.5 Photoluminescence Spectroscopy studies

The luminescence properties of chiral CdSe nanoparticles were investigated by photoluminescence (PL) spectroscopy. The emission spectra for all three types of dots were initially recorded using 420 nm as the excitation wavelength. The spectral distributions of photoluminescence (PL) in each case are very broad covering the region between 430 and 780 nm and with maximum at 545 nm, 543 nm, 553 nm, for *D*-, *L*-, and *Rac*- Pen stabilised CdSe QDs, respectively, so that in all cases there is very

significant shift between the first absorption (or excitation) and emission band maxima. The PL spectral data for these three are shown in Figure 5.7.

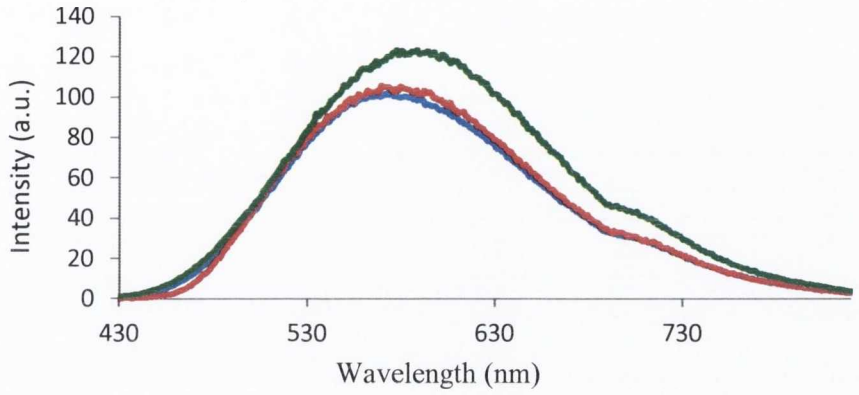

Figure 5.7: Photoluminescence spectra of D- (blue), L- (red), Rac- (green) Pen CdSe QDs.

It can be seen that the luminescence of all three enantiomerically stabilised QDs is very broad, covering almost the entire visible spectrum, emitting what may be deemed 'white' light. The peak maxima for each are in close alignment to each other, but with that for the *Rac*- stabilised particles exhibiting greater intensity compared to the *D*- and *L*- enantiomers. This may be explained by the fact that, as both complimentary enantiomers are present, they pack more efficiently on the particle surface, thus leading to an improvement in both the passivation of the atoms at the nanocrystal surface, as well as enhanced exclusion of other species in solution, including water itself, which can result in quenching of the luminescence.

To classify these QDs, the particles' full width half maximum (FWHM) and Stokes shift were examined, both measured in nm. These two values are used as a rough guide to classify the type of luminescence emitted. Values for these features of approximately 30 nm or less result in the QDs being called 'intrinsic', exhibiting 'intrinsic emission'. This means that the luminescence is (at least mainly) a result of direct recombination of the exciton's electron and hole, with little interaction with other energy states. For values that are over 30 nm, particularly the FWHMs, the QDs are considered to be 'defect' in nature. This means they emit so called defect luminescence. This type of luminescence originates from interactions between the exciton's electron

and/or hole with defects within the nanocrystal and on the surface, which provide alternative energy paths for exciton recombination. A wide range of defects results in emissive recombinations having a broad range of wavelengths and thus resulting in a broad luminescence signature[43-45]. Exceptions to this are when there is a large size distribution of intrinsic nanoparticles, the overlapping emission signals may appear to be broad defect luminescence, and some QDs are intrinsic emitting but may have a large Stokes shift. For this reason it is essential to ensure monodispersity in a sample of QDs. The FWHM is more often used over Stokes shift for this classification of QDs.

Figure 5.8 compares our defect emitting synthesised CdSe Pen QDs to our typical intrinsic CdTe TGA QDs described previously in this work (Chapter 3).

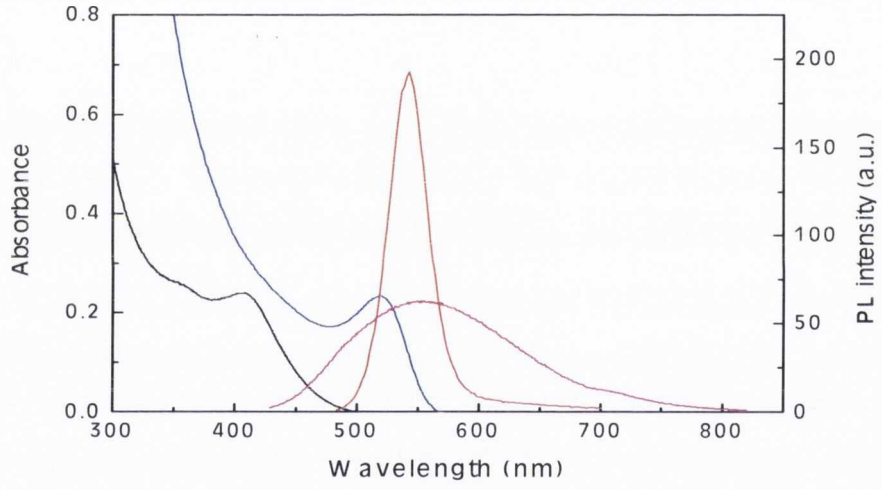

Figure 5.8: Comparison of the absorbance and emission spectra of *L*-Pen CdSe QDs (black and pink) and CdTe TGA QDs (blue and red).

For these *D*-, *L*- and *Rac*- Pen stabilised CdSe nanoparticles, as the FWHM and Stokes shifts were 128/128 nm, 130/132 nm and 126/135 nm respectively, this raises the question of whether the luminescence is actually defect in nature or the overlapping of intrinsic signals from different QDs. To answer this, intrinsic emitting CdSe QDs stabilised with penicillamine were also synthesised via refluxing the precursors in water for several hours. This method supplies enough energy over an extended period of time to allow the nanocrystal to rearrange, leading to the removal of defects. This is proven by a narrowing of the luminescence FWHM, coupled with a reduction in the Stokes

shift to a certain minimum (approx. 40 nm), after which further refluxing results in the synchronous red shift of both the absorbance and emission characteristics of these intrinsic QDs. The comparison of both these types of *L*-Pen CdSe QDs, synthesised via reflux and microwave, is shown in Figure 5.9.

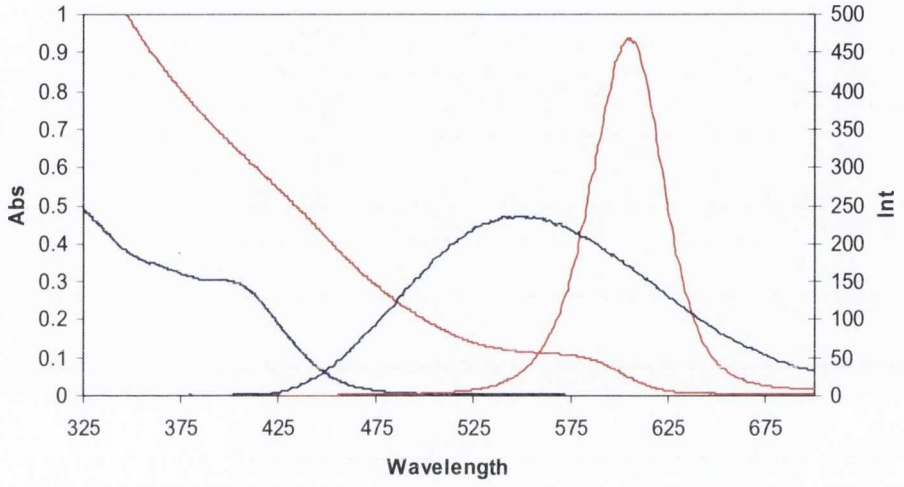

Figure 5.9: Comparison of the absorbance and emission spectra of *L*-Pen CdSe QDs synthesised via microwave irradiation (blue) and under reflux (red).

It is thus easily demonstrated, given the fixed Stokes shift of 40 nm of intrinsic *L*-Pen CdSe, that if this broad emission of up to ca. 800 nm was the result of overlaid intrinsic emission bands, there would be required, in the absorbance spectrum, significant corresponding absorbance spectral features. This is clearly not the case, and it can be established that the broad emission does not originate from superposition of many intrinsic signals from a wide size distribution of QDs, and that this microwave synthesis yields relatively monodisperse penicillamine stabilised CdSe QDs with the broad defect emission. This was corroborated further using low and High Resolution Transmission Electron Microscopy (HRTEM), showing nanoparticle CdSe with a size of 4.2 nm ± 0.5 nm (Figure 5.10).

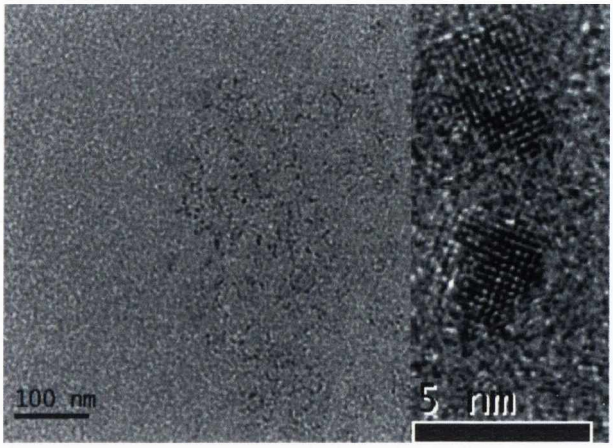

Figure 5.10: (a) Transmission Electron Microscopy (TEM) and (b) High Resolution TEM of *L*- Pen CdSe QDs.

5.6 Time Resolved (TR) Spectroscopy studies of Defect Luminescence

The evidence outlined above, such as the lack of a significant emission band close to the absorption band-edge, indicates that the exciton emission is quenched. The main contribution to the photoluminescence is therefore due to defect centres or trapped states on the surfaces of the quantum dots rather than being exciton-based. In order to probe the nature of this room temperature luminescence in more detail, a thorough time-resolved study as a function of both excitation and emission wavelength was then undertaken.

The emission lifetimes of the three CdSe QDs types were examined using time correlated single photon counting (TCSPC) methods. In all cases the decay was non-exponential and triple exponential analysis was required to obtain satisfactory χ^2 values (between 0.9 and 1.1). The possibility that these decays are due to a distribution of lifetimes may be possible, but was not further investigated in this work. Table 5.1 gives the resulting lifetime values obtained for the *D*-, *L*- and *Rac*- Pen stabilised CdSe particles measured at the maximum of their respective emission bands using a 370 nm "Nanoled" as the excitation source.

Table 5.1: Quantum yields and tri-exponential fitting parameters (lifetimes and relative contributions) for the fluorescence decays measured at the maximum of the PL bands using a 370 nm "Nanoled".

Sample	QY (%)	$\chi 2$	B_1(%)	τ_1(ns)	B_2(%)	τ_2 (ns)	B_3(%)	τ_3(ns)
D-	10 ± 1	1.03	9	8 ± 1	39	41 ± 4	52	145 ± 3
L-	10 ± 1	1.03	8	9 ± 1	32	45 ± 5	61	162 ± 3
Rac-	15 ± 1	1.02	7	10 ±1	34	51 ± 5	59	161 ± 3

5.7 Dependence of Emission Lifetimes on Emission Wavelength

Whereas the CD spectra of the three samples clearly show different chiral signals, the basic optical response (PL and time-resolved PL) was the same. Therefore we subsequently focused our attention on the photoluminescence of enantiomeric L-Pen capped quantum dots. Firstly, the photoluminescence decay curves of *L-* Pen capped CdSe were measured as a function of the emission wavelength in the spectral range from 450 nm to 770 nm (in 5 nm steps). In this experiment the acquisition was limited to 300 seconds at each particular wavelength, resulting in a 3-dimensional (3-D) map of the emission decay curves (Figure 5.11).

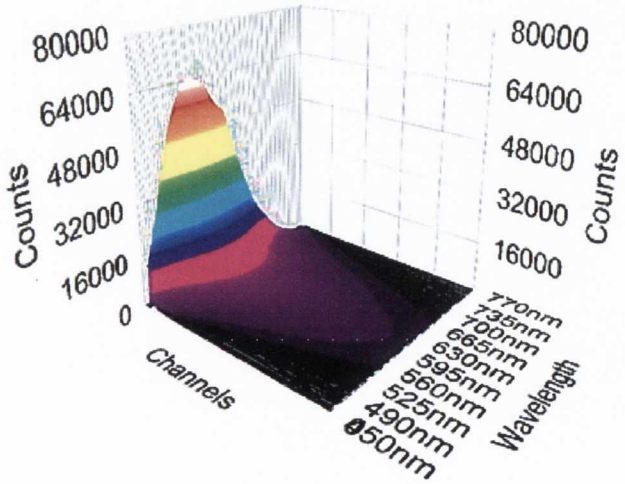

Figure 5.11: 3-D plot of emission decay curves showing the fluorescence *intensity* dependence vs. wavelength.

The shape of this 3-D curve illustrates the luminescence intensity dependence on emission wavelength, and matches the obtain PL spectra shown earlier. Such a result is to be expected with a time limited acquisition spectrum. In order gain more information, time resolved scans of the photoluminescence decay curves of *L*- Pen capped CdSe were again measured as a function of the emission wavelength, in the spectral range from 450 nm to 770 nm (in 5 nm steps). In this experiment the acquisition was limited to 5000 counts at each particular wavelength, resulting in a 3-D plot of normalized emission decay curves (Figure 5.12), along with focus on the grow in and termination at longer wavelengths (Figure 5.13). Figure 5.14 shows a contour plot constructed from such a map for *L*- Pen capped CdSe in Figure 5.12.

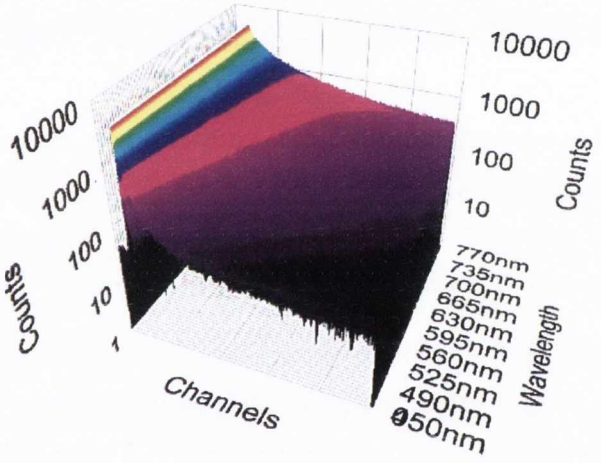

Figure 5.12: 3-D plot of emission decay curves showing the fluorescence *lifetime* dependence vs. wavelength.

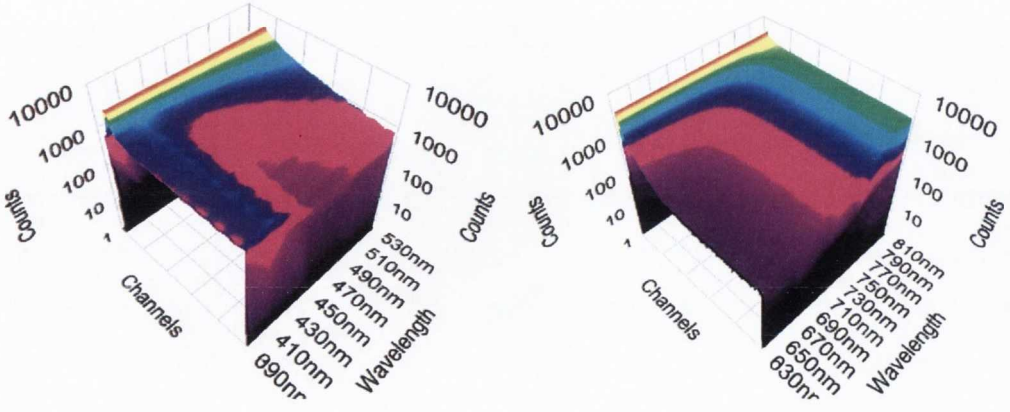

Figure 5.13: 3-D plot of emission decay curves focusing of either extremes of the spectrum.

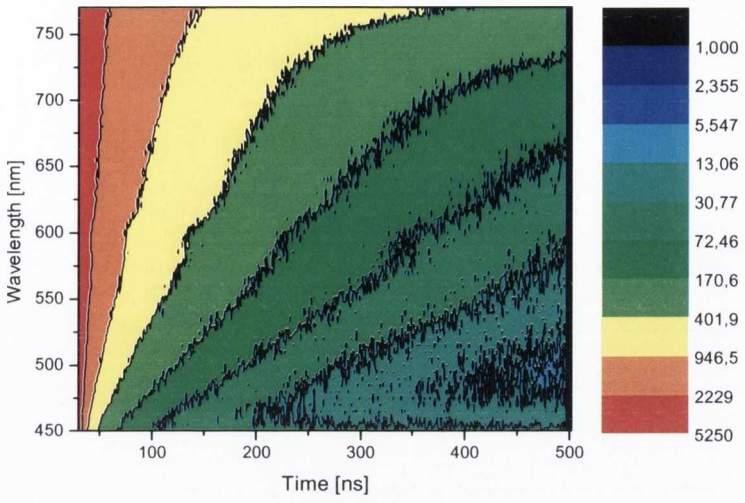

Figure 5.14: Contour plot constructed from the normalized emission decay curves of CdSe L- Pen measured at different wavelengths with step 5nm (PL intensity scale is logarithmic)

From these 3-D maps, the lifetime dependence on emission wavelength is clearly evident. The corresponding decay curves at chosen wavelengths (20 nm steps) are presented in Figure 5.15.

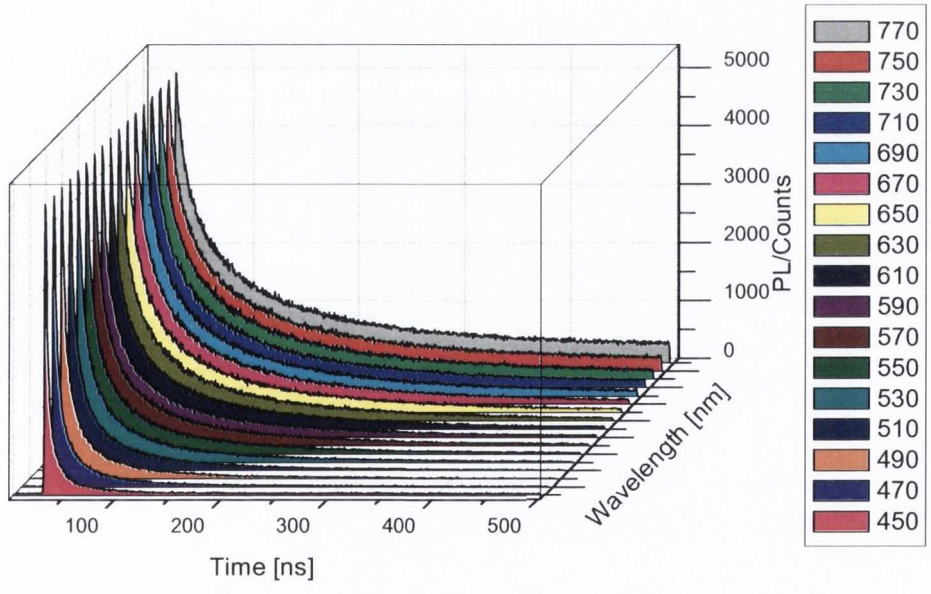

Figure 5.15: Plot of chosen decays curves constructed from slices of 450 – 770 nm scan @ 20 nm intervals. Excited with 295 nm "Nanoled".

The results of tri-exponential analysis of the decay curves at 450 nm, 576 nm and 705 nm are presented in Table 5.2. It may be noted that at longer detection wavelengths both the proportion and lifetime of the longer lived species is increased, implying that the defects emitting at lower energy are more stable.

Table 5.2: The fitting parameters (lifetimes and relative contributions) obtained from a tri - exponential fit to PL decay data for *L*- Pen capped CdSe measured at different emission wavelengths and excited with a 295 nm "Nanoled".

Wavelength	B1%	τ_1 (ns)	B2%	τ_2 (ns)	B3%	τ_3 (ns)
450 nm	32	1.7 ± 0.3	42	9 ± 2	26	46 ± 4
560 nm	7	9 ± 1	32	44 ± 4	61	158 ± 4
705 nm	3	10 ± 2	21	52 ± 3	76	184 ± 5

As such longer-lived states might possibly be affected by dissolved oxygen in solution, particularly if these states are related to surface defects, the PL lifetimes for *L*-Pen stabilised CdSe at a chosen wavelength were also determined for an argon purged sample (Table 5.3). These results show that there is no significant difference in lifetime values for aerated and argon purged samples indicating that quenching of excited states by oxygen has a negligible effect.

Table 5.3: The fitting parameters (lifetimes and relative contributions) obtained from a tri – exponential fit to PL decay data for argon degassed *L*- Pen capped CdSe measured at different emission wavelengths and excited with a 295 nm "Nanoled".

Degassed	B1%	τ_1 (ns)	B2%	τ_2 (ns)	B3%	τ_3 (ns)
450 nm	30	2.0 ± 0.2	45	11± 2	25	45 ± 3
560 nm	8	9 ± 1	32	42 ± 3	60	161 ± 3
705 nm	4	9 ± 2	22	49 ± 3	74	187 ± 3

The strong variation of the decay times with detection wavelength implies that emission spectra should shift to longer wavelengths with time and for this reason the time-resolved emission spectra (TRES) were determined by slicing the emission TCSPC decay curves and setting an identical acquisition time for each wavelength measurement. The TRES for *L*-Pen CdSe quantum dots (at different times between 0 and 430 ns) are presented in Figure 5.16 and reveal, as expected, that there is a red shift of the emission band maximum from ca. 560 nm to 600 nm over this time range. The

population of lower lying traps thus becomes more significant over time. As the full width half max (FWHM) changes by only 80 mEV – these results are not caused by a large size distribution in the sample.

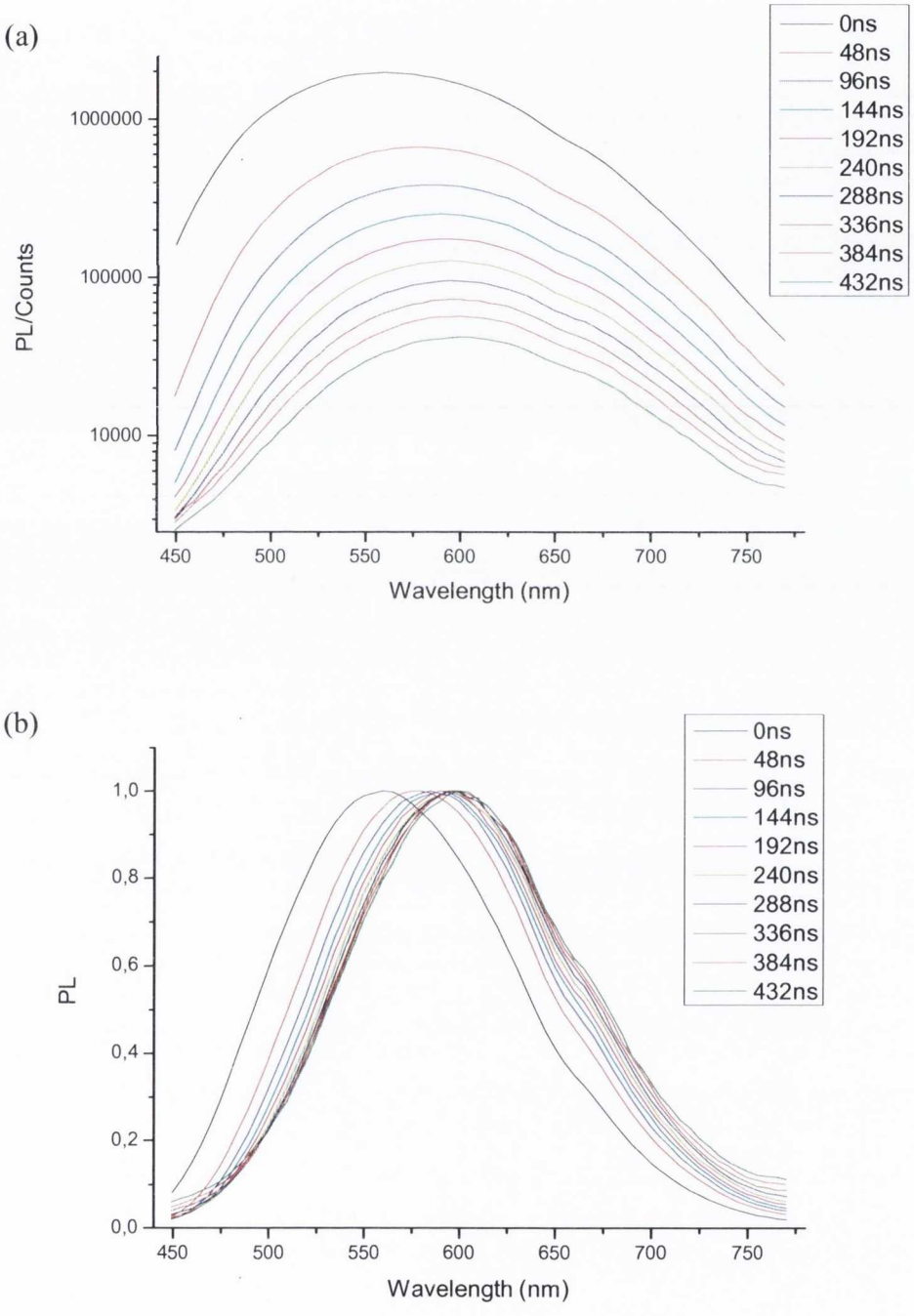

Figure 5.16: Time resolved emission spectra of CdSe *L*- Pen obtained by PL kinetic traces slicing (using a moving time window (ca. 48ns) at delays given in the legend. (a) Cumulative log counts measured at constant acquisition time and (b) normalized to unity. The full width half max for these curves are decreasing from 580 (top curve) to 500 meV (bottom curve).

5.8 Dependence of Emission Lifetimes on Excitation Wavelength

Given the strong dependence of the measured lifetimes of the excited states on the detection wavelength it was of interest to see whether the excitation wavelength had a similarly strong effect. As will be discussed below, a strong excitation wavelength effect would be expected if the reason for the longer-lived nature of the long-wavelength emission was a non-homogenous sample. However, as may be seen in Table 5.4, the PL lifetimes at 450, 560 and 705 nm determined using different excitation sources 295 nm, 340 nm and 370 nm "Nanoleds" are closely similar in each case, supporting the hypothesis that these particles have a relatively narrow size distribution.

Table 5.4: The fitting parameters (lifetimes and relative contributions) obtained as a result of a tri -exponential fit to PL decay data for *L*- Pen capped CdSe collected at 450, 560 and 705 nm from excitation at 295, 340 and 370 nm.

CdSe *L*-Pen @ 450 nm	B1 %	T1 (ns)	B2 %	T2 (ns)	B3 %	T3 (ns)
LED 295nm	32	1.7 ± 0.3	42	9 ± 2	26	46 ± 4
LED 340nm	31	1.4 ± 0.3	40	8 ± 2	29	40 ± 3
LED 370nm	33	1.7 ± 0.3	40	10 ± 2	27	45 ± 4
CdSe *L*-Pen @ 560 nm	B1 %	T1 (ns)	B2 %	T2 (ns)	B3 %	T3 (ns)
LED 295nm	7	9 ± 1	32	44 ± 4	61	158 ± 4
LED 340nm	7	10 ± 2	30	44 ± 7	63	157 ± 5
LED 370nm	8	9 ± 1	32	48 ± 5	61	162 ± 3
CdSe *L*-Pen @ 705 nm	B1 %	T1 (ns)	B2 %	T2 (ns)	B3 %	T3 (ns)
LED 295nm	3	10 ± 2	21	52 ± 3	76	184 ± 5
LED 340nm	2	8 ± 2	21	50± 4	77	189 ± 8
LED 370nm	4	9 ± 2	25	52 ± 3	71	189 ± 5

The CdSe nanoparticles all show photoluminescence, covering the region between 430 and 800 nm (Figure 5.7). The lack of a significant emission band close to

the absorption band-edge indicates that the exciton emission is quenched and that the main contribution to the photoluminescence is due to defects or trapped states on the surfaces of the quantum dots. While in principle a broad emission could be caused by excitonic emission from a distribution of nanoparticles of varying size, from the evidence obtained this is not believed to be the case here.

Generally, time resolved photoluminescence of quantum dots reveals various processes and the emission decay profile needs to be described using multiexponential distribution[46]. In the case of simple biexponential analysis it is assumed that each dot's emission lifetime is made up of two components[47,48] and the shorter lifetime, τ_1, is typically attributed to the intrinsic recombination of the initially populated core states[49-52]. The origin of the longer component τ_2, although long disputed, is now considered to be a result of the interference of surface states (i.e. the presence or absence of surface defects), with the recombination of the electron-hole pairs[53,54]. However, in many cases higher order kinetics have been required to analyze decay traces[46,55]. As bi-exponential analysis of emission decay curves gave unsatisfactory fits (due to unacceptable residuals and chi-squared (χ^2) values) we used a tri-exponential decay model to determine the emission lifetimes of these particles (Table 5.1). As can be seen, the lifetime τ_1, τ_2 and τ_3 values and the relative amplitude factors (B_1, B_2 and B_3) are all quite similar for *D*-, *L*- and *Rac*- Pen CdSe. From the two plots (Figure 5.14 and 5.15), and Table 5.2, it is evident that both the lifetimes of the emitting excited states and the contribution of the long-lived component strongly depends on the emission wavelength i.e. the longer the emission wavelength the larger the lifetime values, and the larger the contribution of the long-lived component. It may be noted, however, that these lifetimes do not depend on the excitation wavelength used, which is as expected if the particles are reasonably monodisperse. Although, as previously mentioned, the observed emission is mainly from defect states, there may be a very small excitonic contribution at the shortest wavelengths. Emission from either the band edge exciton (BEE) or the charged exciton (CE) could explain the observed multiexponential photoluminescence[56]. In addition, the presence of dark exciton states, which was suggested for other CdSe quantum dots, may also contribute to further complications in the emission decay profile as they may be involved in energy transfer of dark excitons[57].

The time-resolved emission spectral study shows that, while the emission maximum shifts significantly over time to longer wavelengths, the overall shape and full width half maximum of these spectra changes only slightly (580 meV between 0 and 48 ns to 500 meV between 430 and 478 ns). In particular, even after a relatively long time (hundreds of nanoseconds) the emission is still very broad. Such a red-shift (see normalized PL spectra Figure 5.15) and lifetime dependence on emission wavelength is consistent with there being many competing emissive states with different lifetimes. If we accept a single particle scenario i.e. that the observed PL dynamic and lifetime distribution is characteristic of all, or at least the majority, of nanocrystals in solution, then the population of lower lying traps becomes more significant over time due to relaxation processes (between emitting defect states). The other possibility is that the broad emission originates from the superposition of photoluminescence signals from many nanocrystals with different types of traps (and hence defect excited states). It would be perhaps be rather naive to believe that all the nanoparticles have identical emitting traps and therefore at this stage of the research we propose that both scenarios may be appropriate. It is worth remembering that, in the case of excitonic emission, the PL lifetime dependence on wavelength is usually explained in terms of QD size distribution[22] or by the energy transfer of the dark exciton[57]. However, in penicillamine stabilized CdSe, emission originates from surface traps and size distribution should not play an important role unless different types of traps are selectively associated with different sizes of nanoparticles. For example, the number of dislocations (which might produce extra states in the bandgap) may be greater for larger nanocrystals[58]. However, analysis of these nanoparticles by TEM has shown them to have a very narrow size distribution of 4.3 ± 0.5 nm (Figure 5.10). Thus, we finally assign the photoluminescence as arising from superposition of PL signals from different nanoparticles, all of which can have multiple and not necessarily the same emitting defect states. In order to address this question directly it will be necessary to carry out single particle fluorescence experiments.

5.9 Synthesis of Chiral Cysteine Stabilised CdSe QDs

In light of the findings outlined above, it was of interest to try to synthesise similar chiral CdSe quantum dots using another amino acid type stabiliser. To this end, the potential of cysteine (Cys), 2-amino-3-mercaptopropionic acid) was investigated in a manner akin to that for penicillamine stabilised CdSe.

The synthesis of cysteine stabilised CdSe was carried out using the method described above, under an atmosphere of argon, with a 2^2 factorial study used to determine the ideal cadmium to stabiliser ratio, keeping the selenium concentration constant. In this study, the last point (vii), again when the concentrations of cadmium and cysteine are equal, was found to produce the best nanoparticles with the strongest luminescence with good optical activity, consequently this ratio was used for all further work. Nanoparticles of *D*-, *L*-, and *Rac*- cysteine CdSe were then synthesised accordingly. From the UV-Vis spectra (Figure 5.17) we can see that the band edge corresponding to the lowest-energy allowed exciton transition, ($1S_{3/2}(h)$–$1S_{1/2}(e)$), again lies at around 420nm, the same as for Pen CdSe. Good correlation was seen between the *D*- and *L*- enantiomerically stabilised QDs, with that of *Rac*-CdSe blue shifted some 10 nm or so. This is sometimes observed with these systems, caused by better packing of the *D*- and *L*- stabilisers in the racemate, yielding smaller nanoparticles.

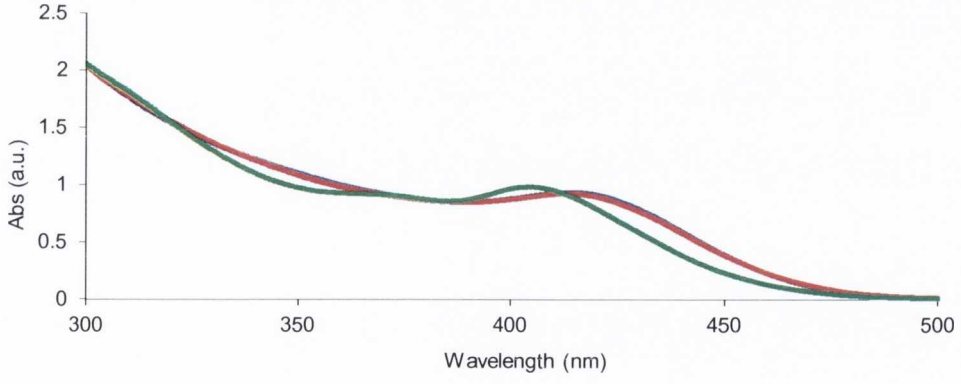

Figure 5.17: UV-vis absorbance spectrum of D- (blue), L- (red), Rac- (green) Cys CdSe QDs.

The quantum yields of these nanoparticles, measured against Coumarin 153 in methanol, were 15%, 16% and 21% respectively. FWHM and Stokes shifts of the *D*-, *L*- and *Rac*- cysteine CdSe nanoparticles were 149/128 nm, 154/127 nm and 162/120 nm respectively (Figure 5.18).

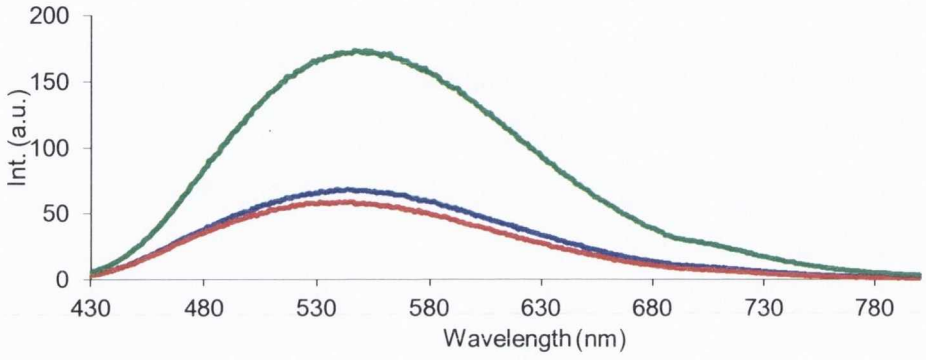

Figure 5.18: Photoluminescence spectra of D- (blue), L- (red), Rac- (green) Pen CdSe QDs.

Investigation into the presence of optical activity using CD spectroscopy showed that these exhibited a similar chiral response (Figure 5.19), with strong correlation between the particles band edge absorbance and the first chiral signals, inferring that the same mechanism of chiral imprinting from stabiliser to QD is occurring here.

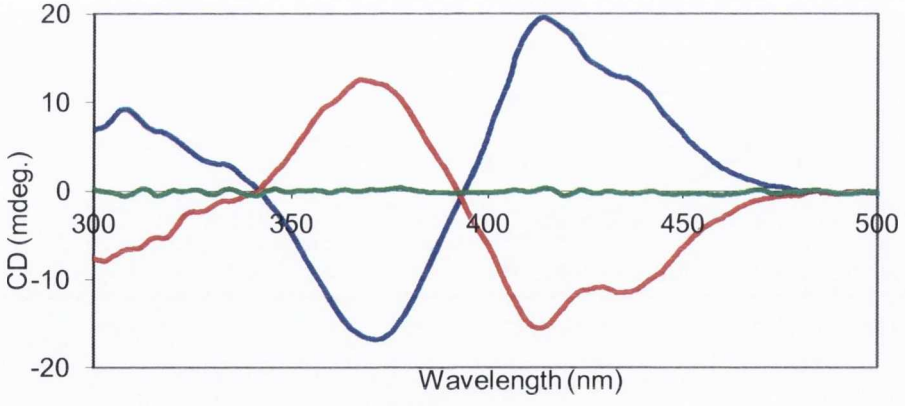

Figure 5.19: Circular dichroism spectra of D- (blue), L- (red), Rac- (green) Pen CdSe QDs.

A more detailed study of these quantum dots has yet to be undertaken, but it may be reasonably assumed that their fluorescence properties mimic those of their

penicillamine stabilised counterparts, given their similar broadband defect emission and optical activity.

5.10 Synthesis of Chiral CdTe QDs

Following on from the earlier success of synthesising chiral CdSe quantum dots, it was then decided to see if it was possible to substitute CdSe for CdTe and obtain the same results.

Here CdTe QDs were prepared using a version of the approach reported by Bao et al.[59], which we modified. The synthesis involved the microwave induced heating of a solution of $Cd(ClO_4)_2$, cysteine, Na_2TeO_3 and $NaBH_4$. Microwave irradiation as a method of producing highly luminescent CdTe nanocrystals is already proven to be a very efficient, with several reports in the literature[60,61]. The *D*-, *L*-, and *Rac*- forms of cysteine, were used individually as the stabilizers. A 2^2 factorial study[62] was also employed to optimise the particle synthesis using quantum yield as the response. It was found that a molar ratio of 4:2:1 cadmium to cysteine to tellurium gave quantum dots with higher quantum yields and without the tell-tale black colour which indicates the formation of elemental Te particles[63,64]. UV-vis, photoluminescence spectroscopy, TEM and fluorescent lifetime data were also recorded for all samples. The average absorbance maxima of these particles were 525 nm for *D*-, 527 nm for *L*- and 520 nm for *Rac*- QDs (Figure 5.20).

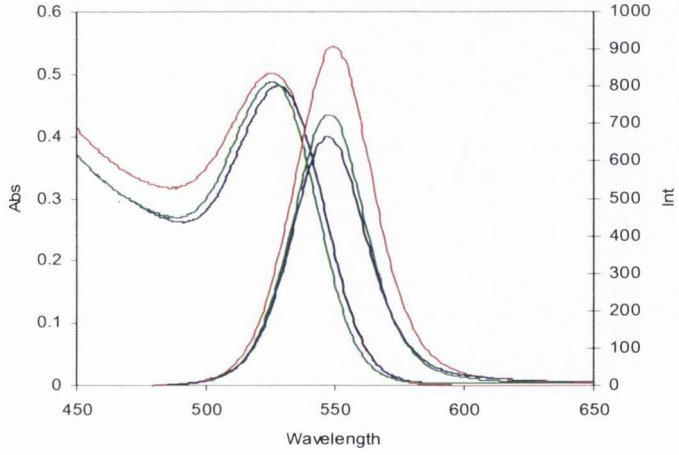

Figure 5.20: Optical spectra (UV-vis absorption - left, and emission – right) of CdTe nanocrystals stabilized with *D*- (blue), *L*- (green) and *Rac*-Cys (red). Excitation wavelength for all emission spectra is 470nm.

All CdTe nanoparticle samples emitted strongly in the green-yellow region of the spectrum when excited at 470nm, with average maxima of 550nm for both *D*- and *L*- Cys stabilized QDs, and 546nm for the *Rac*-Cys QDs. Excitation spectra taken at 580 nm were in agreement with their corresponding absorption spectra within 1 - 2 nm deviation. These spectral characteristics are typical for CdTe nanocrystals with excitonic emission, which possess a high degree of monodispersity and have very little surface defects.

In addition particles with variable *D*- and *L*- cysteine stabilizer ratios (75% *D*- : 25% *L*-, and 25% *D*- : 75% *L*-) have been prepared. The QYs of all these particles were calculated using Rhodamine G as the standard. These quantum yield measurements gave values of 24 ± 2, 26 ± 1 and 32 ± 1% for *D*-, *L*- and *Rac*- QDs respectively (Figure 5.21).

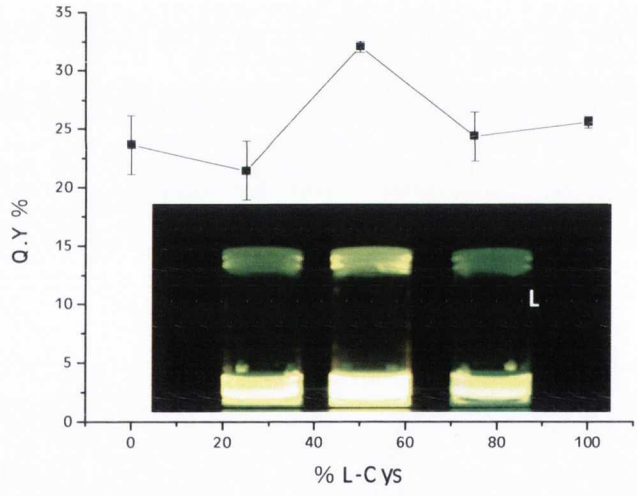

Figure 5.21: The observed changes in the QYs are dependent on the ratio of *D*- to *L*-cysteine present on the quantum dots. 0% *L*-Cys corresponds to pure *D*- cysteine, 100% *L*-Cys corresponds to pure *L*-cysteine stabilised dots. The point at 50% is, of course, the racemate. Insert: a photograph of *D*-, *Rac*- and *L*- Cysteine stabilised CdTe QDs under UV light.

We believe that the increase in the QY in the case of the racemic stabilizer comes from the complementary nature of the racemic ligands, allowing for closer packing of the stabilizer on the nanoparticles surfaces. This closer packing leads to an increase in the hydrophobicity of the QD surface and as a result to a more efficient

elimination of water molecules and surface bound oxygen. Both of these molecules acts as potential traps for surface recombining excitons, therefore their removal contributes to the observed luminescence and QY increases. The luminescent decay curves of *D*- *L*- and *Rac*- particles were fitted using a bi-exponential model. It is generally accepted that the short lifetime (τ_1) is attributed to intrinsic recombinations of populated core states, while the longer lifetime (τ_2) is linked to the surface associated luminescence[49,54,65]. By examining the contribution, (**B**), of both τ_1 and τ_2 to the overall lifetime, it is possible to compare and contrast the surface conditions, i.e. the degree of surface defects, of each type of dot[66]. The particles with highest quantum yields (the *Rac*- QDs) are expected to have a higher contribution from the surface states (τ_2) to the overall luminescence. This is because their higher quantum yield suggests the *Rac*- particles have less defects present on their surfaces than either the *D*- or *L*- particles. The $\mathbf{B}_2$ value for *Rac*-CdTe is 52 ± 1% , while the $\mathbf{B}_2$ value for the *D*- and *L*- particles is lower (at 42 ± 2%), this indicates that the *D*- and *L*- particles possess more disordered surfaces than the *Rac*- stabilized QDs.

The utilization of 3:1 and 3:1 mixtures of *D*- and *L*- Cys stabilizers resulted in the formation of CdTe QDs whose quantum yields were close to those of the individual *D*- or *L*- enantiomer stabilized particles. In this case the reduction in the QY can be explained most likely by the non-uniform distribution of *D*- and *L*- stabilizer molecules on the QD surface leading to extra defects and kinks (Figure 5.21).

HR TEM (Figure 5.22) showed the dots to have a diameter of 4-5nm. This is consistent with CdTe particles which absorb around 520nm. All QDs were strongly aggregated, that is clearly visible in TEM images.

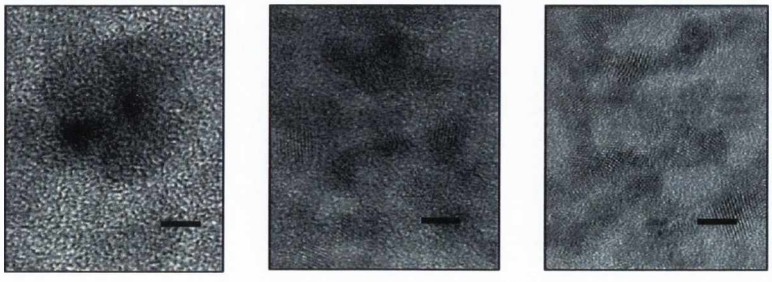

Figure 5.22: HRTEM images of *D*-, *L*- and *Rac*- of cysteine stabilised CdTe nanocrystals.

Circular dichroism measurements demonstrated that these CdTe nanoparticles are only weakly CD active (Figure 5.23). This is, we believe, due to the absence of any defects on the surface of the nanoparticles. The presence of surface defects in the previously reported penicillamine stabilized CdS QDs were caused by the formation of a chiral (defective) shell on an achiral core. Therefore, it is our belief that surface defects must be present on dots for them to be strongly CD active at or around their band edge regions[10,11].

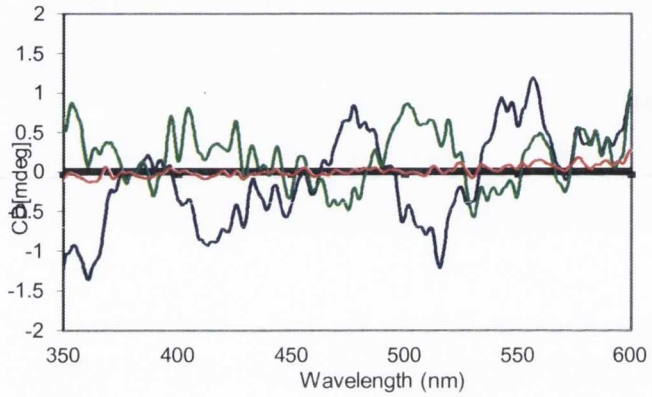

Figure 5.23: CD spectra of *D*- (blue), *L*-(green), and *Rac*-(red) cysteine stabilised CdTe. Despite the clear structure and the mirror imaging of the *D*- and *L*- scans, the signals are extremely weak.

Examination of the formation of the CdTe QDs using CD spectroscopy showed the initial creation of a chiral Cd-Cys complex once the cysteine and $Cd(ClO_4)_2$ solutions were combined, (Figures 5.24, (a) and (b)). Upon the addition of Te^{2-} ions small chiral weakly luminescent nanoparticles are formed, as can be seen from the appearance of signals up to 400 nm, (Figure 5.24, (c)). These signals, though weak, are well structured and clearly visible. After microwave irradiation these particles rearrange as highly luminescent nanocrystals. The CD signal red shifts, as reported before, in accordance with particle growth[10]. However, the heat and growth processes also result in the partial removal of surface defects and consequently in the reduction of the intensity of CD signal to the point where it is impossible to distinguish the excitonic signal from background noise.

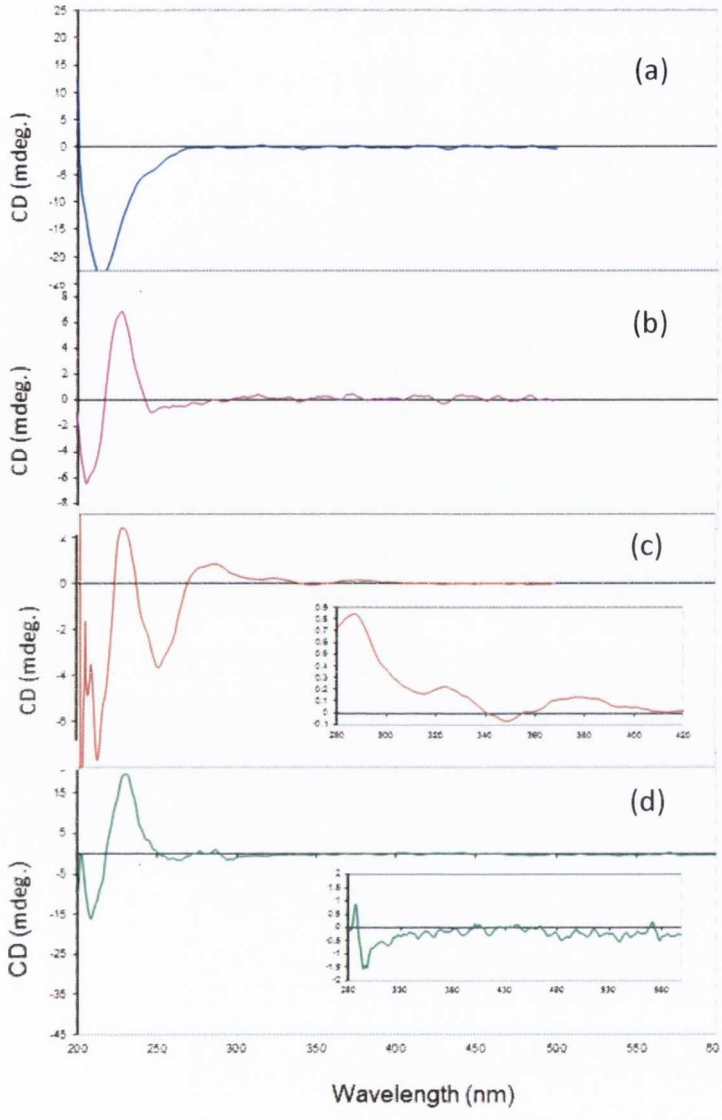

Figure 5.24: CD spectra monitoring the formation of *D*-Cys CdTe QD's. a) *D*-Cys stabiliser absorbs negatively at ~210 nm. b) The addition of Cd ions forms a Cd-Cys complex and causes the appearance of a new band at ~233nm. c) The clusters after addition of the sodium tellurite before the microwave treatment – new bands from 250 to 405 nm (blue). d) CdTe QD's after the microwave treatment –all signals beyond 255nm have practically disappeared with only the Cd-Cys complex signal remaining strong.

Due to this lack of optical activity at the band edge region of the quantum dots after microwave treatment, cysteine was replaced with penicillamine. Using the same experimental method *D*-, *L*- and *Rac*- penicillamine (Pen) stabilized CdTe QDs were also prepared. While these penicillamine stabilized QDs were found to give strong CD responses at the band edge region they were unfortunately only very weakly luminescent; their quantum yields were only around 1%. Thus Pen-stabilized CdTe

QDs demonstrated strong circular dichroism, but with very poor luminescence. This was in direct contrast to the highly luminescent but poorly optically active cysteine coated CdTe described previously. Therefore, in order to produce both chiral and luminescent CdTe nanocrystals a mixture of Cysteine and Penicillamine stabilizers was used in the synthesis of a third type of dot.

In total five batches of Cys:Pen CdTe quantum dots were produced. The first of these batches was simply cysteine stabilized CdTe, with each following batch containing a 20% increase in penicillamine. The fifth and final batch of which was 80% penicillamine and 20% cysteine. A summary of these results for the *L*- stabilised CdTe particles can be seen in Table 5.5, the *D*-CdTe particles (not shown) followed a similar trend. With the overall concentration of stabilizer remaining unchanged, a series of dots were produced with an increasing ratio of penicillamine to cysteine. As expected, the presence of both cysteine and penicillamine on the surface of the dots produced CdTe nanoparticles which were both luminescent and CD active (Figures 5.25 and 5.26). However, as the CD activity increased the PL intensity decreased. It was also noticed that the emission peak steadily widened as the Pen concentration was increased. A widening emission peak is indicative of increased defect emission and we believe that this continual increase in the FWHM was a result of increasing surface disorder on these particles.

A close examination of the luminescent lifetime contributions, i.e. the B factors, to the overall luminescent decay were performed by using both bi and tri-exponential fits. The initial bi-exponential fit showed particles which possessed a short core lifetime of 12 ± 2 ns and a longer shell lifetime of 37 ± 3 ns, depending on the Pen:Cys ratio.

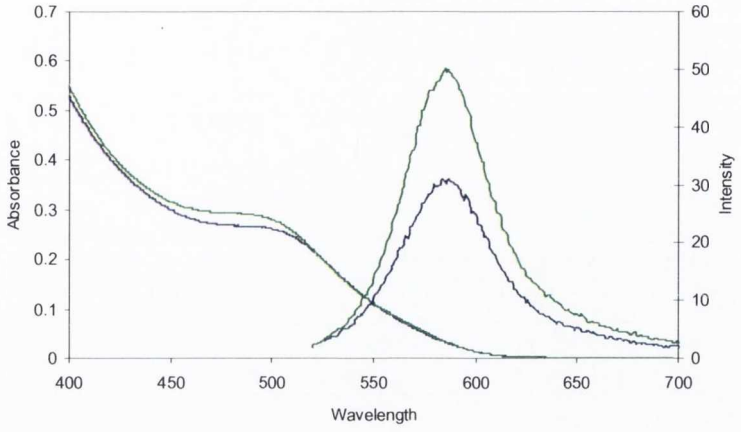

Figure 5.25: UV-Vis and Pl spectra of *D*- (blue) and *L*- (green) Cys/Pen mixed ligand CdTe nanoparticles. Particles were excited at 500nm. The ratio of cysteine to penicillamine used here was 2:3.

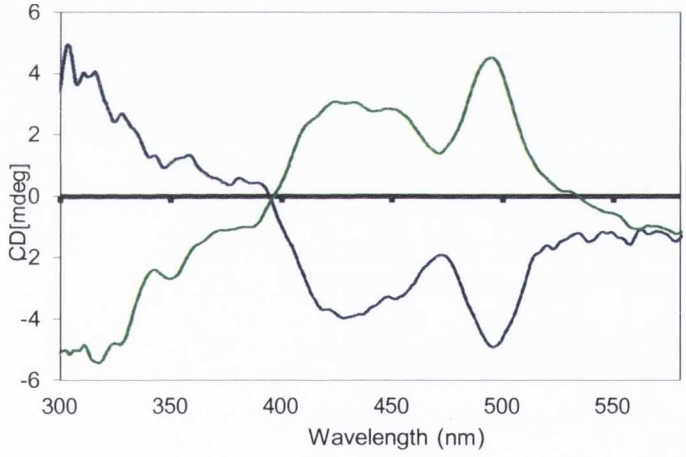

Figure 5.26: CD spectra of *D*- (blue) and *L*- (green) Cys/Pen mixed ligand CdTe nanoparticles. The ratio of cysteine to penicillamine is 3:2.

As the penicillamine concentration was increased, the contribution of the surface ($\mathbf{B}_2$) to the overall lifetime dropped, indicating an increase in surface disorder. The lifetimes themselves also changed, with the τ_1 decreasing and the τ_2 increasing as the concentration of penicillamine was increased. The χ^2 value has also increased.Due to this increase in the χ^2 value as the ratio of penicillamine to cysteine increased, we also fitted the decay curves using a tri-exponential to allow for a better overall fit. This refit gave average τ_1 and τ_2 values of 14 ± 2 ns and 35 ± 4 ns, with a longer average τ_3

value of 124 ± 11 ns, depending on the ratio of penicillamine to cysteine used. No discernible pattern was seen in either the τ_1 and τ_2 or the $\mathbf{B}_1$ and $\mathbf{B}_2$ values as the Pen:Cys ratio was altered. However, both the τ_3 and $\mathbf{B}_3$ values increased with the increasing penicillamine concentration (Table 5.5). Normally in a tri-exponential fit the longest lifetime is associated with the contribution of the defect emission and its lengthening along with its increased contribution to the overall lifetime of the particles, indicates an increase in the number of surface defects[15]. This increase in surface disorder coincides with an increased CD activity.

Table 5.5: Lifetime, FWHM and QY data for mixed stabilizer *L*-CdTe dots. Note the increase in the length and the contribution of the longest lifetime (τ_3), as the concentration of Penicillamine is increased.

CdTe	Cys:Pen	FWHM	QY	τ_3	B_3 / B_{total}
1	1:0	33nm	46.4%	109 ns	2%
2	0.8:0.2	39nm	34.2%	124 ns	2.5%
3	0.6:0.4	43nm	13.3%	125 ns	3%
4	0.4:0.6	50nm	5.3%	127 ns	4.1%
5	0.2:0.8	55nm	2.3%	136 ns	4.8%

Thus the lifetime studies, the reduction in the quantum yield and the broadening of the emission peaks all point toward the appearance of surface defects on the particles, as the penicillamine to cysteine ratio is increased. We believe that the type of luminescence a QD exhibits is directly relevant to QDs chirality. The higher the intrinsic luminescence, the more ordered nanocrystal's surface, and so the less chance of producing a CD active QD. In opposite, QDs which possess defect emission can demonstrate a strong CD response, due to the presence of chiral defects at the surface. Therefore, a controlled balance between the defect and excitonic emission is required to produce CD active semiconductor nanocrystals.

5.11 Conclusions

In summary, we have prepared a range of new chiral CdSe and CdTe nanoparticles with different chiral stabilisers. CdSe QDs showed a very broad distribution of photoluminescence which originates from emissive defect states. It is also apparent that there must be a range of states associated with each individual quantum dot, with the shift of the emission band to longer wavelengths at longer times after excitation suggesting traps of varying depth. If this is indeed the case then it is unlikely that the particles will show circularly polarised emission, but it is expected to confirm this in future experiments. We also intend to carry out further photophysical measurements (and in particular transient absorption measurements) to better characterise the complex luminescence dynamics.

In addition we produced strongly luminescent but weakly CD active cysteine stabilized CdTe quantum dots. It was demonstrated that the quantum efficiency of these dots is strongly dependant on the ratio of enantiomers used as stabilizers. It was found that the dots prepared using the racemic mixture of cysteine enantiomers results in QDs with the highest QY. We have also shown that the CD activity of CdTe QDs can be introduced by utilizing the mixture of two different stabilizers (Pen and Cys) of the same chirality. This results in the enhanced CD activity, but causes a decrease in the quantum yield and widening of the emission due to the presence of chiral defects at the nanoparticle surface.

Further research will include detailed studies of the photophysical properties of CdSe and CdTe QDs with different chiral stabilizers and the investigation of the electron transfer and energy transfer processes in these systems. We believe that our approach can be used for development of many other QDs with controlled chirality, quantum yield, photochemical and photophysical characteristics. These QDs could find important potential applications such as fluorescent chemical and biochemical chirality sensors or nanoprobes in asymmetric synthesis, catalysis, enantioseparation, biochemical analysis and medical diagnostics.

References

(1) Kitaev, V. *Journal of Materials Chemistry* **2008**, *18*, 4745.

(2) Govorov, A. O.; Fan, Z.; Hernandez, P.; Slocik, J. M.; Naik, R. R. *Nano Letters* **2010**, *10*, 1374.

(3) Zhang, J.; Albelda, M. T.; Liu, Y.; Canary, J. W. *Chirality* **2005**, *17*, 404.

(4) Schaaff, T. G.; Whetten, R. L. *The Journal of Physical Chemistry B* **2000**, *104*, 2630.

(5) Yao, H.; Miki, K.; Nishida, N.; Sasaki, A.; Kimura, K. *Journal of the American Chemical Society* **2005**, *127*, 15536.

(6) Shemer, G.; Krichevski, O.; Markovich, G.; Molotsky, T.; Lubitz, I.; Kotlyar, A. B. *Journal of the American Chemical Society* **2006**, *128*, 11006.

(7) Lieberman, I.; Shemer, G.; Fried, T.; Kosower, E. M.; Markovich, G. *Angewandte Chemie-International Edition* **2008**, *47*, 4855.

(8) Dukovic, G.; Balaz, M.; Doak, P.; Berova, N. D.; Zheng, M.; McLean, R. S.; Brus, L. E. *Journal of the American Chemical Society* **2006**, *128*, 9004.

(9) Peng, X.; Komatsu, N.; Bhattacharya, S.; Shimawaki, T.; Aonuma, S.; Kimura, T.; Osuka, A. *Nat Nano* **2007**, *2*, 361.

(10) Moloney, M. P.; Gun'ko, Y. K.; Kelly, J. M. *Chemical Communications* **2007**, 3900.

(11) Elliott, S. D.; Moloney, M. c. l. P.; Gun'ko, Y. K. *Nano Letters* **2008**, *8*, 2452.

(12) Nakashima, T.; Kobayashi, Y.; Kawai, T. *Journal of the American Chemical Society* **2009**, *131*, 10342.

(13) Carrillo-Carrión, C.; Cárdenas, S.; Simonet, B. M.; Valcárcel, M. *Analytical Chemistry* **2009**, *81*, 4730.

(14) Zhou, Y.; Yang, M.; Sun, K.; Tang, Z.; Kotov, N. A. *Journal of the American Chemical Society* **2010**, *132*, 6006.

(15) Hines, M. A.; Guyot-Sionnest, P. *The Journal of Physical Chemistry* **1996**, *100*, 468.

(16) Burda, C.; Link, S.; Mohamed, M.; El-Sayed, M. *The Journal of Physical Chemistry B* **2001**, *105*, 12286.

(17) Shieh, F.; Saunders, A. E.; Korgel, B. A. *The Journal of Physical Chemistry B* **2005**, *109*, 8538.

(18) Gaponik, N.; Talapin, D. V.; Rogach, A. L.; Hoppe, K.; Shevchenko, E. V.; Kornowski, A.; Eychmuller, A.; Weller, H. *The Journal of Physical Chemistry B* **2002**, *106*, 7177.

(19) Tian, Y.; Newton, T.; Kotov, N. A.; Guldi, D. M.; Fendler, J. H. *The Journal of Physical Chemistry* **1996**, *100*, 8927.

(20) Achermann, M.; Petruska, M. A.; Koleske, D. D.; Crawford, M. H.; Klimov, V. I. *Nano Letters* **2006**, *6*, 1396.

(21) Zhang, Q.; Russell, T. P.; Emrick, T. *Chemistry of Materials* **2007**, *19*, 3712.

(22) Liu, J.; Tanaka, T.; Sivula, K.; Alivisatos, A. P.; Frechet, J. M. J. *Journal of the American Chemical Society* **2004**, *126*, 6550.

(23) Locklin, J.; Patton, D.; Deng, S.; Baba, A.; Millan, M.; Advincula, R. C. *Chemistry of Materials* **2004**, *16*, 5187.

(24) Querner, C.; Benedetto, A.; Demadrille, R.; Rannou, P.; Reiss, P. *Chemistry of Materials* **2006**, *18*, 4817.

(25) Chen, J.; Gao, Y.; Guo, C.; Wu, G.; Chen, Y.; Lin, B. *Spectrochimica Acta Part A: Molecular and Biomolecular Spectroscopy* **2008**, *69*, 572.

(26) Chen, Y.; Rosenzweig, Z. *Analytical Chemistry* **2002**, *74*, 5132.

(27) Bao, H.; Wang, E.; Dong, S. *Small* **2006**, *2*, 476.

(28) Huang, F.; Chen, G. *Spectrochimica Acta Part A: Molecular and Biomolecular Spectroscopy* **2008**, *70*, 318.

(29) Liu, F.-C.; Cheng, T.-L.; Shen, C.-C.; Tseng, W.-L.; Chiang, M. Y. *Langmuir* **2008**, *24*, 2162.

(30) Liu, W.; Choi, H. S.; Zimmer, J. P.; Tanaka, E.; Frangioni, J. V.; Bawendi, M. *Journal of the American Chemical Society* **2007**, *129*, 14530.

(31) Zhang, Y.-h.; Zhang, H.-s.; Guo, X.-f.; Wang, H. *Microchemical Journal* **2008**, *89*, 142.

(32) Alivisatos, P. *Nat Biotech* **2004**, *22*, 47.

(33) Bruchez, M., Jr.; Moronne, M.; Gin, P.; Weiss, S.; Alivisatos, A. P. *Science* **1998**, *281*, 2013.

(34) Ni, T.; Nagesha, D. K.; Robles, J.; Materer, N. F.; Müssig, S.; Kotov, N. A. *Journal of the American Chemical Society* **2002**, *124*, 3980.

(35) Yang, Y. J.; Xiang, B. J. *Journal of Crystal Growth* **2005**, *284*, 453.

(36) Raevskaya, A. E.; Stroyuk, A. L.; Kuchmiy, S. Y.; Azhniuk, Y. M.; Dzhagan, V. M.; Yukhymchuk, V. O.; Valakh, M. Y. *Colloids and Surfaces A: Physicochemical and Engineering Aspects* **2006**, *290*, 304.

(37) Bhuse, V. M.; Hankare, P. P.; Garadkar, K. M.; Khomane, A. S. *Materials Chemistry and Physics* **2003**, *80*, 82.

(38) Kappe, C. O.; Stadler, A. *Microwaves in Organic and Medicinal Chemistry*; Wiley-VCH, 2005.

(39) *http://www.biotage.com/DynPage.aspx?id=22052.*

(40) Peng, X.; Wickham, J.; Alivisatos, A. P. *Journal of the American Chemical Society* **1998**, *120*, 5343.

(41) Fery-Forgues, S.; Lavabre, D. *Journal of Chemical Education* **1999**, *76*, 1260.

(42) Talapin, D. V.; Rogach, A. L.; Shevchenko, E. V.; Kornowski, A.; Haase, M.; Weller, H. *J. Am. Chem. Soc.* **2002**, *124*, 5782.

(43) Yu, Z.; Li, J.; O'Connor, D. B.; Wang; Barbara, P. F. *The Journal of Physical Chemistry B* **2003**, *107*, 5670.

(44) Spanhel, L.; Haase, M.; Weller, H.; Henglein, A. *Journal of the American Chemical Society* **1987**, *109*, 5649.

(45) Okamura, M.; Ebina, K.; Akimoto, S.; Yamazaki, I.; Uosaki, K. *Journal of Photochemistry and Photobiology A: Chemistry* **2006**, *178*, 156.

(46) Rawalekar, S.; Kaniyankandy, S.; Verma, S.; Ghosh, H. N. *The Journal of Physical Chemistry C* **2009**, *114*, 1460.

(47) Gill, R.; Willner, I.; Shweky, I.; Banin, U. *The Journal of Physical Chemistry B* **2005**, *109*, 23715.

(48) Pan, D.; Wang, Q.; Pang, J.; Jiang, S.; Ji, X.; An, L. *Chemistry of Materials* **2006**, *18*, 4253.

(49) Bawendi, M. G.; Carroll, P. J.; William, L. W.; Brus, L. E. *The Journal of Chemical Physics* **1992**, *96*, 946.

(50) Pietryga, J. M.; Schaller, R. D.; Werder, D.; Stewart, M. H.; Klimov, V. I.; Hollingsworth, J. A. *Journal of the American Chemical Society* **2004**, *126*, 11752.

(51) Schlegel, G.; Bohnenberger, J.; Potapova, I.; Mews, A. *Physical Review Letters* **2002**, *88*, 137401.

(52) Wang, X.-Y.; Zhang, J.-Y.; Nazzal, A.; Darragh, M.; Xiao, M. *Applied Physics Letters* **2002**, *81*, 4829.

(53) Wang, X.; Qu, L.; Zhang, J.; Peng, X.; Xiao, M. *Nano Letters* **2003**, *3*, 1103.

(54) Zhao, K.; Li, J.; Wang, H.; Zhuang, J.; Yang, W. *J. Phys. Chem. C* **2007**, *111*, 5618.

(55) Boulesbaa, A.; Huang, Z.; Wu, D.; Lian, T. *The Journal of Physical Chemistry C* **2009**, *114*, 962.

(56) Javier, A.; Magana, D.; Jennings, T.; Strouse, G. F. *Applied Physics Letters* **2003**, *83*, 1423.

(57) Gong, H.-M.; Zhou, Z.-K.; Song, H.; Hao, Z.-H.; Han, J.-B.; Zhai, Y.-Y.; Xiao, S.; Wang, Q.-Q. *Journal of Fluorescence* **2007**, *17*, 715.

(58) Baker, D. R.; Kamat, P. V. *Langmuir* **2010**, *26*, 11272.

(59) Haifeng Bao, E. W. S. D. *Small* **2006**, *2*, 476.

(60) He, Y.; Lu, H. T.; Sai, L. M.; Lai, W. Y.; Fan, Q. L.; Wang, L. H.; Huang, W. *J. Phys. Chem. B* **2006**, *110*, 13352.

(61) He, Y.; Sai, L. M.; Lu, H. T.; Hu, M.; Lai, W. Y.; Fan, Q. L.; Wang, L. H.; Huang, W. *Chem. Mater.* **2007**, *19*, 359.

(62) *Statistics for the quality control chemistry laboratory*; Mullins, E., Ed.; The Royal Society of Chemistry, Cambridge, 2003.

(63) Tang, Z.; Wang, Y.; Shanbhag, S.; Kotov, N. A. *J. Am. Chem. Soc.* **2006**, *128*, 7036.

(64) Zheng, R.; Guo, S.; Dong, S. *Inorg. Chem.* **2007**, *46*, 6920.

(65) Byrne, S. J.; Corr, S. A.; Rakovich, T. Y.; Gun'ko, Y. K.; Rakovich, Y. P.; Donegan, J. F.; Mitchell, S.; Volkov, Y. *Journal of Materials Chemistry* **2006**, *16*, 2896.#

(66) Yu, W. W.; Wang, Y. A.; Peng, X. *Chem. Mater.* **2003**, *15*, 4300.

Chapter 6: Time Resolved Ultrafast Spectroscopy Studies of Chiral CdSe QDs

6.1 Introduction

The synthesis of chiral, optically active, light emitting penicillamine (Pen) stabilised CdS and CdSe QDs was relatively recently developed by our group[1-4]. Previously we have demonstrated that our chiral quantum dots show complementary circular dichroism for the *D*- and *L*- penicillamine stabilised CdSe, in the spectral region characteristic of the exciton bands[1,3,4] (see also previous Chapter). These QDs are also luminescent with relatively broad band emission. It was shown that this emission is not due to intrinsic recombination of the hole-electron pairs but rather originates from surface-defect states[2]. It was found that the emission decays multiexponentially and the photoluminescence lifetime strongly depends on the wavelength of the emission. These results have suggested the presence of a wide range of emitting excited states in the electronic structure of the system[4]. Since one of the key properties determining the behaviour and functionality of these nanoparticles is their surface, knowledge about the types of electron (and hole) surface defects, trapping mechanisms and their impact on energy relaxation and charge recombination processes is particularly important. The main aim of this part of the project was to investigate chiral CdSe nanoparticles using ultrafast transient spectroscopic techniques. The relaxation dynamics of photo-excited carriers in water-soluble, penicillamine capped, optically active and luminescent chiral CdSe quantum dots (QDs) were investigated with three pump-probe techniques. Broad-band UV-visible transient absorption (TA) complemented by picosecond time resolved infrared (ps-TRIR) transient absorption was used to gain insight into the ultrafast relaxation dynamics of these chiral CdSe QDs. Nanosecond laser flash photolysis spectroscopy has also been applied in order to probe longer lived species record transient decays. This range of spectroscopic techniques allows us to investigate from the picosecond up to the millisecond timescale. Importantly, ps experiments were carried out at a range of energies down to ca. 30 μJ cm^{-2}, where only single photon excitation is expected. Although these methods have been previously applied to investigate the relaxation properties of the excitonic

transitions in intrinsic CdSe nanoparticles and various core-shell QD structures,[5,6] the relaxation properties of defect emitting chiral QDs have not previously been reported.

6.2 UV-visible Transient Absorption Spectroscopy Studies of Penicillamine Stabilised CdSe QDs

Penicillamine stabilised CdSe QDs have been prepared according to our published procedure[4] (Chapter 5) by microwave heating of $Cd(ClO_4)_2$, Na_2SeSO_3 and penicillamine in an appropriate ratio in basic aqueous solution. The penicillamine stabilising ligand was used in both its enantiomeric forms, as well as the racemate. As we previously observed the photoluminescence properties of both enantiomerically stabilised (*D*-, *L*-) penicillamine, as well as the racemate (*Rac*-) CdSe QDs were very similar[4]. The relaxation properties probed by ultrafast techniques were also found to be quite similar with no significant difference between observed behaviour.

The representative picosecond-transient absorption spectra of enatiomerically (*L*- Pen) capped CdSe quantum dots after excitation at 400 nm are shown in Figure 6.1 (a). The spectra display two distinct features; the strong bleach centred at 422 nm, in line with the first allowed energy transition, and broad transient absorption above 470 nm. Similar results were obtained for *D*- and *Rac*- Pen CdSe QDs. The strong bleaching in the region of excitonic absorption can be explained by the filling of the lowest lying electron quantized level (1S) in the conduction band[7]. The intraband relaxation in CdSe QDs is an extremely fast process[8,9], so the transient absorption can originate from both the 1S state or lower lying defect traps (if depopulation of 1S state is fast enough). In order to address this question directly the kinetics of the bleach and transient absorption recovery were compared. It is clearly visible that both the transient decay profile (e.g. measured at 600 nm) and the bleaching recovery (measured at 422 nm) have almost identical kinetics. The normalised data is shown in Figure 6.1 (b). This indicates that the process causing the transient decay leads to reformation of the ground state. The decay profile at 100 nJ (ca. 0.56 mJ cm^{-2}) shows a substantial amount (35%) of a very rapid process (less than 4 ps). Data was also recorded at a range of pulse energies (e.g. 5 nJ, Figure 6.1 (c)). The contribution of this rapid process is significantly reduced (from 35 to 15 %) under conditions where single photon

excitation is expected i.e. when a lower excitation energy (e.g. 5 nJ; ca. 30 μJ cm^{-2}) pulse is used (Normalised Figure 6.1 (d)). The very rapid process observed at higher energies can be attributed to multi-excitonic processes. Analysis of the decay profiles supports this, as low energy decays (5 nJ) can be successfully fitted using only a biexponential function, whereas higher energies (100 nJ) require triexponentials, indicating the presence of new (multi-excitonic) processes occurring (Table 6.1).

As expected, the bleach decay is not completed even 3 ns after excitation due to long-lived species, including radiative electron-hole recombination processes or caused by trapping at defects, as reported previously[4].

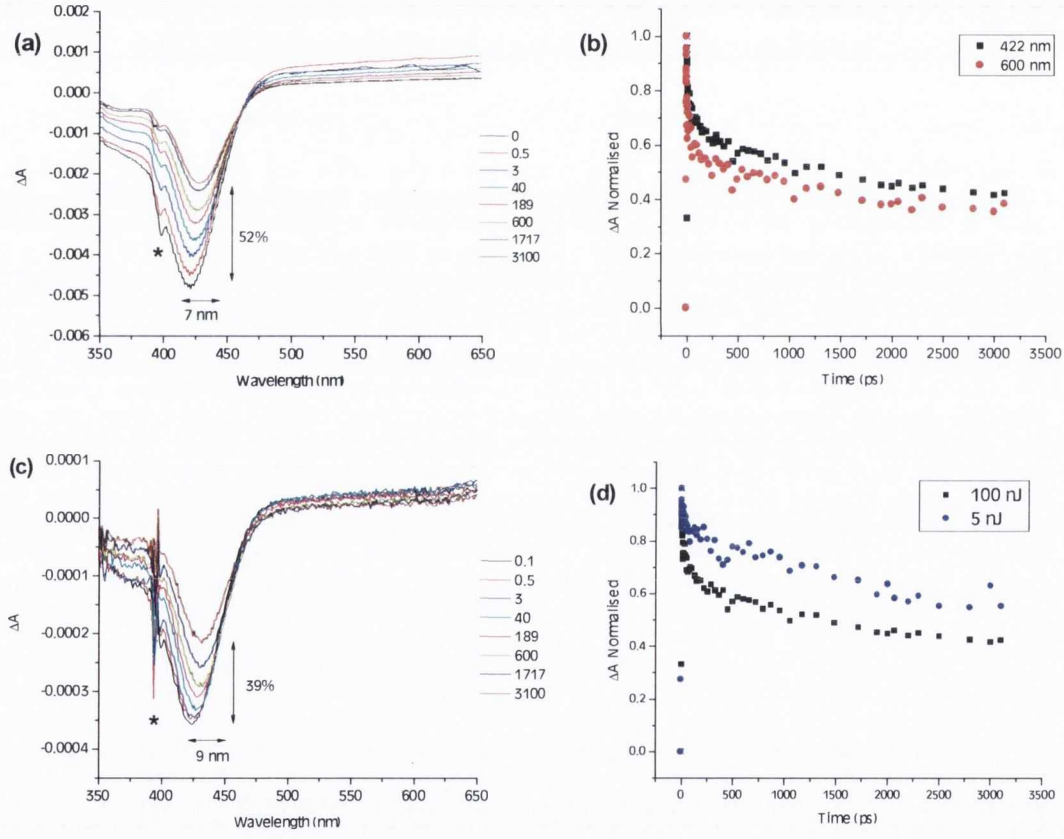

Figure 6.1: (a) and (c) Picosecond transient absorption spectra following 400 nm excitation of *L*-Pen CdSe at 100 nJ (0.56 mJ/cm^2) and 5 nJ (28 μJ/cm^2), respectively. Artefact (*) at about 400 nm is due to excitation line. (b) Normalized decay curves of the bleach (422 nm, black) and transient absorption (600 nm, red) following 400 nm excitation of L-Pen CdSe at 100 nJ. The bleach decay curve has been inverted for comparison. (d) Comparison of the normalised bleach decays at 100 nJ (black) and 5 nJ (blue) at 422 nm.

Table 6.1: Lifetime parameters obtained from tri- and bi- exponential fitting of ps-TA decay curves for pulse energies of at 100 nJ (0.56 mJ/cm^2) and 5 nJ (28 μJ/cm^2), respectively.

CdSe L Pen	τ_1 (ps)	τ_2 (ps)	τ_3 (ps)
100 nJ tri-exp	3.94	109	1863
5 nJ bi-exp	64	3004	N/A

6.3 Picosecond Time-Resolved Infrared Spectroscopy (ps-TRIR) of Penicillamine Stabilised CdSe QDs

It has been previously demonstrated that mid-IR is a useful tool to monitor relaxation properties of various QDs systems[10-14]. In fact, intra-band transitions (between electron quantized states) should appear as a broad transient in the mid-IR region[10,11]. Additionally we intended to see if the surface defect states might have a characteristic signature, possibly originating from the capping ligands, in the mid-IR.

The ps-TRIR spectrum of *L*- Pen stabilized CdSe QDs measured in H_2O is presented in Figure 6.2. The transient absorption band is very broad owing to the electronic nature of intra-band transitions. Similar structureless features were also observed in the very wide spectral range covered by the ULTRA system ca. 1300 cm^{-1} to 2800 cm^{-1} for *D*- and *Rac*-Pen CdSe samples (Figure 6.3). Significantly no structured absorption for the surface-bound penicillamine capping ligands is observed.

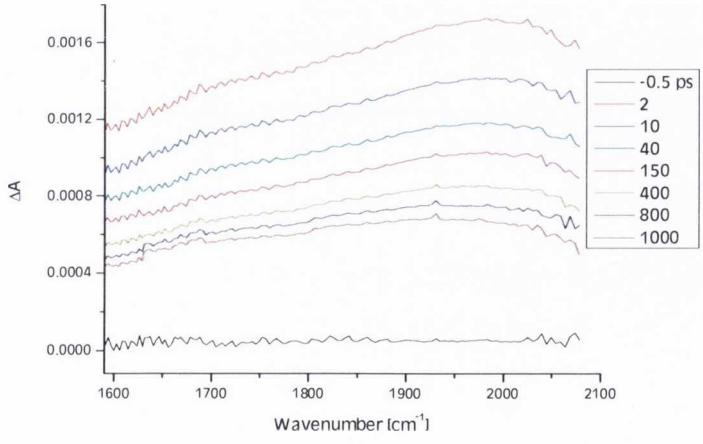

Figure 6.2: TRIR spectra following 400 nm excitation of *L*-Pen CdSe at 50 nJ (0.28 mJ/cm^2) in H_2O

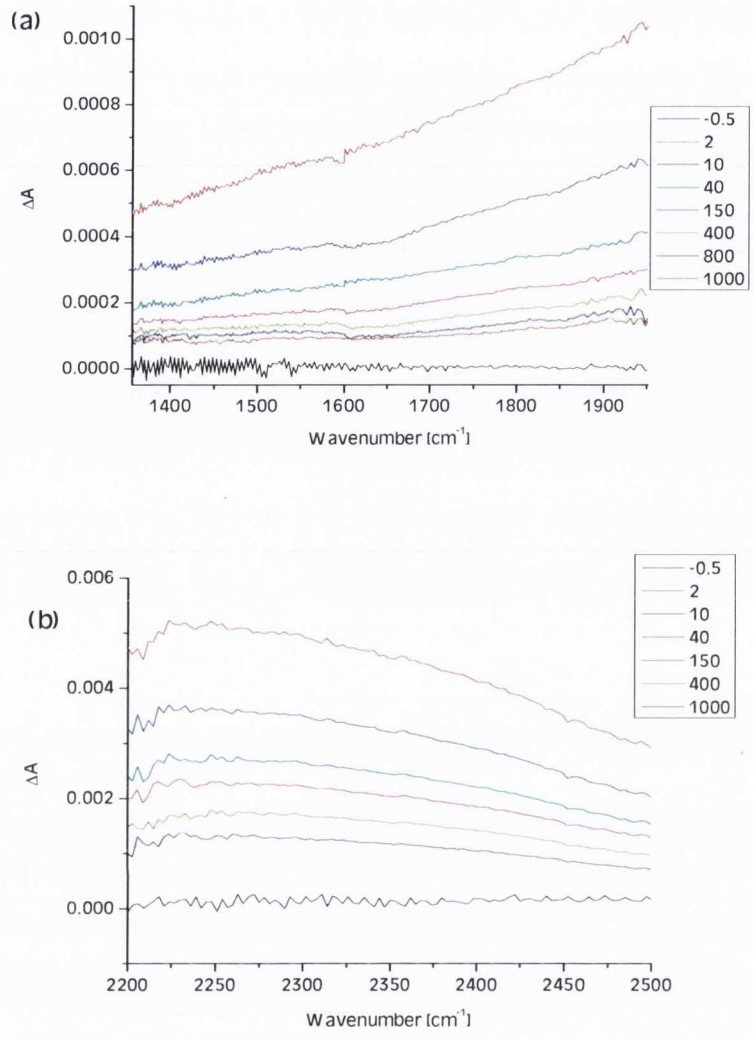

Figure 6.3: TRIR spectra following 400 nm excitation of (a) *D*-Pen and (b) *Rac*-Pen CdSe at 50 nJ (0.28 mJ/cm^2) in H_2O.

Taking advantage of the excellent time resolution of the ULTRA system, the growth of the IR band was also studied with femtosecond resolution (Figure 6.4 (a)). One can see that the transient absorption reaches a maximum signal within about 200 fs (limited by ULTRA resolution), consistent with extremely fast intra-band relaxation. It is evident (Figure 6.4 (b)) that the IR transient decay is distinctly non-exponential. The excellent quality of the kinetics data in the IR region allows for easily distinguishing the order of multiexponential decay. We found that for both enantiomeric (*D*-, *L*- Pen) and racemic (*Rac*- Pen) forms of QDs, the decay curves could be satisfactorily analysed using a three exponential decay model. Similar kinetics were obtained for *D*-, *L*- and *Rac*- Pen QDs (Figure 6.4 (b), 6.5 (a), 6.5 (b)). The corresponding time constants (τ) of

the particular components on the picosecond timescale are summarised in Table 6.2. The decays show the existence of three regions with different time constants: a fast initial stage with a time constant of the order of single ps, followed by two slower decays of the order of ten and hundreds of picoseconds. Although the corresponding lifetime values for all three samples are comparable in order of magnitude, it may be noted that all three lifetime values associated with the racemate, *Rac*-Pen, are smaller than for the enantiomerically capped CdSe.

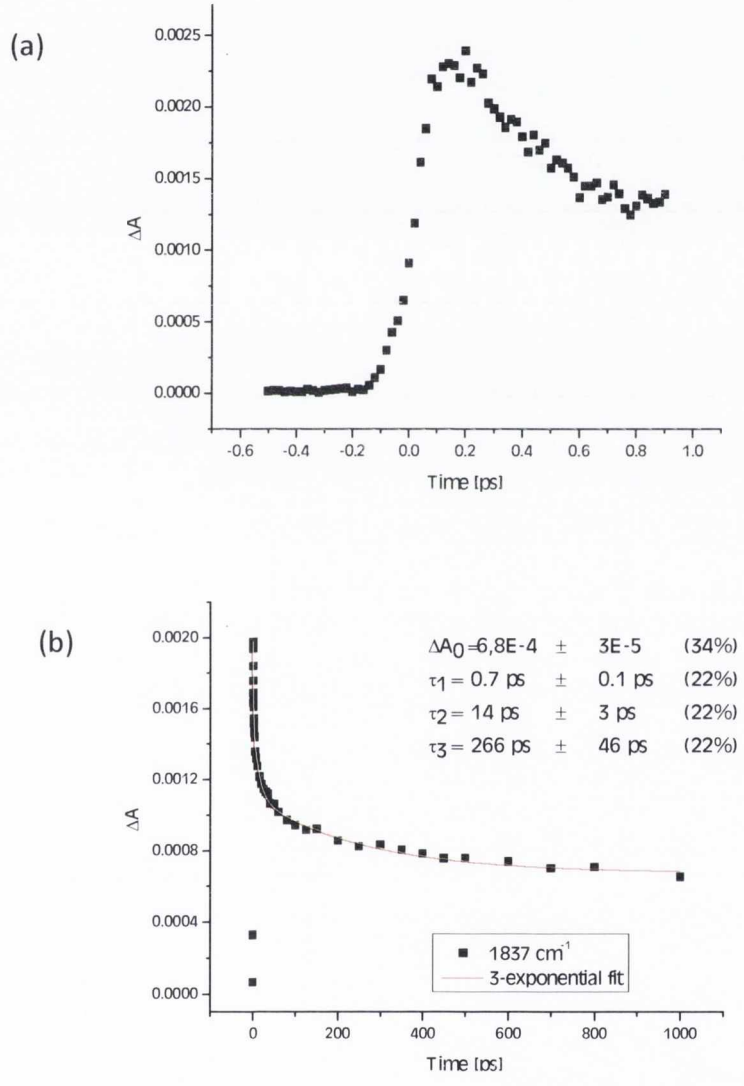

Figure 6.4: (a) The fs growth of the IR transient and (b) triexponential fit of the IR transient absorption decay curve of *L*- Pen CdSe (1837 cm^{-1}). The fitting parameters (baseline parameter A_0, lifetimes τ and percentage contributions) are given in the inset.

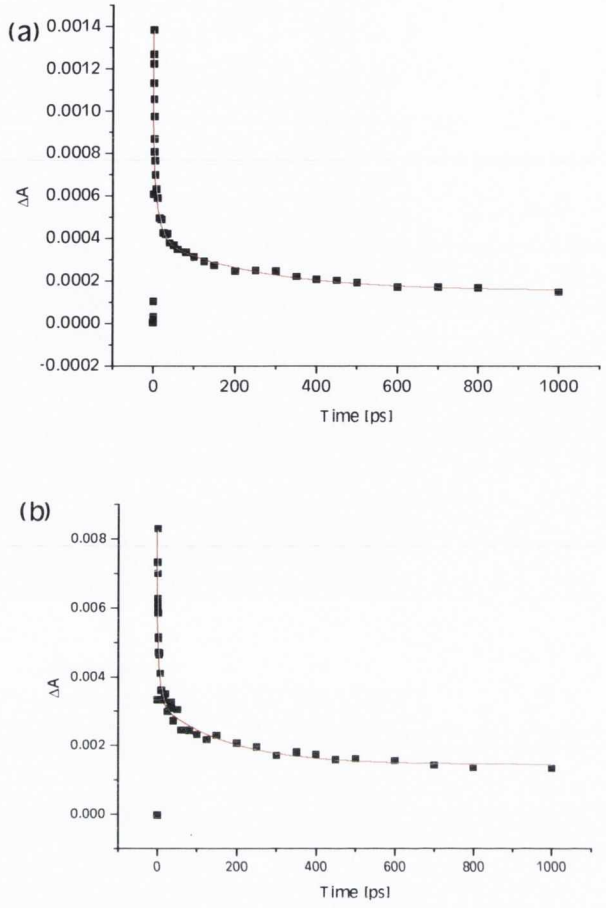

Figure 6.5: Triexponential fit of the IR transient absorption decay curve of (a) *D*- and (b) *Rac*-Pen CdSe (1837 cm^{-1}) for comparison.

Table 6.2: Lifetime parameters obtained from 3-exponential fitting of ps-TRIR decay curves. Pulse energy at 50 nJ (0.28 mJ/cm^2).

Sample	τ_1 [ps]	τ_2 [ps]	τ_3 [ps]
L-Pen	0.7 ± 0.1	14 ± 3	266 ± 46
D-Pen	1.1 ± 0.1	13 ± 2	254 ± 41
Rac-Pen	0.5 ± 0.1	7 ± 2	178 ± 37

The transient decay kinetics in the mid-IR are quite similar to those observed in visible range (see Figure 6.6, the bleach decay has been inverted for comparison). The contribution of very fast component differs only slightly and there is excellent

agreement at longer delays. This is not surprising if, as expected, both techniques are probing the depopulation of the lowest lying electron quantized 1S state.

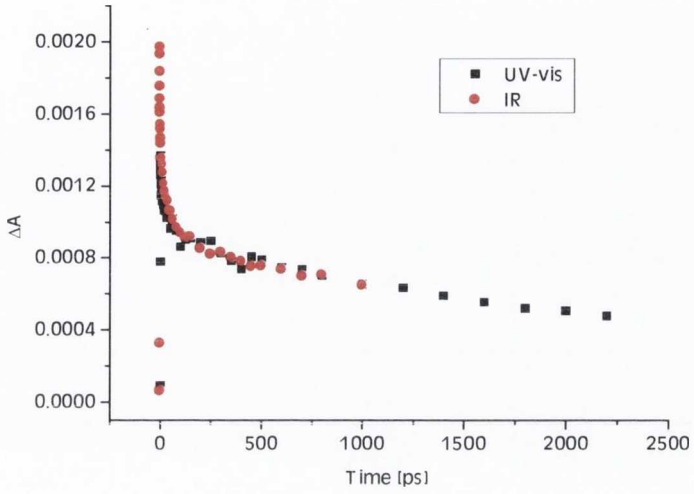

Figure 6.6: Comparison of bleach (420nm, inverted) and IR kinetics at 1000 ps (50nJ, 1837 cm^{-1}), 400nm excitation.

6.4 Power Dependent Studies

Owing to the high sensitivity of the ULTRA system in the mid-IR region, low pump intensity (at 10 nJ) studies were performed. Figure 6.7 shows the comparison of normalized IR transient decay curves for *L*-Pen stabilized CdSe recorded at 50 nJ and 10 nJ. It is evident that, at lower pump intensities, the contribution of the fast initial ps component is strongly (but not entirely) diminished. Similar behaviour was observed in the visible region for *Rac*-Pen capped CdSe QDs. This strong power dependence points towards the importance of exciton-exciton annihilation processes. This is consistent with our calculations which show that the average number of excitons per quantum dot is about 7 and 1 for 50 nJ and 10 nJ, respectively.

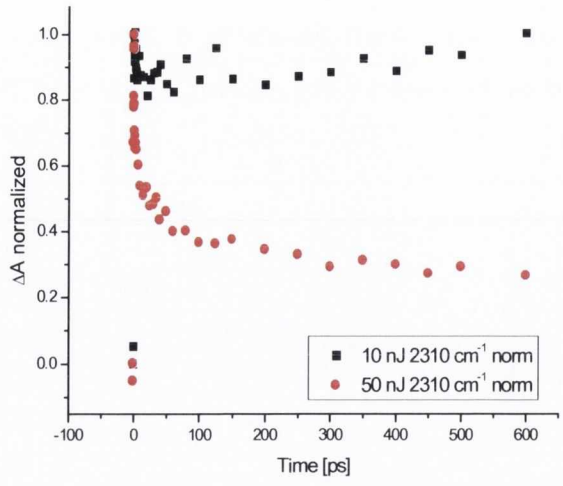

Figure 6.7: Normalised IR transient absorption decay curves recorded using 10 nJ and 50 nJ, 400 nm excitation.

6.5 Nanosecond Laser Flash Photolysis Studies

As the quantum yield of emission of these chiral CdSe particles does not exceed 10%[4], and as the picosecond traces, e.g. Figure 6.4 (b), provide evidence for long-lived species, the question arises if there are any states (below the emitting defect states) which may trap a charge and constitute competitive non-radiative deactivation pathways? And if so, what is the nature of these non-radiative deactivation channels? To address this question laser flash photolysis of *L*-Pen capped CdSe using an excimer laser (308 nm pulses) was performed.

The transient absorption spectra (Figure 6.8) at longer time scales were recorded using two kinetics method (data slicing of point-by point scanning through the spectral range in 10 nm steps using PMT and scope) and spectral mode (using an ICCD camera) of a spectrometer. The transient absorption spectra on the longer time scale are quite similar to those recorded in the ps scale. The strong bleach corresponding to the ground state depletion is centred at 440 nm. Above 470 nm a broad transient absorption band is observed. Since deactivation of the 1S state for CdSe QDs should proceed in a timescale of tens of nanoseconds we believe that the long-lived transient originates from deep levels associated with surface defects. It is clearly visible that the broad transient absorption band (above 470 nm) decays faster than the bleach, consistent with kinetic traces (see Figure 6.8). There is also a significant transient absorption band in the range of 350-400 nm which was not observed in the ps study. The fact that this low

wavelength transient appears in the microsecond range suggests that it originates from deep lying states which become filled after relatively long time (more than 3 ns) following 308 nm excitation. The question of whether this is indeed a single band or a net effect of overlapping between transient and bleach (from second excitonic transition at 360 nm) remains to be elucidated. The hypothesis of strong overlapping of the bleach and transient bands is consistent with the observed position of the long-lived bleach which is at 440 nm (in contrast to first excitonic transition centred at 422 nm).

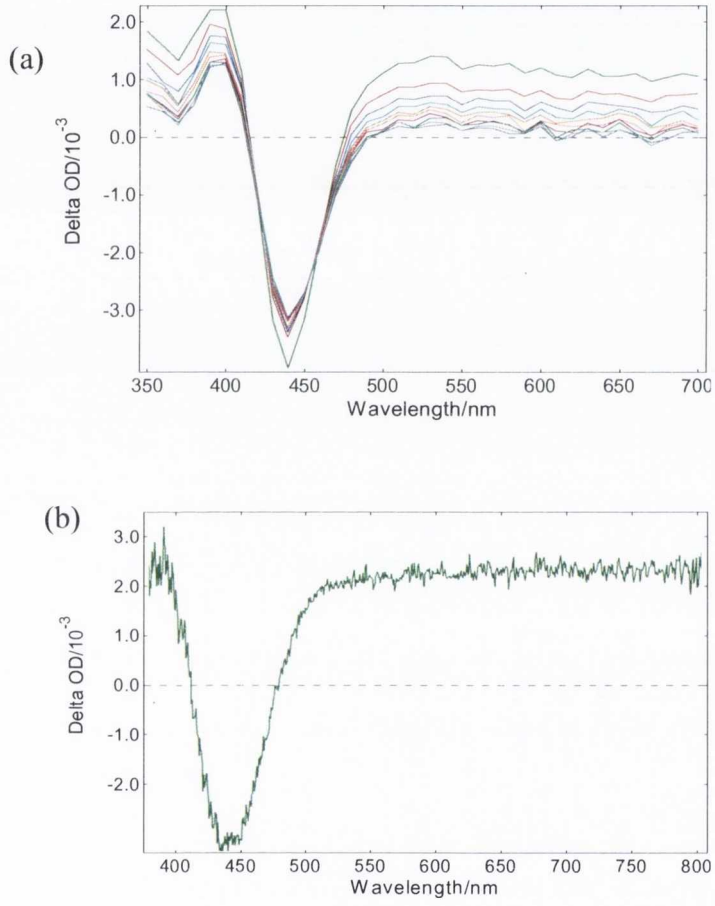

Figure 6.8: (a) Time resolved absorption spectra of *L*-Pen CdSe obtained by kinetic traces slicing at desired time windows and delays (0, 16, 31, 47, 62, 78, 95, 109, 125, 140 μs) measured at 308 nm excitation (58 mJ/cm^2). Kinetic curves were recorded by averaging 10 laser shots per one wavelength measurement with steps of 10 nm.
(b) Transient absorption spectrum of *L*-Pen stabilized CdSe recorded using an ICCD camera over initial 3 μs after excitation (signal was averaged from 60 laser shots).

Figures 6.9 (a) and 6.9 (b) show the transient absorption kinetic traces for *L*-Pen capped CdSe QDs measured at 440 nm and 600 nm, respectively, in the millisecond

range. It is visibly apparent that both the transient absorption and the bleach recovery are not fully decayed, even several milliseconds after excitation. The transient absorption at 600 nm decays bi-exponentially to less than 1/3 of its initial value in the microsecond range (calculated lifetimes are 71 μs and 749 μs). On the same timescale the bleach decays mono-exponentially and significantly slower with a lifetime of > 1.7 ms. Since deactivation of the 1S state for CdSe QDs should proceed on a timescale of tens of nanoseconds, this data suggests that below the emitting states (which have ns kinetics) there are a range of non-radiative deep traps constituting the initial states for transient absorption (above 500 nm). Depopulation of these microsecond states occurs via new longer lived (ms range) state(s), which control the rate of slow bleach recovery (in the nanosecond scale the bleach decays incompletely with kinetics comparable to photoluminescence). It is important to emphasise that the photoluminescence decay is essentially completed within 200 nanoseconds (depending on wavelength)[4] and no luminescence signal has been detected in the micro- or milli-second timescale.

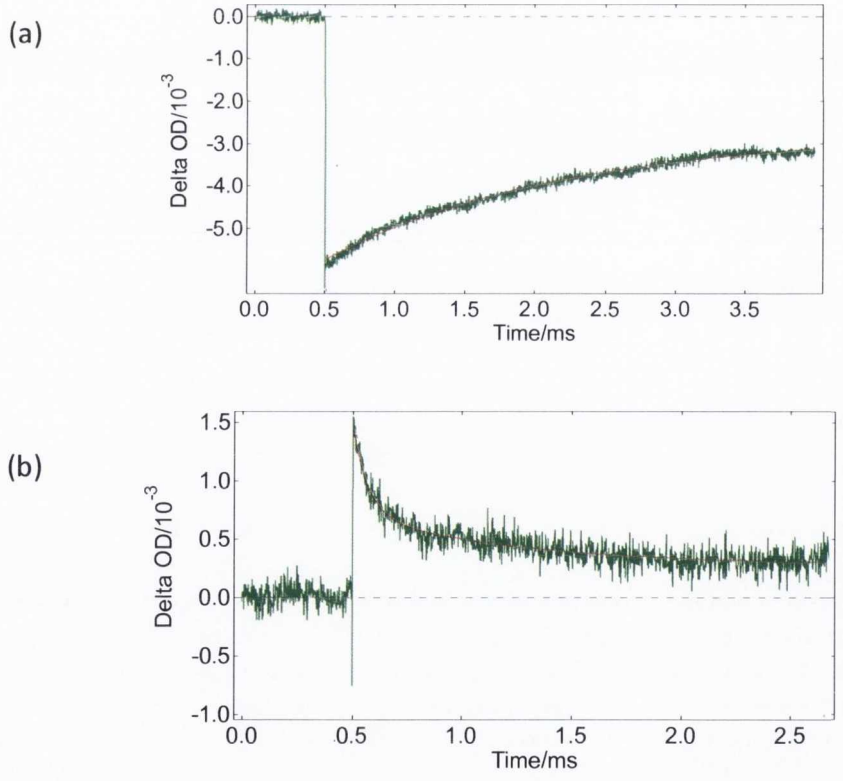

Figure 6.9: (a) The decay curve of the bleach at 440 nm and (b) transient at 600 nm for *L*-Pen capped CdSe. Red lines represent (a) mono and (b) biexponential fits to the data. Kinetic curves were recorded by averaging 50 laser shots.

The overall results of the above data, combined with those detailed previously in Chapter 5, can best be illustrated in the form of an energy diagram for CdSe Pen QDs (Figure 6.10). This clearly highlights the wide range of defect-related energy levels present in the system, and the competing pathways for the exciton recombination upon excitation, both radiative and non-radiative.

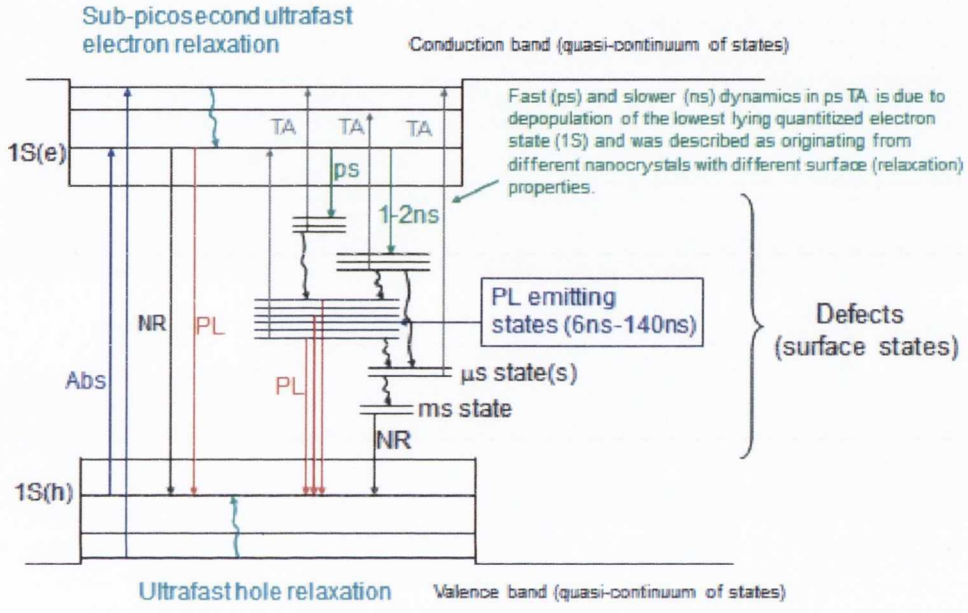

Figure 6.10: Suggested electronic structure of chiral CdSe QDs.

An important question which appears is what is the physical origin of the initial fast ps component? In as much as direct electron intra-band relaxation is an extremely fast process (<1 ps), the bleaching decays should represent depopulation rate of the lowest electron quantized states. However, initial picoseconds decays are definitely too fast to be explained by direct electron-hole recombination between quantized electron and hole states. It is therefore more likely that depopulation of the lowest electron quantized state is either a direct consequence of exciton-exciton annihilation processes or is due to new, surface-defect related states. Our power dependent studies show that exciton-exciton annihilation processes are important for the fast (ps) relaxation at energies greater than 10 nJ. However, even at energies as low as 5 nJ, the fast initial component does not disappear completely. It was earlier suggested that both fast (ps)

and slower dynamics in CdSe QDs arise from different quantum dots with different numbers and/or types of traps, implying different relaxation (surface) properties[15]. This suggests that depopulation of the 1S state via defects cannot be excluded in the ultrafast timescale.

In addition, the visible bleach decay exhibits a small redshift as a function of time (422 nm at 2 ps to 429 nm at 3.1 ns). This effect appears to be independent of pulse energy, at least in the 5-100 nJ range. This could be due to size distribution, but more probably arises from a shift in transient absorption which overlaps the bleach. Alternatively, at higher laser power the shift might also be induced by effects such as a trapped-carrier-induced Stark effect. Relatively slow relaxation dynamics suggest that excited carriers are localized in trap states for a long time and the electric field caused by this localization might induce field (Stark) effects in QDs. An induced Stark effect results in the synchronous shift of all optical transitions and redistribution of oscillator strength mainly due to spatial separation of electron and holes[6,16-18]. The presence of an electric field can also result in access to transitions which normally are forbidden (by selection rules). It was previously demonstrated in previous published work that high excitation intensities cause red-shifted exciton absorption (corresponding to the bleach bands) of the CdS and CdSe nanocrystals and the appearance of the new transient[19,20], however, the origin of observed new transient bands has not been unambiguously determined.

Another effect which should be considered is the possibility of biexcitonic transitions which are strongly enhanced through the presence of impurities and defects. Such transitions were predicted theoretically and experimentally observed as the induced absorption feature on the high energy side of the bleached exciton[21,22]. In the microsecond time range the bleach position is invariant with time and deep levels (traps) seems to be the most likely reason for the observed transient absorption. These deep lying levels which give contribution to the extremely long bleach decay can probably be associated with surface defects, however, the exact nature of these states and the trapping mechanisms requires further detailed power dependent investigations.

6.6 Investigation of Chiral CdSe Prepared in D_2O

In theory, if the IR bands corresponding to H_2O could be eliminated, signals arising from the stabilising ligands on the surface these particles could possibly be detected and studied using TRIR. In order to achieve this, CdSe Pen QDs were synthesised exactly as before, but substituting D_2O in place of H_2O in every step. The results obtained were quite interesting and intriguing. According to the absorbance spectra these QDs are much smaller than those synthesised in H_2O for the same time duration of microwave irradiation. As a result these QDs demonstrate a dramatically blue-shift by almost 50 nm band edge (Figure 6.11).

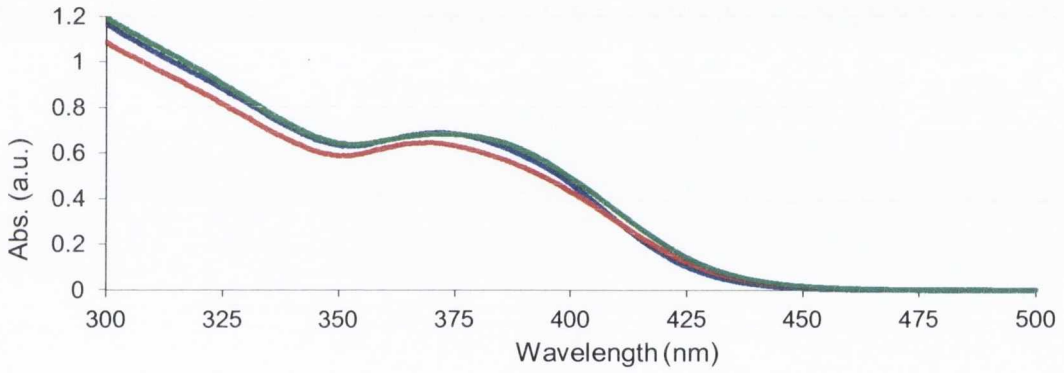

Figure 6.11: Uv-vis absorbance spectrum of D-, L- and Rac- Pen CdSe QDs synthesised in D_2O.

The corresponding fluorescence spectra of QDs in D_2O are also shifted from their H_2O synthesised counterparts (Figure 6.12).

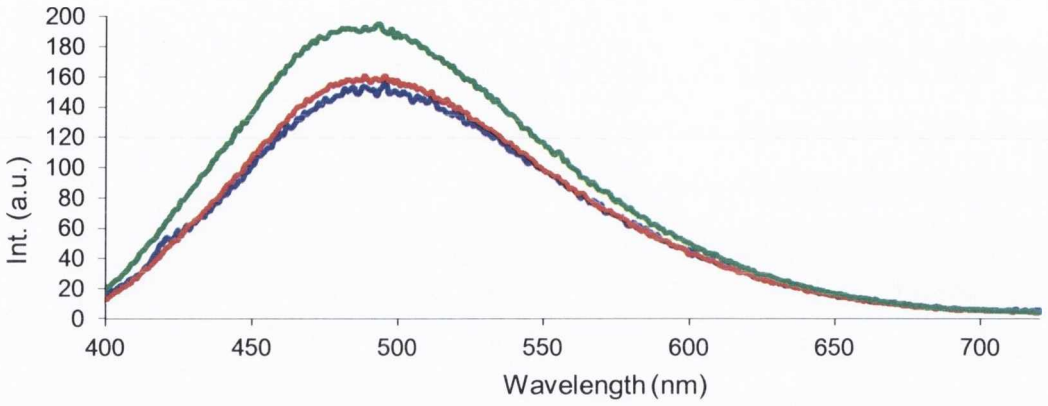

Figure 6.12: PL spectrum of D-, L- and Rac- Pen CdSe QDs synthesised in D_2O.

As can be seen, these QDs still exhibit broad band defect emission, with the emission maximum again blue-shifted when compared to the equivalent QDs synthesised in H_2O. Detailed lifetime studies still have to be completed on these QDs but initial experiments show that these defect emitters have similar long lived emission that is best analysed using tri-exponential fittings.

TRIR measurements on these QDs, carried out in exactly the same manner as outlined before, showed strikingly different results when compared to those in H_2O (Figure 6.13). There is now the clear presence of peaks which were absent in the TRIR scans of similar QDs in H_2O. The exact origin of these signals still needs to be elucidated.

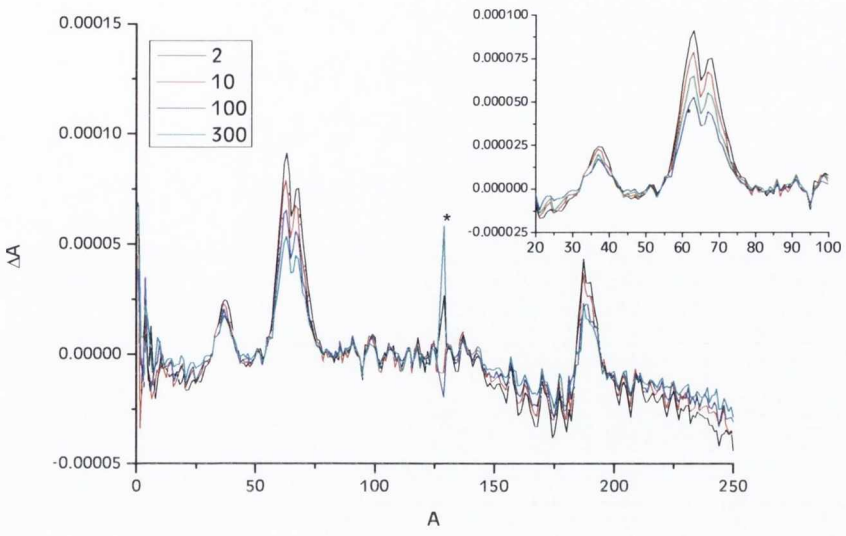

Figure 6.13: TRIR spectra following 400 nm excitation of *L*-Pen CdSe at 100 nJ (0.56 mJ/cm^2) in D_2O. Artefact (*) is due to switching from the 1st to the 2nd IR detector.

Thus we have a clear isotope effect here, which results in dramatic changes in QD sizes and behaviour. Such isotopic related phenomena have never before been reported for semiconducting QDs, and indeed there is scant literature of this effect in the whole field of nanoparticle research, the only relevant papers related to gold nanoparticles[23,24]. The results obtained here, while entirely novel, are still preliminary and a great deal of further research is necessary to understand and explain the changes brought about by D_2O. The most likely explanation of the blue-shift effect and synthesis of smaller particles is that, as the hydrogen atom is lighter than deuterium; the H-O bonds can vibrate at lower frequency and energy than D-O. This means that microwave irradiation of the H_2O based reactions results in greater energy transfer to the solution and the dissolved precursors than it does in D_2O. The increased amount of supplied energy in the case of H_2O thus drives the reaction further than in D_2O, resulting in larger QDs. To corroborate this, more detailed investigation is required, such as comparison of these two solvent reactions under conventional heating and the results of the corresponding spectroscopic studies.

6.7 Conclusions

In conclusion, we have successfully investigated the electronic dynamics of synthesised chiral CdSe quantum dots and discovered that they are determined by both exciton interactions and the trapping at defect sites. In particular, UV-visible transient absorption and picosecond TRIR transient absorption spectroscopy studies have demonstrated that transient absorption in the ultrafast scale originates from the lowest lying electron quantized state and that the rate of depopulation of this state is strongly power dependent. Whereas ps-UV-visible TA spectra show both bleach and transient features which are associated with depopulation of the lowest lying electron quantized state, the infrared transient bands are broad and structureless owing to the nature of intraband transitions. The mid-IR transient absorption and excitonic bleach recovery is only partial and its decay kinetics were found to be multiexponential in nature. The initial picosecond decay component is attributed to exciton-decay processes and to trapping by surface states.

Using nanosecond laser flash photolysis spectroscopy we have also provided direct evidence that there are, in the electronic structure, non-emitting and relatively long-lived (up to the millisecond timescale), deep levels which constitute additional, competitive deactivation channels to the photoluminescence. The broad transient absorption in flash photolysis spectroscopy was ascribed as arising from the defect states.

Successful synthesis of CdSe Pen was also achieved in D_2O, giving very interesting results, which are caused by isotope effects. We plan to investigate this phenomenon in detail in the near future.

References

(1) Moloney, M. P.; Gun'ko, Y. K.; Kelly, J. M. *Chem. Commun.* **2007**, 3900.

(2) Elliott, S. D.; Moloney, M. c. l. P.; Gun'ko, Y. K. *Nano Letters* **2008**, *8*, 2452.

(3) Govan, J. E.; Jan, E.; Querejeta, A.; Kotov, N. A.; Gun'ko, Y. K. *Chem. Commun.* **2010**, *46*, 6072.

(4) Gallagher, S. A.; Moloney, M. P.; Wojdyla, M.; Quinn, S. J.; Kelly, J. M.; Gun'ko, Y. K. *J. Mater. Chem.* **2010**, *20*, 8350.

(5) Cretí, A.; Anni, M.; Rossi, M. Z.; Lanzani, G.; Leo, G.; Della Sala, F.; Manna, L.; Lomascolo, M. *Physical Review B* **2005**, *72*, 125346.

(6) Rawalekar, S.; Kaniyankandy, S.; Verma, S.; Ghosh, H. N. *The Journal of Physical Chemistry C* **2009**, *114*, 1460.

(7) Huang, J. E.; Huang, Z. Q.; Jin, S. Y.; Lian, T. Q. *Journal of Physical Chemistry C* **2008**, *112*, 19734.

(8) Malko, A. V.; Mikhailovsky, A. A.; Petruska, M. A.; Hollingsworth, J. A.; Klimov, V. I. *Journal of Physical Chemistry B* **2004**, *108*, 5250.

(9) Klimov, V. I. *Journal of Physical Chemistry B* **2000**, *104*, 6112.

(10) Burda, C.; Link, S.; Mohamed, M.; El-Sayed, M. *Journal of Physical Chemistry B* **2001**, *105*, 12286.

(11) Mikhailovsky, A. A.; Xu, S.; Klimov, V. I. *Review of Scientific Instruments* **2002**, *73*, 136.

(12) Burda, C.; Link, S.; Mohamed, M. B.; El-Sayed, M. *Journal of Chemical Physics* **2002**, *116*, 3828.

(13) Jhonsi, M. A.; Kathiravan, A.; Renganathan, R. *Journal of Luminescence* **2009**, *129*, 854.

(14) Peng, P.; Sadtler, B.; Alivisatos, A. P.; Saykally, R. J. *Journal of Physical Chemistry C* **2010**, *114*, 5879.

(15) Klimov, V. I.; McBranch, D. W.; Leatherdale, C. A.; Bawendi, M. G. *Physical Review B* **1999**, *60*, 13740.

(16) Norris, D. J.; Sacra, A.; Murray, C. B.; Bawendi, M. G. *Physical Review Letters* **1994**, *72*, 2612.

(17) Rawalekar, S.; Kaniyankandy, S.; Verma, S.; Ghosh, H. N. *Journal of Physical Chemistry C* **2010**, *114*, 1460.

(18) Klimov, V.; Hunsche, S.; Kurz, H. *Physical Review B* **1994**, *50*, 8110.

(19) Burda, C.; El-Sayed, M. A. *Pure and Applied Chemistry* **2000**, *72*, 165.

(20) Burda, C.; Link, S.; Green, T. C.; El-Sayed, M. A. *Journal of Physical Chemistry B* **1999**, *103*, 10775.

(21) Hu, Y. Z.; Koch, S. W.; Lindberg, M.; Peyghambarian, N.; Pollock, E. L.; Abraham, F. F. *Physical Review Letters* **1990**, *64*, 1805.

(22) Achermann, M.; Hollingsworth, J. A.; Klimov, V. I. *Physical Review B* **2003**, *68*.

(23) Ojea-Jiménez, I.; Romero, F. M.; Bastús, N. G.; Puntes, V. *The Journal of Physical Chemistry C* **2010**, *114*, 1800.

(24) Keul, H. A.; Moeller, M.; Bockstaller, M. R. *The Journal of Physical Chemistry C* **2008**, *112*, 13483.

Chapter 7: QD-nanocomposites as components of DSSCs

7.1 Introduction

The tuneable absorption and emission properties of QDs, combined with their large absorption cross sections, resistance to photobleaching, and the possibility of multiple exciton generation, makes them theoretically capable of exceeding the Shockley–Queisser limit when used as the light harvesting entity of a solar device, yielding higher efficiency solar cells. As such, they are ideal candidates for the replacement of organic dyes in dye-sensitised solar cells (DSSCs)[1-9].

On the other hand, nano-dimensional carbon allotropes, such as multi-walled carbon nanotubes (MWNTs) and graphene, have exceptional physical and electronic properties, with phenomenally high conductivity[10,11]. This makes them highly attractive for use as components in DSSCs, to improve charge mobility across the cell and thus the efficiency of the cell itself[12-18]. The advent of, and growing research into, the use of ionic liquids (ILs) as electrolytes[19], makes this aspect of these carbon materials of even greater interest. Despite the many potential benefits resulting from using ILs as electrolytes (negligible vapour pressure, non-volatility and superior thermal stability at both very low and elevated temperatures[20-23]), their extremely high viscosities impedes the diffusion of the redox couple through the device[24]. Thus the excellent conductivity exhibited by MWNTs and graphene makes them ideally placed for use as additives to the electrolyte of an IL-based DSSC[16,17,25].

The main aim of this segment of my work is to incorporate the novel chiral CdSe and CdTe QDs synthesised previously, in a solar device. The chiral defect emitting CdSe QDs are of particular interest as the wide range of populated energy levels available, coupled with the extremely long lived separation of the exciton's charged species, may increase the possibility of electron injection into the working electrode when incorporated into a solar cell.

The first aim is to incorporate these QDs into a solar cell modelled on the DSSC platform, using them as the light harvester component in place of the typical dye

molecule, creating as it were quantum dot sensitised solar cells (QDSSCs). This work initially required extensive optimisation of the fabrication of the TiO_2 based working electrode.

The second approach endeavours to covalently bind these QDs to two carbon allotropes, MWNTs and graphene, to create QD-carbon composites. These are to be incorporated into an IL electrolyte and used in a DSSC.

7.2 Preparation of Solar Cells – Optimisation of the Working Electrode

For the fabrication of these QDSSCs, the synthesis and optimisation of the working electrode had to be initially carried out before any complete cells could be made and tested. The working photoanode is based on FTO-TiO_2 and required testing several possible variables including different TiO_2 pastes with differing particle sizes and compositions, varying the deposition layer thickness, changing drying times and sintering heating profiles.

The working electrode was produced onto 2 mm x 2 mm slides of non-conductive glass. These were coated on one side with a layer of transparent conducting oxide (TCO), in this case fluorine-doped tin oxide (FTO) and obtained from Pilkington Group Ltd. (glass specification: NSC TEC™ C15). The TCO layer is crucial since, as it is the front face of the cell, it must be transparent to the incoming sunlight while providing transport for the necessary charge carriers to leave the cell. These glass sheets were cleaned thoroughly with Millipore water, followed by ethanol, and then dried in an oven, following which they were allowed to cool. The presence of the FTO layer was confirmed through SEM (Figure 7.1) and sheet resistance measurements (23.5 Ω/m^2). The measured thickness of this layer was ~330 nm.

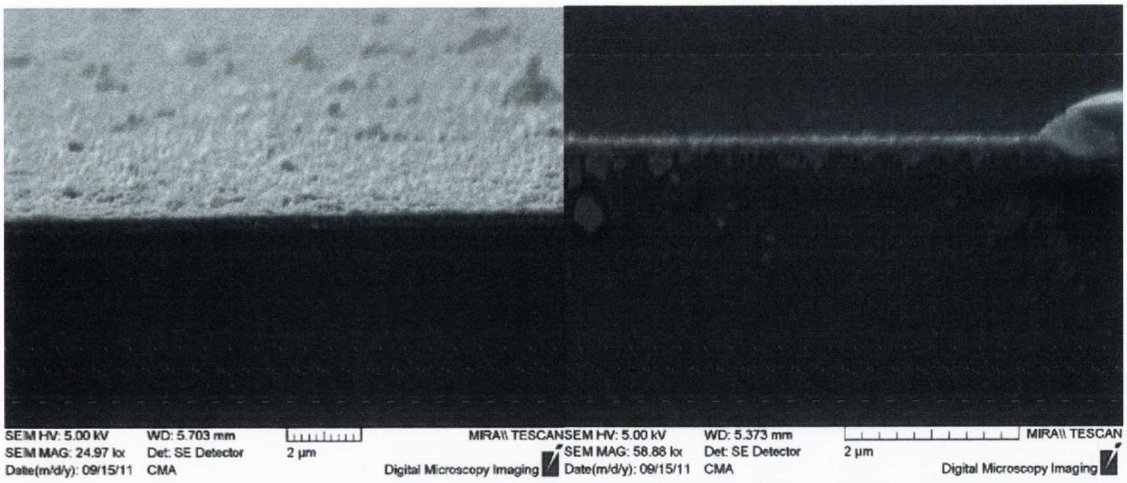

Figure 7.1: SEM of the FTO layer on glass. Thickness is measured to be approximately 330 nm.

To create templates for the fabrication of the solar cells, circular holes (dia. 6 mm) were cut out of sticky tape using a standard hole punch. These templates were stuck onto the FTO coated surface of the slides as a mask, thus leaving a 6 mm diameter hole exposed. The type of tape used was standard black electrical tape (tape thickness 125 µm).

For the fabrication of the working electrode and the deposition of the TiO_2 layers, four different titania based pastes were used. These were as follows:

a) Dyesol DSL 18NR-T, a 20 nm anatase TiO_2 particle paste.
b) Dyesol DSL 90T, a 20 nm anatase TiO_2 particle paste.
c) Eternal Company Ti-2105-3, a 20 nm anatase TiO_2 particle paste.

These three pastes, while all containing 20 nm TiO_2 particles, differ in the composition of their additives, changing their deposition, drying and thus final layer thickness.

d) Solaronix Ti-Nanoxide D, a 15-20 nm anatase TiO_2 particle paste also containing diffusing anatase TiO_2 particles with a size greater than 100 nm.

Using a razor blade, a layer of one of the above TiO_2 nanoparticle pastes was then applied across the open hole of the mask, onto the surface of the FTO-slide *via* the doctor blade technique. The resulting thickness of the deposited layer thus depends on the tape thickness, as well as the composition and concentration of the paste. This layer

was allowed to dry in air for a day, and subsequently further dried in an oven at 75°C. For the deposition of further layers of TiO_2, the tape template was then reapplied to the slide, taking care to align the hole with the previous layer.

Our initial approach, based on previous work in the group, was to deposit multiple layers of TiO_2 (up to a maximum of four layers in total). These were deposited on top of the first, in the same manner using the doctor blade method, drying after each deposition as before. The aim was to increase the total depth of TiO_2 layer, thus increasing the total surface area and the resulting overall QD absorption, in an effort to maximise the cell's light harvesting ability.

After the addition of the final layer the tape mask was removed and the final TiO_2 coated FTO-glass slides were then dried as before and sintered at 450°C in an oven for one hour. The films were analysed using Scanning Electron Microscopy (SEM), profilometry and Raman spectroscopy in order to determine their quality and the nature of the TiO_2. The initial results from this approach were poor quality films showing a lot of defects as well as poor adhesion of the TiO_2 layer to the FTO, as shown below in Figures 7.2 and 7.3. Cracks in the film measured by SEM were approximately 50 μm across and visible even to the naked eye. The best result was from the Raman spectrum (Figure 7.4), showing at least that the phase of the TiO_2 is anatase, required for our photovoltaic cells. It must be noted that the uneven baseline and appearance of square segments in the film and glass, seen in the profilometer measurements (Figure 7.3), is a result of the software stitching the entire map together and not an actual feature of the electrode itself.

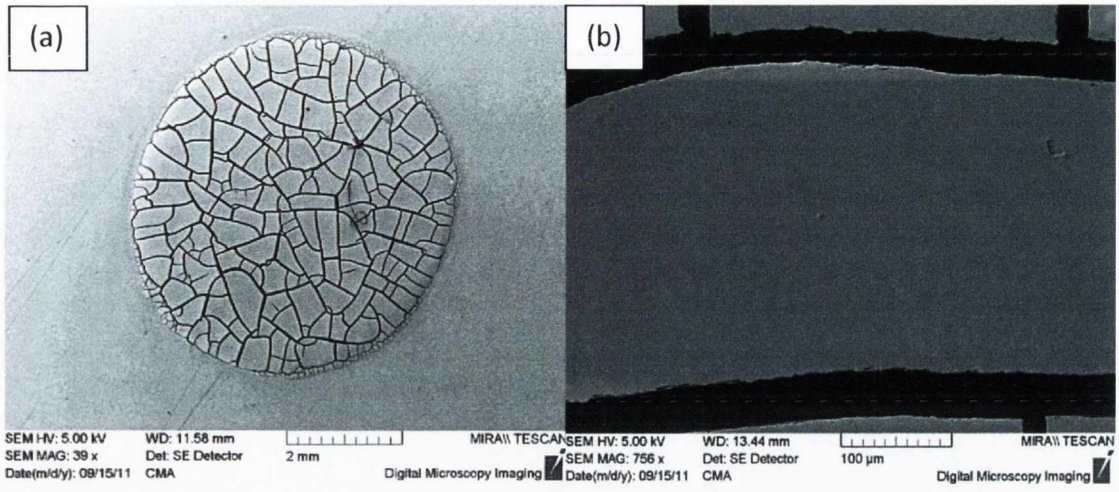

Figure 7.2: Sample SEM images of the resulting TiO_2 films obtained after multiple layer deposition and sintering. (a) The entire cell layer, (b) the cracks throughout the film.

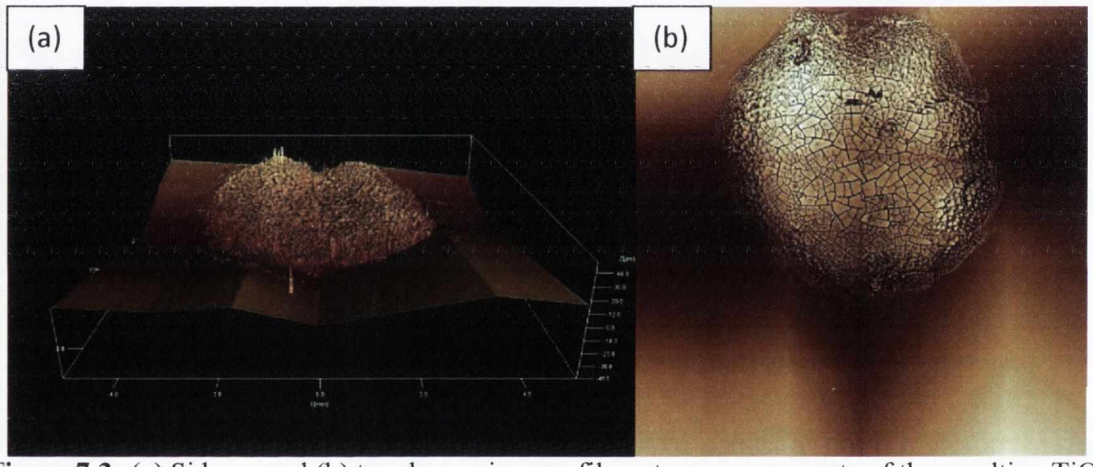

Figure 7.3: (a) Side on and (b) top down view profilometer measurements of the resulting TiO_2 films obtained after multiple layer deposition and sintering.

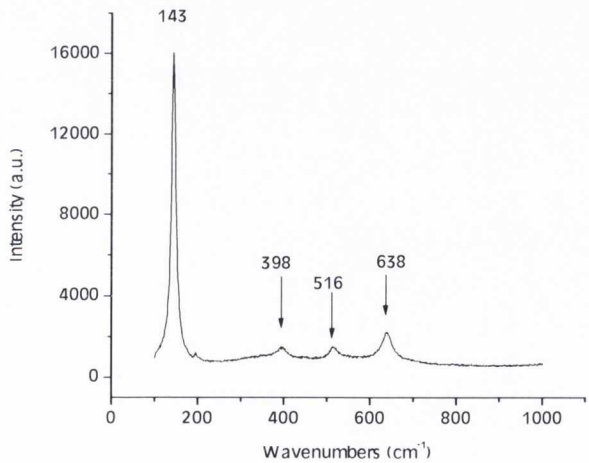

Figure 7.4: Raman spectra of TiO_2 film, showing the characteristic anatase peaks.

To investigate whether these cracks and defects went through the entire TiO_2 layer, and to see whether there were interfaces forming between each deposition, an undesired property, substrates were broken and cross-section SEM was attempted. Unfortunately, this showed that the faults in the layer went down through the layer to the FTO. However, though this multi-layer approach was subsequently abandoned, there is promise some promise in that, no evidence could be seen of interfaces forming between each deposited layer, a more positive result given that this is a current problem in the fabrication of thicker TiO_2 films (Figure 7.5).

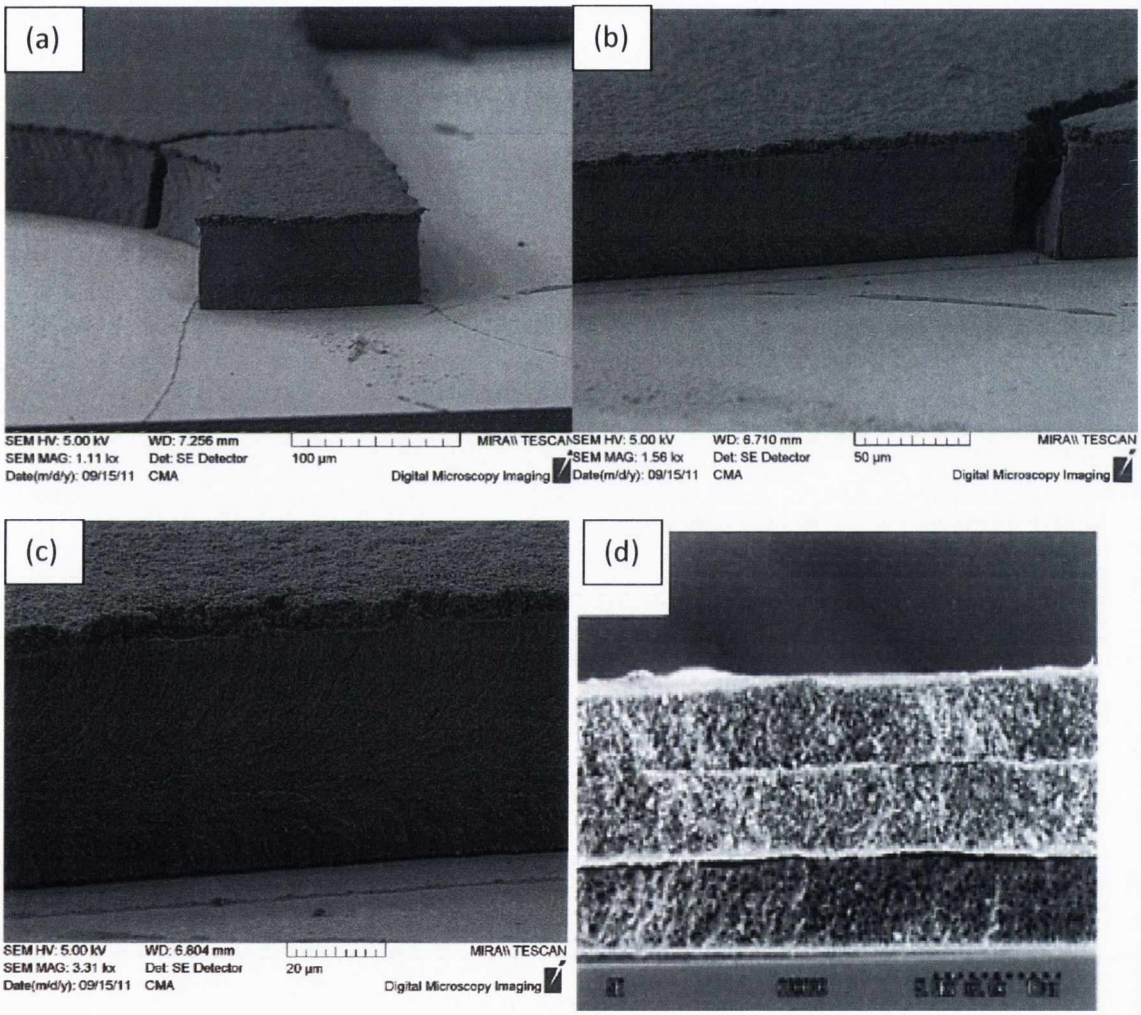

Figure 7.5: (a-c) Side on SEM images of four layers TiO_2. The depth of the cracking along with the poor adhesion to the base FTO is obvious. The lack of interface between the TiO2 layers is also clear, compared to (d), reproduced from[26]. Note the top layer seen in (a-c) is larger particulate TiO_2.

In an attempt to improve this result, before deposition of the TiO_2 paste, the slides were first treated by immersing them in an aqueous TiO_2 solution, created by the hydrolysis of $TiCl_4$ in water. This forms a base layer of TiO_2 on the exposed FTO and has been shown to increase the degree of binding between the FTO and the subsequent deposited TiO_2 layer[27]. After this the slides were washed and then dried. The deposition of this initial TiO_2 film was unable to be verified by SEM, due to the extremely thin nature of the layer and difficulty in distinguishing it from the FTO. It was confirmed however, by an increase in the sheet resistance, from 23.5 to 35.9 Ω/m^2. A different heating profile was also used in accordance with one already reported[27]. It consists of the following several stages;

1) a heating phase from room temperature to 200°C at a rate of 8°C per minute
2) a dwell time of 15 minutes at 200°C
3) a second heating ramp stage to 450°C at a rate of 12°C per minute
4) a dwell time of 30 minutes at 400°C
5) a slow cooling phase back to room temperature, no faster than 10°C per minute.

The importance of the temperature regime cannot be underestimated. During heating, organic solvents and other dispersants present in the TiO_2 paste start to decompose and evaporate or burn off. This can induce mechanical stress in the TiO_2, causing cracks and poor adhesion of the layer to the base. For this reason the heating rate is kept to 8°C per minute under 200°C and 12°C per minute from 200°C to 450°C. The slow cooling rate is also essential in order to avoid glass misshape and further stress to the TiO_2 layer(s).

Following sintering, the resulting TiO_2-FTO-slides were then treated again by immersing them in a solution of $TiCl_4$ in Millipore water (0.05 M, 70°C, 30 minutes). The reason for the second treatment is the resulting enhancement in the cell efficiency, due to the development of inter-particle bridges in the TiO_2 film[27]. After this the slides were washed, dried, sintered for a second time using the same heating profile, then washed again and dried.

However, as can be seen in Figure 7.6 (a-d), after sintering, all of the resulting films from the four different pastes were still of poor quality, with multiple cracks visible in

the TiO_2 layer. This was coupled with poor adhesion to the FTO and it can be seen that the surface of the TiO_2 layer is pitted with defects (Figure 7.6 (e-f)).

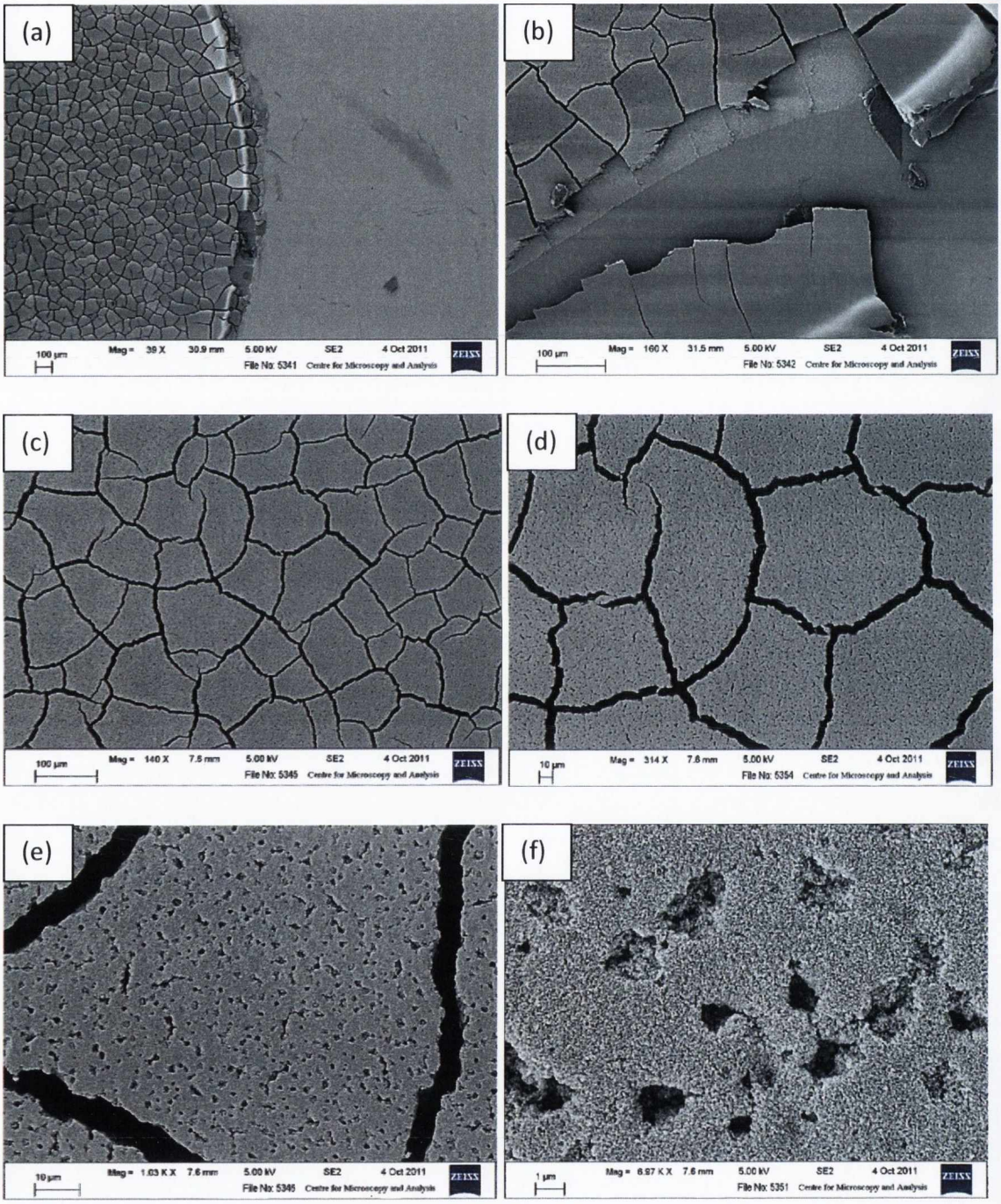

Figure 7.6: Sample of SEM images showing the poor resulting layer quality obtained from multi-layer deposition of TiO_2. (a-e) Cracking can be seen throughout the entire layer, (b) there is poor adhesion to the cell base, and (d-f) obvious pitting in the TiO_2 surface.

These cracks was attributed to the fact that the final deposited layers were still too thick, the combination of excess organics evaporating/ burning off upon heating and the greater mechanical strain this exerts on the larger mass of TiO_2 resulting in the cracking of the layers. To combat this and further improve the quality of the TiO_2 layer, only single-layer TiO_2 deposited slides were used as these showed little to no defects in their surfaces. Another, thinner tape (Scotch Magic 3M tape, thickness 60 µm) was also used for layer deposition in exactly the same manner as outlined above to try to improve the quality of the layers.

Both of the Dyesol TiO_2 pastes (18NR-T and 90T), even when only deposited as a single layer using the black electrical tape as a mask, still showed a high degree of cracking after sintering by SEM (Figure 7.7) and profilometry (Figure 7.8). This was attributed to the layers deposited still being too thick.

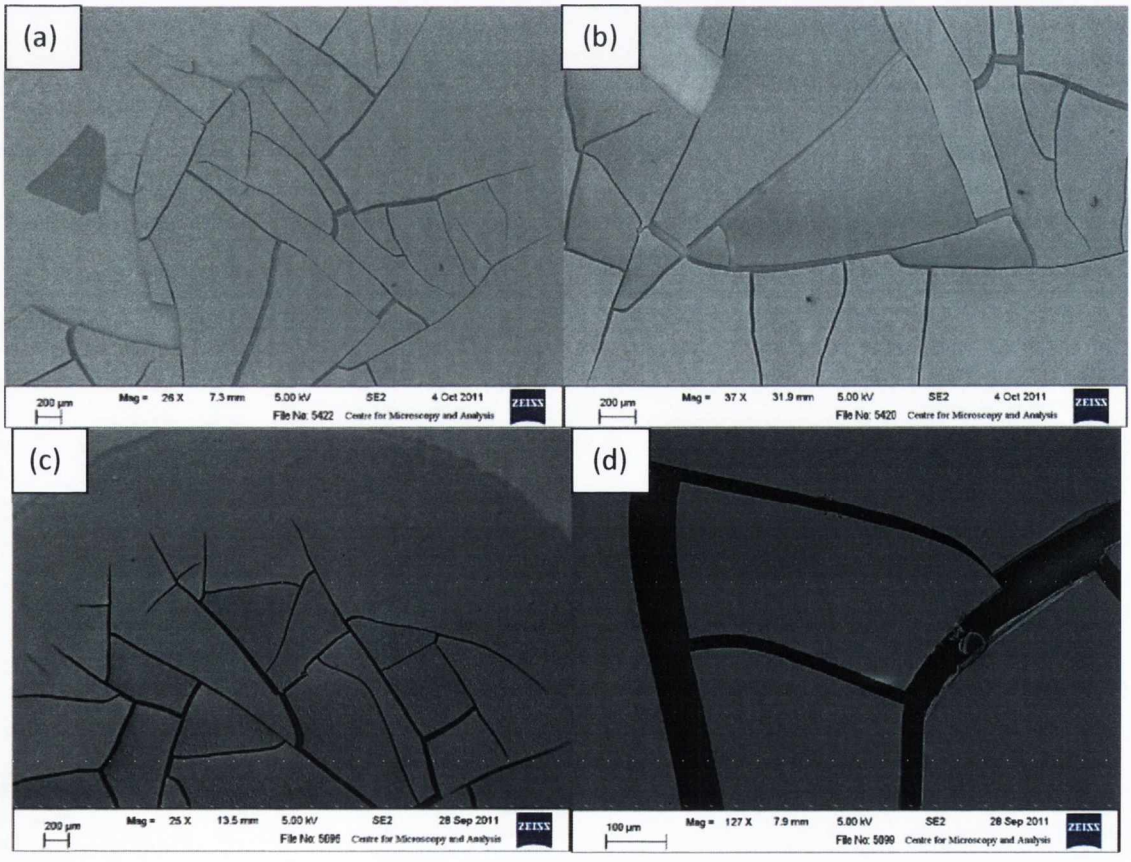

Figure 7.7: SEM images of single layer (a, b) Dyesol 18NR-T, and (c, d) Dyesol 90T TiO_2 pastes deposited using black tape.

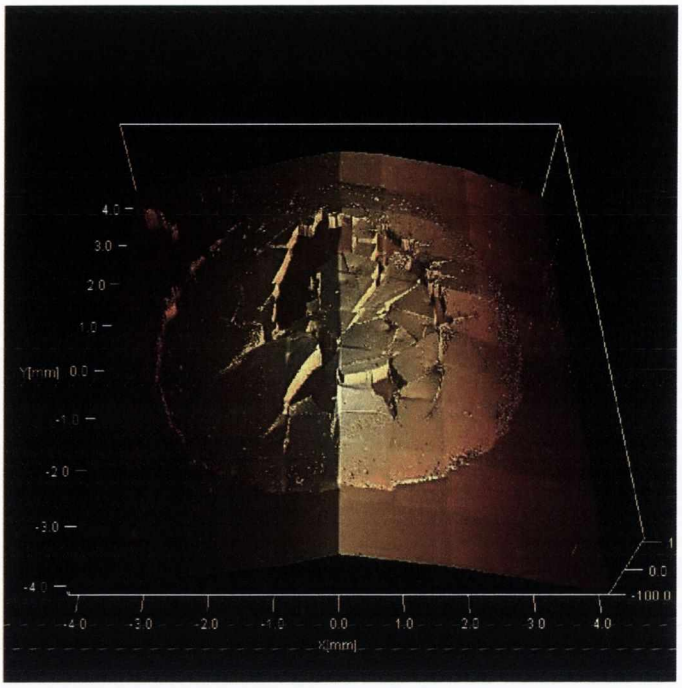

Figure 7.8: Profilometer measurement of single layer Dyesol paste deposited with black electrical tape. The 'squaring' of the image and rise towards the middle is again software related, caused by stitching the map together.

It must be noted that both of these pastes are designed particularly with thin films in mind. This fact is highlighted by examining the results obtained from these two pastes deposited with the thinner Scotch Magic 3M tape (tape thickness now only 60 μm). The difference can clearly be seen (Figure 7.9 - 7.11), the layer is smoother with little to no cracking and few defects in the surface.

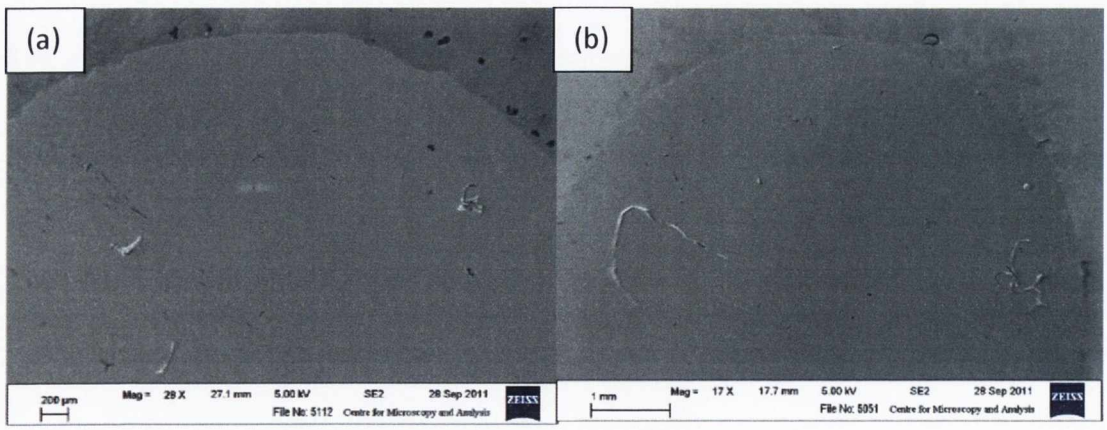

Figure 7.9: SEM images of single layer Dyesol 18NR-T TiO_2 paste deposited using Scotch tape.

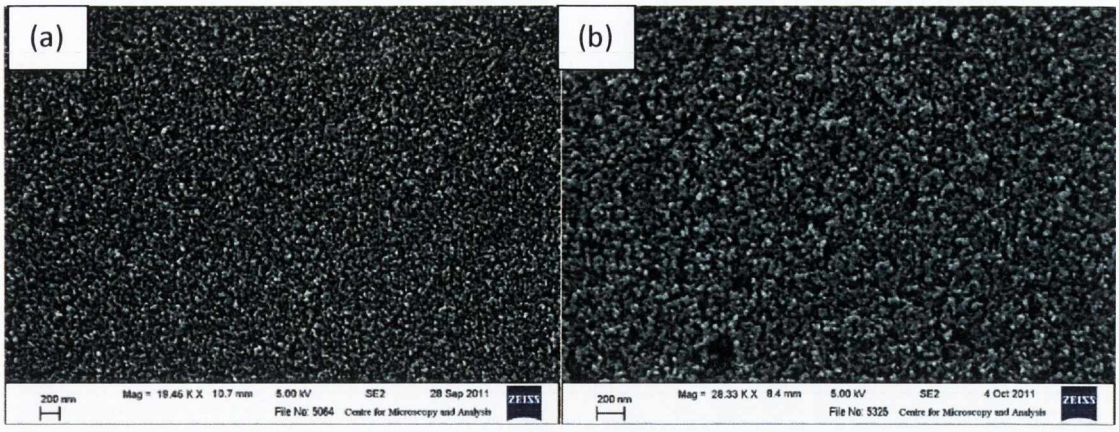

Figure 7.10: SEM images of single layer Dyesol 90T TiO_2 pastes deposited using Scotch tape.

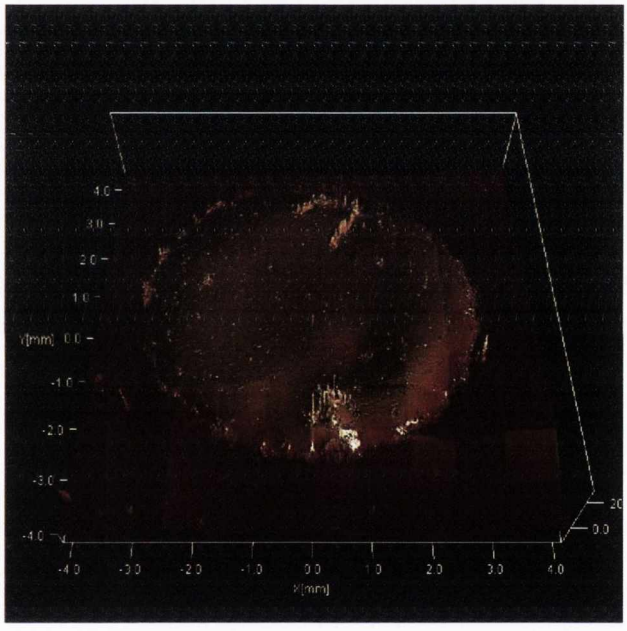

Figure 7.11: Profilometer measurement of single layer Dyesol paste deposited with Scotch tape. The 'squaring' of the image and rise towards the middle is again software related, caused by stitching the map together.

For the Eternal Company Ti-2105-3 paste, it was found that the black electrical tape gave better results with a more even layer obtained after sintering and fewer cracks (Figure 7.12 (a-c) and Figure 7.13). On the other hand, the Scotch Magic 3M tape resulted in too thin a layer being deposited, with a visibly uneven surface and non-uniform coverage of the FTO (Figure 7.12 (d-f)). Both, however, had a high amount of pitting in the TiO_2 surface.

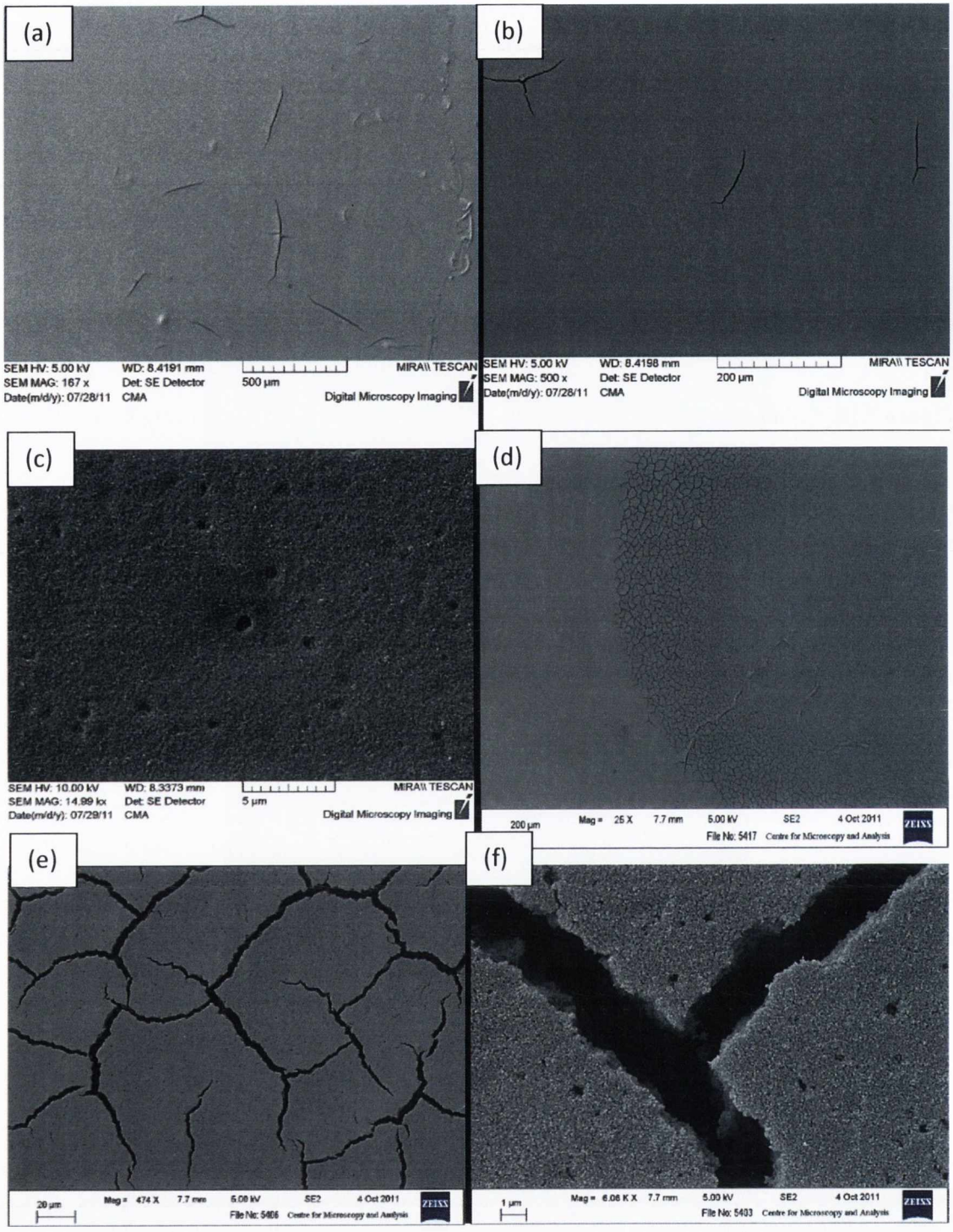

Figure 7.12: SEM images of single layer Eternal Company Ti-2105-3 paste deposited using (a-c) black tape, and (d-f) Scotch tape respectively.

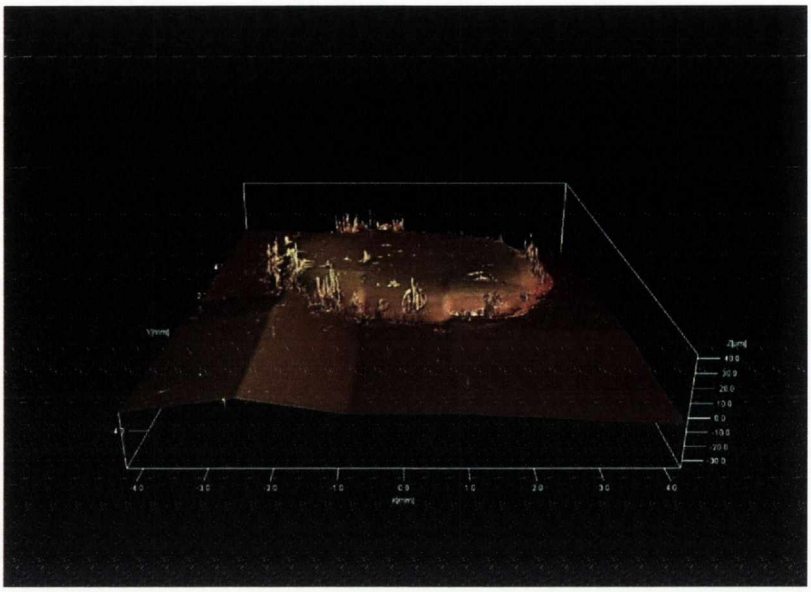

Figure 7.13: Profilometer measurement of single layer Eternal Company Ti-2105-3 paste deposited with black tape. The 'squaring' of the image is again software related.

Results obtained from the Solaronix Ti-Nanoxide D paste showed the black electrical tape giving a cracked defective layer while a good even monolayer with few defects resulted from deposition with the Scotch tape (Figure 7.14 and 7.15).

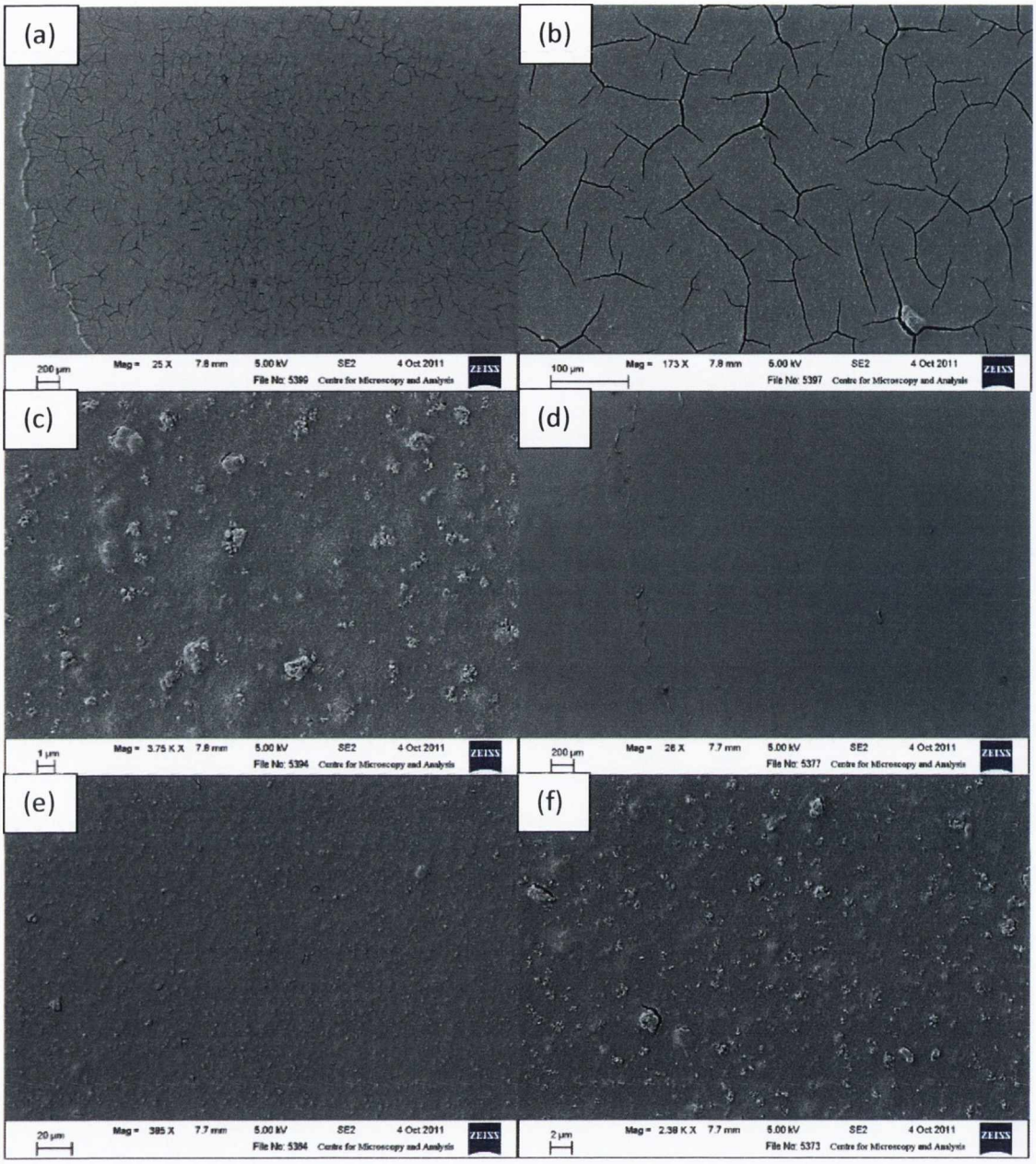

Figure 7.14: SEM images of single layer Solaronix Ti-Nanoxide D paste deposited using (a -c) black tape, and (d-f) Scotch tape respectively. The presence of the larger scattering TiO_2 particles also present in this paste can be seen in (c) and (f).

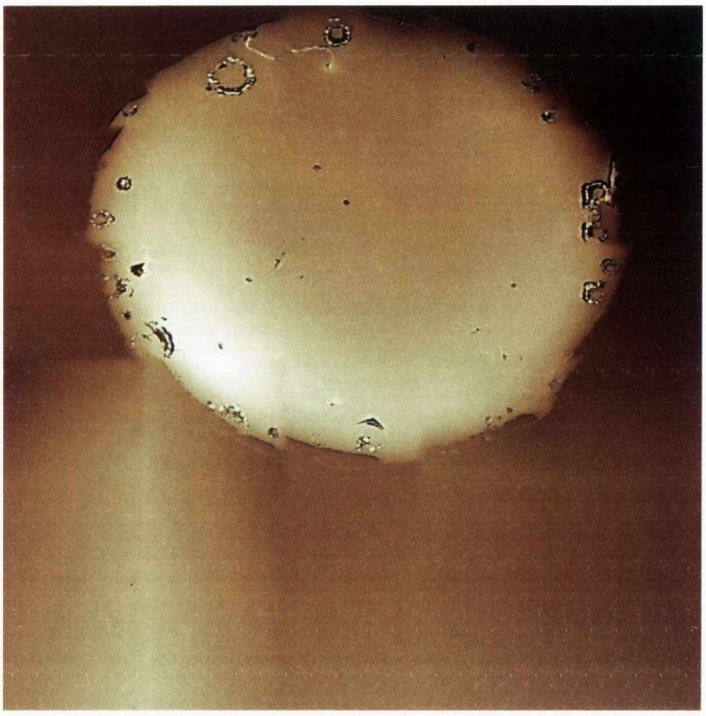

Figure 7.15: Profilometer measurement of single layer Solaronix Ti-Nanoxide D paste deposited with Scotch tape. The 'squaring' of the image is again software related.

The varying results obtained for all of the above paste-tape combinations is due to the differing compositions of the pastes. They each contain different, and various amounts of, dispersants along with other organic compounds. This gives rise to a diverse layer thickness for each paste upon drying and sintering, as well as a different inherent optimal thickness. Furthermore, due to the varying compositions, there are various degrees of stress induced upon evaporation and burn off of these organics during drying and sintering. All of these aspects influence the resulting quality of the final TiO_2 film produced.

The results from the eight total combinations of single layer depositions using the two tapes and four pastes are outlined below in Table 7.1;

Table 7.1: Results from the various combinations of pastes and tapes used.
X = poor quality film with cracks, ✓= good quality film deposited with little to no defects.

Paste / Tape	Dyesol 18NR-T	Dyesol 90T	Eternal Company Ti-2105-3	Solaronix Ti-Nanoxide D
Black electrical tape	X	X	✓	X
Scotch Magic 3M tape	✓	✓	X	✓

Based on these findings, only the following four relatively successful combinations of tapes and pastes were developed further for solar cell fabrication and testing:

1) Dyesol TiO_2 18NR-T paste with Scotch Magic 3M tape.
2) Dyesol TiO_2 90T paste with Scotch Magic 3M tape.
3) Eternal Company Ti-2105-3paste with black electrical tape.
4) Solaronix Ti-Nanoxide D paste with black electrical tape.

As well as the above in-house fabricated working electrodes, premade TiO_2-FTO based electrodes were also obtained from a separate source and tested as a comparison. These were also made using the same 3.2 mm, FTO coated NSC TEC™ C15 glass (sheet resistance 8Ω/sq) from Pilkington Group Ltd. The electrodes were fabricated by SolarPrint using an Eversolar® P-200, 20-50 nm TiO_2 paste. It must also be noted that instead of the doctor blade technique outlined above, these were manufactured *via* screen printing. The active area of these electrodes is rectangular instead of circular, with dimensions of 8 mm x 11 mm.

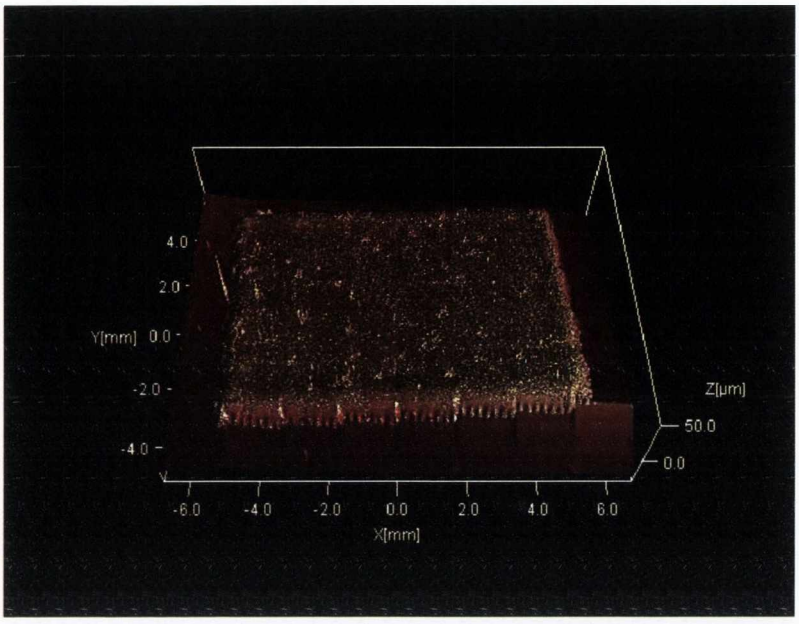

Figure 7.16 : Profilometer map of the SolarPrint electrode made from Eversolar® P-200, 20-50 nm TiO_2 paste via screen printing. The relatively smooth nature of the film is clearly evident.

As can be seen in Figure 7.16, profilometer measurements of the purchased electrode showed that the overall nature of the TiO_2 film is relatively smooth (again, the division of the map into squares is an artefact from the stitching software and not an actual feature of the film itself). However, closer inspection with SEM (Figure 7.17) shows pitting and cracking is also evident in these commercially available electrodes, the degree of which being on a par with films deposited via doctor blading.

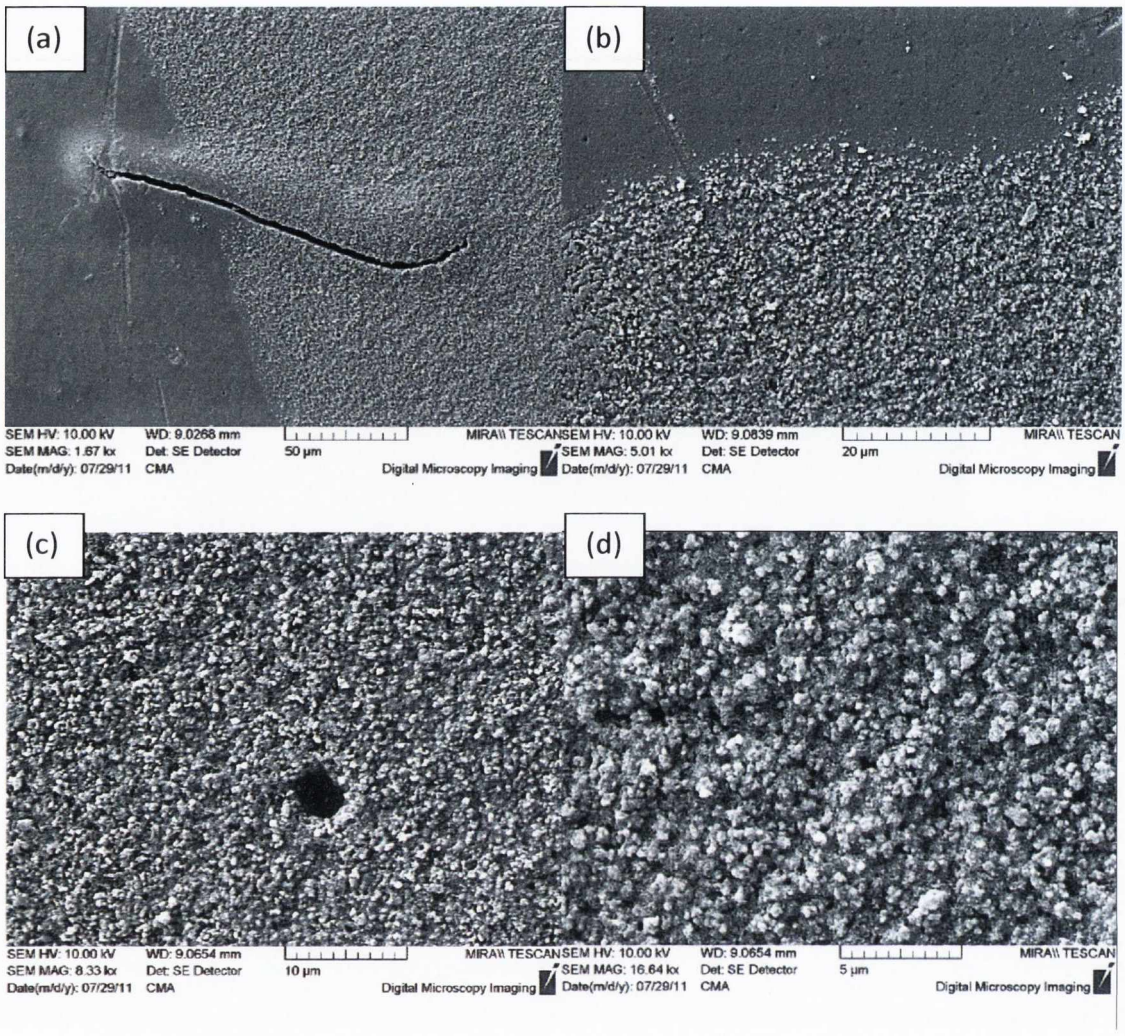

Figure 7.17: SEM images of SolarPrint electrode made from Eversolar® P-200, 20-50 nm TiO_2 paste via screen printing.

Comparing these screen printed electrodes, which are available commercially, to those fabricated ourselves, it would appear that the process of optimisation for deposition and sintering of the TiO_2 film has been successful and the best electrodes produced ourselves via doctor blading (such as single layer Dyesol 18NRT and 90T using Scotch tape) are as good as, if not better, in terms of the degree of cracking and surface defects/pits. This in itself is a very strong and promising result, and a solid base from which further relevant PV-cell research can be developed. There are also other immediate benefits arising from this successful optimisation, the most obvious being financial. The cost of pursuing this line of research is now dramatically reduced, as the combined price of raw materials and production of the working electrode is far less when compared to the purchase of these electrodes commercially. This is of particular

importance given the one-use-only nature of these films, and the high number needed in order to optimise the remaining cell components for a successful, high efficiency final solar device.

7.3 Fabrication and Testing of QD /TiO_2 Based Solar Cells

The quantum dots synthesised previously in this work have been used to produce components for solar cell application. Racemic cysteine stabilised CdSe and CdTe QDs, as well as racemic penicillamine stabilised CdSe were chosen due to their higher quantum yields, as compared to their enantiomeric counterparts. The total set of electrodes and QD combinations tested are outlined in Table 7.2

Table 7.2: The total combinations of QDs and electrodes brought further for testing

Cells / QDs	Dyesol DSL 18NR-T (Scotch tape)	Dyesol DSL 90T (Scotch tape)	Eternal Company Ti-2105-3 (black tape)	Solaronix Ti-Nanoxide D (Scotch tape)	SolarPrint Electrode
CdSe *Rac*-Pen	✓	✓	✓	✓	✓
CdSe *Rac*-Cys	✓	✓	✓	✓	✓
CdTe *Rac*-Cys	✓	✓	✓	✓	✓

The first approach for using quantum dots in solar cells, as outlined above, is as a replacement for standard dyes in a DSSC style cell. To do this the TiO_2 must be sensitised with the QDs. As described previously, the QDs are all stabilised with amino acid style stabilisers containing carboxylic acid group. This group is a known binder to TiO_2[28-30] and thus these QDs may well be suitable for such an application. It is believed that despite the nature of the chirality being induced through the tri-dentate nature of the

stabiliser, there are still some COOH terminal groups unattached and sticking out from the QD surface. These will link the QD and TiO_2 through the stabilising ligand, creating a bridge to allow charge to flow to the working electrode upon photo-excitation. The adsorption of the QDs was achieved by soaking the prepared working electrodes in an aqueous solution of QDs overnight. The electrodes were then removed, cleaned and dried. QD absorption was evident by the slight colour change of the TiO_2 layer, turning from white to faint yellow in the case of CdSe QDs and faint orange for the CdTe QDs. It must be noted however that the degree of colour variation was not very significant, indicating that total absorption of the QDs onto the TiO_2 layer was low.

The same style counter electrode was used for all the above combinations of cells and is created in much the same manner as the working electrode, using the same FTO coated NSC TEC™ C15 glass. A film of platinum containing paste (Dyesol, PT1) was applied via the doctor blade method. The mask was removed and the glass slides were then sintered at 450°C for 30 minutes after which they were allowed to cool to room temperature. The purpose of the platinum is to act as a catalyst and regenerate the electron back into the electrolyte.

The electrolyte used (Dyesol EL-141) is an acetonitrile based electrolyte, containing inorganic and organic iodide salts as additives, particularly lithium iodide. The LiI liberates iodine in solution which sets up the iodine/tri-iodide (I^-/I_3^-) redox couple, allowing regeneration of the separated charges upon photo-excitation and completing the circuit.

The respective quantum yields of the three QD types used were as follows; 25% for CdTe *Rac*-Cys, 16% for CdSe *Rac*-Cys and 15% for CdSe *Rac*-Pen.

Solar testing was carried out by a setup created in-house using a xenon lamp and source meter, calibrated to one sun with a solar standard.

7.4 Efficiencies

The efficiencies for the different cells are shown in Table 7.3 and discussed below.

Table 7.3: Efficiencies obtained from the various QD-electrode combinations

Cells / QDs	Dyesol DSL 18NR-T (Scotch tape)	Dyesol DSL 90T (Scotch tape)	Eternal Company Ti-2105-3 (black tape)	Solaronix Ti-Nanoxide D (Scotch tape)	SolarPrint Electrode
CdSe *Rac*-Pen	0.06%	0.05%	0.02%	0.03%	0.1%
CdSe *Rac*-Cys	0.05%	0.06%	0.02%	0.05%	0.07%
CdTe *Rac*-Cys	0.09%	0.08%	0.04%	**0.16%**	0.06%

Overall, the increases in efficiencies obtained from these QDSSCs were very low, and in the majority of cases only a marginal increase was achieved from a baseline of 0.01% for no QDs present, both for the cells based on the prefabricated SolarPrint electrodes and the ones synthesised myself. The best efficiencies across the range, with the exception of the SolarPrint electrodes were obtained for CdTe Rac-Cys QDs (red), with the best result being 0.16% (highlighted in yellow) for the combination of CdTe *Rac*-Cys and the Solaronix Ti-Nanoxide D paste when deposited using Scotch tape.

What is surprising is that, in the case of the SolarPrint electrodes, higher efficiencies were obtained for the cells made using the defect emitting CdSe QDs over those with intrinsic CdTe (purple). In this case we could suggest that a lower quantum yield (or higher degree *per se* of defect emission) results in higher solar cell efficiency. While this seems to be contradictory to common sense and the current literature position, it may be possible that the broad defect emission exhibited by these QDs is somewhat beneficial. The wide range of energies of the photogenerated excitons, and thus electrons (Chapter 5), coupled with the extremely long charge separation lifetime of the exciton, shown to be on the millisecond timescale by the flash photolysis

experiments (Chapter 6), may result in a greater probability of the electron being transferred to the TiO_2. This is however a relatively speculative conclusion, as all recorded efficiencies are very low and lie close to the margin of error of each other, and a more anomalous result when put in the scope of the efficiencies obtained from cells using other working electrodes. A great deal of further work therefore is required to ensure that these results are definitive.

The reason for the overall poor efficiency obtained from these QDSSCs is attributed mainly to very low QDs adsorption onto the TiO_2 surface (as seen by only marginal colour change and no evidence of the QDs in UV-vis spectra of the electrodes). The exact reason for this is hard to determine and could be the result of a number of factors. The nature of the tri-dentate capping ligand, and the possible small percentage (if any) of free COOH groups available for binding to the TiO_2, most likely plays an important role. A possible solution would be ligand exchange, which has shown to achieve higher loading of the QDs onto the TiO_2 surface[31].

Penetration of the QDs into the TiO_2 layer may also be inhibited by the small free-space between the TiO_2 particles. Also, if the QDs bind to the surface layer, this may further block the path of QDs from adsorbing deeper into the TiO_2 layer. To overcome this, electrodes could be fabricated using larger TiO_2 particles, increasing the interspatial distance and allowing greater penetration of the QDs into the layer.

In order to elucidate the true cause however, a much more detailed investigation is required, and further optimisation of the entire cell fabrication process is essential, with particular focus on the adsorption of QDs onto the TiO_2.

7.5 Preparation of Solar Cells Using QD-Carbon Composites

The main aim of this part of our work was to prepare new QD–carbon composites using the novel chiral CdSe and CdTe QDs outlined previously (Chapter 5). We have chosen MWNTs and graphene as carbon nanomaterials. Again the chiral CdSe QDs are particularly interesting due to their broadband emission covering the entire visible spectrum. As the QDs are stabilised by chiral amino acids and exhibit optical activity, there is the added possibility of a chiral-chiral interaction. In this

section, MWNTs and graphene were modified with appropriate functional groups that would facilitate the covalent binding of the chiral CdSe and CdTe QDs to their surface. The intention is to test these nanomaterials as components in a solar cell. This is to be achieved by incorporating these QD-carbon composite into an ionic liquid (IL) based electrolyte. A typical DSSC style cell will be used to test these additives, again fabricated in-house.

7.6 Carbon Nanomaterials Functionalisation

Sainsbury and Fitzmaurice have previously reported covalently binding organic molecules to a nanotube surface, and it is a variation of this method we will use for our work[32]. In this work, the molecules we will attach are cysteamine and 11-mercaptoundecanoic acid (Figure 7.18).

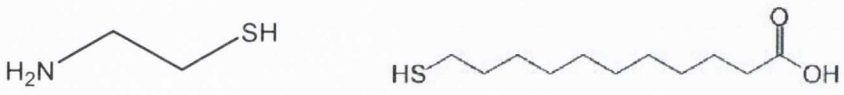

Figure 7.18: (Right) Cysteamine molecule and (left) 11-mercaptoundecanoic acid.

These particular molecules were chosen as they are simple alkyl chains which possess a terminal thiol group, thus making it chemically similar to the stabilising molecules being used to make our quantum dots. The aim of this part of the work was to synthesise our quantum dots in the presence of these functionalised MWNTs and graphene. This *in-situ* approach has already been demonstrated successfully for the attachment of QDs to the surface of CNTs[33]. The cysteamine/ 11-mercaptoundecanoic acid will act in a similar manner to the amino acid stabiliser in solution (indeed cysteamine is often used itself as a stabiliser for nanoparticles), binding via the thiol group to cadmium atoms on the surface of the nanoparticle. This would yield covalently bound carbon-quantum dot composites. Covalent bonding of the two species via the linker molecule is important as it should allow for charge transfer to occur from one nanomaterial to the other, through the linker.

A schematic outline of the coupling reaction is shown in Figure 7.19. Initially MWNTs were oxidised by sonication in nitric acid for 15 minutes and then refluxed for

24 hours. This results in tubes, which are functionalised with hydroxyl, carbonyl and carboxyl groups at defects on the carbon nanotube surface, potential reactive sites. It also removes impurities such as Fe ions left over from the manufacture of the nanotubes, where they are used as a catalyst. The hydroxyl and carboxyl groups were further oxidised to carbonyl groups by treatment of the MWNTs with potassium permanganate and perchloric acid. The potassium permanganate was then quenched by the addition of citric acid. After oxidation of all the other groups e.g. alcohols to carboxylic acid using $KMnO_4$, the functionalisation reaction is now a simple amide coupling, and one can attach a wide range of molecules containing an NH_2 group using this method. This was achieved using 1-ethyl-3-(3-dimethylaminopropyl) carbodiimide (EDC), a coupling agent, Figure 7.19. The nanotubes were filtered and washed with Millipore water. The resulting cysteamine functionalised tubes were dispersed in Millipore water by sonication and were then ready for further functionalisation.

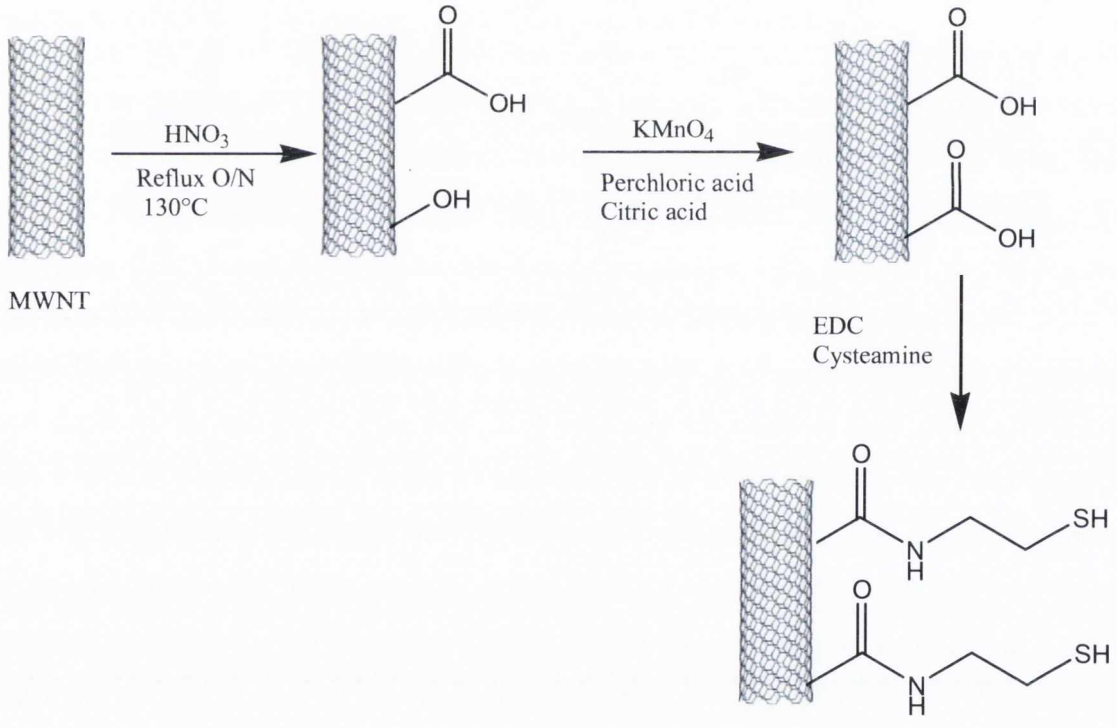

Figure 7.19: Reaction scheme for functionalisation of MWNTs with cysteamine.

The mechanism of EDC coupling is outlined in Figure 7.20. It promotes the leaving of the OH group and facilitates attack from the amine by creation of an intermediate. Here the EDC is in excess compared to the desired linker molecule to

drive the reaction forward and to ensure enough of it survives, as it can also react with water when used in aqueous solutions. The purpose of the DMAP is to act as a base, mopping up HCl as the EDC used is EDC.HCl. It also helps stabilise the intermediate of the coupling reaction.

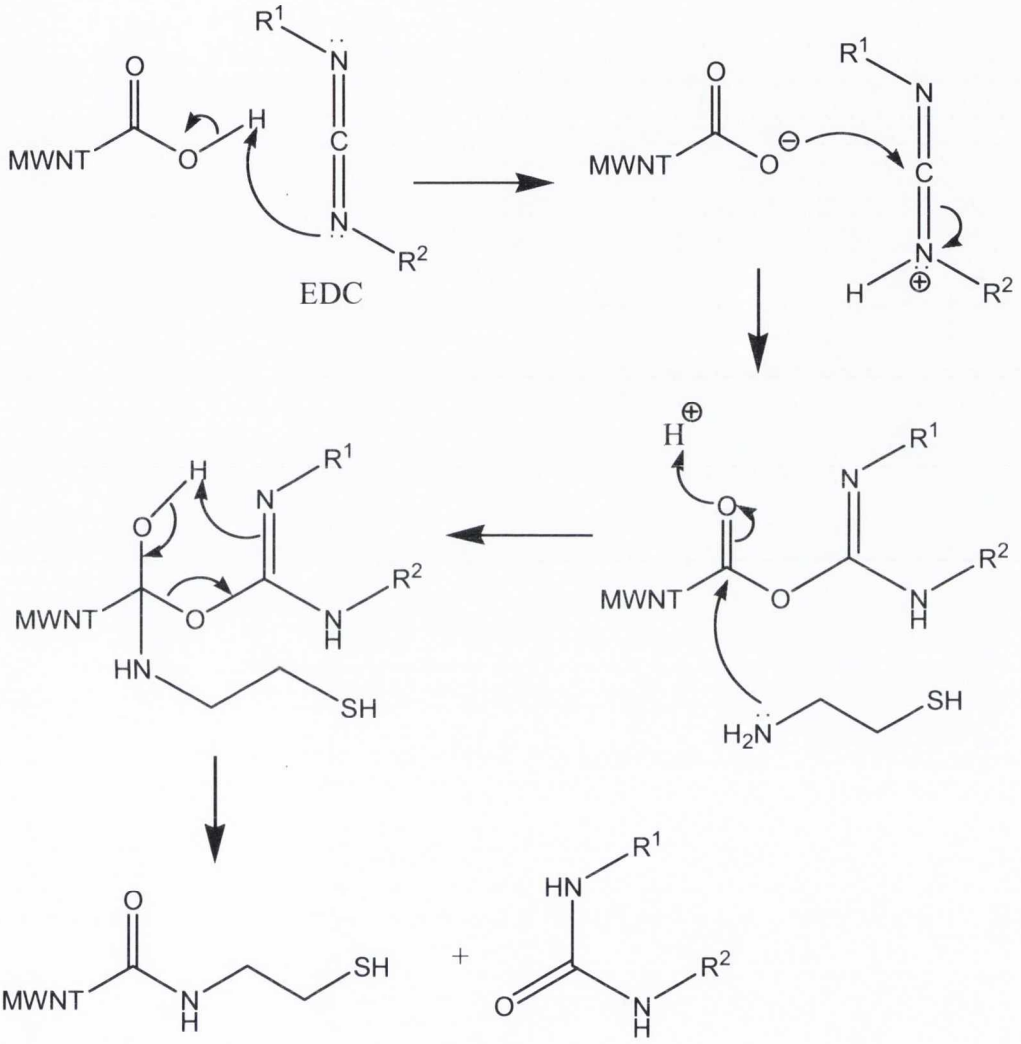

Figure 7.20: Mechanism illustrating the role of EDC in facilitating the amide coupling reaction.

To attach the 11-mercaptoundecanoic acid, after oxidation the nanotubes were refluxed in thionyl chloride ($SOCl_2$), converting the COOH groups to acyl chlorides. This was then evaporated off and ethylenediamine is added. This yielded an amine terminal group and subsequently the same coupling reaction as above can be used to attach the 11-mercaptoundecanoic acid.

The functionalisation of graphene and production of GO was achieved using an improved Hummer method, developed by our group[34]. Briefly, graphene oxide is obtained from stirring graphite in sodium nitrite with sulphuric acid and the addition of $KMnO_4$. Subsequent washing in dilute HCl and ethanol yielded GO. This was then treated in the same manner as the acidified MWNTs outlined above, with EDC coupling giving the required funtionalisation.

TGA analysis (Figure 7.21) showed that functionalisation has occurred. This is demonstrated by the small variations in the two curves from 200 - 400 °C. The thiol functionalised MWNTs also burn off at a lower temperature. This also indicates the reaction proceeded as such functionalisation introduces defects into the MWNT structure, making them less thermally stable.

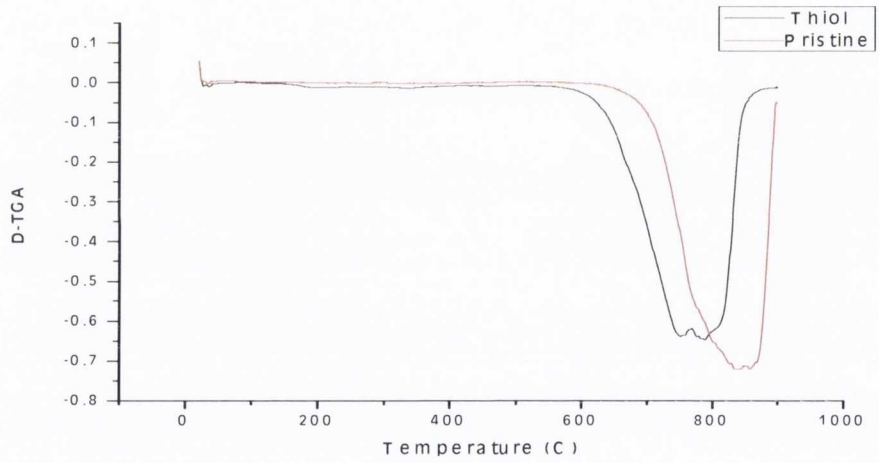

Figure 7.21: TGA analysis of pristine and functionalised MWNTs (derivative graph).

7.7 Synthesis of QD-carbon nanomaterials composites

After functionalisation of both the MWNTs and the GO, the QDs were then synthesised, as described in previous chapters, with a slight variation. Initially 0.5 mg of the functionalised carbon was added to the reaction, followed by the cadmium perchlorate precursor. The solution was sonicated for 10 minutes before the amino acid stabiliser was added. After this point the synthesis proceeded as outlined previously. This reverse order of addition of Cd and stabiliser is to enable the Cd atoms to bind to the thiol groups of the functionalised carbon, thereby creating reaction sites for the

formation of QDs. The QD-carbon composite was then extracted by centrifugation and filtration. The presence of QDs on the surface of both the MWNTs and graphene was evidenced by Transmission Electron Microscopy (TEM) analysis shown below in Figures 7.22 -7.25.

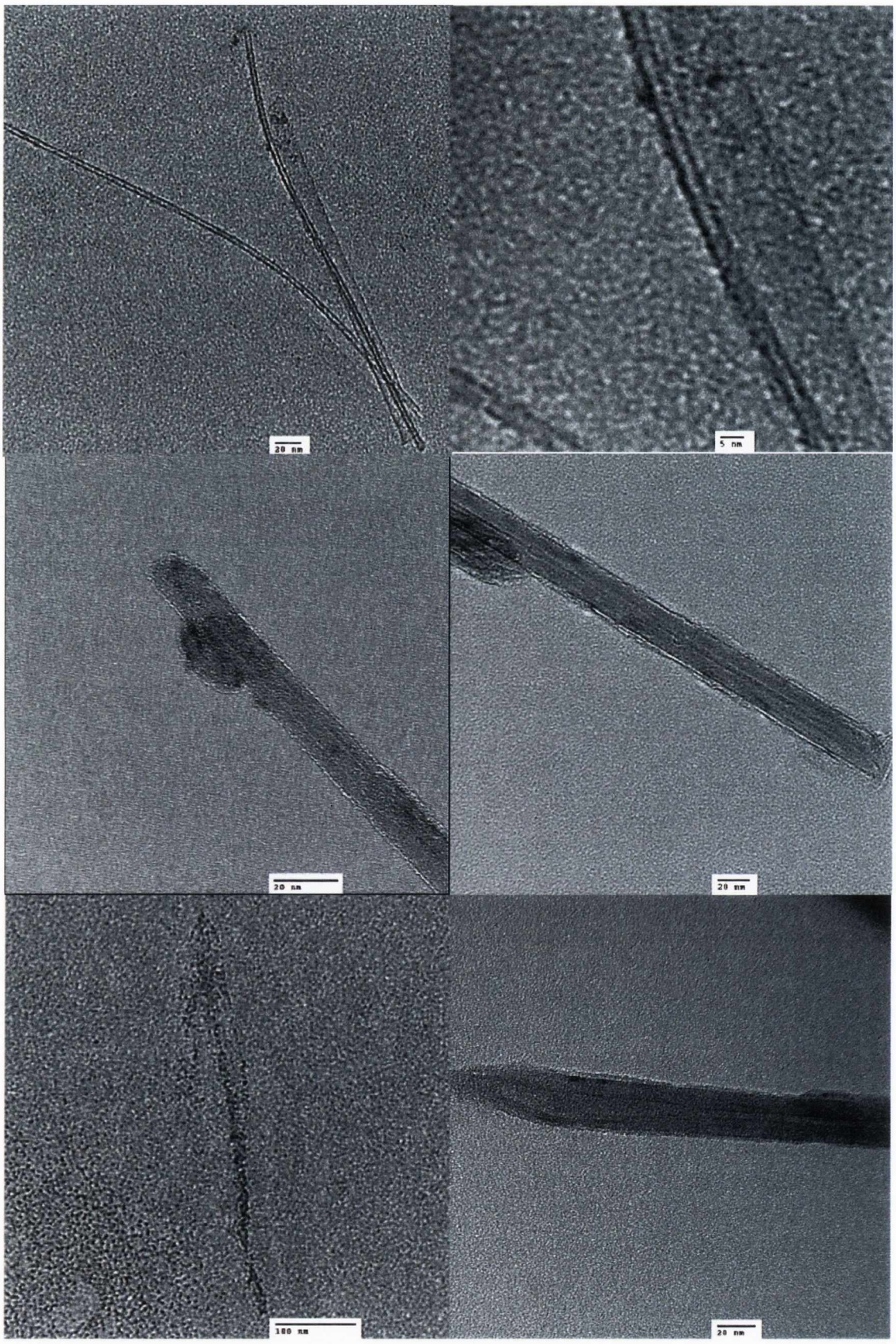

Figure 7.22: Selection of TEM images showing the presence of QDs on the surface of the functionalised graphene.

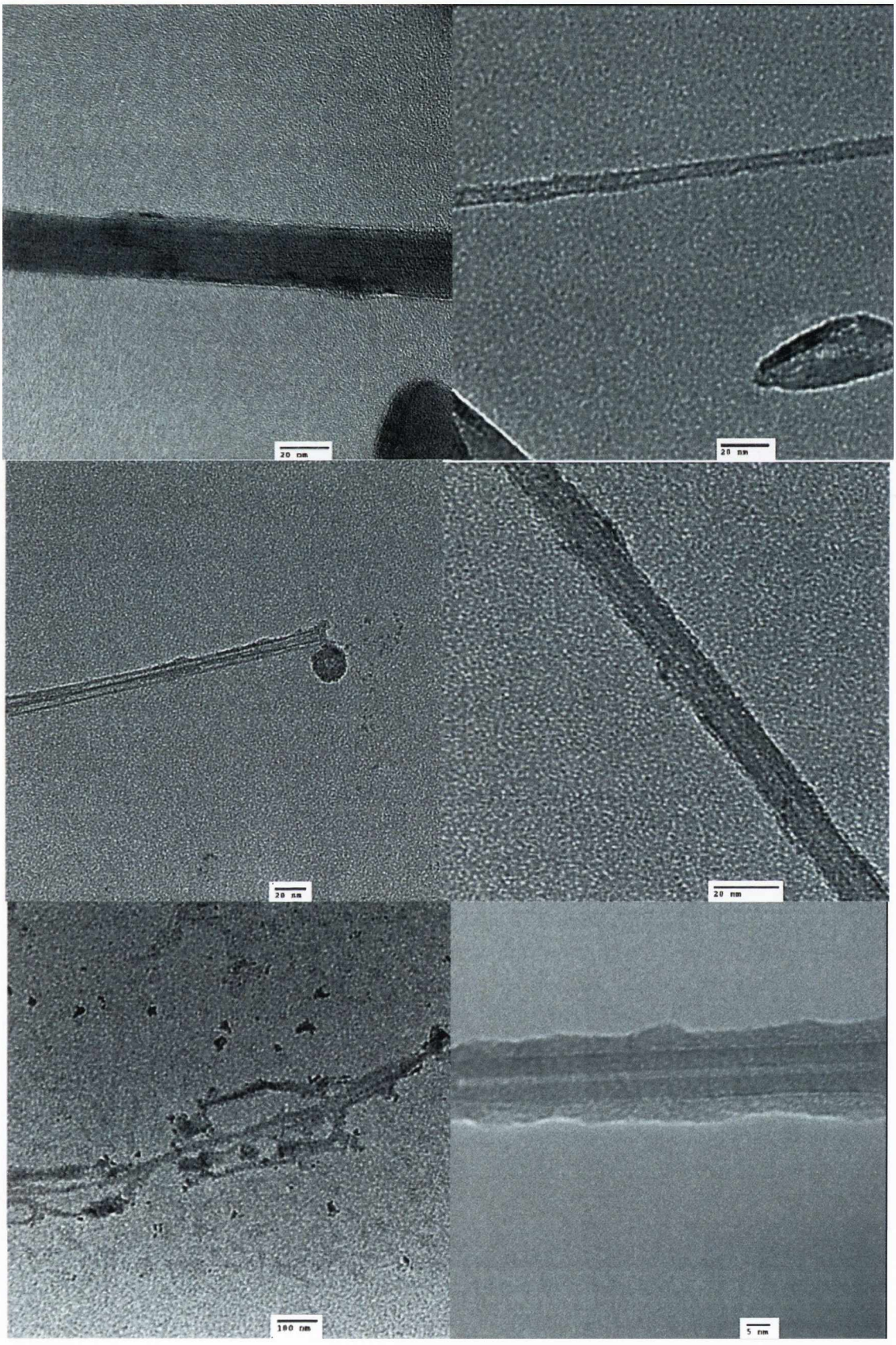

Figure 7.23: Selection of TEM images showing the presence of QDs on the surface of the functionalised graphene.

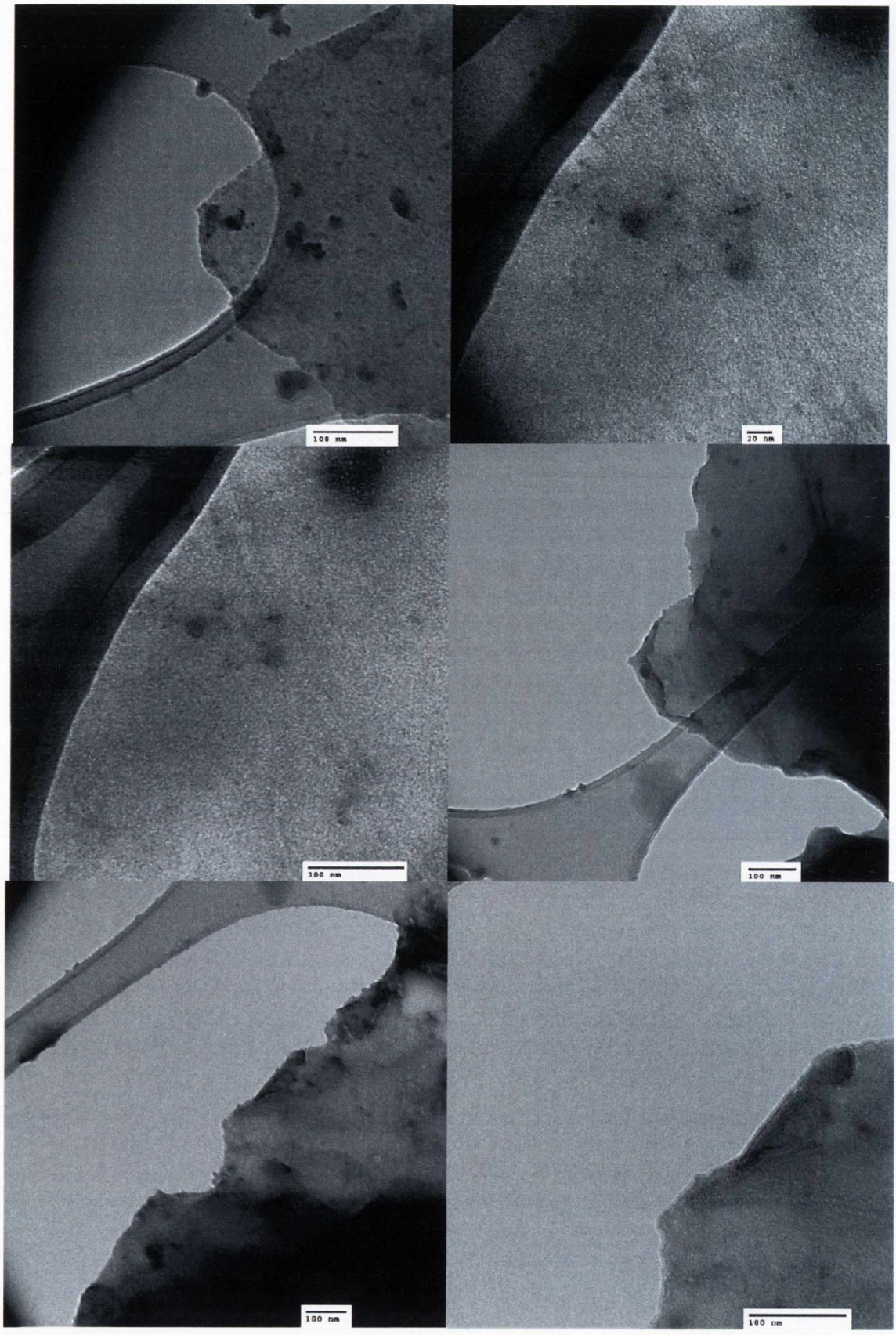

Figure 7.24: Selection of TEM images showing the presence of QDs on the surface of the functionalised graphene.

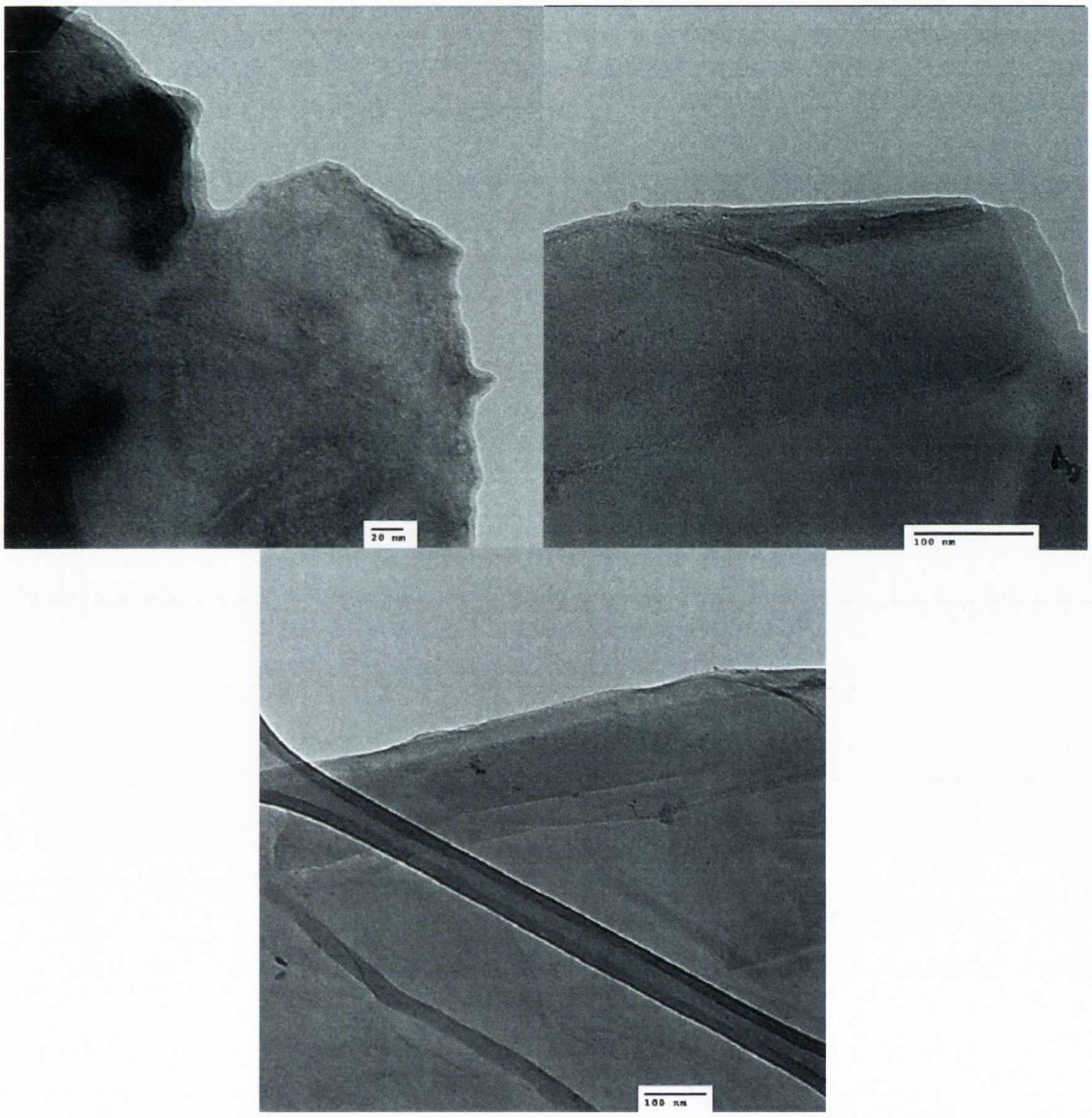

Figure 7.25: Selection of TEM images showing the presence of QDs on the surface of the functionalised graphene.

These composites are now ready to be tested in a solar cell in the nearest future. The approach will utilise the optimised TiO_2 deposition from the earlier section, as this will also serve as the working electrode here. The counter electrode will be a Pt electrode as synthesised previously. The key difference in this cell fabrication is to be the electrolyte. Whereas, in the previous section we used an acetonitrile electrolyte containing dissolved LiI, here we plan to use an ionic liquid based electrolyte, 1-methyl-3-propylimidazolium iodide (Figure 7.26).

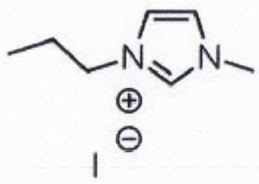

Figure 7.26: Structure of the IL electrolyte, 1-methyl-3-propylimidazolium iodide.

As well as acting as a good electrolyte, setting up the necessary redox couple, an IL such as this should suspend the G-QD and MWNT-QD composites in solution. The attachment of our QDs to the carbon allotropes should also facilitate electron transport, while acting in a secondary role as light harvesters. This work is currently under investigation.

7.8 Conclusions and Future Work

The main result emergin from the first section of this area of research is the successful optimisation of the TiO_2 film deposition to create the working electrode for solar cell fabrication. This allows for savings in both cost and time to be realised when further work is to be carried out. Following from this, as the QD doping of the TiO_2 was low, improvement in this is the obvious next step for the production of a successful, efficient, final QDSSC device. Possible methods for this are already being explored, for example ligand exchange has been shown to help loading of the QDs onto the TiO_2 surface and this is to be pursued in the future. The focus of future work will be mainly on using intrinsic CdTe QDs, as they yielded the best efficiency, 0.16% for any cell. Investigations using broadband emitting CdSe QDs will also continue and the concept of whether these QDs were the reason for enhanced efficiency over CdTe in the SolarPrint based electrode situation is also to be determined.

The second part of this research focused on the synthesis of several different QD-carbon composite nanomaterials. This was successfully realised and these materials are due to undergo testing in a DSSC very shortly by incorporation into an

ionic liquid electrolyte. This research also draws on the success of the earlier cell fabrication and optimisation process.

We expect that this research will lead to the fabrication of a new solar cell based on our novel QDs. We hope to produce these types of cells at low cost and achieve reasonably solar efficiency comparable to the current literature.

References

(1) Nozik, A. J. *Annual Review of Physical Chemistry* **2001**, *52*, 193.

(2) Tisdale, W. A.; Williams, K. J.; Timp, B. A.; Norris, D. J.; Aydil, E. S.; Zhu, X.-Y. *Science* **2010**, *328*, 1543.

(3) Stubbs, S. K.; Hardman, S. J. O.; Graham, D. M.; Spencer, B. F.; Flavell, W. R.; Glarvey, P.; Masala, O.; Pickett, N. L.; Binks, D. J. *Physical Review B* **2010**, *81*, 081303.

(4) Beard, M. C.; Knutsen, K. P.; Yu, P.; Luther, J. M.; Song, Q.; Metzger, W. K.; Ellingson, R. J.; Nozik, A. J. *Nano Letters* **2007**, *7*, 2506.

(5) Kim, S. J.; Kim, W. J.; Sahoo, Y.; Cartwright, A. N.; Prasad, P. N. *Applied Physics Letters* **2008**, *92*, 031107.

(6) Kamat, P. V. *The Journal of Physical Chemistry C* **2008**, *112*, 18737.

(7) Wang, X.; Koleilat, G. I.; Tang, J.; Liu, H.; Kramer, I. J.; Debnath, R.; Brzozowski, L.; Barkhouse, D. A. R.; Levina, L.; Hoogland, S.; Sargent, E. H. *Nat Photon* **2011**, *5*, 480.

(8) Fuke, N.; Hoch, L. B.; Koposov, A. Y.; Manner, V. W.; Werder, D. J.; Fukui, A.; Koide, N.; Katayama, H.; Sykora, M. *ACS Nano* **2010**, *4*, 6377.

(9) Semonin, O. E.; Luther, J. M.; Choi, S.; Chen, H.-Y.; Gao, J.; Nozik, A. J.; Beard, M. C. *Science* **2011**, *334*, 1530.

(10) Saito, R. D. *Imperial College Press* **2001**.

(11) Frank, S. P., P.; Wang, Z. L.; Heer, W. A. n. d. *Science* **1998**, *280*, 1744.

(12) Byrne, M. T.; Gun'ko, Y. K. *Advanced Materials* **2010**, *22*, 1672.

(13) Sgobba, V.; Guldi, D. M. *Journal of Materials Chemistry* **2008**, *18*, 153.

(14) Wang, X.; Zhi, L.; Mullen, K. *Nano Letters* **2007**, *8*, 323.

(15) Kazaoui, S.; Minami, N.; Nalini, B.; Kim, Y.; Hara, K. *Journal of Applied Physics* **2005**, *98*, 084314.

(16) Chen, P. Y.; Lee, C. P.; Vittal, R.; Ho, K. C. *J. Power Sources* **2010**, *195*, 3933.

(17) Lee, C.-P.; Chen, P.-Y.; Vittal, R.; Ho, K.-C. *Journal of Materials Chemistry* **2010**, *20*, 2356.

(18) Usui, H.; Matsui, H.; Tanabe, N.; Yanagida, S. *Journal of Photochemistry and Photobiology A: Chemistry* **2004**, *164*, 97.

(19) Papageorgiou, N.; Athanassov, Y.; Armand, M.; Bonhote, P.; Pettersson, H.; Azam, A.; Gratzel, M. *Journal of The Electrochemical Society* **1996**, *143*, 3099.

(20) Ferrari, A. C. M., J. C.; Scardaci, V.; Casiraghi, C.; Lazzeri, M.; Mauri, F.; Piscanec, S.; Jiang, D.; Novoselov, K. S.; Roth, S.; Geim, A. K. *Physical Review Letters* **2006**, *97*, 187401.

(21) Rogers, R. D.; Seddon, K. R. *Science* **2003**, *302*, 792.

(22) Gratzel, M. *Nature* **2001**, *414*, 338.

(23) Fukushima, T.; Aida, T. *Chemistry – A European Journal* **2007**, *13*, 5048.

(24) Kubo, W.; Kambe, S.; Nakade, S.; Kitamura, T.; Hanabusa, K.; Wada, Y.; Yanagida, S. *The Journal of Physical Chemistry B* **2003**, *107*, 4374.

(25) Noda, A.; Hayamizu, K.; Watanabe, M. *The Journal of Physical Chemistry B* **2001**, *105*, 4603.

(26) Ito, S.; Kitamura, T.; Wada, Y.; Yanagida, S. *Solar Energy Materials & Solar Cells* **2003**, *76*, 3.

(27) Lee, K. E.; Charbonneau, C.; Shan, G.; Demopoulos, G. P.; Gauvin, R. *JOM* **2009**, *61*, 52.

(28) Petrone, L.; McQuillan, A. J. *Appl. Spectrosc.* **2011**, *65*, 1162.

(29) Lee, K. E.; Gomez, M. A.; Elouatik, S.; Demopoulos, G. P. *Langmuir* **2010**, *26*, 9575.

(30) Bae, E.; Choi, W.; Park, J.; Shin, H. S.; Kim, S. B.; Lee, J. S. *The Journal of Physical Chemistry B* **2004**, *108*, 14093.

(31) Ju, T.; Graham, R. L.; Zhai, G.; Rodriguez, Y. W.; Breeze, A. J.; Yang, L.; Alers, G. B.; Carter, S. A. *Applied Physics Letters* **2010**, *97*, 043106.

(32) Sainsbury, T.; Fitzmaurice, D. *Chem. Mater.* **2004**, *16*.

(33) Li, X.; Liu, Y.; Fu, L.; Cao, L.; Wei, D.; Y., W. *Advanced Functional Materials* **2006**, *16*, 2431.

(34) Satti, A.; Larpent, P.; Gun'ko, Y. *Carbon* **2010**, *48*, 3376.

Chapter 8: Conclusions and Future Work

8.1 Conclusion

In this work, a series of new nanoparticles and nanocomposite materials based on cadmium II-VI semiconducting quantum dots have been prepared and investigated. These materials could have a broad range of potential applications in the areas of nanotechnology, chemistry, biosciences and solar technology.

Aqueous CdTe TGA capped QDs were successfully synthesised and characterised in detail. Using these QDs, novel QD-lanthanide conjugate systems were successfully prepared by binding of a Eu(III) cyclen complex. It was found that binding occurs *via* coordination of the COO^- of the TGA. We have demonstrated that the QDs are extremely sensitive to the presence of the Eu ion, with detection on the nanomolar concentration range achieved. The mechanism is understood to be electron transfer from the QD to the Eu(III), which is accompanied by reduction of Eu(III) to Eu(II). This system was demonstrated to be moderately successful for use as an off/on sensor for a selected biologically relevant molecule. This paves the way for potential application of this nanocomposite in the field of bioterrorism defence and assessment of sterile environments.

Three systems, which are based on CdTe TGA QDs and three separate porphyrin molecules have been studied. In the case of the free-base porphyrin, deprotonation of the central porphyrin hydrogen was shown to occur, highlighting a new ability of our QDs to act as deprotonating agents. Quenching of the emission occurred on formation of these conjugates in all three cases. The possibility of multiple binding has been proven and it has been shown that larger assemblies of these composites exist in solution. Ultrafast transient absorption spectroscopy has shown evidence for highly efficient electron transfer from the QD to the porphyrin moiety. These composites thus hold promise for use as, but not limited to, charge separation and light harvesting species in solar devices.

A range of novel chiral CdSe and CdTe nanoparticles were prepared with the use of chiral amino acid stabilisers. The CdSe QDs showed a very broad distribution of photoluminescence which originates from emissive defect states. It is also apparent that

there must be a range of states associated with each individual QD, with the shift of the emission band to longer wavelengths at longer times after excitation, suggesting traps of varying depth. In addition, strongly luminescent but weakly CD active cysteine stabilized CdTe quantum dots were produced. The quantum efficiency of these dots is strongly dependant on the ratio of enantiomers used as stabilizers. We have also shown that the CD activity of CdTe QDs can be introduced by utilizing the mixture of two different stabilizers (Pen and Cys) of the same chirality. This resulted in enhanced CD activity, but causes a decrease in the quantum yield and widening of the emission due to the presence of chiral defects at the nanoparticle surface. These QDs have strong potential for applications such as fluorescent chemical and biochemical chirality sensors or nanoprobes in asymmetric synthesis, catalysis, enantioseparation, biochemical analysis and medical diagnostics.

In addition, the electronic dynamics of novel chiral CdSe quantum dots were successfully investigated in depth, and it was demonstrated that they are determined by both exciton interactions and the trapping at defect sites. This study has highlighted that transient absorption in the ultrafast scale originates from the lowest lying electron quantized state and that the rate of depopulation of this state is both multiexponential in nature, and strongly power dependent. We have also provided direct evidence that there are, in the electronic structure, non-emitting and relatively long-lived (up to the millisecond timescale), deep levels which constitute additional, competitive deactivation channels to the photoluminescence. The successful synthesis of CdSe Pen was also achieved in D_2O, showing for the first time, isotope effects in QD synthesis.

Finally, the successful fabrication of a high quality titanium dioxide based working electrode for use in a photovoltaic device has been realised through extensive optimisation. This allows for savings in both cost and time to be realised in further developing this area of research. Following on from this, the use of our novel chiral QDs as dye replacements in a DSSC was investigated, though met with little success. Novel QD-carbon composites were prepared, covalently binding these QDs to both MWNTs and graphene. Testing of these nanomaterials in a DSSC is still underway. If successful, these materials could find use as additives to electrolytes, increasing charge transport and efficiency in solar cells.

Overall, we expect that the new nanomaterials developed in this project will also find a broader range of potential applications. We believe that our research will contribute to further progress of relevant areas of nanotechnology, chemistry, biosciences, photonics and solar cell technology.

8.2 Future Work

As has been shown in this work, the nanomaterials synthesised and investigated here may have a great potential. Several areas of interest have emerged from the research undertaken for this thesis as potential avenues for future work.

Specifically, the development of our CdTe-Eu conjugate as a sensor for dpa is to be pursued further, investigating the limits of sensitivity offered by this system, as well as testing a wider variety of molecules. The reasons behind the irreversible quenching of QD emission is also of interest.

Future work with the QD-porphyrin conjugates is to be based around investigating both the free-base-QD and PtP-QD systems using transient absorption, in an attempt to further determine the mechanism of emission quenching and corroborate the findings from our work with QD-ZnP. Coupled with the findings from this work, the use of CdTe TGA QDs as deprotonating agents is also of great interest.

With our chiral CdSe QDs, the luminescence originates from defect traps of varying depth. If this is indeed the case then it is unlikely that the particles will show circularly polarised emission, but this is to be confirmed in future experiments. Photophysical measurements (and in particular transient absorption measurements) are also planned to better characterise the complex luminescence dynamics exhibited by these unique species.

Further research will include detailed studies of the photophysical properties of CdSe and CdTe QDs with different chiral stabilizers and the investigation of the electron transfer and energy transfer processes in these systems. We believe that our approach can be used for development of many other QDs with controlled chirality, quantum yield, photochemical and photophysical characteristics.

Testing of these chiral CdSe QDs in a biological application is currently underway, in collaboration with Dr. Tatsiana Rakovich, and preliminary results from cell studies available. They have shown that remarkably these chiral QDs exhibit very low cytotoxicity effect. The results are shown below for CdSe-Cys (Figure 8.1) and CdSe-Pen (Figure 8.2) and graphed against CdTe QDs for comparison. This negligible toxicity is evidenced by the static levels observed in both lysosomal activity (it would increase if cell is taking up quantum dots which are toxic, as observed in CdTe), and permeability (which would also increase if the cells are stressed).

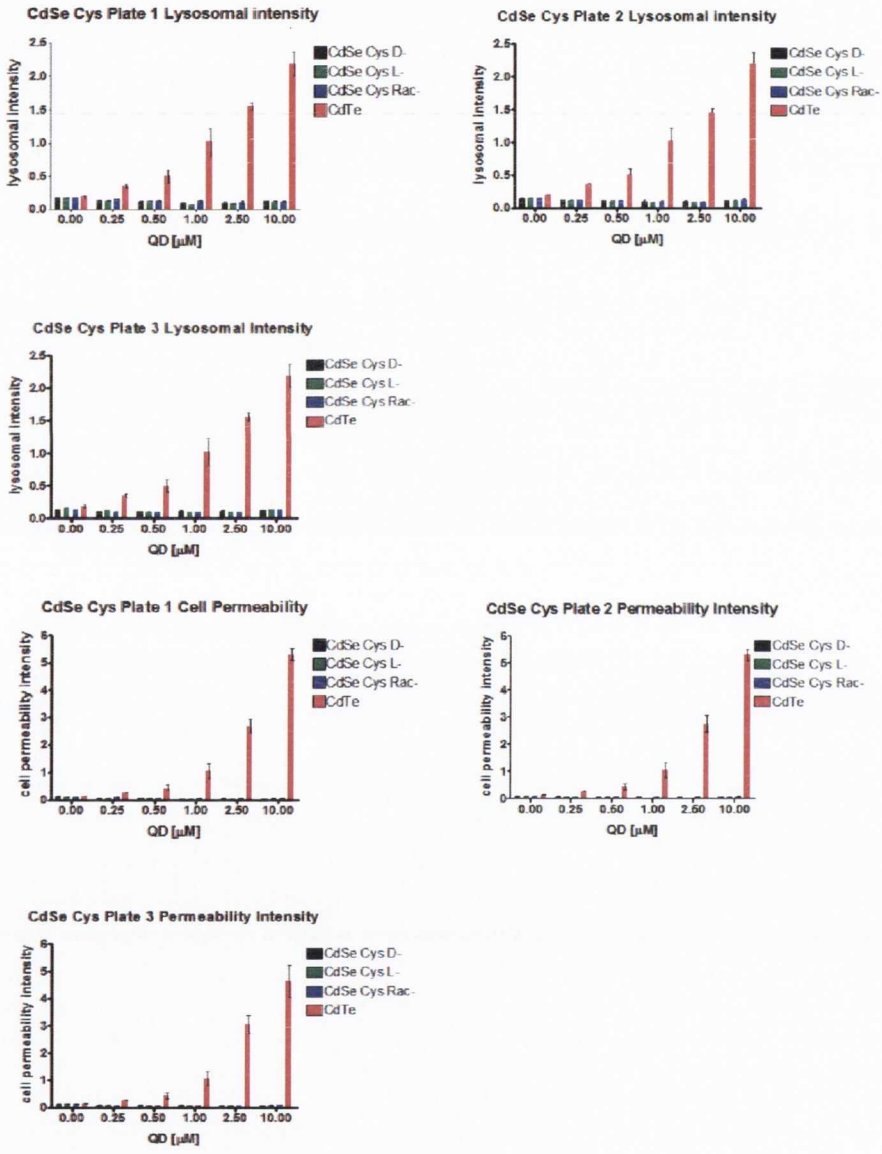

Figure 8.1: Graphs of (top) lysosomal activity, and (bottom) cell permeability intensity with increasing concentration of CdSe-Cys QDs. CdTe QDs plotted for comparison.

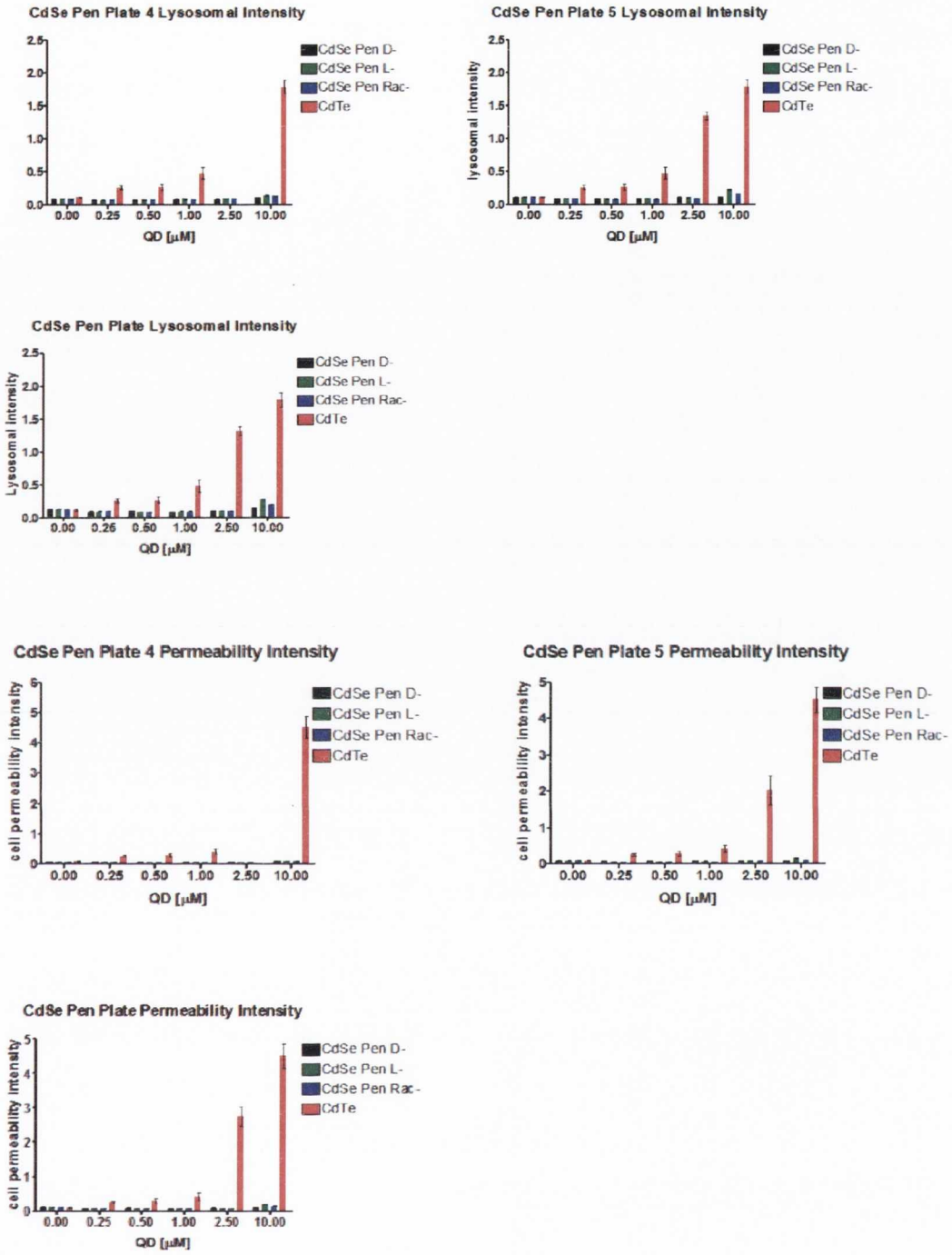

Figure 8.2: Graphs of (top) lysosomal activity, and (bottom) cell permeability intensity with increasing concentration of CdSe-Pen QDs. CdTe QDs plotted for comparison.

An interesting effect was however seen in the cell count graphs which showed an increase with the increasing concentration of quantum dots. The cell number increased with the increased quantum dot concentration more so with the CdSe Cys

QDs (Figure 8.3) than with CdSe Pen QDs (Figure 8.4), but this decrease in not significant when compared to negative control of CdTe quantum dots.

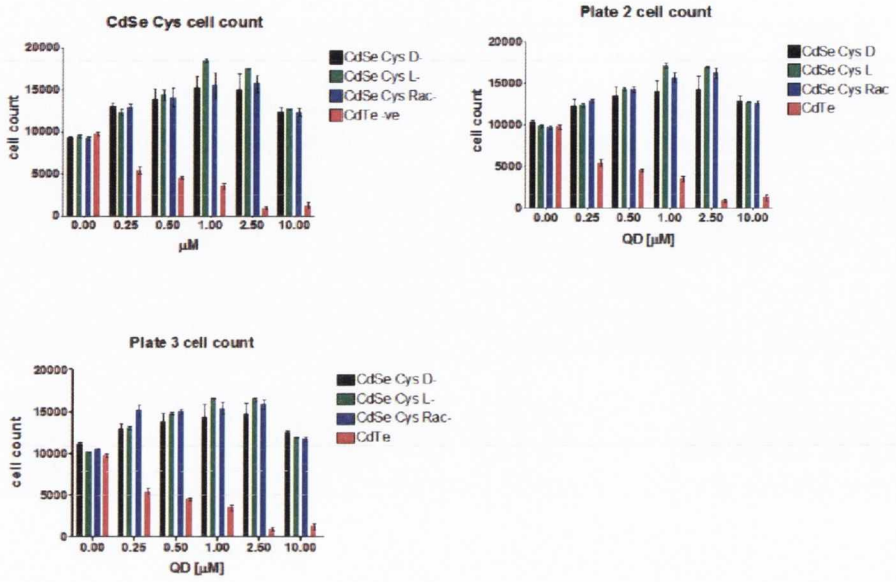

Figure 8.3: Cell count graphs with increasing concentration of CdSe-Cys QDs. CdTe QDs plotted for comparison.

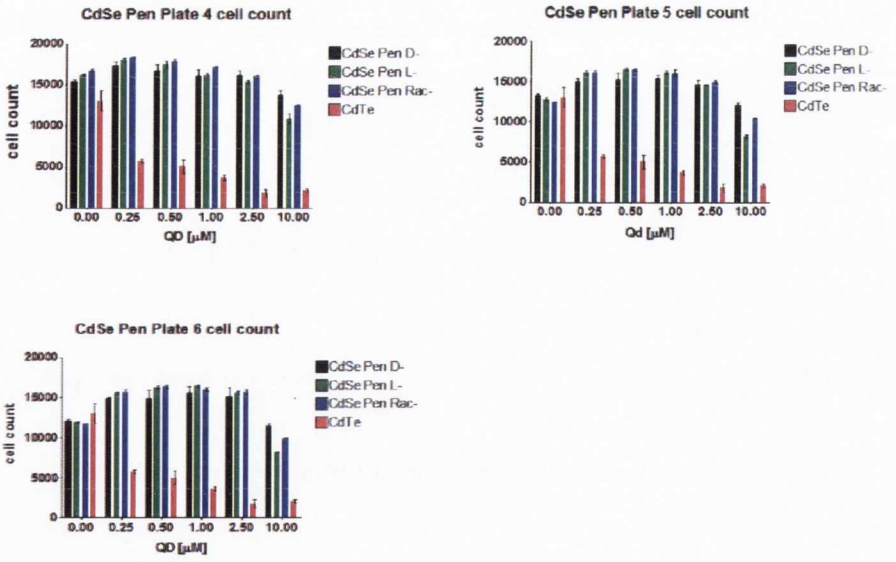

Figure 8.4: Cell count graphs with increasing concentration of CdSe-Pen QDs. CdTe QDs plotted for comparison.

The effects causing such unusual cell growth behaviour are still to be thoroughly investigated but with their lack of cytotoxicity, it appears these chiral QDs are ideally suited for application in areas such as *in vitro* biological imaging and biochemical chirality sensors or nanoprobes for biochemical analysis and potentially medical diagnostics.

Another direction of interest that is to be pursued is the effect of D_2O on the synthesis of QDs. The lack of literature regarding isotope effects on the synthesis of nanoparticles makes this an entirely new area of research, and a thorough investigation into the observed behaviour is to be undertaken in the near future, such as comparison of H_2O and D_2O reactions under conventional heating and the results of the corresponding spectroscopic studies.

Finally, as the QD doping of the TiO_2 was low, an improvement on this is the obvious next step for the production of a successful, efficient, final QDSSC device. Possible methods for this are already being explored, for example ligand exchange has shown to help loading of the QDs onto the TiO_2 surface. The focus of future work will primarily be on using intrinsic CdTe QDs, as they yielded the best efficiency, 0.16% for any cell. Investigations using broadband emitting CdSe QDs will also continue and the concept of whether these QDs were the reason for enhanced efficiency over CdTe in the SolarPrint based electrode situation is also to be determined. The optimisation of the working electrode also allows for testing of a wide range of possible light harvesting materials, such as the QD-porphyrin composites detailed earlier, as well as other novel types of QDs. The investigation of the prepared QD-carbon composites as electrolyte additives in a DSSC is also to be carried out. Further future work on solar cells will involve the investigation of the potential of the QD-MWNT and QD-GO composites in replacing the TiO_2 as the working electrode.

Publications

- **Features of the interaction of quantum dots in CdSe and CdTe systems**
  Anna. V. Savel'eva, Shane A. Gallagher, Alexei. V. Baranov, and Yurii Gun'ko
  J. Opt. Technol., **2011**, 78, 149-150.

- **Synthesis and spectroscopic studies of chiral CdSe quantum dots**
  Shane A. Gallagher, Mícheál P. Moloney, Michal Wojdyla, Susan J. Quinn, John M. Kelly and Yurii K. Gun'ko
  J. Mater. Chem., **2010**, 20, 8350-8355.

- **New quantum dot sensors**
  Yurii. K. Gun'ko, Mícheál. P. Moloney, Shane A. Gallagher, Joseph E. Govan and Cormac Hanley
  Proceedings SPIE, **2010**, 7679, 76791V

- **Chiral CdTe Quantum Dots**
  Mícheál P Moloney, Shane A. Gallagher and Yurii K Gun'ko
  Proceedings MRS, **2009**, 1241: 1241-XX02-10.

- **Ultrafast transient absorption studies on CdTe and chiral CdSe quantum dots**
  Michal Wojdyla, Shane A. Gallagher, Yurii K Gun'ko, John M. Kelly, Susan J. Quinn, Ian. P. Clark, Greg. M. Greetham, Mike Towrie
  Central Laser Facility Annual Report, **2008/2009**, 193-196.

- **Picosecond to Millisecond Transient Absorption Spectroscopy of Chiral CdSe-Penicillamine Quantum Dots**
  Michal Wojdyla, Shane A. Gallagher, Mícheál P. Moloney, Yurii K. Gun'ko, John M. Kelly, Luis M. Magno, Susan J. Quinn, Ian. P. Clark, Greg. M. Greetham and Mike Towrie
  J Phys Chem C, **2012**, *Approved.*

Presentations

Presentations

- **Synthesis and Spectroscopic Studies of Chiral and Achiral Quantum Dots**, 63rd Irish Universities Chemistry Research Colloquium, UCD, Ireland, *24th June 2011.*

- **Synthesis and Spectroscopic Studies of Chiral CdSe Quantum Dots**, Dublin Chemistry Graduate Seminar Programme, UCD, Ireland, *26th May, 2010.*

Poster Presentations

- **Synthesis and Spectroscopic Studies of Chiral CdSe Quantum Dots**, SFI Meeting, Trinity College Dublin, Ireland, *12th May, 2011.*

- **Synthesis and Spectroscopic Studies of Chiral CdSe Quantum Dots**, International Materials Research Congress (MRS), Cancun, *17th August, 2010.*